frontiers | Research Topics

Image-guided particle therapy

Edited by
Lanchun Lu, Heng Li, Lin Kong, Marco Durante and Oliver Jäkel

Published in
Frontiers in Oncology

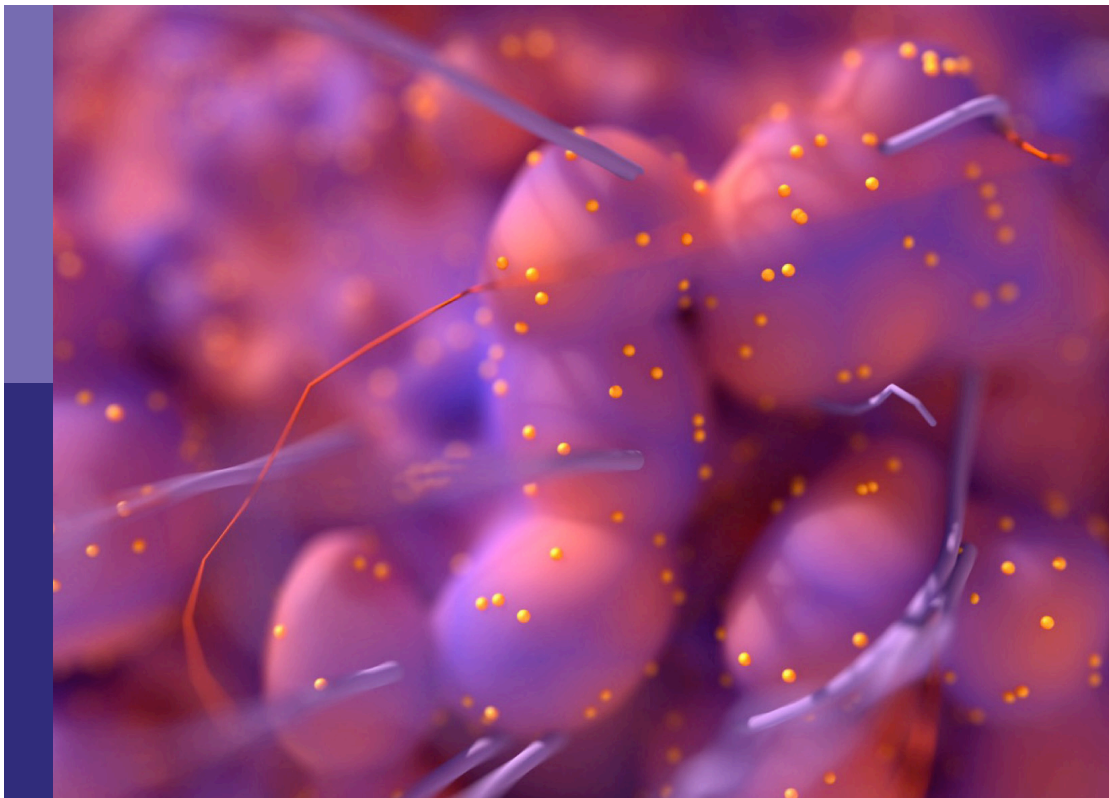

ISSN 1664-8714
ISBN 978-2-8325-2209-7
DOI 10.3389/978-2-8325-2209-7

About Frontiers

Frontiers is more than just an open access publisher of scholarly articles: it is a pioneering approach to the world of academia, radically improving the way scholarly research is managed. The grand vision of Frontiers is a world where all people have an equal opportunity to seek, share and generate knowledge. Frontiers provides immediate and permanent online open access to all its publications, but this alone is not enough to realize our grand goals.

Frontiers journal series

The Frontiers journal series is a multi-tier and interdisciplinary set of open-access, online journals, promising a paradigm shift from the current review, selection and dissemination processes in academic publishing. All Frontiers journals are driven by researchers for researchers; therefore, they constitute a service to the scholarly community. At the same time, the *Frontiers journal series* operates on a revolutionary invention, the tiered publishing system, initially addressing specific communities of scholars, and gradually climbing up to broader public understanding, thus serving the interests of the lay society, too.

Dedication to quality

Each Frontiers article is a landmark of the highest quality, thanks to genuinely collaborative interactions between authors and review editors, who include some of the world's best academicians. Research must be certified by peers before entering a stream of knowledge that may eventually reach the public - and shape society; therefore, Frontiers only applies the most rigorous and unbiased reviews. Frontiers revolutionizes research publishing by freely delivering the most outstanding research, evaluated with no bias from both the academic and social point of view. By applying the most advanced information technologies, Frontiers is catapulting scholarly publishing into a new generation.

What are Frontiers Research Topics?

Frontiers Research Topics are very popular trademarks of the *Frontiers journals series*: they are collections of at least ten articles, all centered on a particular subject. With their unique mix of varied contributions from Original Research to Review Articles, Frontiers Research Topics unify the most influential researchers, the latest key findings and historical advances in a hot research area.

Find out more on how to host your own Frontiers Research Topic or contribute to one as an author by contacting the Frontiers editorial office: frontiersin.org/about/contact

Image-guided particle therapy

Topic editors

Lanchun Lu — The Ohio State University, United States
Heng Li — The Johns Hopkins Hospital, Johns Hopkins Medicine, United States
Lin Kong — Fudan University, China
Marco Durante — GSI Helmholtz Center for Heavy Ion Research, Helmholtz Association of German Research Centres (HZ), Germany
Oliver Jäkel — German Cancer Research Center (DKFZ), Germany

Citation

Lu, L., Li, H., Kong, L., Durante, M., Jäkel, O., eds. (2023). *Image-guided particle therapy*. Lausanne: Frontiers Media SA. doi: 10.3389/978-2-8325-2209-7

Table of contents

05 Editorial: Image-guided particle therapy
Heng Li, Marco Durante, Oliver Jäkel, Lin Kong and Lanchun Lu

08 Linear Energy Transfer Incorporated Spot-Scanning Proton Arc Therapy Optimization: A Feasibility Study
Xiaoqiang Li, Xuanfeng Ding, Weili Zheng, Gang Liu, Guillaume Janssens, Kevin Souris, Ana M. Barragán-Montero, Di Yan, Craig Stevens and Peyman Kabolizadeh

17 Radioactive Beams for Image-Guided Particle Therapy: The BARB Experiment at GSI
Daria Boscolo, Daria Kostyleva, Mohammad Javad Safari, Vasiliki Anagnostatou, Juha Äystö, Soumya Bagchi, Tim Binder, Georgios Dedes, Peter Dendooven, Timo Dickel, Vasyl Drozd, Bernhard Franczack, Hans Geissel, Chiara Gianoli, Christian Graeff, Tuomas Grahn, Florian Greiner, Emma Haettner, Roghieh Haghani, Muhsin N. Harakeh, Felix Horst, Christine Hornung, Jan-Paul Hucka, Nasser Kalantar-Nayestanaki, Erika Kazantseva, Birgit Kindler, Ronja Knöbel, Natalia Kuzminchuk-Feuerstein, Bettina Lommel, Ivan Mukha, Chiara Nociforo, Shunki Ishikawa, Giulio Lovatti, Munetaka Nitta, Ikechi Ozoemelam, Stephane Pietri, Wolfgang R. Plaß, Andrej Prochazka, Sivaji Purushothaman, Claire-Anne Reidel, Heidi Roesch, Fabio Schirru, Christoph Schuy, Olga Sokol, Timo Steinsberger, Yoshiki K. Tanaka, Isao Tanihata, Peter Thirolf, Walter Tinganelli, Bernd Voss, Uli Weber, Helmut Weick, John S. Winfield, Martin Winkler, Jianwei Zhao, Christoph Scheidenberger, Katia Parodi, Marco Durante and the Super-FRS Experiment Collaboration

32 Robust Angle Selection in Particle Therapy
Yuan Zhou, Yang Li, Yoshiki Kubota, Makoto Sakai and Tatsuya Ohno

46 Investigate the Dosimetric and Potential Clinical Benefits Utilizing Stereotactic Body Radiation Therapy With Simultaneous Integrated Boost Technique for Locally Advanced Pancreatic Cancer: A Comparison Between Photon and Proton Beam Therapy
Peilin Liu, Xian-shu Gao, Zishen Wang, Xiaomei Li, Xi Cao, Chenghao Jia, Mu Xie, Feng Lyu, Shiyu Shang and Xuanfeng Ding

58 Erratum: Investigate the Dosimetric and Potential Clinical Benefits Utilizing Stereotactic Body Radiation Therapy With Simultaneous Integrated Boost Technique for Locally Advanced Pancreatic Cancer: A Comparison Between Photon and Proton Beam Therapy
Frontiers Production Office

60 Predicting Disease-Free Survival With Multiparametric MRI-Derived Radiomic Signature in Cervical Cancer Patients Underwent CCRT
Bing Liu, Zhen Sun, Zi-Liang Xu, Hong-Liang Zhao, Di-Di Wen, Yong-Ai Li, Fan Zhang, Bing-Xin Hou, Yi Huan, Li-Chun Wei and Min-Wen Zheng

71 Experimental Comparison of Fiducial Markers Used in Proton Therapy: Study of Different Imaging Modalities and Proton Fluence Perturbations Measured With CMOS Pixel Sensors
Claire-Anne Reidel, Felix Horst, Christoph Schuy, Oliver Jäkel, Swantje Ecker, Katrin Henkner, Stephan Brons, Marco Durante and Uli Weber

89 Evaluating Proton Dose and Associated Range Uncertainty Using Daily Cone-Beam CT
Heng Li, William T. Hrinivich, Hao Chen, Khadija Sheikh, Meng Wei Ho, Rachel Ger, Dezhi Liu, Russell Kenneth Hales, Khinh Ranh Voong, Aditya Halthore and Curtiland Deville

100 Imaging Strategies in Proton Therapy for Thoracic Tumors: A Mini Review
Carlo Algranati and Lidia Strigari

106 Considerations for Upright Particle Therapy Patient Positioning and Associated Image Guidance
Lennart Volz, Yinxiangzi Sheng, Marco Durante and Christian Graeff

119 Combined proton radiography and irradiation for high-precision preclinical studies in small animals
Moritz Schneider, Elisabeth Bodenstein, Johanna Bock, Antje Dietrich, Sebastian Gantz, Lena Heuchel, Mechthild Krause, Armin Lühr, Cläre von Neubeck, Sindi Nexhipi, Michael Schürer, Falk Tillner, Elke Beyreuther, Theresa Suckert and Johannes Richard Müller

133 The impact of tumor metabolic activity assessed by ^{18}F-FET amino acid PET imaging in particle radiotherapy of high-grade glioma patients
Maria Waltenberger, Jennifer Furkel, Manuel Röhrich, Patrick Salome, Charlotte Debus, Bouchra Tawk, Aoife Ward Gahlawat, Andreas Kudak, Matthias Dostal, Ute Wirkner, Christian Schwager, Christel Herold-Mende, Stephanie E. Combs, Laila König, Jürgen Debus, Uwe Haberkorn, Amir Abdollahi and Maximilian Knoll

148 *In-vivo* range verification analysis with in-beam PET data for patients treated with proton therapy at CNAO
Martina Moglioni, Aafke Christine Kraan, Guido Baroni, Giuseppe Battistoni, Nicola Belcari, Andrea Berti, Pietro Carra, Piergiorgio Cerello, Mario Ciocca, Angelica De Gregorio, Micol De Simoni, Damiano Del Sarto, Marco Donetti, Yunsheng Dong, Alessia Embriaco, Maria Evelina Fantacci, Veronica Ferrero, Elisa Fiorina, Marta Fischetti, Gaia Franciosini, Giuseppe Giraudo, Francesco Laruina, Davide Maestri, Marco Magi, Giuseppe Magro, Etesam Malekzadeh, Michela Marafini, Ilaria Mattei, Enrico Mazzoni, Paolo Mereu, Alfredo Mirandola, Matteo Morrocchi, Silvia Muraro, Ester Orlandi, Vincenzo Patera, Francesco Pennazio, Marco Pullia, Alessandra Retico, Angelo Rivetti, Manuel Dionisio Da Rocha Rolo, Valeria Rosso, Alessio Sarti, Angelo Schiavi, Adalberto Sciubba, Giancarlo Sportelli, Sara Tampellini, Marco Toppi, Giacomo Traini, Antonio Trigilio, Serena Marta Valle, Francesca Valvo, Barbara Vischioni, Viviana Vitolo, Richard Wheadon and Maria Giuseppina Bisogni

frontiers | Frontiers in Oncology

TYPE Editorial
PUBLISHED 04 April 2023
DOI 10.3389/fonc.2023.1175511

OPEN ACCESS

EDITED AND REVIEWED BY
Zaver Bhujwalla,
School of Medicine, Johns Hopkins University, United States

*CORRESPONDENCE
Heng Li
hengli@jhu.edu

SPECIALTY SECTION
This article was submitted to Cancer Imaging and Image-directed Interventions, a section of the journal Frontiers in Oncology

RECEIVED 27 February 2023
ACCEPTED 24 March 2023
PUBLISHED 04 April 2023

CITATION
Li H, Durante M, Jäkel O, Kong L and Lu L (2023) Editorial: Image-guided particle therapy. *Front. Oncol.* 13:1175511. doi: 10.3389/fonc.2023.1175511

Editorial: Image-guided particle therapy

Heng Li[1]*, Marco Durante[2], Oliver Jäkel[3], Lin Kong[4] and Lanchun Lu[5]

[1]The Johns Hopkins Hospital, Johns Hopkins Medicine, Baltimore, MD, United States, [2]GSI Helmholtz Center for Heavy Ion Research, Helmholtz Association of German Research Centres (HZ), Darmstadt, Germany, [3]Department of Medical Physics in Radiation Oncology, German Cancer Research Center (DKFZ), Heidelberg, Germany, [4]Department of Radiation Oncology, Shanghai Proton and Heavy Ion Center (SPHIC), Shanghai, China, [5]Department of Radiation Oncology, The Ohio State University, Columbus, OH, United States

KEYWORDS

image guidance, particle therapy, radiation oncology, ion beam radiotherapy, proton therapy

Editorial on the Research Topic
Image-guided particle therapy

Particle beam (e.g., Proton and Carbon) therapy has become a popular treatment modality in the field of radiation therapy for cancer treatments (1). Compared with photon beams, particle beams could administer a therapeutic dose to the tumor while limiting the dose to the surrounding healthy tissues or critical organs, thanks to the distinct depth dose distribution of the particle beam, including the characteristic Bragg Peak. Particle therapy has thus become a unique and important cancer treatment modality, with more and more particle therapy facilities have been opened or are going to be opened for clinical practice around the world. However, building a particle therapy facility costs over an order of magnitude higher than a photon therapy facility. The challenges for particle therapy are in three major areas (2) (1): image guidance (2); radiobiology (3); beam configuration and delivery. This edition of Frontiers in Oncology consists of 11 manuscripts (including 8 original research papers and 3 reviews) that cover a broad spectrum of topics associated with image-guided particle therapy.

Algranati and Strigari performed a mini-review on imaging strategies in proton therapy for thoracic tumors. Imaging is essential in a clinic's proton beam treatment workflow: simulation, planning, setup, adaption, monitoring, and delivery. Waltenberger et al. investigated the role of ^{18}F-FET PET in high-grade glioma (HCG) patients. Analyzing ^{18}F-FET-PET data from a total of 76 patients, the authors found that ^{18}F-FET-PET imaging might assist in prognostic stratification of HCG patients, as high SUV max value is linked to worse prognosis and unfavorable whole-blood transcriptome liquid biopsy readouts. ^{18}F-FET-PET on gross tumor volume definition for particle radiotherapy should be further evaluated. The authors, therefore, suggested that larger, prospective studies were warranted.

Range verification, in addition to patient positioning, is crucial to the accurate delivery of particle beam dose. Several image modalities, including PET, CBCT, and proton radiography, were investigated in this edition for this purpose. Boscolo et al. investigated enhancing the PET signal, which could be used for range verification, with radioactive ion

beams for particle therapy. The Biomedical Applications of Radioactive ion Beams (BARB) project aims to treat mice tumors with radioactive ion beams (^{11}C and ^{15}O). The current study showed the system's design and plan comparison that suggests RIB could lead to margin reduction and sparing of the optical nerve in more than 50% of the patients. Schneider et al., on the other hand, reported the combination of proton radiography and irradiation for high-precision radiotherapy of small animals. The authors developed a preclinical experimental setup for small animal brain proton irradiation using proton radiography with a flat panel detector that achieved a lateral target position accuracy of <0.26 mm. Moglioni et al. analyzed patient data acquired with an in-beam Positron Emission Tomography (PET) scanner, which enabled *in-vivo* range monitoring in proton and carbon therapy treatments at the National Center of Oncological Hadrontherapy (CNAO), Italy. Eight patients treated with protons were analyzed in the work, where the author found the overall standard deviation in activity range difference to be 2.5 mm. The author also found a larger observed range difference with PET for patients with morphological changes than those without. Li et al. evaluated the proton range uncertainty with daily cone-beam CT of phantom and patient data. They found that the range uncertainties from CBCT images were larger than from CT but could still be used for daily dose validation in selected patients. Reidel et al. studied the image artifacts in CT, visibility in daily imaging, and dose perturbations in proton beams resulting from different fiducial markers that were composed of different materials, including gold, platinum, and ZrO_2. Notably, high-resolution CMOS pixel sensors were used to quantify fluence perturbations due to fiducial marks in proton beams. The authors found that the perturbations were reduced for small and low-density marks of mass lower than 6mg. The authors thus suggested that the trade-off between image quality and dose perturbation needs to be considered in the fiducial selection for setup.

Advance in imaging also enables advanced treatment delivery techniques requiring precise treatment delivery. Zhou et al. reviewed methods of robust angle selection in particle therapy in various disease sites. The authors noted that with technological development, including improving imaging technologies in particle RT, robust angle selection would become more precise and individualized, improving the effectiveness of particle RT. Li et al. investigated the feasibility of incorporating linear energy transfer (LET) in spot-scanning proton arc therapy optimization. The authors demonstrated that incorporating LET into the proton arc optimization could maximize the LET distribution wherever desired inside the target while averting the high LET away from the adjacent organ at risk. Liu et al. compared the dosimetric and potential benefits of using Stereotactic body radiotherapy (SBRT) with the simultaneous integrated boost (SIB) technique for locally advanced pancreatic cancer. Analyzing 19 patients, the authors found that the tumor location could play a critical role in determining clinical benefits among different treatment modalities: two-field IMPT might be a better option for the pancreas head, whereas VAMT could offer better protection when the tumor is located in the pancreas body. Volz et al. reviewed considerations for upright particle therapy patient positioning and associated image guidance. Based on the literature review, the author found that upright patient positioning could have distinct economic and clinical benefits but also face clinical and engineering challenges in order to achieve highly accurate and stable patient positioning. The authors suggested that the advancement of upright positioning systems, including imaging systems, could bring a paradigm shift for the future of particle therapy.

In summary, the treatment's precision and accuracy are crucial for particle therapy's efficiency and efficacy, partly due to the need to accurately place the Bragg Peak. Imaging is critical throughout particle therapy workflow, improving targeting, dosimetry, and treatment delivery accuracy. Currently, the imaging modalities used for imaging guidance for almost all particle therapy treatments are CBCT or kV X-ray. Although CBCT and kV X-ray guidance are widely accepted image guidance techniques for radiation therapy, there are some well-known limitations for these radiation-based imaging modalities, including poor soft tissue contrast and difficulty performing online/real-time monitoring during treatments and hence the adaptive radiation therapy. Developing imaging techniques that improve soft tissue contrast, such as MRI-guided particle therapy, and real-time image guidance methods, such as PET and prompt gamma imaging, is therefore valuable. Such development would overcome the limitations of state-of-the-art radiation-based imaging guidance and add the capabilities of treatment outcome assessment and prognosis with functional image features and with the potential to reduce the treatment cost of particle therapy. Additionally, incorporating artificial intelligence (AI) in image guidance for particle therapy could further improve the treatment (3). While AI has been implemented for IGRT in some capacity, prospective studies are still required to expand these AI-related applications and realize their potential.

Author contributions

All authors listed have made a substantial, direct, and intellectual contribution to the work and approved it for publication.

Acknowledgments

We thank the authors of the papers published in this Research Topic for their valuable contributions and the referees for their review effort.

Conflict of interest

The authors declare that the research was conducted in the absence of any commercial or financial relationships that could be construed as a potential conflict of interest.

The handling editor ZB declared a shared affiliation with the author HL at the time of review.

Publisher's note

References

1. Durante M, Flanz J. *Charged particle beams to cure cancer: strengths and challenges*. Seminars in oncology (2019) 46(3):219–25.

2. Durante M, Debus J, Loeffler JS. Physics and biomedical challenges of cancer therapy with accelerated heavy ions. *Nat Rev PhyS* (2021) 3(12):777–90. doi: 10.1038/s42254-021-00368-5

3. Zhao W, Shen L, Islam MT, Qin W, Zhang Z, Liang X, et al. Artificial intelligence in image-guided radiotherapy: a review of treatment target localization. *Quantit Imaging Med Surg* (2021) 11(12):4881. doi: 10.21037/qims-21-199

frontiers in Oncology

ORIGINAL RESEARCH
published: 12 July 2021
doi: 10.3389/fonc.2021.698537

Linear Energy Transfer Incorporated Spot-Scanning Proton Arc Therapy Optimization: A Feasibility Study

Xiaoqiang Li[1], Xuanfeng Ding[1], Weili Zheng[1], Gang Liu[1,2], Guillaume Janssens[3], Kevin Souris[4], Ana M. Barragán-Montero[4], Di Yan[1], Craig Stevens[1] and Peyman Kabolizadeh[1]*

[1] Department of Radiation Oncology, Beaumont Health System, Royal Oak, MI, United States, [2] Cancer Center, Union Hospital, Tongji Medical College, Huazhong University of Science and Technology, Wuhan, China, [3] Advanced Technology Group, Ion Beam Applications SA, Louvain-la-Neuve, Belgium, [4] Center for Molecular Imaging and Experimental Radiotherapy, Institut de Recherche Expérimentale et Clinique, UCLouvain, Brussels, Belgium

OPEN ACCESS

Edited by:
Heng Li,
Johns Hopkins Medicine, United States

Reviewed by:
Wenhua Cao,
University of Texas MD Anderson Cancer Center, United States
Chuan Zeng,
Memorial Sloan Kettering Cancer Center, United States

***Correspondence:**
Xiaoqiang Li
Xiaoqiang.Li@beaumont.org

Specialty section:
This article was submitted to Cancer Imaging and Image-directed Interventions, a section of the journal Frontiers in Oncology

Received: *21 April 2021*
Accepted: *22 June 2021*
Published: *12 July 2021*

Citation:
Li X, Ding X, Zheng W, Liu G, Janssens G, Souris K, Barragán-Montero AM, Yan D, Stevens C and Kabolizadeh P (2021) Linear Energy Transfer Incorporated Spot-Scanning Proton Arc Therapy Optimization: A Feasibility Study. Front. Oncol. 11:698537. doi: 10.3389/fonc.2021.698537

Purpose: To integrate dose-averaged linear energy transfer (LET_d) into spot-scanning proton arc therapy (SPArc) optimization and to explore its feasibility and potential clinical benefits.

Methods: An open-source proton planning platform (OpenREGGUI) has been modified to incorporate LET_d into optimization for both SPArc and multi-beam intensity-modulated proton therapy (IMPT) treatment planning. SPArc and multi-beam IMPT plans with different beam configurations for a prostate patient were generated to investigate the feasibility of LET_d-based optimization using SPArc in terms of spatial LET_d distribution and plan delivery efficiency. One liver and one brain case were studied to further evaluate the advantages of SPArc over multi-beam IMPT.

Results: With similar dose distributions, the efficacy of spatially optimizing LET_d distributions improves with increasing number of beams. Compared with multi-beam IMPT plans, SPArc plans show substantial improvement in LET_d distributions while maintaining similar delivery efficiency. Specifically, for the liver case, the average LET_d in the GTV was increased by 124% for the SPArc plan, and only 9.6% for the 2-beam IMPT plan compared with the 2-beam non-LET_d optimized IMPT plan. In case of LET optimization for the brain case, the SPArc plan could effectively increase the average LET_d in the CTV and decrease the values in the critical structures while smaller improvement was observed in 3-beam IMPT plans.

Conclusion: This work demonstrates the feasibility and significant advantages of using SPArc for LET_d-based optimization, which could maximize the LET_d distribution wherever is desired inside the target and averts the high LET_d away from the adjacent critical organs-at-risk.

Keywords: proton therapy, arc therapy, linear energy transfer, plan optimization, spot scanning

INTRODUCTION

In the status quo of clinical proton therapy, most centers use a presumed constant relative biological effectiveness (RBE) value of 1.1 (1, 2) regardless of the dose, linear energy transfer (LET), physiological and biological factors, and clinical endpoint (3, 4). Historically, such RBE value was chosen conservatively for tumor control based on the *in vitro* and *in vivo* measurements at the center of spread-out Bragg Peak (SOBP) (2, 3). Recent experiments (5) and clinical studies (6) show that RBE value may increase towards the distal dose fall-off of SOBP as the LET increases, and this could be up to the magnitude of 1.7 (3). Hence, more than expected rate of toxicities may be seen if the distal end of the Bragg peaks ends up in the adjacent critical structures and such higher rate of toxicities, including necrosis have been reported in multiple studies (7–9). Therefore, being able to manipulate the location of high LET is very helpful to further improve modern proton beam therapy.

Nevertheless, in the era of traditional passive-scattering proton therapy (PSPT) delivery technique, the high LET region is inevitably located at the distal end of each beam and it is impossible to modulate its distribution. To avoid any overlapping high LET regions with the abutting critical organs, it is common to use the beam angles without aiming directly toward those organs. Fortunately, in the past few years, the pencil beam scanning (PBS) technique has emerged and quickly been adopted by new proton centers as the most advanced proton beam delivery technology (10, 11). Intensity-modulated proton therapy (IMPT), based on PBS, optimizes the intensities of individual spot from different energy layers. Compared with the PSPT, IMPT offers not only a more conformal radiation dose (12–14), but also has the potential to modify the LET distribution by incorporating the LET optimization into the planning process (4, 15–21). However, the ability of IMPT to spatially place the LET value is limited by the number of beam angles (22, 23) and thus not clinically feasible given the prolonged PBS treatment delivery time.

Such obstacles could be overcome by using spot-scanning proton arc therapy (SPArc) which is a novel spot scanning delivery technique that can deliver a treatment plan in an arc mode (24). SPArc has manifested significant advantages over the multi-beam IMPT (25–28) to improve dose distributions and delivery. A prototype of SPArc delivery has proven its feasibility on a state-of-the-art proton therapy system (29). Since the SPArc plans are delivered from hundreds of beam angles selected from a smart energy and spot selection algorithm (24), we hypothesize that with such increased degrees of freedom for optimization, SPArc can further improve the LET distribution while maintaining the delivery efficiency. Thus, we develop a novel LET-based SPArc optimization algorithm and explore its potential to improve the spatial LET distribution.

Abbreviations: LET_d, dose-averaged linear energy transfer; SPArc, spot-scanning proton arc therapy; MPT, intensity-modulated proton therapy; RBE, relative biological effectiveness; SOBP, spread-out Bragg Peak; SPT, passive-scattering proton therapy; PBS, pencil beam scanning; OARs, organs-at-risk; DVH, dose-volume histogram; LVH, LET_d-volume histogram; 2B w/o, 2-beam IMPT plan without LET_d optimization; SIB, simultaneously integrated boost; GTV, gross tumor volume.

METHODS AND MATERIALS

Dose-Averaged LET (LET_d)-Based SPArc Optimization Workflow

The LET_d-based SPArc optimization engine was implemented based on an open-source proton planning platform (OpenREGGUI) (30). This platform uses a fast Monte Carlo dose calculation engine (MCSquare) (31–33) and an optimizer (MIROpt) (34) for dose-based multi-beam IMPT planning. Such platform was modified to incorporate the LET_d-based objective functions (*e.g.*, minimum and maximum LET_d) into optimization and to iteratively generate the SPArc plans (24, 29). The details of LET_d-based SPArc planning implementation is shown in **Figure 1** which consists of (1) the planner defines the arc start and stop angles, (2) the engine coarsely samples the initial beams (3) the MCSquare calculates the voxel dose and LET_d values from each spot, (4) the optimizer finds a solution by iteratively calculating the dose and LET_d and minimizing the dose and LET_d based objective functions for target volume and organs-at-risk (OARs), (5) iteratively increases the beam sampling frequency and reduces the energy layers by repeating step (3) and (4) until desired sampling frequency is reached, (6) and finally, perform deliverable optimization by specifying the minimum MU (0.02 MU) per spot. The details of the LET implementation are described as follow.

LETd Optimization Implementation

In MCSquare calculation, the 'stopping power' method (35) was selected, in which LET_d was scored by dose-weighted average of the stopping power of particles through each voxel (36). Secondary particles were handled by specifying the options in the configuration file as: secondary photons and neutrons are not taken into account while the secondary electrons are considered as locally absorbed. Secondary protons, deuterons, and alpha's are simulated for the dose and LET_d. The calculated dose and LET values from each spot j projected to voxel i are expressed as (D_{ij} and LET_{ij}). The dose and dose-averaged LET value for voxel i can be calculated from the intensity (monitor unit) of the spot j (ω_j) as follow:

$$D_i = \Sigma_j D_{ij} \omega_j \tag{1}$$

$$LET_i = \frac{\Sigma_j LET_{ij} D_{ij} \omega_j}{\Sigma_j D_{ij} \omega_j} \tag{2}$$

For the optimization, we used a standard quadratic objective function to control both dose and LET_d distributions:

$$\begin{aligned} Obj(w_j) &= Obj_{dose}(w_j) + Obj_{LET(w_j)} \\ &= \sum_{i \in CTV} P_{CTV}(D_i - D_{0,CTV})^2 \\ &+ \sum_{i \in OARs} P_{OARs} H(D_i - D_{0,OARs})(D_i - D_{0,OARs})^2 \\ &+ \sum_{i \in CTV} P_{CTV,LET} H(LET_{0,CTV} - LET_i)(LET_i - LET_{0,CTV})^2 \\ &+ \sum_{i \in OARs} P_{OARs,LET} H(LET_i - LET_{0,OARs})(LET_i - LET_{0,OARs})^2 \end{aligned} \tag{3}$$

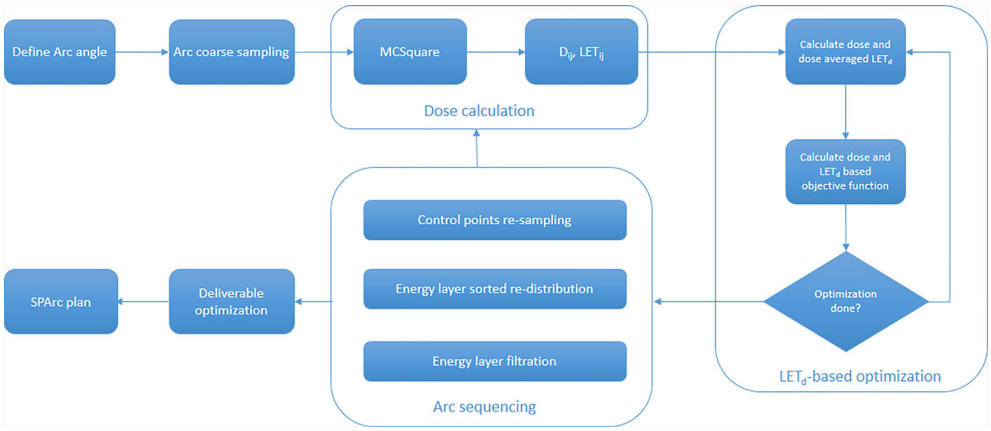

Figure 1 The workflow of LET_d based SPArc optimization engine.

where p denotes the penalty weights, D_0 and LET_0 correspond to the target or constraint dose and LET value respectively. The Heaviside step function $H(D_i - D_0)$ is defined as convention (*i.e.*, equals to unity if $D_i > D_0$, otherwise equals to zero). Dose-based, dose volume based, and LET-based objective functions are implemented and used for this study.

Treatment Planning

All the SPArc and multi-beam IMPT plans (without arc sequencing part in **Figure 1**) were generated using this optimization engine with similar parameters (*e.g.*, 10^4 particles per spot for D_{ij}, LET_{ij} matrix calculation, 10^8 particles for final dose calculation to ensure the plan is within 1% statistical uncertainties for the dose in the target volume (37), and same optimization criteria). For each patient, the IMPT plan was generated first to achieve an optimized dose distribution to the target volume and OARs without taking LET_d distribution into account. Based on those dose objective functions, IMPT plan was then generated by adding LET_d objectives of the target and OARs in the optimization. The relative weights between dose and LET_d objectives were further adjusted to maintain similar or superior dose distribution while maximizing and minimizing the average LET_d values in the target volume and OARs. In terms of SPArc planning, the plans initiated from a coarse sampling frequency of 20 degree and achieved 2.5 degree final sampling frequency using the similar objective functions to the IMPT plans with LET_d optimization.

Patient Study

To quantitatively investigate the effect of the LET_d distribution with the relationship of beam number, a prostate patient was selected given its easy anatomical structures. A full arc SPArc and multi-beam IMPT plans with 2, 4, 6, and 8 equally spaced beams were generated to achieve similar clinical target volume (CTV, 134 cc) coverage (78 Gy in 39 fractions, using RBE of 1.1) and high dose sparing of rectum and bladder while maximizing the LET_d value using similar objective functions inside the CTV. Urethra was not considered as an avoidance structure for the simplicity of the analysis. However any OAR can be used as an avoidance structure in optimization although this will result in a more complicated and longer calculation process. The dose, LET_d, corresponding dose-volume histograms (DVHs) and LET_d-volume histograms (LVHs) of all plans were analyzed and compared with the 2-beam IMPT plan without LET_d optimization (2B w/o). To evaluate the treatment delivery efficiency among different plans, the delivery time was simulated based on a full gantry geometry with a rotation speed of one rotation per minute, spot switching time of 2 milliseconds, and energy-layer-switching-time of 0.6 seconds (24).

To further quantify the relationship between high LET_d concentration and the size of LET_d boost volume in SPArc optimization, different virtual simultaneously integrated boost (SIB) volumes (77.9, 39.9, 16.5, 4.5, and 0.3 ccs) were generated by shrinking the CTV at a step size of 0.5 cm. Multiple SPArc plans were generated to provide similar CTV coverage while maximizing the high LET_d concentrating in the SIB volumes using the similar plan parameters such as arc trajectory, sampling frequency, as well as target objective functions and weights.

A liver and a brain case were then selected to compare the resulted LET_d optimization between SPArc and multi-beam IMPT. For the liver case, a partial arc from 160 – 40 degree (IEC 61217) was used to prescribe 75 Gy (constant RBE of 1.1) in 25 fractions (38) to the CTV, while minimizing the mean dose to the normal liver, and maximizing the LET_d value in the gross tumor volume (GTV). For the brain case, the full arc was used to optimize a uniform dose to the CTV (54 Gy in 30 fractions, constant RBE of 1.1) (39) and minimize the dose to the surrounding OARs, while maximizing the LET_d value in CTV and minimizing the LET_d value to the OARs. The multi-beam IMPT plans using the clinical beam angles (two beams for the liver case, and three beams for the brain cases) were also re-optimized using the same platform with and without LET_d optimization. The dose, LET_d, corresponding DVHs and LVHs were evaluated for all plans.

RESULTS

Dose and LET_d distributions for a 2-beam IMPT plan without LET_d optimization, and IMPT plans (2, 4, 6, 8 beam angles) and SPArc plans with LET_d optimization are shown in **Figure 2**. This comparison shows the power of SPArc to concentrate the high LET_d in the desired area of target volume. **Figures 3A, B** display the corresponding DVHs for CTV, rectum, and bladder for all plans. The corresponding LVHs for CTV are also shown in **Figure 3C**. With similar RBE 1.1 dose distributions in terms of target coverage and high dose OARs sparings, the average LET_d in the target increases with the number of beams used. Compared to multi-beam IMPT plans, SPArc has a better capability of spatially centralizing the LET_d distributions in the target while maintaining the delivery efficiency. Specifically, with LET_d optimization, the average value of LET_d in the target was 4.38, 4.65, 4.85, 4.85, and 5.06 keV/μm for IMPT plans of 2, 4, 6, 8 beams and SPArc plans, respectively. Compared with the 2-beam non-LET_d optimized plan, the corresponding increase of LET_d value was 21%, 29%, 34%, 34%, and 40% for the IMPT plans (2, 4, 6, 8 beams) and SPArc plans respectively. The estimated delivery time for the IMPT plans (2, 4, 6, 8 beams) and SPArc plans was 96, 150, 171, 188, and 125 seconds respectively. Hence, SPArc can enhance the LET_d distribution in the target volume more efficiently.

Moreover, the ability of SPArc to concentrate the LET_d depends on the volume as shown in **Figure 4**. The average LET_d value in the SIB volume for the prostate case could increase up to 8.5 keV/um as the size of the SIB volume decreases while maintaining similar dose distributions.

To validate the capability of SPArc to optimize LET distribution, other clinical scenarios such as liver and brain

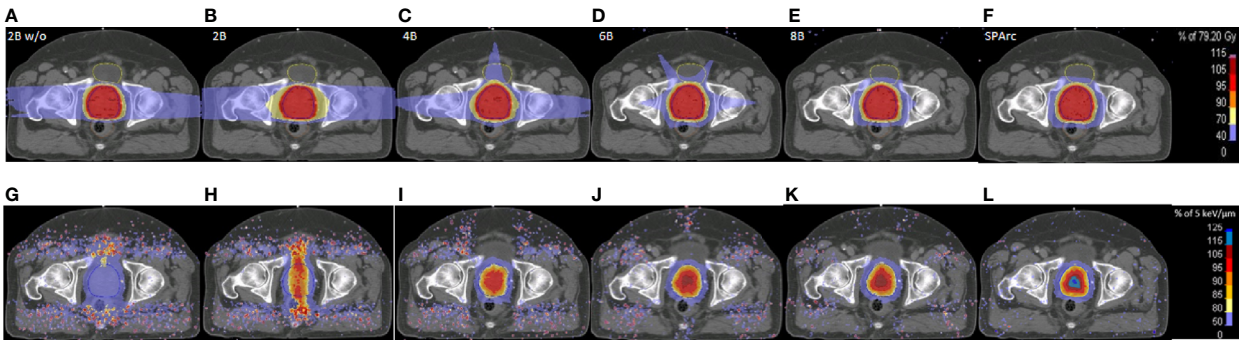

FIGURE 2 | The dose (upper row) and the LET_d (lower row) distributions for 2 beams without LET_d based optimization (2Bw/o, **A, G**), and with LET_d based optimization for 2 (2B, **B, H**), 4 (4B, **C, I**), 6 (6B, **D, J**), 8 (8B, **E, K**) beams and SPArc **(F, L)** for a prostate case.

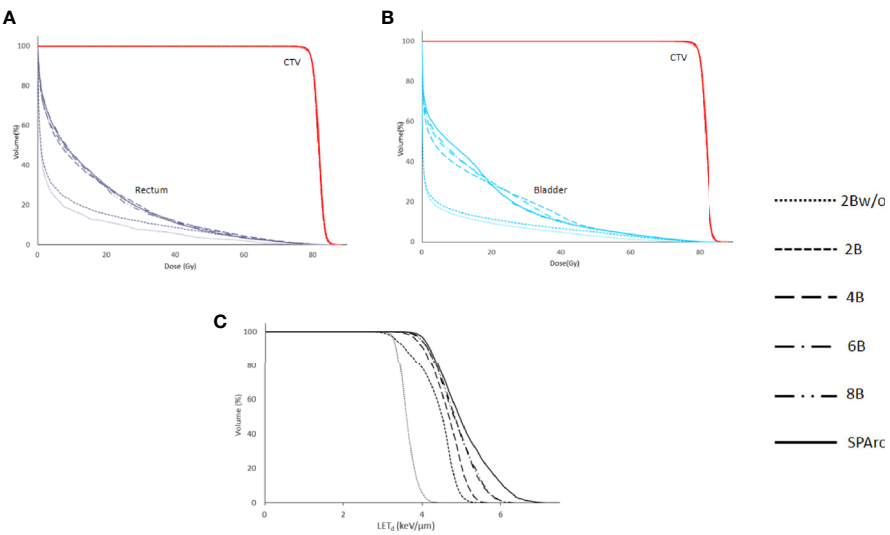

FIGURE 3 | The dose volume histograms (DVHs) **(A, B)** and LET_d volume histograms (LVHs) **(C)** for 2Bw/o and for 2, 4, 6, 8 beams and SPArc with LET_d based optimization.

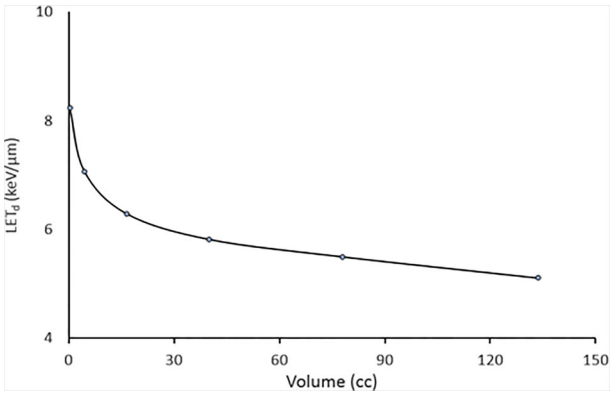

FIGURE 4 | The relation with average achievable LET_d versus volume using SPArc while keeping similar dose to the target volume for the prostate case.

cases were examined. The dose, DVHs, and LVHs for the liver case generated using two beams without LET_d optimization, with LET_d optimization, and SPArc are shown in **Figure 5**. With similar target coverage, the SPArc plans reduced the mean dose of normal liver by 1.4 Gy (RBE 1.1), and 1.5 Gy (RBE 1.1) when compared with the 2-beam IMPT plan without and with LET_d optimization respectively. Moreover, the SPArc could effectively escalate the high LET_d value in the GTV. Specifically, the average value of LET_d in the GTV for the liver case was 4.88 and 2.39 keV/μm for the SPArc and 2-beam IMPT plans with LET_d optimization respectively. Compared with the 2-beam non-LET_d optimized plan, the corresponding increase in LET_d was 124% for SPArc plan, and only 9.6% for the IMPT plan given the limited number of beam angles.

Similar results were noted in simulation of the brain case, where SPArc with LET_d optimization could effectively maximize the LET_d enhancement to the target volume while restricting the high LET_d away from the OARs. Specifically, the average value of LET_d for the SPArc plan was increased by 29% (4.03 *vs.* 3.13 keV/μm) for CTV, and was decreased by 22% (2.14 *vs.* 2.74 keV/μm), 30% (2.43 *vs.* 3.45 keV/μm), 28% (2.96 *vs.* 4.09 keV/μm), and 17% (2.66 *vs.* 3.22 keV/μm) for brainstem, chiasm, left, and right optical nerves, respectively, compared with the 3-beam non-LET_d optimized plan. In contrast, the corresponding improvements were only 4%, 12%, 22%, 21%, and -3% for 3-beam IMPT plan compared with the 3-beam non-LET_d optimized plan (**Figures 6**, **7**).

DISCUSSION

This is the first study to quantitatively evaluate the feasibility of SPArc to spatially optimize LET_d distributions using the fully

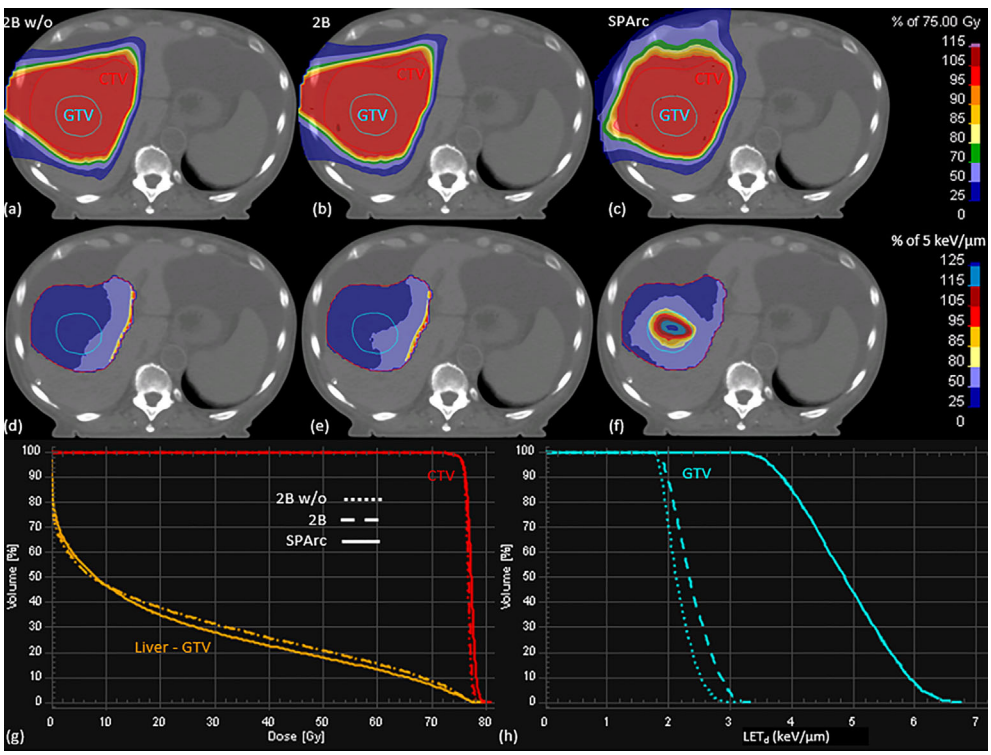

FIGURE 5 | The dose (first row) and LET_d (second row) distributions, the DVHs **(G)** and LVHs **(H)** of 2Bw/o **(A, D)**, 2B **(B, E)**, and SPArc **(C, F)** plans for the liver patient.

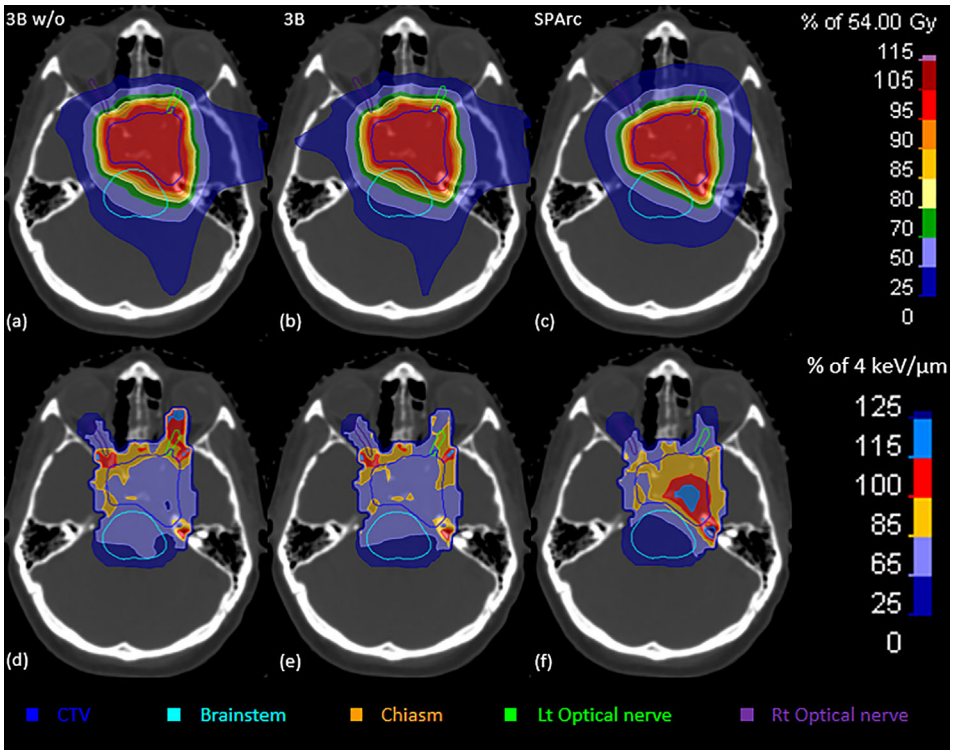

FIGURE 6 | The dose (upper row) and LET_d (lower row) distributions of 3Bw/o **(A, D)**, 3B **(B, E)**, and SPArc **(C, F)** plans for the brain patient.

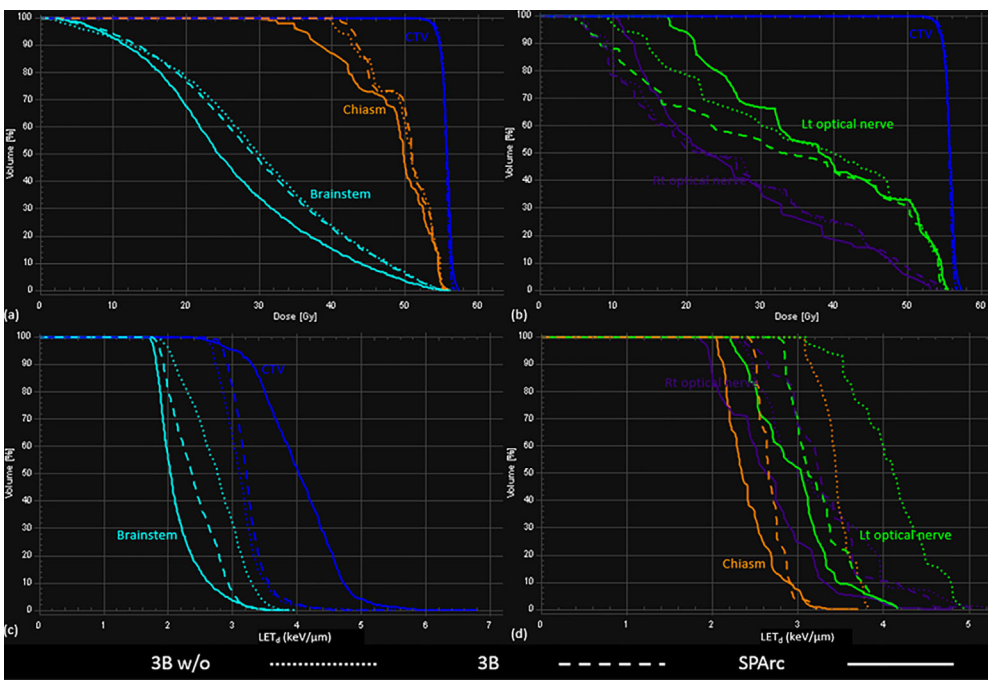

FIGURE 7 | The DVHs **(A, B)** and LVHs **(C, D)** for 3Bw/o, 3B, and SPArc plans for the brain patient.

LET_d incorporated SPArc optimization engine. Our results demonstrate that SPArc has the great capability to concentrate the high LET_d inside the target volume while restricting it from the OARs. Nevertheless, as the number of beam angles increases, IMPT plans may be able to achieve similar plan quality as SPArc, however this is not feasible in clinical practice due to its prolonged treatment delivery time. Several groups (40, 41) have proposed to shorten the delivery time by filtering the energy layers for IMPT plans. Such procedure is still limited and not preferable especially for multi-room proton center due to room switching time between beams (24). Conversely, SPArc has more degrees of freedom for delivering hundreds of beamlets along the arc trajectory therefore to effectively optimize the dose and LET_d distributions simultaneously without sacrificing the delivery efficiency.

More importantly, SPArc has demonstrated its capability of elevating the LET_d value inside the target. The level of elevation is dependent on the target volume (**Figure 4**). For small target volumes (*i.e.*, less than 5 cc), the average LET_d in the target volume could reach values higher than 7 keV/um. Compared to the average mid-SOBP LET_d value of 2-3 keV/um (3), the increment can be up to 250%. However, the magnitude and the conformity of LET_d concentration in the target volume depends on the target size, its location and more importantly on adjacent critical normal structures and their dose and LET constraints. For instance, the maximum average LET_d achieved in the GTV was compromised in the liver case (**Figure 5**) as only a partial arc could be used due to the location of the target. Furthermore, the irregular shape and complex geometry of the target volume and OARs can affect the distribution, conformity and the magnitude of LET_d in the target volume shown in the brain case (**Figure 6**) as the average LET_d value could only reach up to 4.03 keV/um. In order to understand the potentials and limitations of the LET_d distribution and its falloff *via* SPArc, more studies on different anatomical sites and patient geometries are necessary and are the mainstay of our future efforts.

This study incorporated LET_d optimization engine into the biological treatment planning to achieve a similar dose distribution with RBE 1.1 as used in current clinical practice. A more comprehensive biological optimization engine based on a variable RBE model could be extended from the current framework by incorporating dose, physiological and biological factors into the optimization. Thus far, none of the variable proton RBE models has been implemented into routine clinical practice due to the discrepancies between model calculations and experimental data (42, 43). In contrast to the physical parameters in the current RBE model, LET can be supported by all the variable RBE models (5), in which RBE value varies with LET values. Therefore, using this approach in this study which is maintaining similar dose (RBE 1.1) while spatially optimizing LET_d distribution, could be possibly clinically adopted to improve the patient outcome.

Moreover, it is important to mention that robust optimization was not incorporated into this LET_d-based SPArc treatment planning due to the slow calculation speed and extra memory allocation. We do recognize that the dose and LET_d distributions could get deteriorated from the uncertainties. However, the previous study (17) have demonstrated the feasibility of improving LET_d distributions by integrating LET_d based optimization with robust optimization in IMPT plans. With the availability of better calculation models and computer hardware, we could integrate the robustness into LET_d-based SPArc planning in our future studies.

CONCLUSION

This is the first fully LET_d incorporated SPArc optimization algorithm and platform which has the capability to spatially optimize LET_d. Our results demonstrate that SPArc can take advantage of arc trajectory to maximize the LET_d concentration to anywhere in the target volume, and to avoid the high LET_d from the OARs, while maintaining similar delivery efficiency. This technique will not only address one of the challenges in proton therapy which is the risk of toxicity associated with the LET uncertainty of the Bragg peak distal edge but also could provide the means to dose escalation *via* LET optimization in the target volume while sparing OARs.

DATA AVAILABILITY STATEMENT

The raw data supporting the conclusions of this article will be made available by the authors, without undue reservation.

ETHICS STATEMENT

The studies involving human participants were reviewed and approved by Beaumont Health Institutional Review Board. Written informed consent for participation was not required for this study in accordance with the national legislation and the institutional requirements.

AUTHOR CONTRIBUTIONS

XL designed the study, performed the data acquisition and analysis, wrote the manuscript. XD, WZ, and GL assisted in designing the study and revising the manuscript. GJ, KS, and AB-M provided intensive feedback to improve the algorithm. DY and CS provided physics and clinical support. PK helped to design the study, provided clinical inputs, and revised the manuscript. All authors contributed to the article and approved the submitted version.

FUNDING

XD and XL received the fund from Ion Beam Applications. The funder was not involved in the study design, collection, analysis, interpretation of data, the writing of this article or the decision to submit it for publication.

REFERENCES

1. Newhauser W. International Commission on Radiation Units and Measurements Report 78: Prescribing, Recording and Reporting Proton-Beam Therapy. *Radiat Prot Dosimetry* (2009) 133(1):60–2. doi: 10.1093/rpd/ncp005
2. Paganetti H, Niemierko A, Ancukiewicz M, Gerweck LE, Goitein M, Loeffler JS, et al. Relative Biological Effectiveness (RBE) Values for Proton Beam Therapy. *Int J Radiat Oncol Biol Phys* (2002) 53(2):407–21. doi: 10.1016/S0360-3016(02)02754-2
3. Paganetti H. Relative Biological Effectiveness (RBE) Values for Proton Beam Therapy. Variations as a Function of Biological Endpoint, Dose, and Linear Energy Transfer. *Phys Med Biol* (2014) 59(22):R419–72. doi: 10.1088/0031-9155/59/22/R419
4. Unkelbach J, Botas P, Giantsoudi D, Gorissen and H. Paganetti BL. Reoptimization of Intensity Modulated Proton Therapy Plans Based on Linear Energy Transfer. *Int J Radiat Oncol Biol Phys* (2016) 96(5):1097–106. doi: 10.1016/j.ijrobp.2016.08.038
5. Guan F, Bronk L, Titt U, Lin SH, Mirkovic D, Kerr MD, et al. Spatial Mapping of the Biologic Effectiveness of Scanned Particle Beams: Towards Biologically Optimized Particle Therapy. *Sci Rep* (2015) 5:9850. doi: 10.1038/srep09850
6. Peeler CR, Mirkovic D, Titt U, Blanchard P, Gunther JR, Mahajan A, et al. Clinical Evidence of Variable Proton Biological Effectiveness in Pediatric Patients Treated for Ependymoma. *Radiother Oncol* (2016) 121(3):395–401. doi: 10.1016/j.radonc.2016.11.001
7. Harrabi S, Gudden C, Adeberg S, Bougatf N, Haberer T, Rieken S, et al. OC-0514: Radiation Necrosis After Proton Beam Therapy - When and Where Does It Happen? *Radiother Oncol* (2017) 123:S271. doi: 10.1016/S0167-8140(17)30954-4
8. Zhang Y, Huo W, Adams JA, Sanford NN, Lam MB, Lu Y, et al. Temporal Lobe Necrosis After Proton for Nasopharyngeal Carcinoma: Predictive Factors and Clinical RBE Estimation. *Int J Radiat Oncol • Biol • Phys* (2017) 99(2):E386. doi: 10.1016/j.ijrobp.2017.06.1526
9. Merchant TE, Hua CH, Sabin ND, Ezell SE, Madey MA, Wu S, et al. Necrosis, Vasculopathy, and Neurological Complications After Proton Therapy for Childhood Craniopharyngioma: Results From a Prospective Trial and a Photon Cohort Comparison. *Int J Radiat Oncol • Biol • Phys* (2016) 96(2):S120–1. doi: 10.1016/j.ijrobp.2016.06.294
10. Lomax A. Intensity Modulation Methods for Proton Radiotherapy. *Phys Med Biol* (1999) 44(1):185–205. doi: 10.1088/0031-9155/44/1/014
11. Lomax AJ, Boehringer T, Coray A, Egger E, Goitein G, Grossmann M, et al. Intensity Modulated Proton Therapy: A Clinical Example. *Med Phys* (2001) 28(3):317–24. doi: 10.1118/1.1350587
12. Zhang XD, Li YP, Pan XN, Li XQ, Mohan R, Komaki R, et al. Intensity-Modulated Proton Therapy Reduces the Dose to Normal Tissue Compared With Intensity-Modulated Radiation Therapy or Passive Scattering Proton Therapy and Enables Individualized Radical Radiotherapy for Extensive Stage Iiib Non-Small-Cell Lung Cancer: A Virtual Clinical Study. *Int J Radiat Oncol Biol Phys* (2010) 77(2):357–66. doi: 10.1016/j.ijrobp.2009.04.028
13. Liu W, Frank SJ, Li X, Li Y, Park PC, Dong L, et al. Effectiveness of Robust Optimization in Intensity-Modulated Proton Therapy Planning for Head and Neck Cancers. *Med Phys* (2013) 40(5):051711. doi: 10.1118/1.4801899
14. Liu W, Li YP, Li XQ, Cao WH, Zhang XD, et al. Influence of Robust Optimization in Intensity-Modulated Proton Therapy With Different Dose Delivery Techniques. *Med Phys* (2012) 39(6):3089. doi: 10.1118/1.4711909
15. Frese MC, Wilkens JJ, Huber PE, Jensen AD, Oelfke U, Taheri-Kadkhoda Z. Application of Constant *vs.* Variable Relative Biological Effectiveness in Treatment Planning of Intensity-Modulated Proton Therapy. *Int J Radiat Oncol Biol Phys* (2011) 79(1):80–8. doi: 10.1016/j.ijrobp.2009.10.022
16. Wilkens JJ, Oelfke U. Optimization of Radiobiological Effects in Intensity Modulated Proton Therapy. *Med Phys* (2005) 32(2):455–65. doi: 10.1118/1.1851925
17. An Y, Shan J, Patel SH, Wong W, Schild SE, Ding X, et al. Robust Intensity-Modulated Proton Therapy to Reduce High Linear Energy Transfer in Organs at Risk. *Med Phys* (2017) 44(12):6138–47. doi: 10.1002/mp.12610
18. Grassberger C, Paganetti H. Elevated LET Components in Clinical Proton Beams. *Phys Med Biol* (2011) 56(20):6677–91. doi: 10.1088/0031-9155/56/20/011
19. Wan Chan Tseung HS, Ma J, Kreofsky CR, Ma DJ, Beltran C. Clinically Applicable Monte Carlo-Based Biological Dose Optimization for the Treatment of Head and Neck Cancers With Spot-Scanning Proton Therapy. *Int J Radiat Oncol Biol Phys* (2016) 95(5):1535–43. doi: 10.1016/j.ijrobp.2016.03.041
20. Cao W, Khabazian A, Yepes PP, Lim G, Poenisch F, Grosshans DR, et al. Linear Energy Transfer Incorporated Intensity Modulated Proton Therapy Optimization. *Phys Med Biol* (2017) 63(1):015013. doi: 10.1088/1361-6560/aa9a2e
21. Grassberger C, Trofimov A, Lomax A, Paganetti H. Variations in Linear Energy Transfer Within Clinical Proton Therapy Fields and the Potential for Biological Treatment Planning. *Int J Radiat Oncol Biol Phys* (2011) 80(5):1559–66. doi: 10.1016/j.ijrobp.2010.10.027
22. Fager M, Toma-Dasu I, Kirk M, Dolney D, Diffenderfer ES, Vapiwala N, et al. Linear Energy Transfer Painting With Proton Therapy: A Means of Reducing Radiation Doses With Equivalent Clinical Effectiveness. *Int J Radiat Oncol Biol Phys* (2015) 91(5):1057–64. doi: 10.1016/j.ijrobp.2014.12.049
23. Toussaint L, Indelicato DJ, Holgersen KS, Petersen JBB, Stokkevag CH, Lassen-Ramshad Y, et al. Towards Proton Arc Therapy: Physical and Biologically Equivalent Doses With Increasing Number of Beams in Pediatric Brain Irradiation. *Acta Oncol* (2019) 58(10):1451–6. doi: 10.1080/0284186X.2019.1639823
24. Ding X, Li X, Zhang JM, Kabolizadeh P, Stevens C, Yan D. Spot-Scanning Proton Arc (SPArc) Therapy: The First Robust and Delivery-Efficient Spot-Scanning Proton Arc Therapy. *Int J Radiat Oncol • Biol • Phys* (2016) 96(5):1107–16. doi: 10.1016/j.ijrobp.2016.08.049
25. Ding X, Li X, Qin A, Zhou J, Yan D, Chen P, et al. Redefine the Role of Range Shifter in Treating Bilateral Head and Neck Cancer in the Era of Intensity Modulated Proton Therapy. *J Appl Clin Med Phys* (2018) 19(5):749–55. doi: 10.1002/acm2.12416
26. Ding X, Li X, Qin A, Zhou J, Yan D, Stevens C, et al. Have We Reached Proton Beam Therapy Dosimetric Limitations? - A Novel Robust, Delivery-Efficient and Continuous Spot-Scanning Proton Arc (SPArc) Therapy Is to Improve the Dosimetric Outcome in Treating Prostate Cancer. *Acta Oncol* (2018) 57(3):435–7. doi: 10.1080/0284186X.2017.1358463
27. Ding X, Zhou J, Li X, Blas K, Liu G, Wang Y, et al. Improving Dosimetric Outcome for Hippocampus and Cochlea Sparing Whole Brain Radiotherapy Using Spot-Scanning Proton Arc Therapy. *Acta Oncol* (2019) 1–8. doi: 10.1080/0284186X.2018.1555374
28. Li X, Kabolizadeh P, Yan D, Qin A, Zhou J, Hong Y, et al. Improve Dosimetric Outcome in Stage III Non-Small-Cell Lung Cancer Treatment Using Spot-Scanning Proton Arc (SPArc) Therapy. *Radiat Oncol* (2018) 13(1):35. doi: 10.1186/s13014-018-0981-6
29. Li X, Liu G, Janssens G, De Wilde O, Bossier V, Lerot X, et al. The First Prototype of Spot-Scanning Proton Arc Treatment Delivery. *Radiother Oncol* (2019) 137:130–6. doi: 10.1016/j.radonc.2019.04.032
30. Available at: https://openreggui.org/.
31. Huang ,S, Kang M, Souris K, Ainsley C, Solberg TD, McDonough JE, et al. Validation and Clinical Implementation of an Accurate Monte Carlo Code for Pencil Beam Scanning Proton Therapy. *J Appl Clin Med Phys* (2018) 19(5):558–72. doi: 10.1002/acm2.12420
32. Souris K, Lee JA, Sterpin E. Fast Multipurpose Monte Carlo Simulation for Proton Therapy Using Multi- and Many-Core CPU Architectures. *Med Phys* (2016) 43(4):1700. doi: 10.1118/1.4943377
33. Sorriaux J, Testa M, Paganetti H, Orban de Xivry J, Lee JA, Traneus E, et al. Experimental Assessment of Proton Dose Calculation Accuracy in Inhomogeneous Media. *Phys Med* (2017) 38:10–5. doi: 10.1016/j.ejmp.2017.04.020
34. Barragan Montero AM, Souris K, Sanchez-Parcerisa D, Sterpin E, Lee JA. Performance of a Hybrid Monte Carlo-Pencil Beam Dose Algorithm for Proton Therapy Inverse Planning. *Med Phys* (2018) 45(2):846–62. doi: 10.1002/mp.12688
35. Wagenaar D, Tran LT, Meijers A, Marmitt GG, Souris K, Bolst D, et al. Validation of Linear Energy Transfer Computed in a Monte Carlo Dose Engine of a Commercial Treatment Planning System. *Phys Med Biol* (2020) 65(2):025006. doi: 10.1088/1361-6560/ab5e97
36. Cortes-Giraldo MA, Carabe A. A Critical Study of Different Monte Carlo Scoring Methods of Dose Average Linear-Energy-Transfer Maps Calculated in Voxelized Geometries Irradiated With Clinical Proton Beams. *Phys Med Biol* (2015) 60(7):2645–69. doi: 10.1088/0031-9155/60/7/2645

37. Bueno M, Paganetti H, Duch MA, Schuemann J. An Algorithm to Assess the Need for Clinical Monte Carlo Dose Calculation for Small Proton Therapy Fields Based on Quantification of Tissue Heterogeneity. *Med Phys* (2013) 40 (8):081704. doi: 10.1118/1.4812682
38. Crane CH, Koay EJ. Solutions That Enable Ablative Radiotherapy for Large Liver Tumors: Fractionated Dose Painting, Simultaneous Integrated Protection, Motion Management, and Computed Tomography Image Guidance. *Cancer* (2016) 122(13):1974–86. doi: 10.1002/cncr.29878
39. Fagundes MA, Hug EB, Liebsch NJ, Daly W, Efird J, Munzenrider JE. Radiation Therapy for Chordomas of the Base of Skull and Cervical Spine: Patterns of Failure and Outcome After Relapse. *Int J Radiat Oncol Biol Phys* (1995) 33(3):579–84. doi: 10.1016/0360-3016(95)02014-3
40. Cao W, Lim G, Liao L, Li Y, Jiang S, Li X, et al. Proton Energy Optimization and Reduction for Intensity-Modulated Proton Therapy. *Phys Med Biol* (2014) 59(21):6341–54. doi: 10.1088/0031-9155/59/21/6341
41. van de Water S, Kooy HM, Heijmen BJ, Hoogeman MS. Shortening Delivery Times of Intensity Modulated Proton Therapy by Reducing Proton Energy Layers During Treatment Plan Optimization. *Int J Radiat Oncol Biol Phys* (2015) 92(2):460–8. doi: 10.1016/j.ijrobp.2015.01.031
42. Polster L, Schuemann J, Rinaldi I, Burigo L, McNamara AL, Stewart RD, et al. Extension of TOPAS for the Simulation of Proton Radiation Effects Considering Molecular and Cellular Endpoints. *Phys Med Biol* (2015) 60 (13):5053–70. doi: 10.1088/0031-9155/60/13/5053
43. Grun R, Friedrich T, Kramer M, Scholz M. Systematics of Relative Biological Effectiveness Measurements for Proton Radiation Along the Spread Out Bragg Peak: Experimental Validation of the Local Effect Model. *Phys Med Biol* (2017) 62(3):890–908. doi: 10.1088/1361-6560/62/3/890

Conflict of Interest: XD, XL, and DY have a patent related to the Particle Arc Therapy (WO2017156419). GJ was employed by Ion Beam Applications SA.

The remaining authors declare that the research was conducted in the absence of any commercial or financial relationships that could be construed as a potential conflict of interest.

frontiers in Oncology

ORIGINAL RESEARCH
published: 19 August 2021
doi: 10.3389/fonc.2021.737050

Radioactive Beams for Image-Guided Particle Therapy: The BARB Experiment at GSI

Daria Boscolo[1], Daria Kostyleva[1], Mohammad Javad Safari[2], Vasiliki Anagnostatou[2], Juha Äystö[3,4], Soumya Bagchi[5], Tim Binder[2], Georgios Dedes[2], Peter Dendooven[6], Timo Dickel[1,7], Vasyl Drozd[1,8], Bernhard Franczack[1], Hans Geissel[1,7], Chiara Gianoli[2], Christian Graeff[1], Tuomas Grahn[3,4], Florian Greiner[1], Emma Haettner[1], Roghieh Haghani[2], Muhsin N. Harakeh[8], Felix Horst[1], Christine Hornung[1,9], Jan-Paul Hucka[1,9], Nasser Kalantar-Nayestanaki[8], Erika Kazantseva[1], Birgit Kindler[1], Ronja Knöbel[1], Natalia Kuzminchuk-Feuerstein[1], Bettina Lommel[1], Ivan Mukha[1], Chiara Nociforo[1], Shunki Ishikawa[10], Giulio Lovatti[2], Munetaka Nitta[2], Ikechi Ozoemelam[11], Stephane Pietri[1], Wolfgang R. Plaß[1,7], Andrej Prochazka[12], Sivaji Purushothaman[1], Claire-Anne Reidel[1], Heidi Roesch[1,9], Fabio Schirru[1], Christoph Schuy[1], Olga Sokol[1], Timo Steinsberger[1,9], Yoshiki K. Tanaka[13], Isao Tanihata[14,15,16], Peter Thirolf[2], Walter Tinganelli[1], Bernd Voss[1], Uli Weber[1], Helmut Weick[1], John S. Winfield[1], Martin Winkler[1], Jianwei Zhao[1,15], Christoph Scheidenberger[1,7], Katia Parodi[2], Marco Durante[1,9] and the Super-FRS Experiment Collaboration*

[1] GSI Helmholtzzentrum für Schwerionenforschung, Darmstadt, Germany, [2] Ludwig-Maximilians-Universität München, Munich, Germany, [3] University of Jyväskylä, Jyväskylä, Finland, [4] Helsinki Institute of Physics, Helsinki, Finland, [5] Indian Institute of Technology, Dhanbad, India, [6] University Medical Center Groningen, Groningen, Netherlands, [7] Justus-Liebig-Universität Gießen, Gießen, Germany, [8] University of Groningen, Groningen, Netherlands, [9] Technische Universität Darmstadt, Darmstadt, Germany, [10] Tohoku University, Sendai, Japan, [11] Fontys University of Applied Sciences, Eindhoven, Netherlands, [12] MedAustron, Wiener Neustadt, Austria, [13] RIKEN High Energy Nuclear Physics Laboratory, Wako, Japan, [14] Research Center for Nuclear Physics, Osaka University, Osaka, Japan, [15] Peking University, Beijing, China, [16] Institute of Modern Physics, Lanzhou, China

Several techniques are under development for image-guidance in particle therapy. Positron (β^+) emission tomography (PET) is in use since many years, because accelerated ions generate positron-emitting isotopes by nuclear fragmentation in the human body. In heavy ion therapy, a major part of the PET signals is produced by β^+-emitters generated *via* projectile fragmentation. A much higher intensity for the PET signal can be obtained using β^+-radioactive beams directly for treatment. This idea has always been hampered by the low intensity of the secondary beams, produced by fragmentation of the primary, stable beams. With the intensity upgrade of the SIS-18 synchrotron and the isotopic separation with the fragment separator FRS in the FAIR-phase-0 in Darmstadt, it is now possible to reach radioactive ion beams with sufficient intensity to treat a tumor in small animals. This was the motivation of the BARB (Biomedical Applications of Radioactive ion Beams) experiment that is ongoing at GSI in Darmstadt. This paper will present the plans and instruments developed by the BARB collaboration for testing the use of radioactive beams in cancer therapy.

Keywords: particle therapy, radioactive ion beams, carbon ions, oxygen ions, PET

OPEN ACCESS

Edited by:
Haibin Shi,
Soochow University, China

Reviewed by:
Guangming Zhou,
Soochow University Medical College (SUMC), China
Hua Zhu,
Beijing Cancer Hospital, China

***Correspondence:**
Marco Durante
m.durante@gsi.de

Specialty section:
This article was submitted to Cancer Imaging and Image-directed Interventions, a section of the journal Frontiers in Oncology

Received: *06 July 2021*
Accepted: *04 August 2021*
Published: *19 August 2021*

Citation:
Boscolo D, Kostyleva D, Safari MJ, Anagnostatou V, Äystö J, Bagchi S, Binder T, Dedes G, Dendooven P, Dickel T, Drozd V, Franczack B, Geissel H, Gianoli C, Graeff C, Grahn T, Greiner F, Haettner E, Haghani R, Harakeh MN, Horst F, Hornung C, Hucka J-P, Kalantar-Nayestanaki N, Kazantseva E, Kindler B, Knöbel R, Kuzminchuk-Feuerstein N, Lommel B, Mukha I, Nociforo C, Ishikawa S, Lovatti G, Nitta M, Ozoemelam I, Pietri S, Plaß WR, Prochazka A, Purushothaman S, Reidel C-A, Roesch H, Schirru F, Schuy C, Sokol O, Steinsberger T, Tanaka YK, Tanihata I, Thirolf P, Tinganelli W, Voss B, Weber U, Weick H, Winfield JS, Winkler M, Zhao J, Scheidenberger C, Parodi K, Durante M and the Super-FRS Experiment Collaboration (2021) Radioactive Beams for Image-Guided Particle Therapy: The BARB Experiment at GSI. Front. Oncol. 11:737050. doi: 10.3389/fonc.2021.737050

INTRODUCTION

Image-guidance is one of the major improvements of radiotherapy in the past years (1). High resolution imaging allows dose escalation, hypofractionation, and treatment of moving tumors with tracking (2). Image-guided particle therapy is currently less mature, even if the problem of range uncertainty is a major caveat compared to conventional radiotherapy (3). Range uncertainty in the patient is typically compensated by using wide target margins: in proton therapy, the margin is about 3.5% of the prescribed range (4). The widening of the margins jeopardizes one of the main advantages of the Bragg peak: the steep distal dose gradients and the potentially high targeting accuracy and precision (5). Actually, the physics of particle therapy offers several imaging methods that are ruled out in photon therapy (6). For instance, prompt γ-rays (PG) generated in nuclear reactions can be detected and the signal fall-off is correlated to the Bragg peak (7). In heavy ion therapy it is also possible to measure the range by detecting secondary charged particles, such as protons emitted at large angles (8, 9). A combination of different methods is under study for animal irradiators (10) and in clinical settings (11, 12).

The range verification method that has been tested most extensively in clinical practice is positron emission tomography (PET) (13). Unlike conventional diagnostic imaging (14), PET in particle therapy exploits β^+-emitting isotopes produced by the particle beam in the patient's body by nuclear fragmentation. In proton therapy, only target fragments can be used for PET imaging, while in heavy ion therapy the projectile fragments provide a large part of the PET signal with better correlation to the dose. Because the time of flight of the ions in the patient is much smaller than the half-life of the β^+-emitters, the positron emission occurs essentially after the fast fragments are stopped in tissue. For instance, ^{12}C-ions, used in a dozen centers worldwide for cancer therapy (15), produce positron emitting ^{11}C ($t_{1/2}$ = 20.3 min) and ^{10}C ($t_{1/2}$ = 19.3 s) nuclei by nuclear fragmentation. The peak in the activity from the isotopic projectile fragments is visualized upstream of the Bragg peak, because such fragments, lighter than the projectile, have shorter ranges at the same velocity of the primary ion (16, 17). Online PET was used for the first time clinically during the ^{12}C-ion pilot therapy project at GSI, Darmstadt, 1997-2008 (18) and a number of particle therapy centers are currently using this technique for range verification off-line (12, 19–21).

However, PET in ^{12}C-ion therapy remains marginal and not really able to reduce the range uncertainty as desired. The half-life of the most abundant induced radionuclides is too long for instantaneous feedback while the short-lived radionuclides are produced at a very low rate and exhibit a long positron range (22) before annihilation. The physical shift in the β^+-activity and ^{12}C dose peaks along with the biological washout requires Monte Carlo (MC) simulations (23) or other analytical calculations (24) currently unavoidable for data analysis. Eventually, the low counting rate of β^+-emitting fragments and the uncertainties in MC calculations limit the accuracy of PET-based range verification to about 2-5 mm (6, 19, 25).

Most of these problems are automatically overcome if β^+-radioactive ion beams (RIB) are directly used for both treatment and imaging. Such radioactive ion beams would improve the count rate by an order of magnitude (26), reduce the shift between measured activity and dose (27), and mitigate the washout blur of the image with short-lived isotopes and in-beam acquisition, eventually leading to sub-mm resolution. Attempts to use RIB in therapy started almost half a century ago during the heavy ion therapy pilot project at the Lawrence Berkeley Laboratory (CA, USA) (28), but they were always hampered by the low intensity of the secondary beams produced by fragmentation of the primary ion used for therapy (29). New, high-intensity accelerators can produce radioactive ion beams with an intensity sufficient for therapeutic treatment (30), and this would pave the way to PET-guided heavy ion treatment. The advantages of using RIB for simultaneous treatment and imaging in comparison to conventional PET imaging in C-ion therapy are shown in the Monte Carlo simulation in **Figure 1**.

The recent upgrade of the SIS-18 accelerator at GSI (Darmstadt, Germany) toward the construction of FAIR (31), i.e. the so-called FAIR-phase-0 (32), gives the opportunity to resume early studies with PET imaging of RIB at GSI (33) and test its application *in vivo*. The BARB (Biomedical Applications of Radioactive ion Beams) project, funded by the European Research Council (ERC) in 2020, aims at treating a tumor in mouse "patients" with RIB (^{11}C and ^{15}O) with an imaging resolution around 0.5 mm. To this goal, within BARB the Ludwig-Maximilians-Universität (LMU) Munich will develop an innovative hybrid detector, able to exploit the PG emission during the synchrotron spill delivery in the target, and counting PET signals in-between the synchrotron spills (34). In this paper, we will present the planned experiments and the technologies that will be developed and applied in BARB to reach the goal of *in vivo* tumor treatment with RIB.

THE FRAGMENT SEPARATOR FRS

The GSI-FAIR accelerators provide intense primary beams of all chemical elements from hydrogen up to uranium and their energies range from a few keV/u up to the relativistic regime. For instance, the heavy ion synchrotron SIS-18 can accelerate protons up to 4.5 GeV, and 2,000 MeV/u can be reached for beams with a mass-to-charge ratio A/Z=2, corresponding to 18 Tm magnetic rigidity. At these energies, light ions like C, O or Ne attain ranges of many centimeters in matter, e.g. in water. At the fragment separator FRS (35), the stable ion beams undergo nuclear reactions in a production target located at its entrance and produce a large variety of secondary beams. These fragments are kinematically focused in forward direction and have velocities that are similar to the primary ions. Due to the nuclear reaction kinematics and atomic effects (such as energy loss, energy-loss straggling and multiple angular scattering) in the production target, the fragments have a large transverse and longitudinal phase-space, much larger than the primary beam.

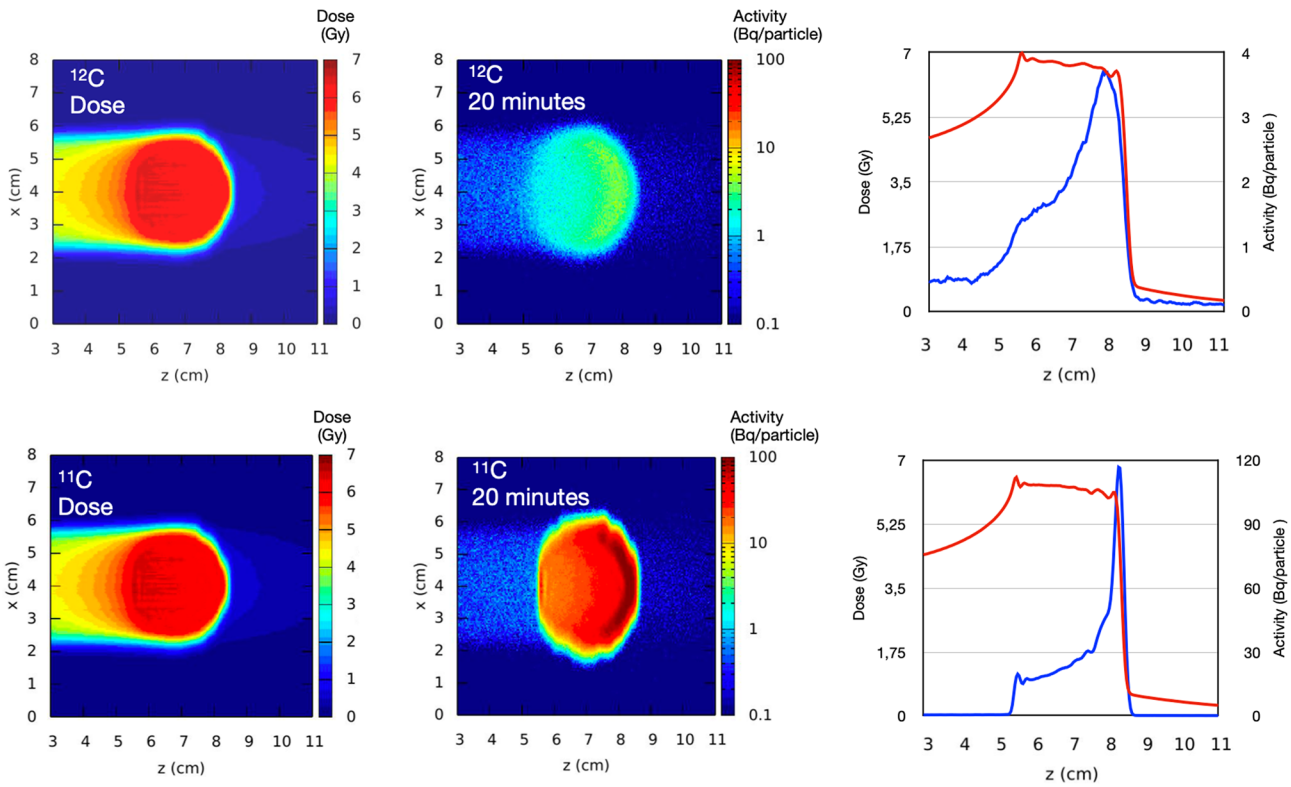

FIGURE 1 | Monte Carlo simulation of ^{12}C and ^{11}C beams stopping in a spherical water volume and visualized by PET in 20 min. The graphs show the dose (red curve) and the activity (blue curve) distribution along the beam direction (z-axis) showing the shift between dose and activity when stable ions are used. Simulation by Monte Carlo code FLUKA.

In particular, the relative momentum spread Δp/p is of the order of a few percent, compared to the primary beam with 5×10^{-4}. This leads consequently to a drastically larger range straggling that is a Bragg Peak with a width of several millimeters when the fragments are stopped in matter. If needed, this range spread can be reduced by combining the dispersive magnetic system of FRS with shaped degraders, which reduces the energy and range straggling of the fragment beams down to the values of primary beams (36, 37). The existing GSI accelerator facility is presented in **Figure 2**.

Due to its dual capability as separator and high-resolution spectrometer, the FRS can be used for production, identification, energy bunching and spatial separation of the secondary beams (in particular of therapy-relevant PET isotopes such as $^{10,11}C$ and $^{14,15}O$), for tailoring specific phase-space properties of the secondary beams as well as for detailed experimental studies of atomic and nuclear processes, that are of basic and practical interest for heavy-ion therapy and related imaging applications. The FRS provides these possibilities at several experimental areas, for instance at the final focus of its symmetric main branch, where first PET measurements have been conducted (38), or *via* its target-hall branch to the medical Cave M, which was recently commissioned. In Cave M, legal permissions exist to irradiate animals. The connecting branch of FRS to Cave-M allows the transport and delivery of isotopically clean secondary beams like ^{11}C or ^{15}O with rates ~10^7 particles per second (pps).

Basic Atomic and Nuclear Studies

The planned basic studies aim at the production yields of isotopes for PET and at a detailed understanding of their atomic and nuclear interactions in matter resp. tissue equivalent materials such as water. For instance, there have been several measurements on the production cross-sections of PET isotopes from stable beams, but the published results widely scatter (39). A systematic investigation of the production cross sections is necessary in order to optimize the yield and the properties of the in-flight separated radioactive ion beams that will be used for mice treatment; for detailed modeling of dose distributions, it will be important to obtain the total interaction and nuclear charge-changing cross sections in the relevant energy regime. The experimental techniques are well established and have been widely used at the FRS (40–43). The isotopes of interest (such as $^{10,11}C$, $^{14,15}O$) will be produced, separated and identified with the first half of the separator, impinge on a secondary reaction target located at the middle focal plane, where secondary reactions are induced, and the reaction products will be analyzed and identified using event-by-event information of magnetic-rigidity, time of flight, and energy deposition; the total interaction cross sections will be

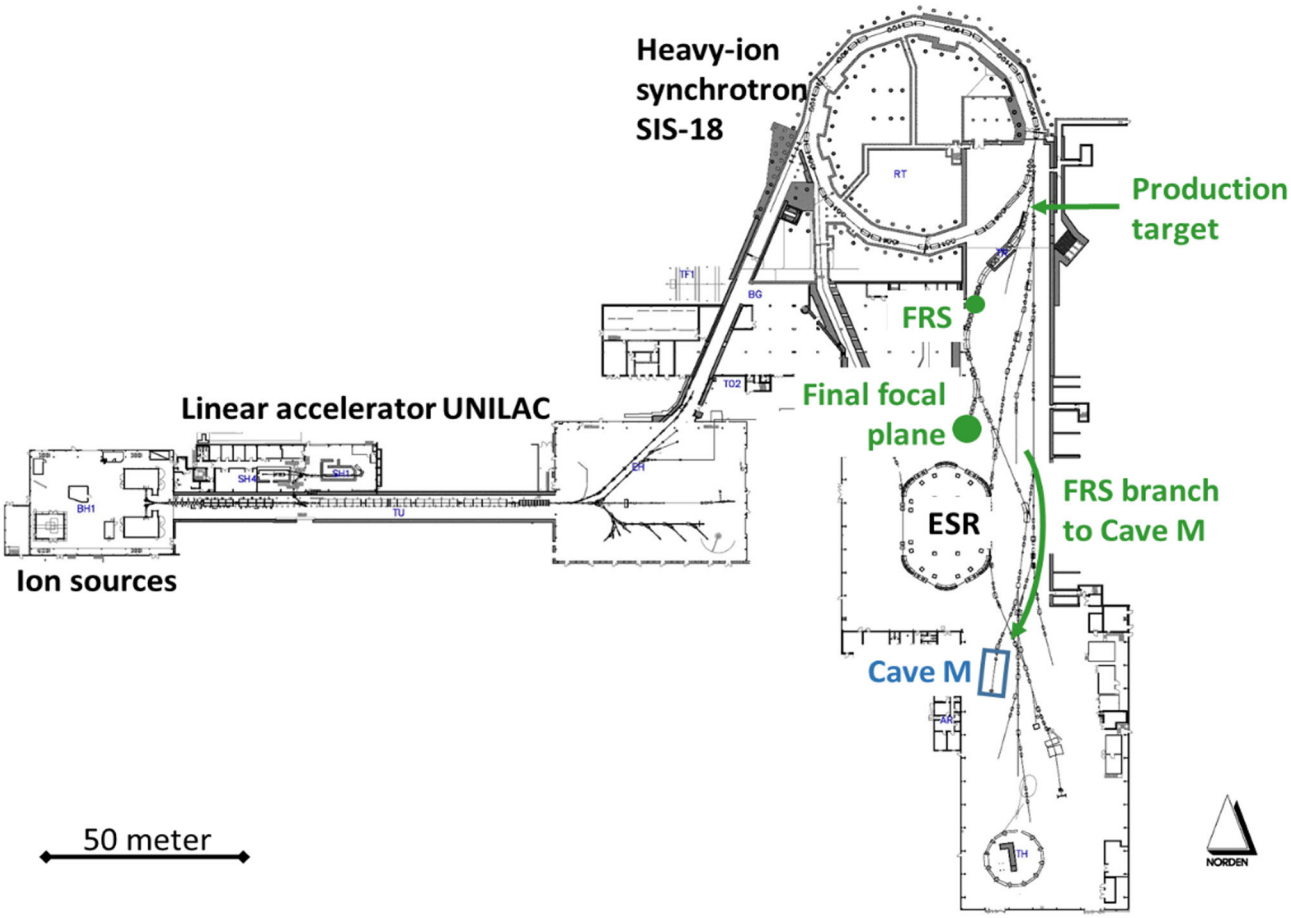

FIGURE 2 | Overview of the existing GSI-FAIR accelerator facility UNILAC-SIS-ESR. The FRS is the radioactive beam facility of GSI and a high-resolution magnetic spectrometer that provides a large variety of secondary nuclear beams ranging from hydrogen up to uranium, among them ^{10,11}C or ^{14,15}O, which can be produced from intense primary beams (like ^{12}C or ^{16}O) in the production target at its entrance. The ions of interest are identified in flight, spatially separated, energy bunched and used for experimental studies at the FRS itself (central and final focal plane, respectively, indicated by green dots) or they are transmitted *via* the FRS branch to the target hall for experiments in Cave M.

determined using the number of non-reacted isotopes. A schematic view of the experimental setup is shown in **Figure 3**.

The atomic interaction (energy loss, energy-loss straggling and angular straggling) of the ion-beam with the tissue is the dominant physical process involved in the ion-beam therapy, and the accurate understanding of corresponding properties like range and range straggling are of very high practical importance. At HIMAC (Japan), the ranges of various PET isotopes (^{10,11}C, ^{14,15}O) have been investigated extensively (27, 44, 45). The range distribution of the selected fragments is primarily determined by the initial energy distribution. The maximum momentum spread of the in-flight separated RIB at the FRS is defined by its longitudinal momentum acceptance, which is approximately ±1%. This momentum spread can be considerably reduced by using a mono-energetic degrader placed at the dispersive focal plane (37), so that the longitudinal range distribution reaches a spread very similar to the range straggling of a primary beam of the same energy.

The latter performance is strongly correlated with the ion-optical resolution (38). Alternatively, by changing the shape of the degrader the momentum distribution can also be increased to achieve a spread-out Bragg-peak (SOBP), if needed. Such studies shall be performed using water phantoms in combination with the University Medical Center Groningen (UMCG) PET camera at the final focus of the FRS (see below).

DOSIMETRY

Dosimetry and beam delivery monitoring of RIBs are necessary to correlate the collected PET and prompt gamma signals with dose deposition maps for range verification. Additionally, beam parameters such as divergence, lateral profiles and energy spread are required as input in transport code, treatment planning and radiobiological models. Dosimetry is therefore an essential

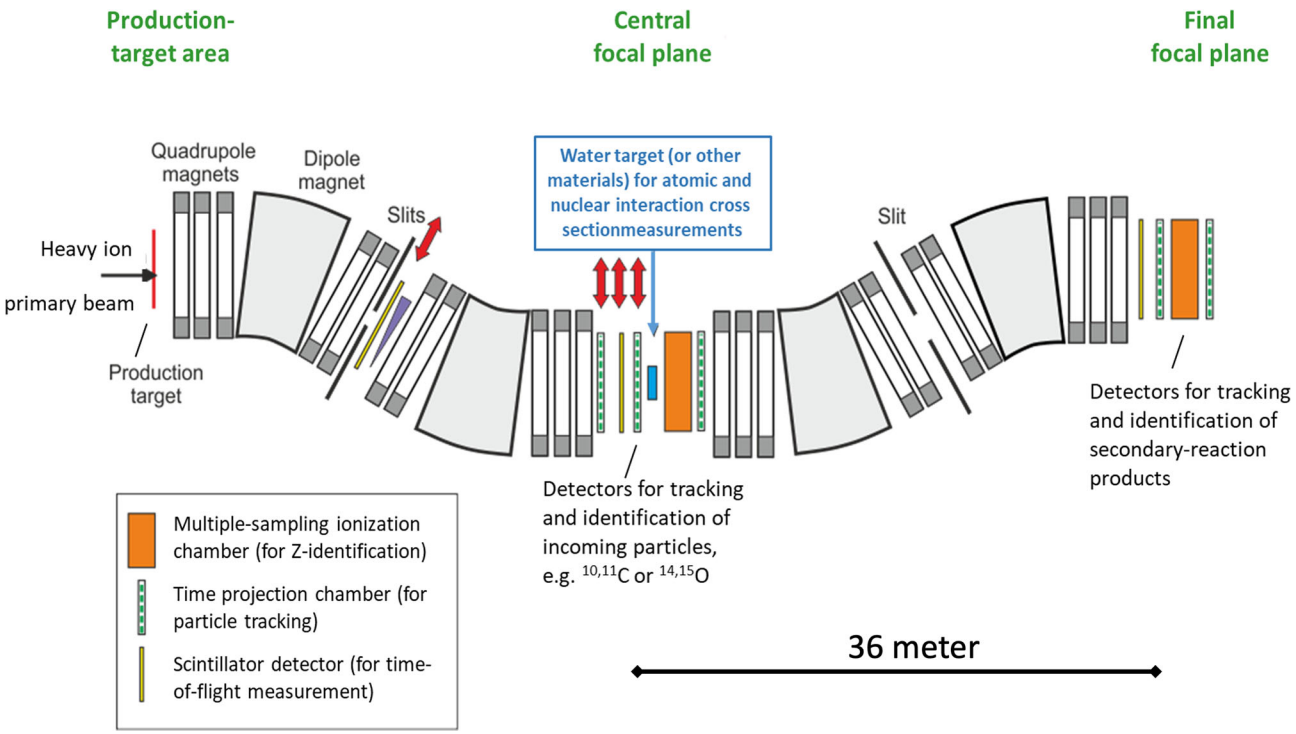

FIGURE 3 | Schematic view of the symmetric FRS branch (projection in the horizontal dispersive plane) and the experimental setup to measure the interaction cross-section and nuclear charge composition of the beam fragmented in water. Red double-sided arrows indicate remotely removable detectors.

component of the BARB experimental campaign, necessary for all other imaging and radiobiological endpoints.

Range monitoring and depth dose distributions of the pristine Bragg peak and SOBP - obtained by using 3D printed modulators (46) - will be measured using the water column setup shown in **Figure 4** (47). Two parallel plate ionization chambers (ICs) are placed at the two extremes of a water phantom with precisely adjustable thickness. The water phantom thickness is controlled by a stepper motor and can be varied with a relative precision down to 10 μm. The ICs are read out with two Keithley K6517A electrometers. The laterally integrated depth dose distribution is then measured as the ratio between the signals collected by the two ICs as a function of the water depth.

To correlate the dose deposition maps with the acquired PET images and to verify treatment plans delivered with RIB, 3D dosimetry will be performed. For this purpose, the water column setup WERNER (WatER column for 2D ioNization chambEr aRray detectors) (48), which was designed for ion beam therapy applications, will be used. This system consists of a plastic water tank of 40 × 33.5 ×35 cm^3 where a watertight detector container attached to a stepper motor is placed inside. The detector position can be changed along the beam direction with a precision of about 100 μm. The system is controlled with a LabVIEW-based control software and synchronized to the beam delivery system. The WERNER detector holder is designed for the PTW 2D IC arrays designed for proton and ion therapy, OCTAVIUS 1500XDR and OCTAVIUS 1000P. The first one consists in a 2D array of 1405 ICs distributed in a chessboard matrix of 27 × 27 cm^2. The center-to-center distance between two ICs is about 7.1 mm and the dose resolution is 0.1 mGy. The OCTAVIUS 1000P is a detector prototype consisting of 977 ICs of 2.3 × 2.3 × 0.5 mm^3 volume with a spatial resolution of 2.5 mm in the 5.5 × 5.5 cm^2 central area and 5 mm in the 11 × 11 cm^2 outer area. A schematic of the WERNER setup and a typical dose map are depicted in **Figure 4**. Additionally, beam profiles and beam divergence will be measured with high spatial resolution Gafchromic® EBT films (International Specialty Products, Wayne, NJ) free in air or a stack of films interlaced with plastic absorbers. An accurate calibration of the beam delivery system in terms of fluence - and thus dose- with the precision standards required for therapy applications will be achieved following the standard GSI protocol for beam monitoring chamber calibration (49).

UMCG PET

The dual-panel positron imaging system of the University Medical Center Groningen (UMCG) is 1/6 of a Siemens Biograph mCT clinical positron emission tomography (PET) scanner (50) with custom-modified detectors. The two detector panels are installed opposite to each other, typically at a distance of 25-30 cm. The phantom in which the beam is stopped is placed in-between the panels (**Figure 5**).

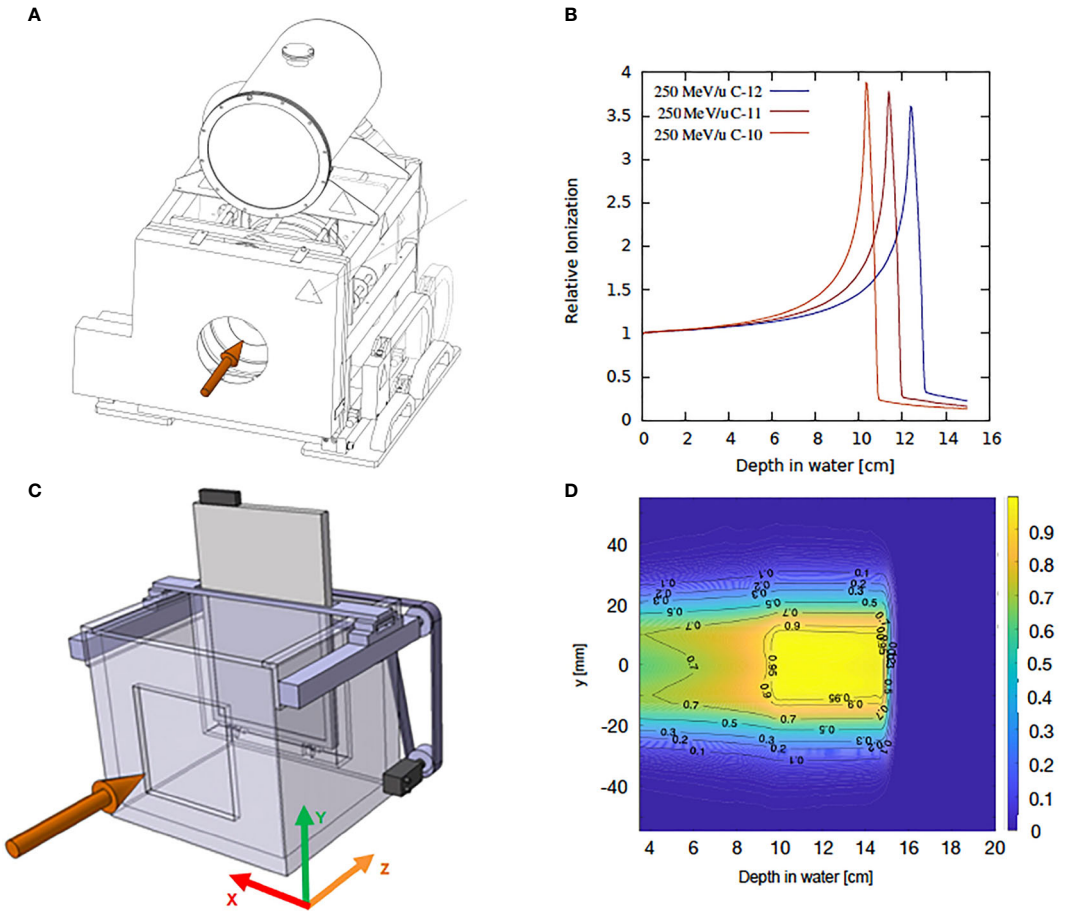

FIGURE 4 | Schematic representation of the experimental setup and typical dose distributions measured with water column and the WERNER setup. **(A)** Technical drawing of the water column. **(B)** FLUKA simulation of laterally integrated 1D depth dose distribution for carbon ion isotopes of 250 MeV/u. **(C)** schematic representation of the WERNER setup. **(D)** 2D dose distribution map for a 4 cm- ^{12}C SOBP.

Being designed for a ring-shaped scanner with a detector ring diameter of 84.2 cm, the detector panels are curved with a radius of curvature of 42.1 cm in one direction and are flat in the other, perpendicular, direction. Each panel covers an area of 22.0×22.5 cm^2 and is composed of a 4×4 array of block detectors. A block detector comprises a 13×13 array of 4×4×20 mm^3 LSO scintillation crystals read out by 4 photomultiplier tubes (PMTs). Anger logic performed on the 4 PMT signals from one event enables to identify the scintillation crystal in which the gamma ray interaction took place. The detectors have been custom-modified such that they can be switched off and on with switching times of less than a millisecond. This switching has been essential in earlier work on nitrogen-12 positron imaging in proton and helium therapy, where short and intense beam pulses were used (51, 52). Whether this option will be useful when imaging radioactive beams will depend on the time structure and intensity of the beams.

Each time a valid coincidence between the two panels is detected, the listmode data acquisition registers which scintillation crystals are involved, the coincidence time (the time difference between the gamma ray detection by the 2 detectors) as well as a clock time stamp with an accuracy of 1 ms. A coincidence is valid if the energy detected is within a user-defined energy window around 511 keV, typically 435-650 keV, and the coincidence time is within the user-defined coincidence time window, typically 4 ns. Knowing which scintillation crystals were involved in a coincidence enables to establish the Line-of-Response (LoR) as the line connecting the two crystals. The LoR's are subsequently used to generate an image. The 550 ps (FWHM) time-of-flight (ToF) resolution of the system restricts the position of positron annihilation along a LoR of about 8 cm (FWHM). The ToF information will be useful to improve the contrast-to-noise ratio of the images in case the size of the irradiated area is comparable to or larger than this 8 cm.

LMU DETECTOR

The hybrid detector able to visualize PET, PG and even triple coincidence emissions (e.g., from ^{10}C) for the BARB project is

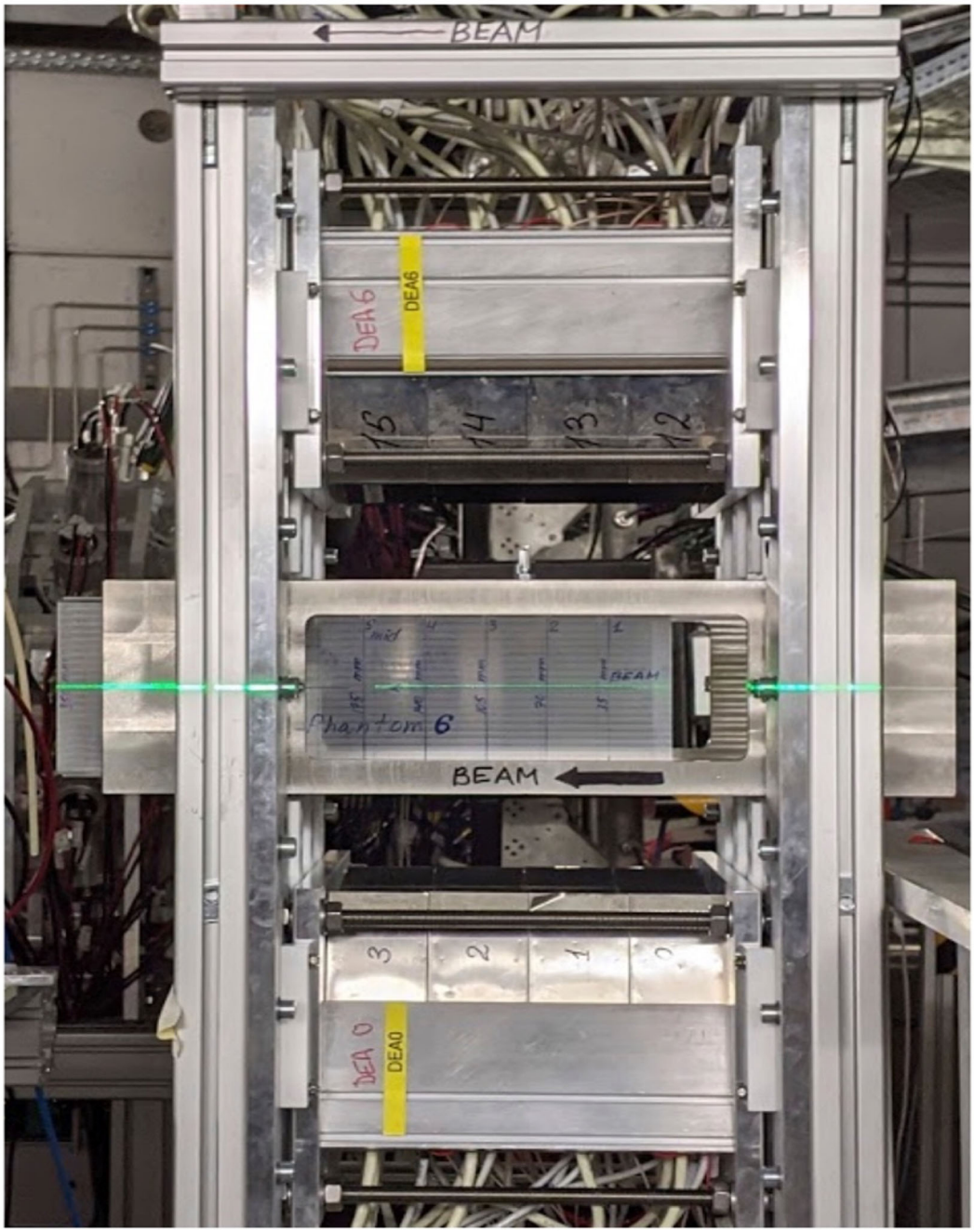

FIGURE 5 | The dual-panel UMCG positron imaging system installed at the Fragment Separator FRS at GSI. A beam of radioactive ions is coming from the right hand side and stopped in the PMMA phantom seen in the middle of the picture. The two detector panels are installed above and below the phantom each at a distance of 30 cm.

going to be developed at LMU by combining detector technologies currently under investigation for PET and PG (7) imaging, as well as a combination thereof in the context of proton therapy (53). In particular, the absorber component of the envisioned hybrid BARB detector will rely on a high resolution PET detector which was recently developed at LMU, in collaboration with NIRS-QST, for an in-beam small animal PET scanner prototype within the ERC-funded project "Small Animal Proton Irradiator for Research in Molecular Image-guided Radiation-Oncology" (SIRMIO) (10). This LMU-PET detector aims to achieve sub-millimeter spatial resolution along with the capability of identifying the Depth-Of-Interaction

(DOI) (54). The latter DOI information reduces the effect of parallax errors, which cause degradation of a PET image at the peripheral areas of a field of view. **Figure 6A** shows the LMU-PET detector, which is composed of a 3-layer $Lu_{1.9}Y_{0.1}SiO_5$ (LYSO, density: 7.25 g/cm^3) scintillator block (EPIC, China) and a SiPM array. The scintillator pixel size is 0.9 mm × 0.9 mm × 6.67 mm. The 1st, 2nd and 3rd layers consist of arrays of 23 × 20, 23 × 23 and 24 × 24 pixels, respectively, to form a staggered DOI detector. An 8 × 8 multi-pixel photon counter array (MPPC, micro-cell size: 50 µm × 50 µm, each sensitive area: 3 mm × 3 mm, total area: 25.8 mm × 25.8 mm, Hamamatsu photonics K.K, S14161-3050HS-08, Japan) is used as photo detector. A light guide with a thickness of 1 mm is inserted between the 3-layer scintillator block and the MPPC array. We use a charge division circuit to reduce the 64 signals from the MPPC array to 4 single-ended readouts (55). The 4 single-ended readouts are processed by an amplifier circuit board and converted to a differential signal. The differential signals are fed to a digitizer (R5560, CAEN, Italy). An Anger calculation is used to project an interaction position between the scintillator pixel and a γ-ray on a 2-D position histogram. The Anger calculation result of the scintillator pixel forms a pixel response as a cluster in the 2-D position histogram, which is called a flood map. Because each pixel response is drawn without overlapping each other, the interaction position can be identified. **Figure 6B** shows the flood map obtained by irradiating 511 keV annihilation γ-rays from a ^{22}Na point source. Pixel responses of each layer are clearly separated, indicating the pixel resolution of 0.9 mm.

BARB4D

The treatment of targets in intrafractionally moving organs poses a significant challenge (56), not only in conformal delivery strategies (57), but especially also in visualizing complex motion within the patient (58). The workhorse for current 4D-treatment planning is time-resolved computed tomography (4DCT) in combination with Deformable Image Registration (DIR). Both have caveats: the 4DCT depicts a single synthesized breathing cycle, and DIR has known inaccuracies and is hard to verify, especially in organs that offer low contrast in the CT, such as the liver or heart.

PET offers an exciting opportunity to study 4D-dose deposition in complex geometries or patients. Time-resolved PET imaging has the advantage of showing the deposited activity, which moves with the respective organ, following also complex deformations or rotations not visible with other methods. Previous research (13, 59) was hampered by low activity and the dissociation of dose and activity, both of which can be resolved with RIBs.

We propose a proof-of-concept study in small, rotating phantoms that both fit into the small Volume-Of-Interest (VOI) of the planned BARB detector and still offer a significant motion amplitude (**Figure 7**). High-resolution PET will resolve both uncompensated interplay distortion of dose and the efficacy of motion mitigation strategies in this complex scenario. Ideally, experiments would continue in a larger animal model, which permits to study realistic complex motion patterns that are difficult to simulate in phantoms. In this way, time-resolved RIB PET provides an endpoint to test motion detection and DIR as well as 4D-dose reconstruction and motion mitigation strategies. This work could be continued in a later clinical facility with human patients, but will already provide valuable input for 4D-delivery research in the project lifetime of BARB.

RADIOBIOLOGY

The final goal of BARB is a tumor treatment in an animal model with RIBs. This will be the final proof of the potential of RIBs in particle therapy, and will assess the real advantages compared to

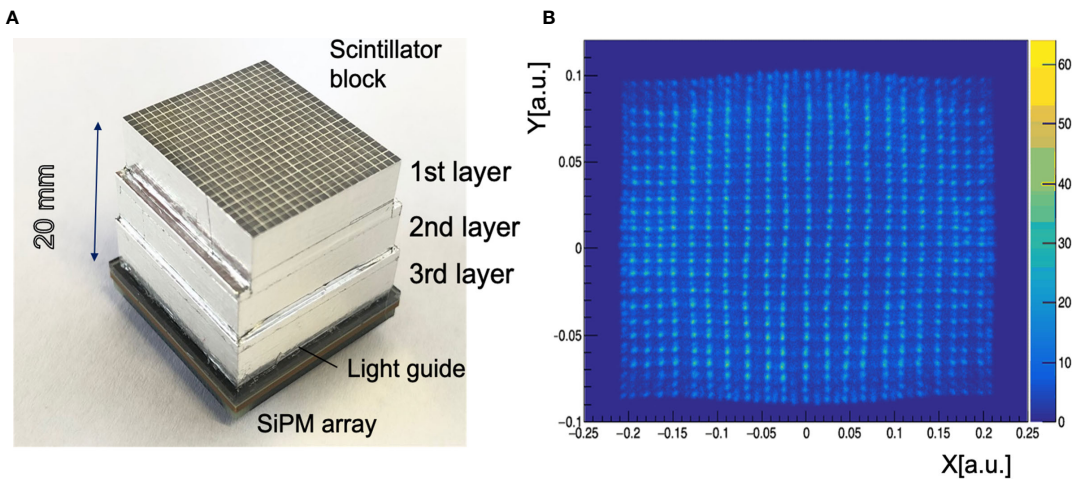

FIGURE 6 | LMU hybrid γ-PET detector **(A)** A 3-layer PET detector developed at LMU Munich in collaboration with NIRS-QST. The PET detector consists of a 3-layer scintillator block, a light guide and an 8 × 8 SiPM array. **(B)** A flood map of the 3-layer PET detector exposed to a ^{22}Na radioactive point source.

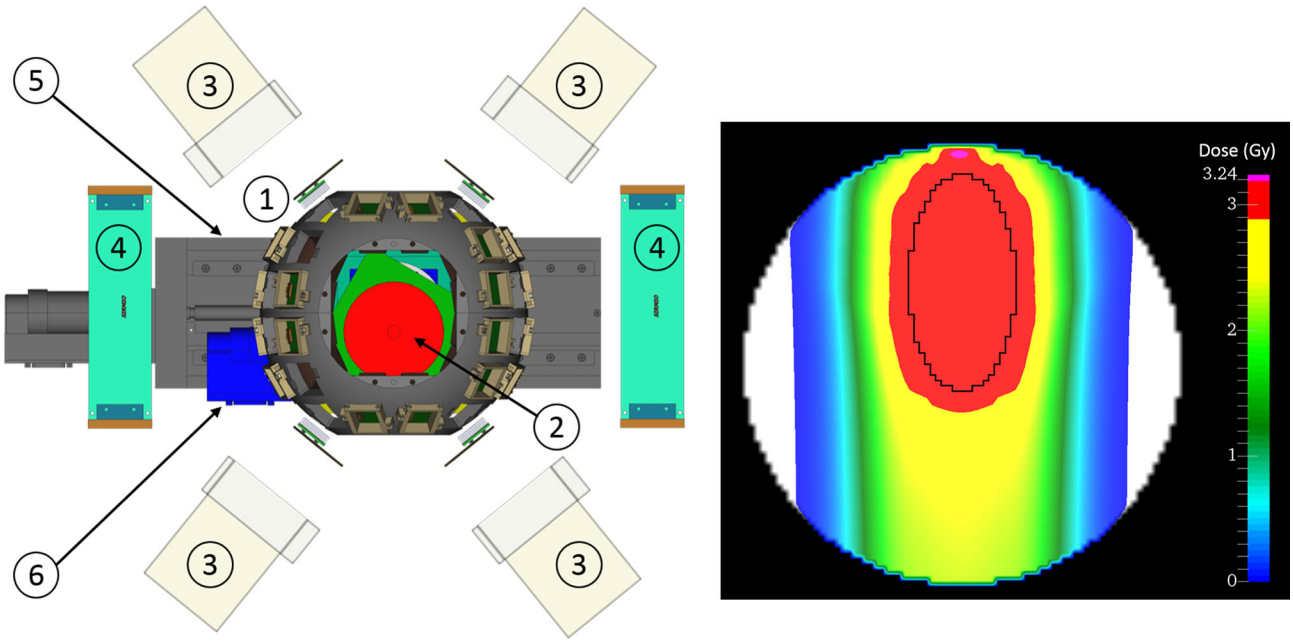

FIGURE 7 | The BARB4D setup: (1) SIRMIO cage with 32 PET detectors, (2) cylindrical phantom, (3) Compton camera, (4) Amplifier circuit boards for PET detectors, (5) translation stage, (6) rotating stage. The beam is entering the phantom from below. Right: Planned dose distribution for a static delivery with ellipsoidal target region.

stable ions. The RIB will be then directed to biological targets, first *in vitro* mammalian cell cultures and finally a mouse tumor.

In Vitro Experiments

Measurement of the Relative Biological Effectiveness (RBE) is essential in heavy ion therapy, because the RBE varies along the Bragg peak and can be high in the distal part (60). The Local Effect Model (LEM), coupled to the deterministic transport code TRiP98, is used in the European clinical centers for treatment planning (61). In fact, LEM reproduces very well the survival of mammalian cells to both carbon (62) and oxygen beams (63). LEM assumes that the RBE depends on the charge and velocity of the ion, so no significant differences are expected between radioactive isotopes and stable ^{12}C and ^{16}O ions. Similar RBE values for stable and radioactive light ions at different depths in the spread-out-Bragg-peak (SOBP) are also predicted by the microdosimetric kinetic model (64, 65). However, models are affected by large uncertainties (66, 67) and differences may be caused by the different nuclear interactions and the production of secondary particles. We will therefore repeat the dosimetry experiments using a cellular phantom (62), where cell killing can be accurately measured at different depths along the SOBP (**Figure 8**). Results of the survival curves in Chinese Hamster Ovary (CHO) cells at different positions will be compared to the TriP98/LEM predictions.

Animal Experiments

The final test of our method will be the first ever treatment of a tumor by RIB. We will use a mouse model, which can be visualized with the small Filed-Of-View (FOV) of our hybrid detector (see *LMU Detector*). We will focus on an orthotopic mouse model and, for comparison, a xenograft. Syngeneic allografts will be prepared for abdominal tumors in nude mice, while xenograft will be implanted in immune-competent strains.

We have previously worked on an autochthonous model of murine soft tissue sarcoma in the mouse leg (68). In that experiment, the tumors were irradiated with a 3-cm SOBP from a 110 MeV/u ^{12}C beam in the whole leg (69). With similar large fields, we have irradiated LM8 osteosarcomas in the hind limb of C3H mice (**Figure 9**) with C-ions (70). In fact, control of the beam in the small mouse tumors would be very difficult without online imaging. Here we aim to reduce the margins to show that we can precisely irradiate small murine tumors whilst sparing the surrounding normal tissue. The choice of the RIB isotope will come from the output of the experiments in *Dosimetry*. A single dose will be used, and the RIB physical dose in Gy will be corrected for the RBE, based on the results in *In Vitro Experiments*, in order to compare equally effective doses. For the orthotopic model, we will plan the mouse treatment based on μCT, available in our experimental room Cave M at GSI, and will apply a very small margin of approximately 0.5 mm for a tumor, whose diameter will be approximately 5-6 mm. The μCT data can be imported into the MEGAlib geometry file (71) of the SIRMIO hybrid detector (10), thus allowing full Monte Carlo simulation of the experiment (**Figure 9**). We will irradiate anesthetized and immobilized mice with a single beam port, a situation where range uncertainty is critical. The hybrid detector prototype for small animals will be used for online monitoring of both stable and radioactive beams. Tumor growth will be measured every

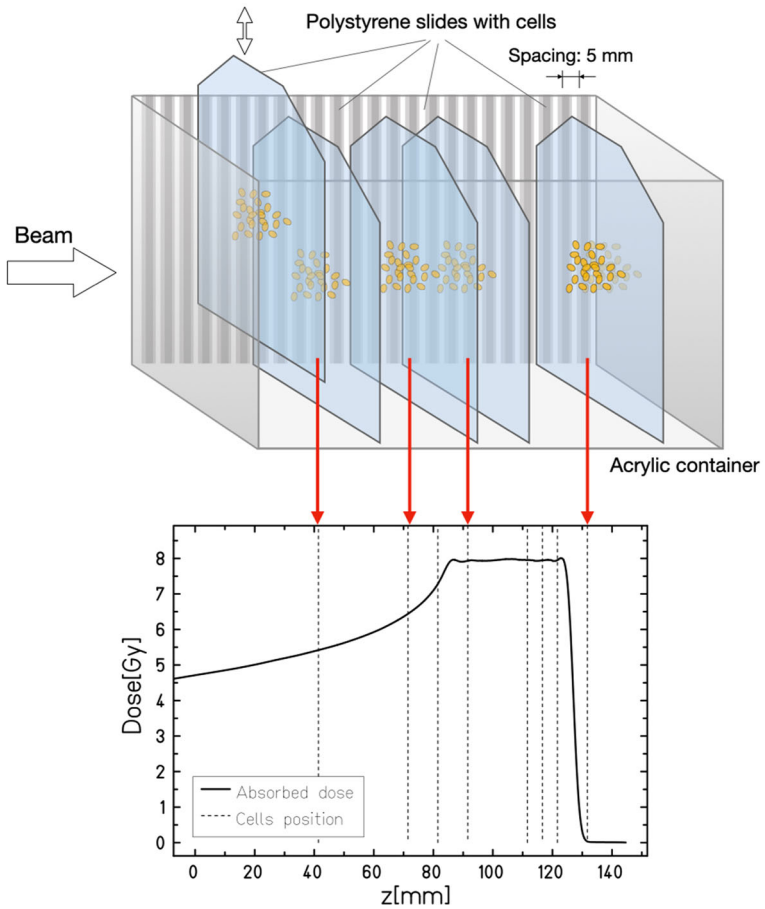

FIGURE 8 | Cellular phantom used for radiobiological measurements along a SOBP. The cells grow in monolayer on plastic plates that can be plunged at different position in the tank filled with water-equivalent growth medium. Plates are then removed after irradiation and the cell survival is measured in every position. In the BARB experiment, stable and radioactive carbon and oxygen isotopes will be used to irradiate CHO cells, under the null-hypothesis that no difference will be observed.

three days. Animals will be finally sacrificed 21 days post-exposure and following a final CT scan. Histological analysis will be used to determine the irradiated tissue. Our working hypothesis is that the improved accuracy with RIB translates into improved local control compared to stable ion treatments with small margins that may miss the target. These experiments will provide the best accuracy achievable *in vivo* with RIB and the impact of the improved precision on the control of small tumors.

RIB as *In Vivo* Tracers

Additional experiments will be performed using RIBs as radioactive tracers implanted in the tumors. The purpose will be to clarify the role of vascular damage in single-fraction high-dose radiotherapy (72). One hypothesis of the clinical success of single-dose radiotherapy (73), even compared to hypofractionation (74), is the vascular dysfunction (75) *via* ischemia/reperfusion injury (76). Other authors contend that the increased effectiveness of single-fraction is well explained by the classical radiobiology in terms of reduced repair, i.e. increased biologically effective dose, and no special role of the vascular system is necessary to explain the clinical results (77, 78). A recent study using dynamic contrast-enhanced magnetic resonance imaging in a rat tumor model showed that high doses of X-rays or C-ions enhance vascular damage and increase permeability of the tumor (79, 80). We have the opportunity of using the RIB as very precise monitor of the vascular permeability, because essentially we deposit a high concentration of radiotracers in the tumor in a very short time. By measuring in PET the washout of the signal with the arrangement shown in **Figure 9**, corrected for the physical half-life after low and high doses, we will assess the different vascular permeability at different doses and will assess whether at doses higher than a threshold this mechanism can lead to tumor control. This will clarify whether vascular damage plays a role in high-dose single-fraction.

CONCLUSIONS AND OUTLOOK

For many years, RIBs have been proposed as the ideal bullet for image-guided particle therapy (29). The practical advantage of

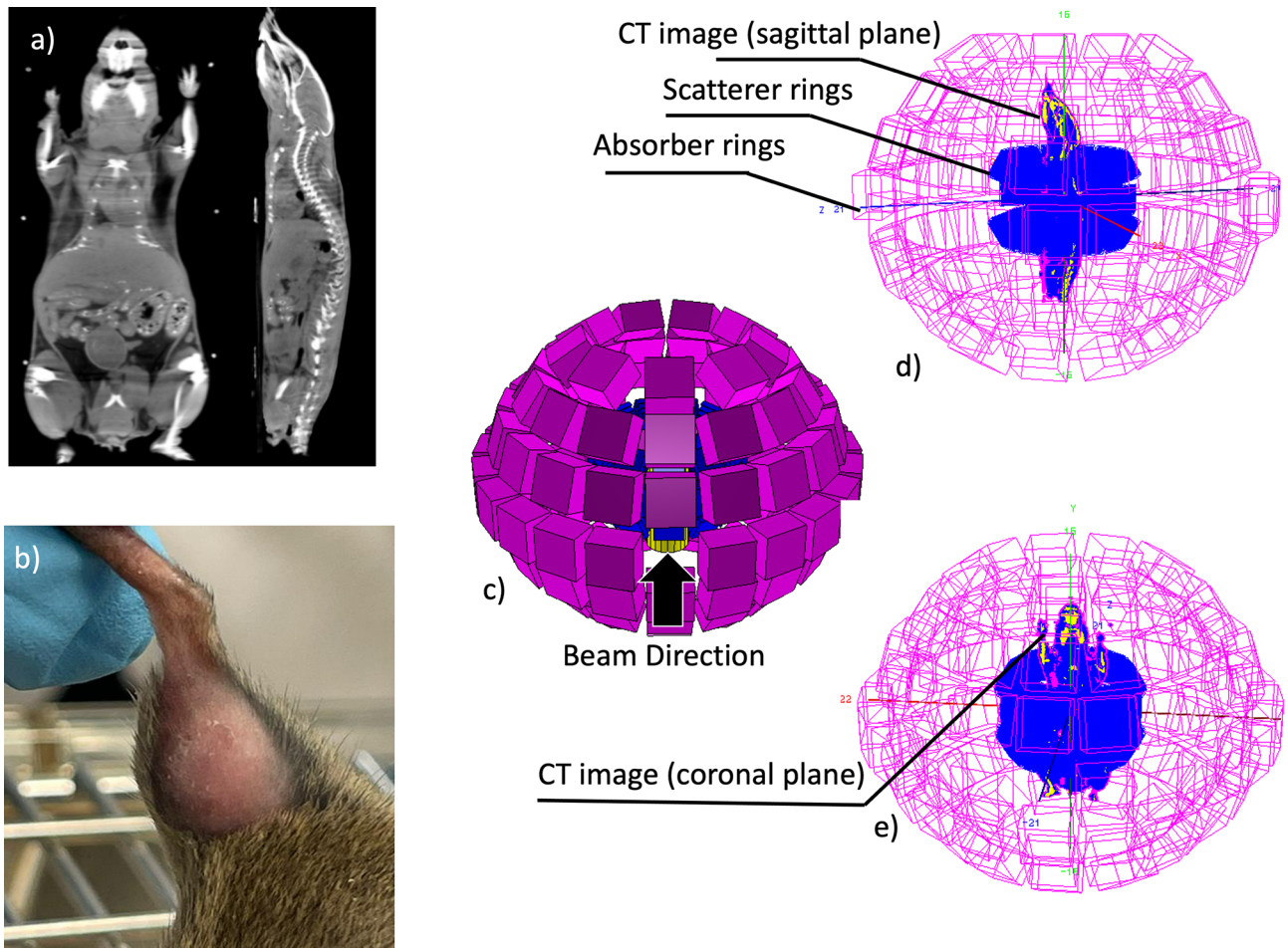

FIGURE 9 | **(A)** Mouse CT image, coronal and sagittal planes, **(B)** example of an osteosarcoma in the C3H mouse hind limb; **(C)** the proposed hybrid Compton-PET scanner for the radioactive ion beam range verification, **(D, E)** the scanner configuration with the CT image of the mouse (sagittal and coronal planes are plotted, respectively) positioned along the scanner bore.

RIB therapy compared to conventional stable-ion treatments remains howbeit unproven. The theoretical advantage can be estimated with a treatment planning calculation of the dosimetric advantage gained by reducing the margins (81). **Figure 1** suggests that beam visualization with RIB can essentially eliminate the range uncertainty (3.5% of the range), leaving only the setup margin. We applied this concept to the patients treated at GSI during the pilot project for adenoid cystic carcinoma (ACC) with a boost of carbon ions after intensity-modulated radiotherapy in Heidelberg (82, 83). We have re-evaluated the C-ions treatment plans using robust planning and looking at the potential reductions in normal tissue toxicity when the clinical target volume (CTV) margin is reduced to the re-positioning uncertainty (3 mm) only. Tolerance of the optic nerve was set according to the recommendations of the European Particle Therapy Network as $D_{0.03\ cc}$<55 Gy and α/β= 2 Gy (84). As shown in **Figure 10**, we found that margin reduction using RIB leads to a significant sparing of the optical nerves in more than 50% of the patients.

The BARB project will therefore clarify the real advantage of RIB therapy, reaching the stage of the treatment of an animal patient with ^{11}C and ^{15}O and simultaneous beam visualization. BARB will exploit the intensity upgrade in FAIR-phase-0 and a novel γ-PET detector for beam visualization. It can be contended that even positive and exciting results will hardly have clinical impact, because in-flight production of RIBs would be impractical in current medical synchrotrons. However, already during the pilot heavy ion project at the Lawrence Berkeley Laboratory (CA, USA), it was proposed to produce the RIBs at low energy and then inject them in the high-energy medical accelerator (85). The idea is to build a small cyclotron that can produce low-energy RIBs with an ISOL system (86), and these ions are then injected in conventional synchrotrons. A source using low-energy electron beams for the production of ^{11}C has been designed and produced at HIMAC (87). Within the MEDICIS-Promed project (88), CERN has proposed a charge breeding scheme based on an Electron Beam Ion Source for beam preparation of a radioactive ^{11}C beam (89). The charge

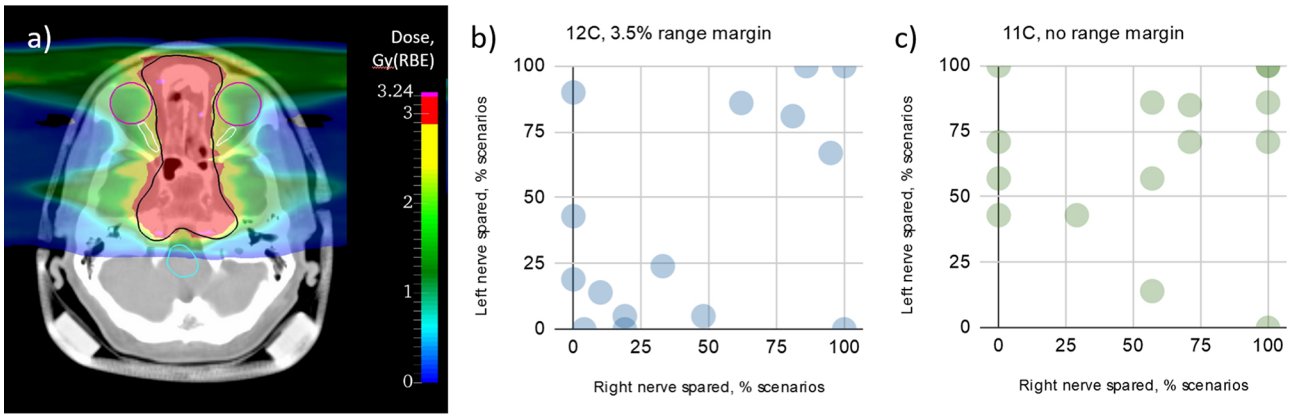

FIGURE 10 | Impact of range margin reduction in robust optimization on the optic nerves sparing for a set of ACC patients. **(A)** Example of CT and two-field dose distribution for one of the analyzed patient plans. CTV, optic nerves, eyes and brainstem are contoured with black, white, purple and turquoise colors, respectively. Color bar represents the dose distribution (prescribed dose 3 Gy(RBE)). Primary goal of the robust optimization was achieving at least 95% of the prescribed dose in 95% of uncertainty scenarios (21 scenarios in total). Graphs represent sparing of left and right optic nerves in the analyzed plans with ^{12}C beams **(B)** (3.5% range and 3 mm setup margin) and ^{11}C plans **(C)** (3 mm setup margin only), respectively. Each point corresponds to a single patient case (15 patients total).

breeder is coupled to a medical synchrotron currently used for ^{12}C-ion therapy to treat patients with ^{11}C using the same beam delivery devices of conventional heavy-ion therapy (90). The future of this ambitious project will depend on the results of the BARB project in the coming five-year period.

DATA AVAILABILITY STATEMENT

The raw data supporting the conclusions of this article will be made available by the authors, without undue reservation.

AUTHOR CONTRIBUTIONS

The authors of this manuscript are all working in the BARB experiment. The paper was read and discussed among different authors. Some lead author took the responsibility to write the different sections: MD drafted sections 1, 6, and 7; CSche drafted section 2; DB and UW drafted section 3; PD drafted section 4; KP, MN, and CGr drafted section 5. All authors contributed to the article and approved the submitted version.

FUNDING

This work is supported by European Research Council (ERC) Advanced Grant 883425 BARB to MD and in part by the ERC Consolidator Grant 725539 SIRMIO to KP. The measurements described here are performed within the experiments S533_Purushothaman and SBio08_Parodi at SIS18/FRS/S4/Cave-M at the GSI Helmholtzzentrum für Schwerionenforschung, Darmstadt (Germany) in the frame of FAIR Phase-0.

ACKNOWLEDGMENTS

We thank the GSI accelerator crew for their outstanding work in providing high-intensity beamtime for BARB and the GSI beamtime coordinator Dr. Daniel Severin for accommodating the experiment's needs and useful discussions about the different options.

REFERENCES

1. Grégoire V, Guckenberger M, Haustermans K, Lagendijk JJW, Ménard C, Pötter R, et al. Image Guidance in Radiation Therapy for Better Cure of Cancer. *Mol Oncol* (2020) 14:1470–91. doi: 10.1002/1878-0261.12751
2. Otazo R, Lambin P, Pignol J-P, Ladd ME, Schlemmer H-P, Baumann M, et al. MRI-Guided Radiation Therapy: An Emerging Paradigm in Adaptive Radiation Oncology. *Radiology* (2021) 298:248–60. doi: 10.1148/radiol.2020202747
3. Lomax AJ. Myths and Realities of Range Uncertainty. *Br J Radiol* (2020) 93:20190582. doi: 10.1259/bjr.20190582
4. Paganetti H. Range Uncertainties in Proton Therapy and the Role of Monte Carlo Simulations. *Phys Med Biol* (2012) 57:R99–117. doi: 10.1088/0031-9155/57/11/R99
5. Durante M, Flanz J. Charged Particle Beams to Cure Cancer: Strengths and Challenges. *Semin Oncol* (2019) 46:219–25. doi: 10.1053/j.seminoncol.2019.07.007
6. Knopf A-C, Lomax A. In Vivo Proton Range Verification: A Review. *Phys Med Biol* (2013) 58:R131–60. doi: 10.1088/0031-9155/58/15/R131
7. Krimmer J, Dauvergne D, Létang JM, Testa É. Prompt-Gamma Monitoring in Hadrontherapy: A Review. *Nucl Instruments Methods Phys Res Sect A Accel Spectrometers Detect Assoc Equip* (2018) 878:58–73. doi: 10.1016/j.nima.2017.07.063
8. Piersanti L, Bellini F, Bini F, Collamati F, De Lucia E, Durante M, et al. Measurement of Charged Particle Yields From PMMA Irradiated by a 220 MeV/u 12C Beam. *Phys Med Biol* (2014) 59:1857–72. doi: 10.1088/0031-9155/59/7/1857
9. Félix-Bautista R, Gehrke T, Ghesquière-Diérickx L, Reimold M, Amato C, Turecek D, et al. Experimental Verification of a Non-Invasive Method to

Monitor the Lateral Pencil Beam Position in an Anthropomorphic Phantom for Carbon-Ion Radiotherapy. *Phys Med Biol* (2019) 64:175019. doi: 10.1088/1361-6560/ab2ca3

10. Parodi K, Assmann W, Belka C, Bortfeldt J, Clevert D-A, Dedes G, et al. Towards a Novel Small Animal Proton Irradiation Platform: The SIRMIO Project. *Acta Oncol (Madr)* (2019) 58:1–6. doi: 10.1080/0284186X.2019.1630752
11. Traini G, Mattei I, Battistoni G, Bisogni MG, De Simoni M, Dong Y, et al. Review and Performance of the Dose Profiler, a Particle Therapy Treatments Online Monitor. *Phys Med* (2019) 65:84–93. doi: 10.1016/j.ejmp.2019.07.010
12. Ferrero V, Fiorina E, Morrocchi M, Pennazio F, Baroni G, Battistoni G, et al. Online Proton Therapy Monitoring: Clinical Test of a Silicon-Photodetector-Based in-Beam PET. *Sci Rep* (2018) 8:4100. doi: 10.1038/s41598-018-22325-6
13. Parodi K. Vision 20/20: Positron Emission Tomography in Radiation Therapy Planning, Delivery, and Monitoring. *Med Phys* (2015) 42:7153–68. doi: 10.1118/1.4935869
14. Gambhir SS. Molecular Imaging of Cancer With Positron Emission Tomography. *Nat Rev Cancer* (2002) 2:683–93. doi: 10.1038/nrc882
15. Durante M, Debus J. Heavy Charged Particles: Does Improved Precision and Higher Biological Effectiveness Translate to Better Outcome in Patients? *Semin Radiat Oncol* (2018) 28:160–7. doi: 10.1016/j.semradonc.2017.11.004
16. Sommerer F, Cerutti F, Parodi K, Ferrari A, Enghardt W, Aiginger H. In-Beam PET Monitoring of Mono-Energetic 16 O and 12 C Beams: Experiments and FLUKA Simulations for Homogeneous Targets. *Phys Med Biol* (2009) 54:3979–96. doi: 10.1088/0031-9155/54/13/003
17. Durante M, Paganetti H. Nuclear Physics in Particle Therapy : A Review. *Rep Prog Phys* (2016) 79:96702. doi: 10.1088/0034-4885/79/9/096702
18. Enghardt W, Parodi K, Crespo P, Fiedler F, Pawelke J, Pönisch F. Dose Quantification From in-Beam Positron Emission Tomography. *Radiother Oncol* (2004) 73:S96–8. doi: 10.1016/S0167-8140(04)80024-0
19. Handrack J, Tessonnier T, Chen W, Liebl J, Debus J, Bauer J, et al. Sensitivity of Post Treatment Positron Emission Tomography/Computed Tomography to Detect Inter-Fractional Range Variations in Scanned Ion Beam Therapy. *Acta Oncol (Madr)* (2017) 56:1451–8. doi: 10.1080/0284186X.2017.1348628
20. Bauer J, Unholtz D, Sommerer F, Kurz C, Haberer T, Herfarth K, et al. Implementation and Initial Clinical Experience of Offline PET/CT-Based Verification of Scanned Carbon Ion Treatment. *Radiother Oncol* (2013) 107:218–26. doi: 10.1016/j.radonc.2013.02.018
21. Nishio T, Miyatake A, Ogino T, Nakagawa K, Saijo N, Esumi H. The Development and Clinical Use of a Beam ON-LINE PET System Mounted on a Rotating Gantry Port in Proton Therapy. *Int J Radiat Oncol* (2010) 76:277–86. doi: 10.1016/j.ijrobp.2009.05.065
22. Buitenhuis HJT, Diblen F, Brzezinski KW, Brandenburg S, Dendooven P. Beam-On Imaging of Short-Lived Positron Emitters During Proton Therapy. *Phys Med Biol* (2017) 62:4654–72. doi: 10.1088/1361-6560/aa6b8c
23. Kraan AC, Battistoni G, Belcari N, Camarlinghi N, Cirrone GAP, Cuttone G, et al. Proton Range Monitoring With in-Beam PET: Monte Carlo Activity Predictions and Comparison With Cyclotron Data. *Phys Med* (2014) 30:559–69. doi: 10.1016/j.ejmp.2014.04.003
24. Pinto M, Kroeniger K, Bauer J, Nilsson R, Traneus E, Parodi K. A Filtering Approach for PET and PG Predictions in a Proton Treatment Planning System. *Phys Med Biol* (2020) 65:095014. doi: 10.1088/1361-6560/ab8146
25. Nischwitz SP, Bauer J, Welzel T, Rief H, Jäkel O, Haberer T, et al. Clinical Implementation and Range Evaluation of *In Vivo* PET Dosimetry for Particle Irradiation in Patients With Primary Glioma. *Radiother Oncol* (2015) 115:179–85. doi: 10.1016/j.radonc.2015.03.022
26. Augusto RS, Bauer J, Bouhali O, Cuccagna C, Gianoli C, Kozłowska WS, et al. An Overview of Recent Developments in FLUKA PET Tools. *Phys Med* (2018) 54:189–99. doi: 10.1016/j.ejmp.2018.06.636
27. Mohammadi A, Tashima H, Iwao Y, Takyu S, Akamatsu G, Kang HG, et al. Influence of Momentum Acceptance on Range Monitoring of 11 C and 15 O Ion Beams Using in-Beam PET. *Phys Med Biol* (2020) 65:125006. doi: 10.1088/1361-6560/ab8059
28. Llacer J, Chatterjee A, Alpen EL, Saunders W, Andreae S, Jackson HC. Imaging by Injection of Accelerated Radioactive Particle Beams. *IEEE Trans Med Imaging* (1984) 3:80–90. doi: 10.1109/TMI.1984.4307660
29. Durante M, Parodi K. Radioactive Beams in Particle Therapy: Past, Present, and Future. *Front Phys* (2020) 8:326. doi: 10.3389/fphy.2020.00326
30. Durante M, Golubev A, Park W-Y, Trautmann C. Applied Nuclear Physics at the New High-Energy Particle Accelerator Facilities. *Phys Rep* (2019) 800:1–37. doi: 10.1016/j.physrep.2019.01.004
31. Durante M, Indelicato P, Jonson B, Koch V, Langanke K, Meißner U-G, et al. All the Fun of the FAIR: Fundamental Physics at the Facility for Antiproton and Ion Research. *Phys Scr* (2019) 94:033001. doi: 10.1088/1402-4896/aaf93f
32. Bai M, Adonin A, Appel S, Bär R, Bellachioma MC, Blell U, et al. Challenges of FAIR-Phase. In: *9th International Particle Accelerator Conference*. pp. 2947–9. Vancouver, Canada: JACoW Publishing (2018). pp. 2947–9. doi: 10.18429/JACoW-IPAC2018-THYGBF3
33. Pawelke J, Byars L, Enghardt W, Fromm WD, Geissel H, Hasch BG, et al. The Investigation of Different Cameras for in-Beam PET Imaging. *Phys Med Biol* (1996) 41:279–96. doi: 10.1088/0031-9155/41/2/006
34. Safari M, Zoglauser A, Lovatti G, Anangnostatou V, Nitta M, Tashima H, et al. Performance of a Novel Hybrid Gamma-Imaging Technique Toward Future 3d Reconstruction of Proton Beam Range. In: *IEEE Med Imaging Conf*. Manchester, UK (2019).
35. Geissel H, Armbruster P, Behr KH, Brünle A, Burkard K, Chen M, et al. The GSI Projectile Fragment Separator (FRS): A Versatile Magnetic System for Relativistic Heavy Ions. *Nucl Instruments Methods Phys Res Sect B Beam Interact Mater Atoms* (1992) 70:286–97. doi: 10.1016/0168-583X(92)95944-M
36. Scheidenberger C, Geissel H, Maier M, Münzenberg G, Portillo M, Savard G, et al. Energy and Range Focusing of in-Flight Separated Exotic Nuclei – A Study for the Energy-Buncher Stage of the Low-Energy Branch of the Super-FRS. *Nucl Instruments Methods Phys Res Sect B Beam Interact Mater Atoms* (2003) 204:119–23. doi: 10.1016/S0168-583X(02)01898-0
37. Geissel H, Schwab T, Armbruster P, Dufour JP, Hanelt E, Schmidt K-H, et al. Ions Penetrating Through Ion-Optical Systems and Matter — Non-Liouvillian Phase-Space Modelling. *Nucl Instruments Methods Phys Res Sect A Accel Spectrometers Detect Assoc Equip* (1989) 282:247–60. doi: 10.1016/0168-9002(89)90148-4
38. Enghardt W, Fromm WD, Geissel H, Heller H, Kraft G, Magel A, et al. The Spatial Distribution of Positron-Emitting Nuclei Generated by Relativistic Light Ion Beams in Organic Matter. *Phys Med Biol* (1992) 37:2127–31. doi: 10.1088/0031-9155/37/11/009
39. Horst F, Adi W, Aricò G, Brinkmann K-T, Durante M, Reidel C-A, et al. Measurement of PET Isotope Production Cross Sections for Protons and Carbon Ions on Carbon and Oxygen Targets for Applications in Particle Therapy Range Verification. *Phys Med Biol* (2019) 64:205012. doi: 10.1088/1361-6560/ab4511
40. Kanungo R, Horiuchi W, Hagen G, Jansen GR, Navratil P, Ameil F, et al. Proton Distribution Radii of 12–19C Illuminate Features of Neutron Halos. *Phys Rev Lett* (2016) 117:102501. doi: 10.1103/PhysRevLett.117.102501
41. Schwab W, Geissel H, Lenske H, Behr K-H, Brnle A, Burkard K, et al. Observation of a Proton Halo In8b. *Z fuer Phys A Hadron Nucl* (1995) 350:283–4. doi: 10.1007/BF01291183
42. Ozawa A, Bochkarev O, Chulkov L, Cortina D, Geissel H, Hellström M, et al. Measurements of Interaction Cross Sections for Light Neutron-Rich Nuclei at Relativistic Energies and Determination of Effective Matter Radii. *Nucl Phys A* (2001) 691:599–617. doi: 10.1016/S0375-9474(01)00563-2
43. Suzuki T, Geissel H, Bochkarev O, Chulkov L, Golovkov M, Hirata D, et al. Neutron Skin of Na Isotopes Studied *via* Their Interaction Cross Sections. *Phys Rev Lett* (1995) 75:3241–4. doi: 10.1103/PhysRevLett.75.3241
44. Mohammadi A, Tashima H, Iwao Y, Takyu S, Akamatsu G, Nishikido F, et al. Range Verification of Radioactive Ion Beams of 11C and 15O Using in-Beam PET Imaging. *Phys Med Biol* (2019) 64:145014. doi: 10.1088/1361-6560/ab25ce
45. Sakurai H, Itoh F, Hirano Y, Nitta M, Suzuki K, Kato D, et al. Positron Annihilation Spectroscopy of Biological Tissue in ^{11} C Irradiation. *Phys Med Biol* (2014) 59:7031–8. doi: 10.1088/0031-9155/59/22/7031
46. Simeonov Y, Weber U, Penchev P, Ringbæk TP, Schuy C, Brons S, et al. 3D Range-Modulator for Scanned Particle Therapy: Development, Monte Carlo Simulations and Experimental Evaluation. *Phys Med Biol* (2017) 62:7075–96. doi: 10.1088/1361-6560/aa81f4
47. Horst F, Schardt D, Iwase H, Schuy C, Durante M, Weber U. Physical Characterization of 3 He Ion Beams for Radiotherapy and Comparison With 4 He. *Phys Med Biol* (2021) 66:095009. doi: 10.1088/1361-6560/abef88

48. Schuy C, Simeonov Y, Durante M, Zink K, Weber U. Technical Note: Vendor-Agnostic Water Phantom for 3D Dosimetry of Complex Fields in Particle Therapy. *J Appl Clin Med Phys* (2020) 21:227–32. doi: 10.1002/acm2.12996
49. Luoni F, Weber U, Boscolo D, Durante M, Reidel C-A, Schuy C, et al. Beam Monitor Calibration for Radiobiological Experiments With Scanned High Energy Heavy Ion Beams at FAIR. *Front Phys* (2020) 8:568145. doi: 10.3389/fphy.2020.568145
50. Jakoby BW, Bercier Y, Conti M, Casey ME, Bendriem B, Townsend DW. Physical and Clinical Performance of the mCT Time-of-Flight PET/CT Scanner. *Phys Med Biol* (2011) 56:2375–89. doi: 10.1088/0031-9155/56/8/004
51. Ozoemelam I, van der Graaf E, van Goethem M-J, Kapusta M, Zhang N, Brandenburg S, et al. Feasibility of Quasi-Prompt PET-Based Range Verification in Proton Therapy. *Phys Med Biol* (2020) 65:245013. doi: 10.1088/1361-6560/aba504
52. Ozoemelam I, van der Graaf E, van Goethem M-J, Kapusta M, Zhang N, Brandenburg S, et al. Real-Time PET Imaging for Range Verification of Helium Radiotherapy. *Front Phys* (2020) 8:565422. doi: 10.3389/fphy.2020.565422
53. Binder TM, Kang HG, Nitta M, Schneider FR, Yamaya T, Parodi K, et al. Performance Evaluation of a Staggered 3-Layer DOI PET Detector Using a 1 Mm LYSO Pitch With PETsys TOFPET2 ASIC: Comparison of HAMAMATSU and KETEK SiPMs. *Phys Med Biol* (2021) 66:125016. doi: 10.1088/1361-6560/abfbf3
54. Liu H, Omura T, Watanabe M, Yamashita T. Development of a Depth of Interaction Detector for γ-Rays. *Nucl Instruments Methods Phys Res Sect A Accel Spectrometers Detect Assoc Equip* (2001) 459:182–90. doi: 10.1016/S0168-9002(00)00939-6
55. Kang HG, Nishikido F, Yamaya T. A Staggered 3-Layer DOI PET Detector Using BaSO 4 Reflector for Enhanced Crystal Identification and Inter-Crystal Scattering Event Discrimination Capability. *BioMed Phys Eng Express* (2021) 7:035018. doi: 10.1088/2057-1976/abf6a8
56. Bert C, Durante M. Motion in Radiotherapy: Particle Therapy. *Phys Med Biol* (2011) 56:R113–44. doi: 10.1088/0031-9155/56/16/R01
57. Saito N, Bert C, Chaudhri N, Gemmel A, Schardt D, Durante M, et al. Speed and Accuracy of a Beam Tracking System for Treatment of Moving Targets With Scanned Ion Beams. *Phys Med Biol* (2009) 54:4849–62. doi: 10.1088/0031-9155/54/16/001
58. Riboldi M, Orecchia PR, Baroni PG. Real-Time Tumour Tracking in Particle Therapy : Technological Developments and Future Perspectives. *Lancet Oncol* (2012) 13:e383–91. doi: 10.1016/S1470-2045(12)70243-7
59. Laube K, Menkel S, Bert C, Enghardt W, Helmbrecht S, Saito N, et al. 4D Particle Therapy PET Simulation for Moving Targets Irradiated With Scanned Ion Beams. *Phys Med Biol* (2013) 58:513–33. doi: 10.1088/0031-9155/58/3/513
60. Tinganelli W, Durante M. Carbon Ion Radiobiology. *Cancers (Basel)* (2020) 12:3022. doi: 10.3390/cancers12103022
61. Grün R, Friedrich T, Elsässer T, Krämer M, Zink K, Karger CP, et al. Impact of Enhancements in the Local Effect Model (LEM) on the Predicted RBE-Weighted Target Dose Distribution in Carbon Ion Therapy. *Phys Med Biol* (2012) 57:7261–74. doi: 10.1088/0031-9155/57/22/7261
62. Elsässer T, Weyrather WK, Friedrich T, Durante M, Iancu G, Krämer M, et al. Quantification of the Relative Biological Effectiveness for Ion Beam Radiotherapy: Direct Experimental Comparison of Proton and Carbon Ion Beams and a Novel Approach for Treatment Planning. *Int J Radiat Oncol Biol Phys* (2010) 78:1177–83. doi: 10.1016/j.ijrobp.2010.05.014
63. Sokol O, Scifoni E, Tinganelli W, Kraft-Weyrather W, Wiedemann J, Maier A, et al. Oxygen Beams for Therapy: Advanced Biological Treatment Planning and Experimental Verification. *Phys Med Biol* (2017) 62:7798–813. doi: 10.1088/1361-6560/aa88a0
64. Chacon A, Safavi-Naeini M, Bolst D, Guatelli S, Franklin DR, Iwao Y, et al. Monte Carlo Investigation of the Characteristics of Radioactive Beams for Heavy Ion Therapy. *Sci Rep* (2019) 9:6537. doi: 10.1038/s41598-019-43073-1
65. Chacon A, James B, Tran L, Guatelli S, Chartier L, Prokopvich D, et al. Experimental Investigation of the Characteristics of Radioactive Beams for Heavy Ion Therapy. *Med Phys* (2020) 47:3123–32. doi: 10.1002/mp.14177
66. Stewart RD, Carlson DJ, Butkus MP, Hawkins R, Friedrich T. Scholz M. A Comparison of Mechanism-Inspired Models for Particle Relative Biological Effectiveness (RBE). *Med Phys* (2018) 45:e925–52. doi: 10.1002/mp.13207
67. Friedrich T, Weyrather W, Elsässer T, Durante M, Scholz M. Accuracy of RBE: Experimental and Theoretical Considerations. *Radiat Environ Biophys* (2010) 49:345–9. doi: 10.1007/s00411-010-0298-9
68. Dodd RD, Añó L, Blum JM, Li Z, Van Mater D, Kirsch DG. Methods to Generate Genetically Engineered Mouse Models of Soft Tissue Sarcoma. *Methods Mol Biol* (2015) 1267:283–95. doi: 10.1007/978-1-4939-2297-0_13
69. Brownstein JM, Wisdom AJ, Castle KD, Mowery YM, Guida P, Lee C, et al. Characterizing the Potency and Impact of Carbon Ion Therapy in a Primary Mouse Model of Soft Tissue Sarcoma. *Mol Cancer Ther* (2018) 17:858–68. doi: 10.1158/1535-7163.MCT-17-0965
70. Helm A, Tinganelli W, Simoniello P, Kurosawa F, Fournier C, Shimokawa T, et al. Reduction of Lung Metastases in a Mouse Osteosarcoma Model Treated With Carbon Ions and Immune Checkpoint Inhibitors. *Int J Radiat Oncol* (2021) 109:594–602. doi: 10.1016/j.ijrobp.2020.09.041
71. Zoglauer A, Andritschke R, Boggs SE, Schopper F, Weidenspointner G, Wunderer CB. MEGAlib: Simulation and Data Analysis for Low-to-Medium-Energy Gamma-Ray Telescopes. In: MJL Turner, KA Flanagan, editors. *SPIE Astronomical Telescopes + Instrumentation*. Marseille, France: Society of Photo-Optical Instrumentation Engineers (SPIE). (2008). p. 70113F. doi: 10.1117/12.789537
72. Song CW, Glatstein E, Marks LB, Emami B, Grimm J, Sperduto PW, et al. Biological Principles of Stereotactic Body Radiation Therapy (SBRT) and Stereotactic Radiation Surgery (SRS): Indirect Cell Death. *Int J Radiat Oncol* (2021) 110:21–34. doi: 10.1016/j.ijrobp.2019.02.047
73. Greco C, Pares O, Pimentel N, Moser E, Louro V, Morales X, et al. Spinal Metastases: From Conventional Fractionated Radiotherapy to Single-Dose SBRT. *Rep Pract Oncol Radiother* (2015) 20:454–63. doi: 10.1016/j.rpor.2015.03.004
74. Zelefsky MJ, Yamada Y, Greco C, Lis E, Schöder H, Lobaugh S, et al. Phase 3 Multi-Center, Prospective, Randomized Trial Comparing Single-Dose 24 Gy Radiation Therapy to a 3-Fraction SBRT Regimen in the Treatment of Oligometastatic Cancer. *Int J Radiat Oncol* (2021) 110:672–9. doi: 10.1016/j.ijrobp.2021.01.004
75. Garcia-Barros M, Paris F, Cordon-Cardo C, Lyden D, Rafii S, Haimovitz-Friedman A, et al. Tumor Response to Radiotherapy Regulated by Endothelial Cell Apoptosis. *Science* (2003) 300:1155–9. doi: 10.1126/science.1082504
76. Bodo S, Campagne C, Thin TH, Higginson DS, Vargas HA, Hua G, et al. Single-Dose Radiotherapy Disables Tumor Cell Homologous Recombination *via* Ischemia/Reperfusion Injury. *J Clin Invest* (2019) 129:786–801. doi: 10.1172/JCI97631
77. Brown JM, Brenner DJ, Carlson DJ. Dose Escalation, Not "New Biology," Can Account for the Efficacy of Stereotactic Body Radiation Therapy With Non-Small Cell Lung Cancer. *Int J Radiat Oncol Biol Phys* (2013) 85:1159–60. doi: 10.1016/j.ijrobp.2012.11.003
78. Shuryak I, Carlson DJ, Brown JM, Brenner DJ. High-Dose and Fractionation Effects in Stereotactic Radiation Therapy: Analysis of Tumor Control Data From 2965 Patients. *Radiother Oncol* (2015) 115:327–34. doi: 10.1016/j.radonc.2015.05.013
79. Bendinger AL, Seyler L, Saager M, Debus C, Peschke P, Komljenovic D, et al. Impact of Single Dose Photons and Carbon Ions on Perfusion and Vascular Permeability: A Dynamic Contrast-Enhanced MRI Pilot Study in the Anaplastic Rat Prostate Tumor R3327-At1. *Radiat Res* (2019) 193:34. doi: 10.1667/RR15459.1
80. Bendinger AL, Peschke P, Peter J, Debus J, Karger CP, Glowa C. High Doses of Photons and Carbon Ions Comparably Increase Vascular Permeability in R3327-HI Prostate Tumors: A Dynamic Contrast-Enhanced MRI Study. *Radiat Res* (2020) 194:466–75. doi: 10.1667/RADE-20-00112.1
81. Tattenberg S, Madden TM, Gorissen BL, Bortfeld T, Parodi K, Verburg J. Proton Range Uncertainty Reduction Benefits for Skull Base Tumors in Terms of Normal Tissue Complication Probability (NTCP) and Healthy Tissue Doses. *Med Phys* (2021) mp:15097. doi: 10.1002/mp.15097
82. Jensen AD, Poulakis M, Nikoghosyan AV, Welzel T, Uhl M, Federspil PA, et al. High-LET Radiotherapy for Adenoid Cystic Carcinoma of the Head and Neck: 15 Years' Experience With Raster-Scanned Carbon Ion Therapy. *Radiother Oncol* (2016) 118:272–80. doi: 10.1016/j.radonc.2015.05.010
83. Jensen AD, Nikoghosyan AV, Poulakis M, Höss A, Haberer T, Jäkel O, et al. Combined Intensity-Modulated Radiotherapy Plus Raster-Scanned Carbon

Ion Boost for Advanced Adenoid Cystic Carcinoma of the Head and Neck Results in Superior Locoregional Control and Overall Survival. *Cancer* (2015) 121:3001–9. doi: 10.1002/cncr.29443

84. Lambrecht M, Eekers DBP, Alapetite C, Burnet NG, Calugaru V, Coremans IEM, et al. Radiation Dose Constraints for Organs at Risk in Neuro-Oncology; the European Particle Therapy Network Consensus. *Radiother Oncol* (2018) 128:26–36. doi: 10.1016/j.radonc.2018.05.001
85. Chu WT, Ludewigt BA, Renner TR. Instrumentation for Treatment of Cancer Using Proton and Light Ion Beams. *Rev Sci Instrum* (1993) 64:2055–122. doi: 10.1063/1.1143946
86. Haustein PE. Application of ISOL-Type Radioactive Nuclear Beams in the Physical, Biomedical and Environmental Sciences. *Nucl Phys A* (1997) 616:469–77. doi: 10.1016/S0375-9474(97)00118-8
87. Katagiri K, Noda A, Nagatsu K, Nakao M, Hojo S, Muramatsu M, et al. A Singly Charged Ion Source for Radioactive 11 C Ion Acceleration. *Rev Sci Instrum* (2016) 87:02B509. doi: 10.1063/1.4935899
88. dos Santos Augusto R, Buehler L, Lawson Z, Marzari S, Stachura M, Stora T. CERN-MEDICIS Collaboration. CERN-MEDICIS (Medical Isotopes Collected From ISOLDE): A New Facility. *Appl Sci* (2014) 4:265–81. doi: 10.3390/app4020265
89. Pitters J, Breitenfeldt M, Pahl H, Pikin A, Wenander F. Summary of Charge Breeding Investigations for a Future 11C Treatment Facility. *CERN-ACC-NOTE-2018-0078* (2018).
90. Augusto RS, Mendonca TM, Wenander F, Penescu L, Orecchia R, Parodi K, et al. New Developments of 11C Post-Accelerated Beams for Hadron Therapy and Imaging. *Nucl Instruments Methods Phys Res Sect B Beam Interact Mater Atoms* (2016) 376:374–8. doi: 10.1016/j.nimb.2016.02.045

Conflict of Interest: Author AP was employed by company MedAuston GmbH.

The remaining authors declare that the research was conducted in the absence of any commercial or financial relationships that could be construed as a potential conflict of interest.

frontiers in Oncology

REVIEW
published: 21 September 2021
doi: 10.3389/fonc.2021.715025

Robust Angle Selection in Particle Therapy

Yuan Zhou[1], *Yang Li*[2,3], *Yoshiki Kubota*[2], *Makoto Sakai*[2*] *and Tatsuya Ohno*[1,2]

[1] Department of Radiation Oncology, Graduate School of Medicine, Gunma University, Maebashi, Japan, [2] Gunma University Heavy Ion Medical Center, Gunma University, Maebashi, Japan, [3] Department of Radiation Oncology, Harbin Medical University Cancer Hospital, Harbin, China

The popularity of particle radiotherapy has grown exponentially over recent years owing to the marked advantage of the depth–dose curve and its unique biological property. However, particle therapy is sensitive to changes in anatomical structure, and the dose distribution may deteriorate. In particle therapy, robust beam angle selection plays a crucial role in mitigating inter- and intrafractional variation, including daily patient setup uncertainties and tumor motion. With the development of a rotating gantry, angle optimization has gained increasing attention. Currently, several studies use the variation in the water equivalent thickness to quantify anatomical changes during treatment. This method seems helpful in determining better beam angles and improving the robustness of planning. Therefore, this review will discuss and summarize the robust beam angles at different tumor sites in particle radiotherapy.

Keywords: particle radiotherapy, beam angle optimization, robust planning, water equivalent pass length, dose distribution

OPEN ACCESS

Edited by:
Marco Durante,
GSI Helmholtz Center for Heavy Ion Research, Germany

Reviewed by:
Marco Schwarz,
The Trento Proton Therapy Centre, Italy
Alessandra Bolsi,
PSI, Switzerland

***Correspondence:**
Makoto Sakai
sakai-m@gunma-u.ac.jp

Specialty section:
This article was submitted to Cancer Imaging and Image-directed Interventions, a section of the journal Frontiers in Oncology

Received: *26 May 2021*
Accepted: *19 August 2021*
Published: *21 September 2021*

Citation:
Zhou Y, Li Y, Kubota Y, Sakai M and Ohno T (2021) Robust Angle Selection in Particle Therapy. Front. Oncol. 11:715025. doi: 10.3389/fonc.2021.715025

1 INTRODUCTION

Radiotherapy (RT) aims to deliver the prescription dose to the target lesion while causing minimal damage to the surrounding normal tissues. Beam-angle selection and optimization play crucial roles in obtaining satisfactory dose distributions. Angle optimization varies with different types of beams owing to the different depth–dose curves. In conventional RT, the photon beam exhibits a characteristic pattern of deposited dose distribution that has an initial dose buildup on the patient's surface and decreases as penetration depth increases on entering the body (1). Consequently, the doses at the surface and the normal tissue upstream of the target are usually higher than those at the target. Thus, conventional RT normally involves applying multiple beams with various angles while modulating the beam intensity to address this concern; thus, the prescribed dose is comparably easy to guarantee by image-guided RT (IGRT) (2). Conversely, the dose distribution deposited by the particle (proton and carbon) beam exponentially increases to a sharp maximum at the end of the trajectory. This is known as the Bragg peak (1, 3). Hence, particle RT can obtain a satisfactory dose distribution with very few beams (only two to four beams are usually required). Recently, a number of studies (4–12) have reported promising clinical outcomes with particle therapy for various tumors.

However, the uncertainty in particle therapy is far more complicated than photon RT, mainly because of the presence of dose perturbation caused by intra- and interfractional changes (13–17). The beam range may vary in daily treatment due to the uncertainty of anatomical changes, thereby leading to severely insufficient dose coverage and overirradiation of organs at risk (OAR), wherein the accumulated

dose volumes covered by 95% of the prescribed dose (V95%) of the clinical target volume (CTV) could drop by approximately 1–10% in thoracic and abdominal tumors with bone matching registration (18–23). To mitigate the uncertainty, research has increasingly focused on robust planning for particle RT. Selecting a beam angle arrangement that can maintain robust dose distribution against intra- (e.g., respiratory motion and gastrointestinal gas movement) and inter- (e.g., setup error and shape change of organs and tumor) variation, defined as robust beam arrangement, is an effective method. Because the variation in the beam range mainly depends on the beam direction, multiple factors should be carefully considered in selecting the beam arrangement of particle RT, such as minimal path length, sparing of nearby OARs, maintaining the beam path as homogenous and continuous as possible, and optimization in the position of both the proximal and distal side of the spread-out Bragg peak (SOBP). In general, the basic principle of angle optimization is to select a particle beam angle where the beam range is relatively robust while avoiding vital organs in the beam path.

With the wide application of the rotating gantry in treatment in recent years, research on angle optimization has also received more attention than previously (**Figure 1**), and the concept of robust beam arrangement is emerging. This is important to enable selection of beam angles that can avoid the uncertainties of anatomical changes along the ray path to achieve satisfactory dose distribution. Thus, this report will primarily review recent research on plan optimization with robust beam angle in particle RT in various tumor sites, which may provide a reference, along with other related information, for physicians in treatment planning. All the descriptions of the angle in this article refer to **Figure 2**.

2 DEVELOPMENT OF BEAM DELIVERY SYSTEMS IN PARTICLE RT

Particle RT was first used clinically in the 1950s (24) with a fixed beam field system. This system can provide horizontal and/or vertical fields, and a 45° angle field has recently been available in some facilities (25, 26) (**Figures 3A, B**). More beam angles can be obtained by adjusting the couch angles (usually within ±15°). However, these angles remain limited in terms of various clinical requirements. Additionally, there may be potential uncertainties in positioning reproducibility when adjusting the couch angles (29). Rotating gantries were developed to solve this problem. In 1991, the Loma Linda University Medical Center became the first hospital-based proton therapy center to have a rotating gantry (30). This rotating gantry can rotate 360° and is composed of several normal-conducting magnets, which means that it can bend proton beams at the desired angles. Presently, rotating gantries have wide application in proton RT and have become standard practice. In addition, some centers equip their treatment rooms with a partially rotating gantry to save space and cost (27) (**Figure 3C**). Although gantries are commonly available for proton therapy, fixed fields are still in use. However, it is extremely difficult to integrate a rotating gantry into a carbon-ion facility. The required magnetic rigidity for carbon beams with an energy of 430 MeV/u is approximately three times higher than that for proton beams of 250 MeV/u energy. Hence, the size and weight of the gantry structure for carbon beams would become considerably larger. In 2009, the first C-ion facility with a 360° rotating gantry was installed at the Heidelberg Ion-Beam Therapy Center; it has a magnetic rigidity of 6.6 Tm, a range of carbon-ion energies between 50 and 430 MeV/u, and a gantry that is roughly 26 m long and weighs 600 tons (31). Owing to its large size, weight, and cost, it is difficult to commercialize a rotating gantry for use in carbon-ion radiotherapy. To promote this technique, the first compact rotational gantry composed of superconducting magnets was developed successfully at the National Institute of Radiological Sciences (NIRS) in 2015 (28). This specific gantry can transport ions with energies of 48–430 MeV/u. The superconducting rotating gantry weighing 300 tons and 13 m in length had its weight and length significantly reduced compared to older models; the performance was also comparable to those of

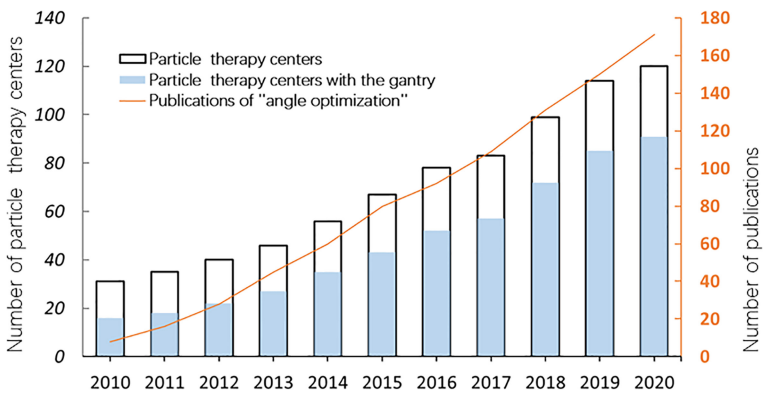

FIGURE 1 | The number of particle therapy centers in operation and publications on "angle optimization" in the past 10 years (2010–2020). The number of facilities was verified on the webpage of the Particle Therapy Cooperative Group (PTCOG https://www.ptcog.ch/). The papers were filtered by searching for the following keywords: "carbon ion radiotherapy" OR "proton radiotherapy" OR "angle optimization" using Google Scholar (https://scholar.google.com/).

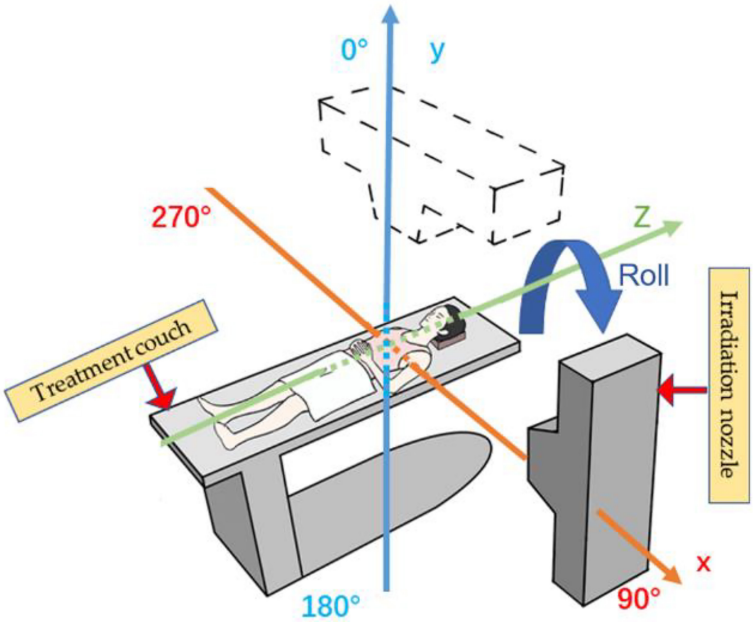

FIGURE 2 | Reference axis for beam angles mentioned in this article. The patient's anterior direction is defined as 0° (supine position). The orange line shows the X-axis, and the blue line shows the Y-axis; the irradiation angle is clockwise.

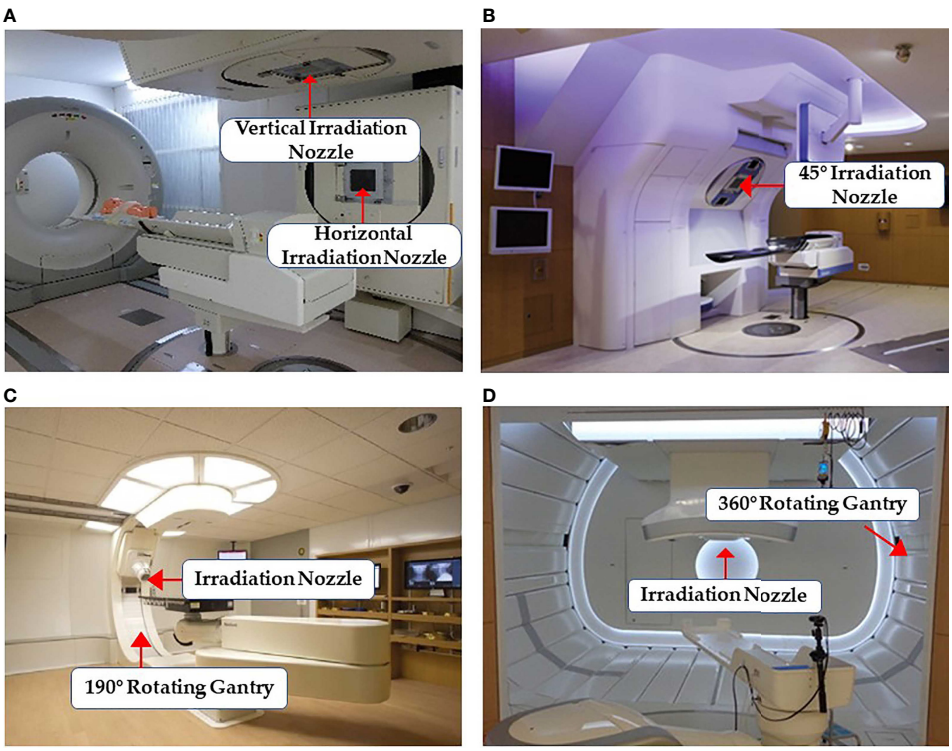

FIGURE 3 | Some common facilities of the beam delivery system in particle RT: **(A)** treatment rooms of carbon-ion RT with vertical and horizontal beam fields at Gunma University (25) (Open Assess); **(B)** horizontal and 45° oblique beam lines in SAGA HIMAT (26) (Open Assess); **(C)** a 190° rotating gantry system range −5° to 185° for proton therapy at Barnes-Jewish Hospital (27) (Source: Missouri Medicine, Copyright 2015. Used with permission); and **(D)** treatment room with the superconducting rotating gantry at the National Institute of Radiological Sciences (28) (Open Assess).

proton gantries in operation (**Figure 3D**). Currently, a better improved version of a gantry is being constructed at Yamagata University (32). In summary, the development of a compact rotating gantry plays a crucial role in promoting gantry system for particle therapy, especially carbon-ion therapy, worldwide.

3 WATER EQUIVALENT THICKNESS IN ANGLES SELECTION

The agreement between the tumor position and the spread-out Bragg peak is important for particle RT, particularly with thoracic and abdominal tumors. Anatomical motion, mainly caused by respiratory and gastrointestinal activity, can take the tumor out of the irradiation field, which may significantly degrade the target dose. Therefore, tumor motion tracking technologies, which mainly involve external motion tracking and internal tumor tracking, have been widely applied in particle RT. External motion tracking can provide tumor movement information by monitoring the respiration using respiratory-correlated imaging, while internal tumor tracking can monitor, in real time, the tumor position directly, with or without fiducial markers (33). Using gated CT, a relatively stable tumor position can be obtained for planning and irradiation, and a 30% amplitude level is generally used in clinical practice (33, 34). However, this is not sufficient compensation for particle RT because the potential changes in surrounding tissues caused by tumor motion should also be considered. Additionally, some anatomical variations in the particle beam path, such as gastrointestinal deformation, have a great impact on the beam range and affect the dose distribution (35, 36). Thus, accurate knowledge of the beam range of a particle beam is very important for particle RT. The range of particle beams is usually calculated in terms of the water equivalent thickness (WET), which is the radiological thickness of all the materials along the path converted to the thickness of water. Many studies have quantitatively analyzed the dose distribution with WET variations (36–38). Chang et al. (37) and Yu et al. (38) concluded that the variation in the dose that covers 95% (D95%) of CTV is <1% when the WET variation is <5 mm in thoracic cancers. Thus, the WET variation can serve as a metric to quantify the impact of anatomical change, thereby optimizing beam angles.

4 ROBUST BEAM ANGLE SELECTION

4.1 Thoracic Malignancies

4.1.1 Lung Cancer

Currently, horizontal and vertical fields are commonly used to treat lung cancer in facilities using fixed fields (18, 19). To obtain a satisfactory dose distribution, the beam angles are usually adjusted by ±15° roll (obtained by rotating the couch along the long axis) according to the tumor site. However, the accumulated doses are sometimes insufficient even in cases in which the internal margin is obtained by four-dimensional computed tomography (4D-CT) because of potential interfraction deviation between treatment fractions. Li et al. (19) reported accumulated doses in 10 patients using fixed fields, wherein the dose distributions of three cases were unacceptable and the worst CTV D95% decreased from 100% to 70.4%. To verify both intra- and interfractional robustness of the current beam angle arrangement, several studies (36, 37, 39) incorporated 4D-CT or images with the breath-hold technique to derive a map of the WET variation to the target (for all relevant studies, beam angles that enter the contralateral lung were excluded) (**Figure 4**).

Chang et al. (37) calculated the intrafractional WET variation over 350° with a rotating gantry and concluded that the intrafractional WET variation is minimal around the anterior and posterior directions and that more than 80% of voxels of the internal gross tumor volume have a WET variation of ≤5 mm in the anterior and posterior directions. Matney et al. (36) reported similar results. However, Casares et al. (40) illustrated that, in peripheral lung cancer, the WET variation of the gantry angle in the right lateral direction (240–270°) is minimal (average WET variation ≤5 mm) in intrafractional change. This may be due to the fact that all beam paths in this study were less affected by diaphragm movement and were comparably shorter at 240°–270°. This indicates that the tumor location (peripheral or central) plays a role in beam angle selection. However, there is limited clinical evidence, and further studies with larger samples are required.

The interfractional changes in WET could be caused by changes in normal tissue or possible tumor displacement and tumor volume changes during the treatment course. It has been observed that the minimum WET change (<3 mm on average) could be obtained in the posterior direction (gantry angles range, 160°–200°) under breath-hold CT, particularly for locally advanced lung cancer, which is associated with a greater potential for interfactional changes in WET than early-stage non-small cell lung cancer, due to larger tumor volume and longer treatment duration than early-stage non-small cell lung cancer (39). Another study (41) reached similar conclusions by simulating the tumor baseline shift and selecting beam angles corresponding to the minimal WET change to compare with the original treatment plan. These results indicated that new gantry angle configuration (295°, 230°, and 185°) with setup uncertainties was more robust than those originally planned (145°, 245°, and 345°). Furthermore, lung relative volumes receiving more than 5 Gy (V_{5Gy}) (26.5 *vs*. 28.5 Gy) and spinal cord D_{max} (21.7 *vs*. 24.9 Gy) were lower than those originally planned, although the results showed slightly worse heart D_{mean} (1.8 *vs*. 0.2 Gy). Additionally, variations in anterior chest wall thickness appear more obvious than those in the posterior wall in fixed anterior–posterior (AP) fields (42). The mean variations in chest wall thickness in the anterior and posterior beams were 2.3 and 1.7 mm, respectively. The greatest changes in thickness were in the upper lung (5.2 *vs*. 2.1 mm). Thus, the posterior angle appears to be more robust than the anterior angle in the interfraction. This result has also been confirmed by other studies (39, 41).

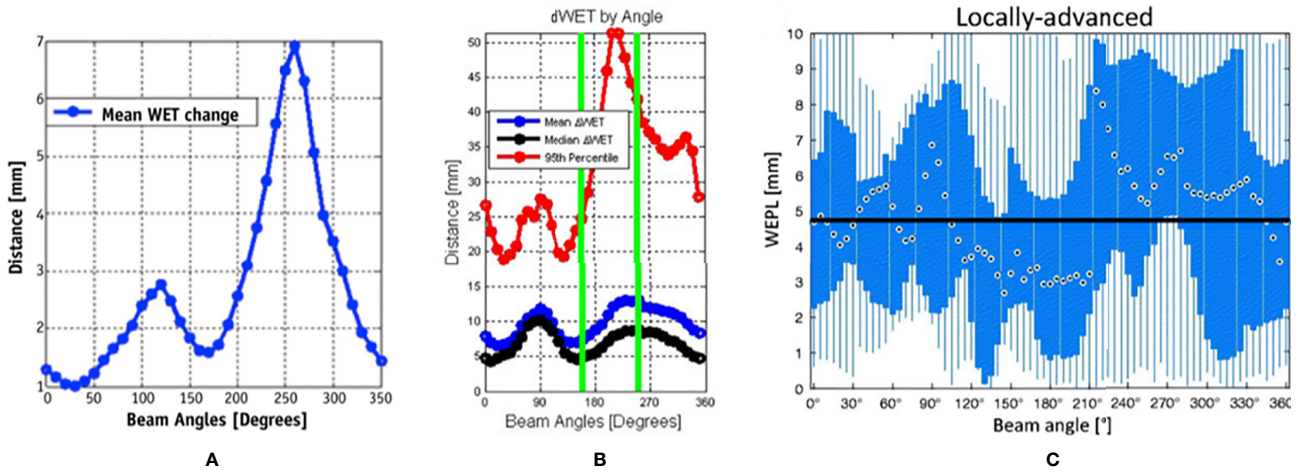

FIGURE 4 | Water equivalent thickness (WET) analysis and beam angle selection in thoracic tumor treatment. **(A)** Mean values of ΔWET of intrafraction as a function of beam angle (37) (Source: Elsevier. Used with permission). **(B)** The mean (blue), median (black), and 95th percentile (red) of the absolute value of the ΔWET of intrafractions as a function of beam angles (36) (Open Assess). **(C)** The absolute difference of water equivalent path length (WEPL) (same as ΔWET) of interfractional variation as a function of the beam angle for locally advanced lung tumor. The black dots indicate the median value over all beam angles, the blue box indicates the 5th and 75th quartiles, and the blue bar indicates the range of ΔWEPL (39) (Source: Taylor & Francis. Used with permission).

Beam angles around the anterior and posterior directions appear to be the most robust in the majority of situations with 4DCT, although beam angles around the posterior direction are probably the better option for dose degradation in the interfractional changes. The dose difference in the OARs between different beam angle arrangements appears small. However, they may not be suitable for some tumor positions, such as peripheral cancer, and nearby vital organs need to be considered as well. Additionally, it should be noted that all the above studies were performed in the supine position setting. For facilities with fixed fields, the posterior beam is irradiated in a prone position setting, which may result in slightly different results.

4.1.2 Esophageal Cancer

The motion of esophageal cancer is small under free breathing, accounting for only 1.6 and 1.4 mm in AP and right–left (RL) directions, respectively (43). However, the intrafractional dose change is significant for different beam configurations. According to a study on intrafractional variation by 13 gantry angle arrangements (44), the anterior (0°) and/or posterior (180°) fields and oblique posterior fields (combinations of 155° and 205°, 135° and 175°, and 185° and 225°) are more reliable for treatment planning than the bilateral horizontal fields or gantry angle arrangements in the horizontal and vertical directions. The V95% in the planning target volume (PTV) of all 4DCT phases was >80% in the oblique posterior field (compared to 50%–95% in the horizontal fields). Additionally, a study with 4DCT examined the WET changes for coplanar beam angle in the supine position and estimated that the average of WET changes on the maximum inhale and exhale phase is minimum (the WET reached approximately 5 mm) around 0° (gantry range, 320°–60°) and 200° (gantry range, 180°–220°); it becomes maximum (WET ≥20 mm) around the bilateral horizontal directions (38). Thus, the anterior and posterior directions appear to be the most robust angles. The most likely explanation for this finding is that the posterior fan-shaped area containing the esophagus is relatively stationary with respect to diaphragm movement because the diaphragm is attached to the lumbar spine through the left and right crus tendons (38). For OARs, Zeng et al. (45) compared the planning dose distribution with the following three beam gantry angle arrangements under respiratory motion with 4DCT: PA (one posterior field), AP (anterior and posterior fields), and LPO (posterior and left posterior oblique fields). The authors found that the PA plan reduced the accumulated dose in the 4DCT of the heart, lungs, and liver at the cost of a slightly higher spinal cord maximum dose (Dmax), while compared to the AP/PA, the PA plan significantly reduced the heart D_{mean} (14.10 *vs.* 24.49 Gy), stomach D_{mean} (22.95 *vs.* 31.33 Gy), and liver D_{mean} (3.79 *vs.* 5.75 Gy). Compared to the LPO, the PA plan achieved better lung V5Gy (17% *vs.* 30%). Although the PA plan resulted in higher spinal cord D_{max} (44.50 *vs.* 35.79 *vs.* 35.15 Gy) than AP and LPO, it was still acceptable.

In summary, even if slightly higher in spinal cord D_{max}, posterior beams between 150° and 220° should be recommended for esophageal cancer with 4DCT in treatment planning.

4.2 Abdominal Malignancies

4.2.1 Pancreatic Cancer

Box arrangements with four fixed fields (anterior, posterior, and bilateral horizontal directions) are commonly used in the particle plan for pancreatic cancer. However, some beam angles of the fixed four fields may cause dose coverage reduction due to anatomical changes (20–22, 35). A previous study (35) found

that although particle therapy plans with respiratory management taking 4D-CT results into consideration effectively mitigate uncertainties of respiratory motion, dose distributions in the anterior and left direction beams are still affected by intra-fractional deviations (**Figure 5**), and the CTV D95% was degraded from 98.2% to 88.3%. This decrease in the dose distribution is also caused by interfractional changes, and the internal CTV (ICTV) D98% of the accumulated dose declined by approximately 16.0% in another study (21). A possible reason for this is that intra- and interfractional gastrointestinal movements in the ray path greatly affect the target coverage.

Thus, angle optimization is a field where one prefers to focus on avoiding gastrointestinal movement to mitigate uncertainties upstream of the target. Pancreatic tumors are seen in limited locations compared with lung and liver tumors; thus, it seems easier to find an optimal beam angle arrangement for most patients. Currently, some facilities with a rotating gantry (46–48) recommend posterior oblique beams as a standard proposal. The study reported by Batista et al. (46), which analyzed the robustness of the treatment plan under the impact of interfractional change with six different beam angle arrangements, found that the single anterior field in the supine position showed the worst coverage (88.7%) and that the two oblique posterior angle arrangements could substantially reduce the impact of interfractional changes to maintain the dose coverage. Yet, another study (47) concluded that a single posterior field appeared to be the most robust plan for different topographical conditions. However, particular attention should be paid to the spinal cord and left kidney, which may be irradiated with a higher dose than the doses in the four-field box treatment (46–48). Overall, a better beam angle arrangement seems to be possible in the posterior direction (the range 150°–245°) for pancreatic cancer, although the dose administered to the kidney and spinal cord should be monitored.

4.2.2 Hepatocellular Carcinoma

The conventional beam angle used in hepatocellular cancer treatment is the fixed horizontal and vertical beam fields, and each field is adjusted within the very restricted limits roll of ±15° by couch depending on tumor location. The robustness of the fixed field for hepatocellular carcinoma appears to be satisfactory. The dose degradations caused by intra- and interfractional changes seem acceptable. Kubota et al. reported that D98% of CTV changed from 99.87% (plan-dose) to 99.20% (intra-dose) and 96.0% (inter-dose) (23). However, the number of samples used in the study was small (only 10 cases), and the insufficient statistical power limits the generalization of these conclusions. Yang et al. (49) studied the effect of the anatomical changes of gastrointestinal filling or liver deformation with three or four beam angles on the liver side with a rotating gantry and found that the average of accumulated dose decreased by only 2.5% (D98% to CTV from 68.90 to 66.48). However, the coverage of some cases was insufficient, and further analysis of the dose degradation revealed that the difference in WET between the planning CT and CT-on-rail of the last fraction showed a

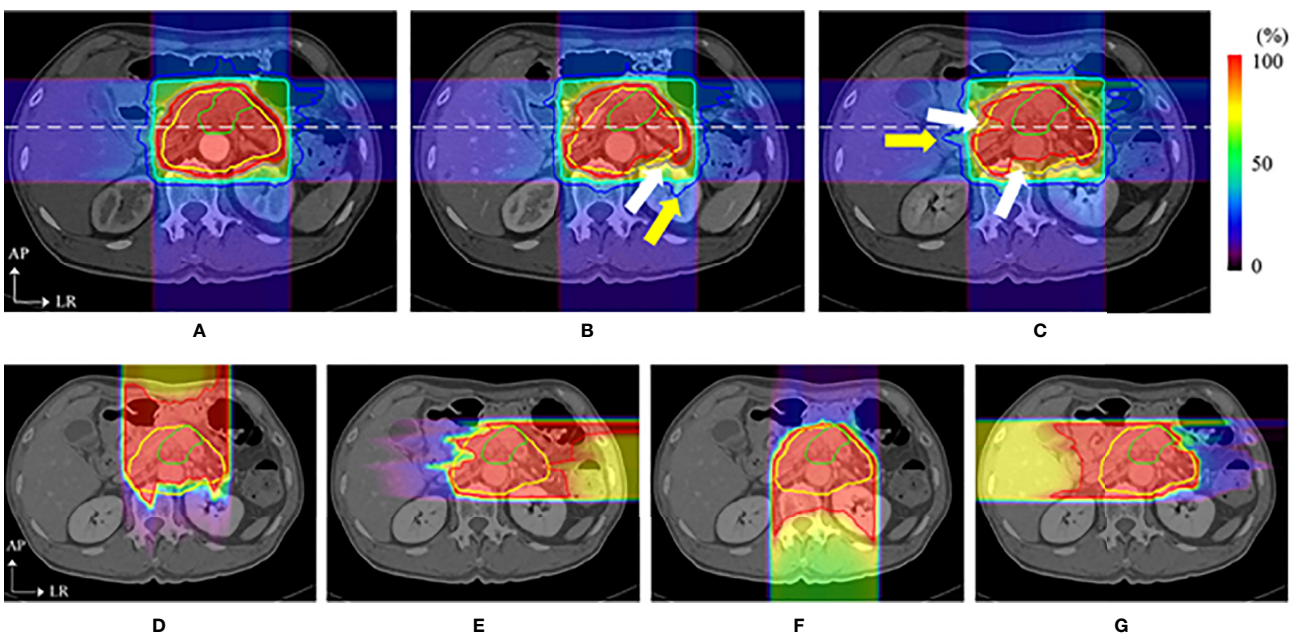

FIGURE 5 | Dose distributions of a carbon ion RT in axial sections. The top images show the dose distribution of planning CT **(A)**, the dose distribution with a delay time of **(B)** 35 s (intra-CT), and **(C)** 145 s (intra-CT), respectively. Beam overshoot (yellow arrows) and undershoot (white arrows) were observed at scan intervals of 35 and 145 s. The bottom images show the dose distributions of **(D)** 0°, **(E)** 90°, **(F)** 180°, and **(G)** 270° at 145 s. The green and yellow lines show the shapes of the gross tumor volume and the clinical target volume, respectively. The rainbow contours show the dose distribution (35) (Source: Elsevier. Used with permission).

noticeable change (the maximum WET change >30 mm), which was observed at 40°, and the smallest WET change of the beam angle was between 230° and 330° (WET change <5 mm) (49) (**Figure 6A**). The authors then evaluated two strategies based on the minimum values of WET changes (four gantry angles of 325°, 295°, 265°, and 235° and seven gantry angles of 30°, 5°, 340°, 315°, 290°, 265°, and 240°) and compared these with the original gantry angle arrangement (25°, 355°, 325°, and 295°). There was a clear improvement in dose coverage of both revised plans, and CTV D95% exceeded 95%, although the normal liver tissue dose was also increased, as shown in **Figure 6B**.

Generally, avoiding cavity organs (range of gantry angles between 230° and 330°) will make the plan more robust but carries the risk of increasing the normal liver tissue dose. In addition, fixed fields treatment for hepatocellular carcinoma may be acceptable under stringent management of the tumor movement with daily CT verification, although studies involving large samples are required to investigate this further.

4.2.3 Prostate Cancer

Particle RT in prostate cancer uses the bilateral horizontal direction as a regular beam angle in many clinical centers. However, with this arrangement, the anterior aspect of the rectum is within the lateral penumbra of the particle beam, and this is associated with a high risk of rectal injury, particularly involving the anterior rectal wall (ARW). To mitigate the high-dose distribution to the rectum and femoral head, many studies (50–52) tried to optimize beam angles instead of using bilateral horizontal beams. Tang et al. (51) attempted two strategies, namely, the straight anterior field and the two anterior-oblique fields with gantry angles of ±30° from the vertical and compared these with the bilateral horizontal field. The study found that the proposed arrangements were superior to the conventional bilateral horizontal fields with regard to sparing the rectum and ARW (with anterior, two anterior-oblique, and bilateral direction beams; rectal V95% were 1.2%, 0.8%, and 9.4% of the prescribed dose, respectively) (**Figure 7**). The anterior-oblique beam angles could be more sensitive than the bilateral horizontal angles for interfractional change. Moteabbed et al. (52) verified the robustness of the anterior-oblique gantry angle (± 35°) for interfractional change and found that the accumulated dose showed an obvious decline. The average V100%/D95%/D_{mean} of the CTV in the anterior-oblique beam plan dropped by 10.6%/3.2 Gy/0.5 Gy, respectively, compared with the planned dose, whereas the reduction in the bilateral horizontal beam plan was only 0.7%/0.1 Gy/0.1 Gy, respectively.

Anatomical variation is a possible cause of target coverage reduction. Prostate displacement is mainly caused by variations in the bladder and rectal volume (53). The variation in rectal volume is irregular, and intrafractional variation is expected to be smaller than interfractional variation because the intrafractional variation of the bladder volume and respiratory motion are small. Thus, a treatment plan that is robust to interfractional variation is also expected to be robust to intrafractional variation. Many clinical centers have investigated prostate displacement (50, 53, 54). Intrafractional prostate motion was found to occur predominantly in the anteroposterior direction far beyond the RL direction (54). The mean magnitude of intrafractional shifts (± SD) was 0.01 ± 0.4 mm, 0.2 ± 1.3 mm, and 0.1 ± 1.0 mm in the left, anterior, and superior directions, respectively. Another study (50) reported similar results in carbon RT for interfractional movement. Therefore, the two parallel-opposed

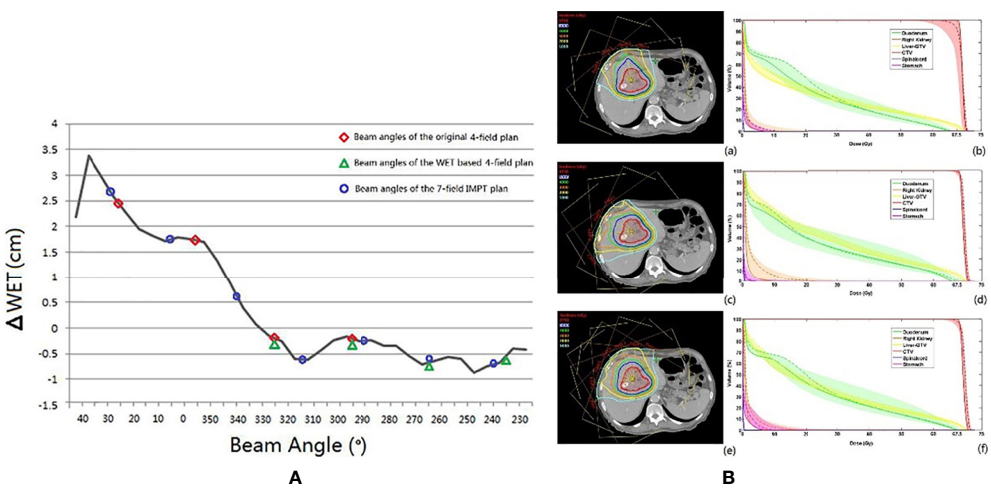

FIGURE 6 | **(A)** The black line is the ΔWET (the difference of water equivalent thickness between the planning CT and the CT-on-rail) curve. The beam angles of the original IMPT plan (25°, 355°, 325°, and 295°), the WET-based four fields plan (325°, 295°, 265°, and 235), and the revised seven fields plan (30°, 5°,340°, 315°, 290°, 265°, and 240°) are indicated with the red circle, the green triangle, and the blue circle, respectively. **(B)** The axial view of the same planar doses and fields for (a) the original IMPT plan, (c) the IMPT plan with beam angles of the minimum values of ΔWET, and (e) the seven-field IMPT plan. The dose–volume histograms of the planned dose (solid line), the accumulated dose (dashed line), and the bands for all fractional doses of (b) the original IMPT plan, (d) the IMPT plan with beam angles of the minimum values of ΔWET, and (f) the seven-field IMPT plan (49) (Source: Elsevier. Used with permission).

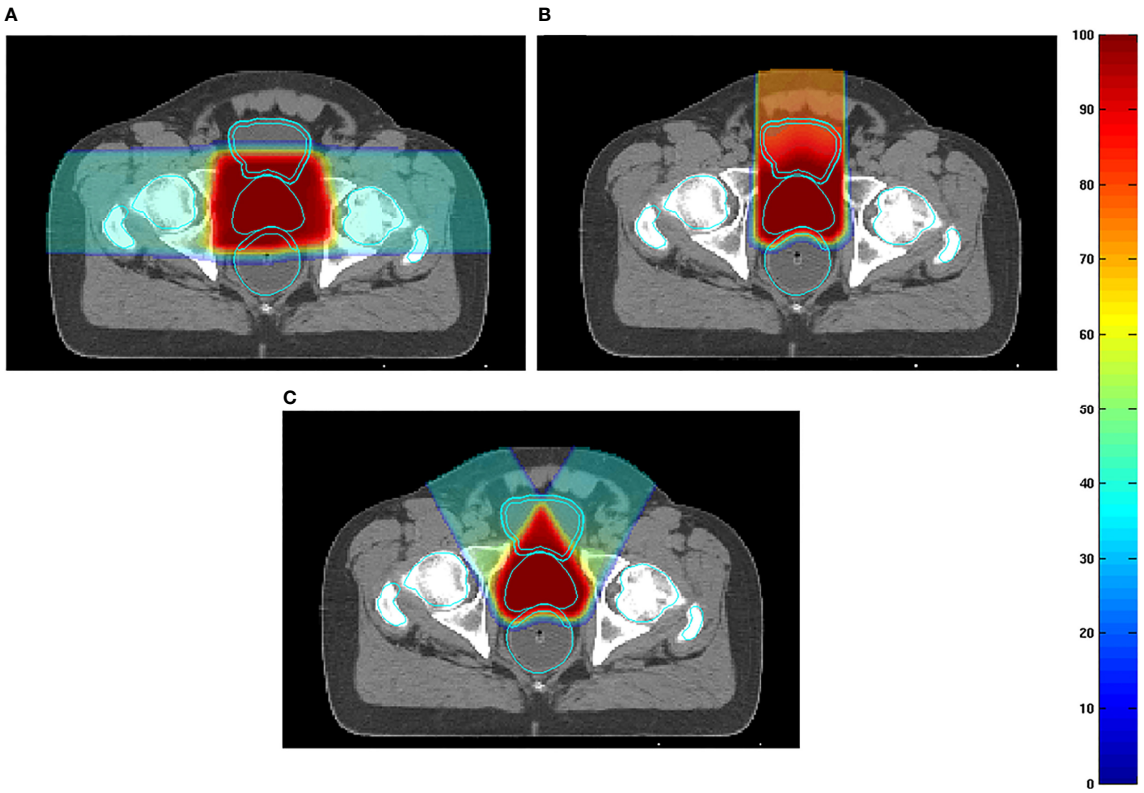

FIGURE 7 | **(A)** Examples of dose distributions for two parallel-opposed lateral fields, **(B)** one straight anterior field, and **(C)** two anterior-oblique fields in an axial plane. The prostate, rectum, anterior rectal wall, bladder, bladder wall, and femoral heads are outlined by cyan lines (51) (Source: Elsevier. Used with permission).

horizontal beam arrangements are more robust than the vertical fields, and the AP may be carefully selected when the dose description cannot be guaranteed with the bilateral horizontal fields in particle RT.

4.3 Head and Neck Malignancies

Achieving an effective treatment plan is particularly challenging in photon RT for head and neck (HN) malignancies, as multiple vital organs around the tumor must be considered. Although particle RT can provide superior dose distribution in tumors and OARs, the distribution is very sensitive considering the proximity of OARs and significant heterogeneities of the HN region.

Toramatsu et al. (55) used the heterogeneity of the trajectory as an indicator to select the beam angle. When a pencil beam passes through a high heterogeneity region, the Bragg peak position becomes unarranged, leading to a gentle dose distribution at the distal fall-off region, which tends to worsen the dose distribution. The dose distributions were significantly improved with this method compared with those with the manually selected beam angles in HN cancer patients (**Figure 8**). In addition, the dose distribution was robust against a setup error of ±2 mm and a range calculation error of ±2.5% (the variation of CTV D95% was reduced to 7.8%–8.2% compared to 8.7%–24.6% for manual selection).

Gu et al. (56) developed a method considering worst-case optimization and heterogeneity to investigate robust planning in proton therapy with a gantry against setup errors of ±3 mm and range calculation errors of ±3%. The worst-case optimization will be discussed later in another section. After optimization of the treatment plans of two bilateral HN cancer patients, three non-coplanar beam directions were selected for each patient, and dose distributions were compared with the plan of the manual beam arrangement method. Against both the setup and range calculation error, the lowest CTV D95% increased while sparing OARs.

In the HN region, intrafractional changes are relatively unlikely, while interfractional changes associated with tumor shrinkage and body mass changes have a large impact. Some studies reported that the accumulated dose to the CTV D95 was decreased by approximately 10% due to tumor volume changes (shrinkage or growth) (57, 58). Kim et al. (59) estimated the angular dependency of geometric changes in the HN tumor using the variation of WET to guide beam angle selection. Their results indicated that posterior oblique gantry angles (120°–160°) and the anterior angle (0°) were the most sensitive and that the WET changes were minimal in the anterior oblique beam gantry angle (40°–90°) for the left side of the tumor. The authors recommended single or bilateral anterior oblique beams as a robust beam angle arrangement.

Regarding the tumors located in the nasopharynx, and sinonasal region, the robustness of dose distribution should consider not only tumor shrinkage but also aeration changes.

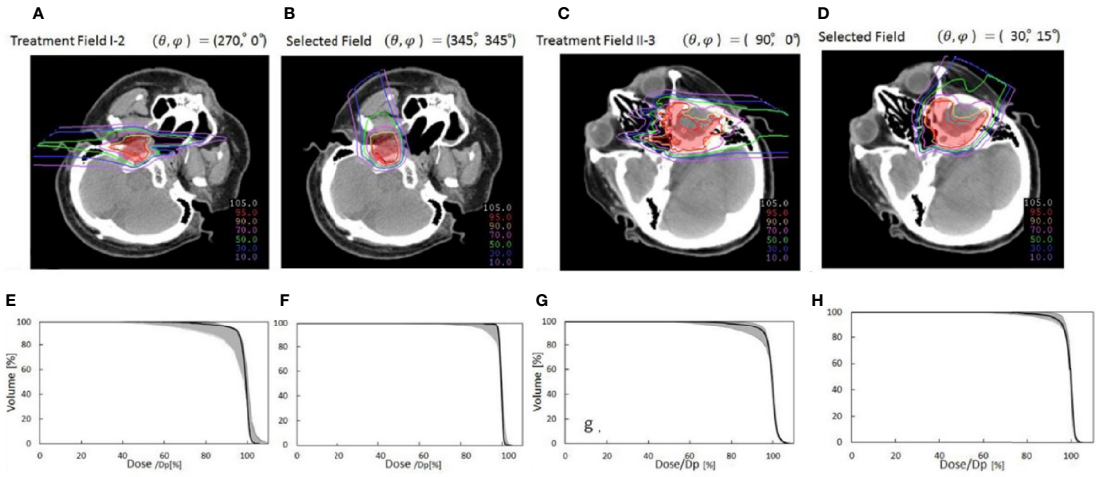

FIGURE 8 | Comparison of dose distributions between selected fields based on low tissue heterogeneities and treatment fields. Panels **(A, C, E, G)** represent dose distribution and the corresponding DVH in the CTV of the manually selected beam angles, and panels **(B, D, F, H)** indicate dose distribution and the corresponding DVH in the CTV of selected fields based on minimal tissue heterogeneities. The gantry and couch pitch angles are θ and ϕ, respectively. The CTVs are visible in red. The solid lines in panels **(C**, **D**, **G**, **H)** are DVHs for the dose distributions without setup and range errors. The shaded areas are the variation of the DVHs with range error (± 2%) and setup error (± 2 mm) (55) (Source: IOP Publishing. Used with permission).

Some studies (60–62) have found that the high irradiation area shifts forward or backward in the direction of the beam as the aeration within the irradiated cavity increases or decreases. Shusharina et al. (61) revealed that the non-involving beams crossing the sinus cavities were the most robust to change in aeration and that with posterior beam directions, aeration changes affect only the exit dose; therefore, the dose distribution was not substantially compromised.

In summary, the heterogeneity of the HN region and the variation in tumor size and aeration need to be considered. In choosing an angle, one must take into account the possibility of increasing dose to critical organs due to the change of the beam range. Despite the great complexity of the HN region, only a limited number of studies with a relatively small number of cases have been reported. Therefore, the possibility of a robust angle remains to be proven. It is necessary to conduct further studies with a large number of cases for each site.

4.4 Intracranial Malignancies

Intracranial tumors are an important target of particle radiotherapy because the physical property of particle therapy allows the suppression of the dose to vital organs, especially the normal brain. In addition, the intracranial tumor is generally located in the region that is surrounded by the skull bone, indicating that anatomical changes are minimal, and it is generally easy to irradiate as expected. However, the effects of range calculation errors, setup errors, changes in tumor volume, and intracranial edema are unavoidable.

For example, in the case of whole brain irradiation and craniospinal irradiation, robustness is important because the brain is irradiated close to many important organs in the HN region, among which the lenses are the most important due to the high sensitivity to low-dose irradiation. Farace et al. (63) evaluated the robustness of the treatment plan with three gantry angle beam arrangements (90°, 270°, and 180°) in 12 patients by worse-case robust evaluation (3.5% range uncertainty and 2 mm setup errors) and compared the dose distribution with two different beam arrangements (two oblique-posterior and two opposed-lateral gantry angles). The results showed that the treatment plan with three fields in the worst scenario still provided adequate target coverage (D98% to PTV >97%) while maintaining lower OARs, among which the lens D_{max} (9 GyE) was lower than that of the other beam arrangements in the nominal scenario (15.7 GyE in two oblique-posterior and 17.5 GyE two opposed-lateral gantry angles).

In addition, due to the extremely complex intracranial structure, the robustness of the plan should consider the tissue heterogeneities of the intracranial region as well, especially for the skull tumor, because high heterogeneity makes the plans sensitive to setup uncertainties and range calculation errors (16, 17, 64). Thus, Ammazzalorso et al. (65) attempted to create a robust plan accounting for setup errors minimizing heterogeneity for skull base tumors. Compared to a conventional plan with manually selected directions (lateral-opposed beam angles), the losses of the dose coverage to CTV (CTV V95%) significantly declined in the plan with minimal heterogeneity-based beam arrangements. Similar results have also been found by Gu et al. (56)

The positional relationship between beam angles and intracranial edema is also important. Intracranial edema should be avoided when selecting the beam angle because the dose to the OARs at the downstream may increase as the edema shrinks. Lassen-Ramshad et al. (66) studied the impact of a change in the volume of intracranial edema on plan robustness and indicated that the dose distribution for the OARs changed significantly as the edema along the field gradually disappeared.

D_{max} of the optical nerve and the brainstem increased by 6.4 and 5.1 Gy, respectively.

In summary, the plan with the beam angles avoiding the edema and high heterogeneity region along the beam path may help improve the treatment robustness.

5 AUTOMATIC ANGLE SELECTION

Currently, beam angle arrangement is often manually selected based on the planner's experience. However, beam angle optimization in particle RT is extremely complex due to the need to consider the dose distribution and the uncertainty factors such as setup errors, range calculation errors, and intra- and interanatomical changes. Thus, beam angle optimization using computational algorithms is more likely to become a common trend for particle RT. In recent years, automatic angle optimization algorithms for particle RT have been proposed by several studies (55, 56, 67–69) with attempts to select the optimal beam angle configuration by optimizing one or more uncertainty factors.

Previously, we discussed in detail the automatic angle selection with quantification of heterogeneity on patients with HN tumors (55, 56). Another study (67) involving patients with lung cancer used a similar method to assess the angular dependence of the heterogeneity variation along the path. Angle selection was based on minimizing heterogeneity, ensuring a satisfactory dose distribution (the path length is maximized within PTV while minimized within OARs) and minimizing the overlap of beam trajectories. The results indicated angles between 300° and 350° as the optimal beam gantry angles for left central lung cancer. This result appears to contradict the studies mentioned above, where the optimal beam is around the posterior directions. This discrepancy may be explained by the fact that although the posterior beam angles may be robust angle against anatomic changes, an obvious variation in heterogeneity is observed in the posterior direction because the beam passes through complex structures such as the spine.

The worst-case robust optimization is one of the main topics in robust planning research on particle RT, which normally seeks to optimize dose distribution based on the selected beam angle arrangement. Even if the selected beam angle arrangement is sensitive for anatomic changes and includes obvious setup errors and range errors, the worst-case robust optimization tries to maintain the robustness of dose distribution, but it may cause more dosimetric compromise. Thus, it is interesting to combine robust beam selection and the worst-case robust optimization. Cao et al. (68) developed algorithms of automatic angle selection, based on the worst-case optimization, and tested these in three patients with prostate cancer patients. The worst-case robust optimization simulates multiple-dose distributions caused by possible uncertainties (such as range uncertainty and setup error). The worst-case dose distribution comprises the minimum (in the target area) and the maximum (in the normal tissue) dose for each voxel. This study manually selected candidate beam angles in advance, and each candidate beam was exchanged with one of its neighbors by a local neighborhood search algorithm; then, a comparison was made between dose distributions that were optimized by worst-case optimization to select improved angle arrangement. In the study by Cao et al., lateral gantry angles (90° and 270°) were mostly selected in optimized beam angle arrangements of prostate cancer. These findings are comparable to the results presented above. Additionally, a further study (69) used the same method to select three gantry angles (10°, 140°, and 270°) as the optimal beam angle arrangement, indicating that the worst-case robust optimization tends to emphasize the horizontal angle to provide a more uniform dose coverage, while limiting dose coverage by the vertical angle (10°) (**Figure 9**). It also shows that the horizontal beam is more robust than the vertical angle, which confirms the above conclusion. However, it is unrealistic to handle the algorithm with full angle optimization and to promote its clinical use because of the extremely long running time.

Automatic angle selection can take into account various indices and can even select non-coplanar beams. This will improve the possibility of minimally invasive treatment. On the other hand, current automatic angle selection is mainly limited to optimization based on the planning-CT information. Heterogeneity is strongly related to setup error and range calculation error and may be robust to interfractional changes. However, it is difficult to take into account the robustness against respiratory movement and anatomical changes only with the planning CT. With the accumulation of further research, the robustness to respiratory motion and anatomical changes should be statistically investigated and incorporated into automatic angle selection methods. Automatic angle selection could be improved by combining with the WET-based angle selection methods, such as the studies introduced in the previous sections.

6 DISCUSSION

Currently, the number of particle therapy facilities is rapidly growing worldwide owing to the advantages of their physical and biological properties. However, robust planning for particle RT remains a considerable challenge. Various methods, including angle optimization, have been proposed to mitigate uncertainties. As the rotating gantry opens new applications, angle optimizations have the opportunity for an in-depth study.

The robust angle selection in particle RT is completely distinct from photon therapy owing to the great advantage of the depth–dose curve. Thus, optimizing beam angles from the viewpoint of WET variation can serve as a metric to quantify the impact of anatomical change, thereby improving the overall robustness of the beam angles. In this article, we summarized the relatively robust beam angles at different tumor sites. For thoracic tumors, particularly esophageal cancer, clinical beam angle arrangement around the posterior direction should be considered first (36–45). In abdominal tumors, the beam angle arrangement avoiding the gastrointestinal tract will improve the robustness of the dose distribution (46–52). Although we could conclude that angle optimization is an effective method for

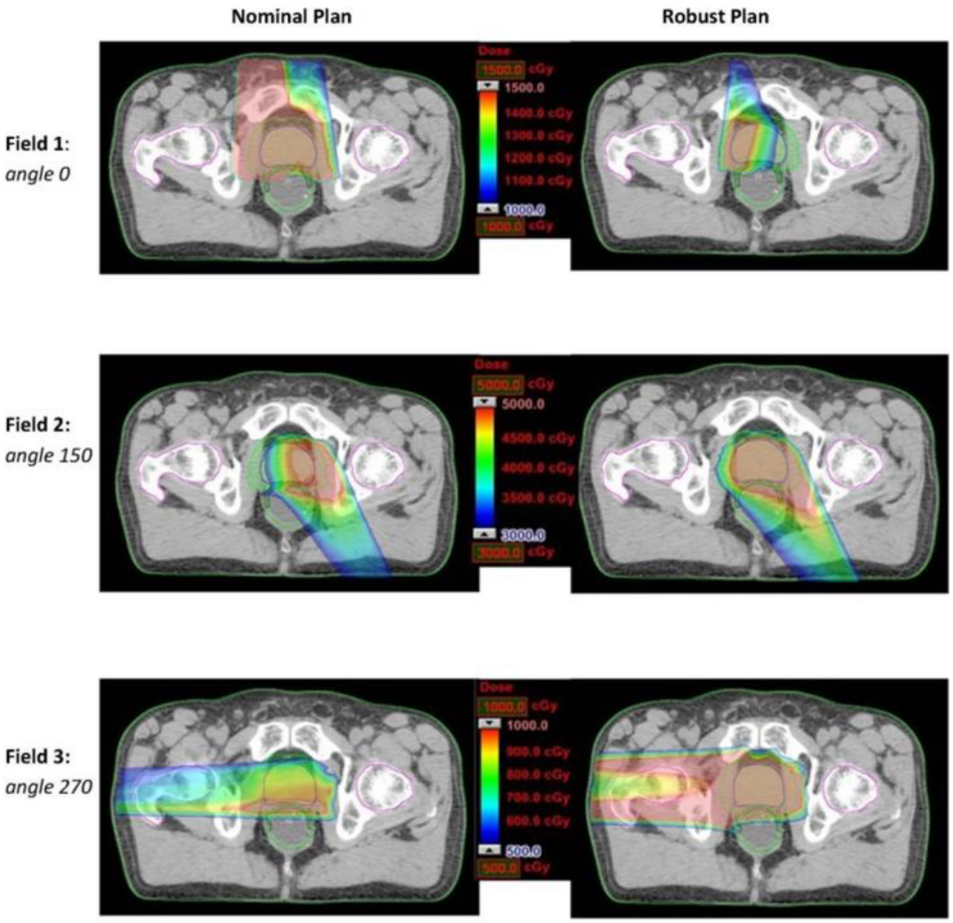

FIGURE 9 | Dose distributions for each beam angle in the transverse plan for comparing the nominal plan and worse-case robust plan of three-beam IMPT plan for one prostate cancer patient (69) (Open Assess).

improving the robustness of the dose distribution, the appropriate directions vary greatly depending on the location of the tumor, particularly in the lungs and HN region, and further studies with larger numbers of cases for each site are needed.

To select optimal direction beams, a flexible and compact full 360° gantry represents a powerful option for particle RT. However, the wide application of the rotating gantry in particle centers, particularly for carbon-ion radiotherapy, is limited by the high cost and large floor space requirements. Additionally, based on the conclusions presented above, most robust angles may be implemented by a partially rotating gantry (27). Therefore, it may be reasonable to encourage the use of partially rotating gantries in particle therapy in view of the lower associated costs and smaller space requirements.

While some studies reviewed in this article have proposed certain fixed angles as optimal angles, in our view, a range of angles should be recommended as a reference for beam selection. It may also be helpful for arc therapy. In recent years, arc therapy in particle therapy has gained increasing attention due to the rotating gantry and spot-scanning technique used in a wide range of applications. Ding et al. (70) first proposed the spot-scanning proton arc (SPArc) as a novel arc optimization algorithm. Compared with IMPT, SPArc based on robust optimization has been demonstrated to provide more conformal dose distribution and a significantly lower dose of OARs in HN cancers, lung cancer, and prostate cancer, and, specifically, parotid D_{mean} decreased by 30% (70); the average lung V5 and V20 for lung doses decreased by 4.6% and 3.2%, respectively (71); and rectum V30 and mean dose were reduced by an average of 12.13% and 7.32 Gy, respectively (72). Moreover, SPArc shortened the total delivery time (70–72). The knowledge of the range of robust angles remains important because the planner can select the arc or adjust the weight of certain directions within the arc by referring to the range of robust angles. However, some obstacles remain, such as developing a submillimeter accuracy rotating gantry and implementing a new arc quality assurance program. Although further multicenter studies involving large samples are required to assess the robustness and quality assurance of arc therapy in particle therapy, proton and carbon-ion arc therapy with a more

flexible and compact rotating gantry represent promising strategies for the future.

Automatic angle selection algorithms have been an important focus in radiotherapy. For photon therapy, several automatic angle optimization algorithms have been applied, such as class solutions (73). However, automatic angle optimization algorithms of particle RT are currently limited and not widely available in the treatment planning system. To date, research on the optimal angle selection is limited, and the number of cases involved is small. Moreover, it is difficult for a single study to consider all aspects (setup errors, range errors, and intra- and interfractional anatomical changes) to optimize beam angle selection. At present, it may be difficult to fully consider the anatomical changes in the studies of automatic angle optimization algorithms. Additionally, it is often necessary to manually select the range of candidate beams before applying the algorithms mentioned in this article. Thus, the robust angles based on the WET change discussed in this article may be used as a reference and a help for automatic angle selection.

With the increasing technological maturity and further development of imaging technologies in particle RT, robust angle selection will become more precise and individualized, improving the effectiveness of particle RT.

AUTHOR CONTRIBUTIONS

All authors were involved in the process of collecting and reading the papers, analyzing the data, and preparing the manuscript. All authors contributed to the article and approved the submitted version.

ACKNOWLEDGMENTS

The authors are grateful to the medical doctors and medical physicists at GHMC for their valuable insights.

REFERENCES

1. Koehler AM, Preston WM. Protons in Radiation Therapy: Comparative Dose Distributions for Protons, Photons, and Electrons. *Radiology* (1972) 104:191–5. doi: 10.1148/104.1.191
2. Mackie TR, Tomé WA. Advanced Image-Guided External Beam Radiotherapy. *Cancer Treat Res* (2008) 139:7–39. doi: 10.1007/978-0-387-36744-6_2
3. Bassler N, Kantemiris I, Karaiskos P, Engelke J, Holzscheiter MH, Petersen JB. Comparison of Optimized Single and Multifield Irradiation Plans of Antiproton, Proton and Carbon Ion Beams. *Radiother Oncol* (2010) 95:87–93. doi: 10.1016/j.radonc.2010.02.026
4. Shiba S, Shibuya K, Kawashima M, Okano N, Kaminuma T, Okamoto M, et al. Comparison of Dose Distributions When Using Carbon Ion Radiotherapy Versus Intensity-Modulated Radiotherapy for Hepatocellular Carcinoma With Macroscopic Vascular Invasion: A Retrospective Analysis. *Anticancer Res* (2020) 40:459–64. doi: 10.21873/anticanres.13974
5. Ohno T. Particle Radiotherapy With Carbon Ion Beams. *EPMA J* (2013) 4:1–7. doi: 10.1186/1878-5085-4-9
6. Shiba S, Shibuya K, Okamoto M, Okazaki S, Komatsu S, Kubota Y, et al. Clinical Impact of Hypofractionated Carbon Ion Radiotherapy on Locally Advanced Hepatocellular Carcinoma. *Radiat Oncol* (2020) 15:1–8. doi: 10.1186/s13014-020-01634-z
7. Ono T, Yamamoto N, Nomoto A, Nakajima M, Isozaki Y, Kasuya G, et al. Long Term Results of Single-Fraction Carbon-Ion Radiotherapy for Non-Small Cell Lung Cancer. *Cancers* (2021) 13:112. doi: 10.3390/cancers13010112
8. Demizu Y, Imai R, Kiyohara H, Matsunobu A, Okamoto M, Okimoto T, et al. Carbon Ion Radiotherapy for Sacral Chordoma: A Retrospective Nationwide Multicentre Study in Japan. *Radiother Oncol* (2021) 154:1–5. doi: 10.1016/j.radonc.2020.09.018
9. Kawamura H, Kubo N, Sato H, Mizukami T, Katoh H, Ishikawa H, et al. Moderately Hypofractionated Carbon Ion Radiotherapy for Prostate Cancer; a Prospective Observational Study "Gunma0702". *BMC Cancer* (2020) 20:1–8. doi: 10.1186/s12885-020-6570-8
10. Ono T. Review of Clinical Results of Charged-Particle Therapy for Esophageal Cancer. *Esophagus* (2020) 10:33–40. doi: 10.1007/s10388-020-00759-0
11. Weber DC, Lim PS, Tran S, Walser M, Bolsi A, Kliebsch U, et al. Proton Therapy for Brain Tumours in the Area of Evidence-Based Medicine. *Br J Radiol* (2020) 93:20190237. doi: 10.1259/bjr.20190237
12. Iwata H, Ogino H, Hattori Y, Nakajima K, Nomura K, Hayashi K, et al. ImageGuided Proton Therapy for Elderly Patients With Hepatocellular Carcinoma:High Local Control and Quality of Life Preservation. *Cancers* (2021) 13:219. doi: 10.3390/cancers13020219
13. Eley JG, Newhauser WD, Richter D, Lüchtenborg R, Saito N, Bert C. Robustness of Target Dose Coverage to Motion Uncertainties for Scanned Carbon Ion Beam Tracking Therapy of Moving Tumors. *Phys Med Biol* (2015) 60:1717–40. doi: 10.1088/0031-9155/60/4/1717
14. Tryggestad EJ, Liu W, Pepin MD, Hallemeier CL, Sio TT. Managing Treatment-Related Uncertainties in Proton Beam Radiotherapy for Gastrointestinal Cancers. *J Gastrointest Oncol* (2020) 11:212–24. doi: 10.21037/jgo.2019.11.07
15. Inoue T, Widder J, van Dijk LV, Takegawa H, Koizumi M, Takashina M, et al. Limited Impact of Setup and Range Uncertainties, Breathing Motion, and Interplay Effects in Robustly Optimized Intensity Modulated Proton Therapy for Stage III Non-Small Cell Lung Cancer. *Int J Radiat Oncol Biol Phys* (2016) 96:661–9. doi: 10.1016/j.ijrobp.2016.06.2454
16. Lomax AJ. Intensity Modulated Proton Therapy and its Sensitivity to Treatment Uncertainties 1: The Potential Effects of Calculational Uncertainties. *Phys Med Biol* (2008) 53:1027–42. doi: 10.1088/0031-9155/53/4/014
17. Lomax A. Intensity Modulated Proton Therapy and its Sensitivity to Treatment Uncertainties 2: The Potential Effects of Inter-Fraction and Inter-Field Motions. *Phys Med Biol* (2008) 531043–56. doi: 10.1088/0031-9155/53/4/015
18. Sakai M, Kubota Y, Saitoh JI, Irie D, Shirai K, Okada R, et al. Robustness of Patient Positioning for Interfractional Error in Carbon Ion Radiotherapy for Stage I Lung Cancer: Bone Matching Versus Tumor Matching. *Radiother Oncol* (2018) 129:95–100. doi: 10.1016/j.radonc.2017.10.003
19. Li Y, Kubota Y, Kubo N, Mizukami T, Sakai M, Kawamura H, et al. Dose Assessment for Patients With Stage I Non-Small Cell Lung Cancer Receiving Passive Scattering Carbon-Ion Radiotherapy Using Daily Computed Tomographic Images: A Prospective Study. *Radiother Oncol* (2020) 144:224–30. doi: 10.1016/j.radonc.2020.01.003
20. Li Y, Kubota Y, Okamoto M, Shiba S, Okazaki S, Matsui T, et al. Adaptive Planning Based on Single Beam Optimization in Passive Scattering Carbon Ion Radiotherapy for Patients With Pancreatic Cancer. *Radiat Oncol* (2021) 16:111. doi: 10.1186/s13014-021-01841-2
21. Houweling AC, Fukata K, Kubota Y, Shimada H, Rasch CR, Ohno T, et al. The Impact of Interfractional Anatomical Changes on the Accumulated Dose in Carbon Ion Therapy of Pancreatic Cancer Patients. *Radiother Oncol* (2016) 119:319–25. doi: 10.1016/j.radonc.2016.03.004
22. Kubota Y, Okamoto M, Shiba S, Okazaki S, Matsui T, Li Y, et al. Robustness of Daily Dose for Each Beam Angle and Accumulated Dose for Inter-Fractional Anatomical Changes in Passive Carbon-Ion Radiotherapy for Pancreatic Cancer: Bone Matching Versus Tumor Matching. *Radiother Oncol* (2021) 157:85–92. doi: 10.1016/j.radonc.2021.01.011
23. Kubota Y, Katoh H, Shibuya K, Shiba S, Abe S, Sakai M, et al. Comparison Between Bone Matching and Marker Matching for Evaluation of Intra-and

Inter-Fractional Changes in Accumulated Dose of Carbon Ion Radiotherapy for Hepatocellular Carcinoma. *Radiother Oncol* (2019) 137:77–82. doi: 10.1016/j.radonc.2019.04.026
24. Tobias CA, Lawrence JH, Born JL, McCombs RK, Roberts JE, Anger HO, et al. Pituitary Irradiation With High-Energy Proton Beams a Preliminary Report. *Cancer Res* (1958) 18:121–34.
25. Li Y, Kubota Y, Tashiro M, Ohno T. Value of Three-Dimensional Imaging Systems for Image-Guided Carbon Ion Radiotherapy. *Cancers* (2019) 11:297. doi: 10.3390/cancers11030297
26. Kudo S, Shioyama Y, Suefuji H, Matsunobu A, Shinoto M, Toyama S, et al. Clinical Experience of SAGA HIMAT. *Int J Part Ther* (2016) 2:464–7. doi: 10.14338/IJPT-15-00017.1
27. Bradley J, Bottani B, Klein E. Proton Therapy. An Update on the S. Lee Kling Proton Therapy Center at Barnes-Jewish Hospital and Washington University. *Mo Med* (2015) 112:335–7.
28. Bhattacharyya T, Koto M, Ikawa H, Hayashi K, Hagiwara Y, Makishima H, et al. First Prospective Feasibility Study of Carbon-Ion Radiotherapy Using Compact Superconducting Rotating Gantry. *Br J Radiol* (2019) 92:20190370. doi: 10.1259/bjr.20190370
29. Devicienti S, Strigari L, D'Andrea M, Benassi M, Dimiccoli V, Portaluri M. Patient Positioning in the Proton Radiotherapy Era. *J Exp Clin Cancer Res* (2010) 29:1–5. doi: 10.1186/1756-9966-29-47
30. Coutrakon G, Hubbard J, Johanning J, Maudsley G, Slaton T, Morton P. A Performance Study of the Loma Linda Proton Medical Accelerator. *Med Phys* (1994) 21:1691–701. doi: 10.1118/1.597270
31. Fuchs R, Weinrich U, Sust E. *Assembly of the Carbon Beam Gantry at the Heidelberg Ion Therapy (HIT) Accelerator*. Genoa, Italy: Proceedings of EPAC-2008 (2008).
32. Kim J-i, Park JM, Wu HG. Carbon Ion Therapy: A Review of an Advanced Technology. *Prog Med Phys* (2020) 31:71–80. doi: 1014316/pmp.2020.31.3.71
33. Mori S, Knopf AC, Umegaki K. Motion Management in Particle Therapy. *Med Phys* (2018) 45:e994–1010. doi: 10.1002/mp.12679
34. Tashiro M, Ishii T, Koya J, Okada R, Kurosawa Y, Arai K, et al. Technical Approach to Individualized Respiratory-Gated Carbon-Ion Therapy for Mobile Organs. *Radiol Phys Technol* (2013) 6:356–66. doi: 10.1007/s12194-013-0208-3
35. Kumagai M, Hara R, Mori S, Yanagi T, Asakura H, Kishimoto R, et al. Impact of Intrafractional Bowel Gas Movement on Carbon Ion Beam Dose Distribution in Pancreatic Radiotherapy. *Int J Radiat Oncol Biol Phys* (2009) 73:1276–81. doi: 10.1016/j.ijrobp.2008.10.055
36. Matney JE, Park PC, Li H, Court LE, Zhu XR, Dong L, et al. Perturbation of Water-Equivalent Thickness as a Surrogate for Respiratory Motion in Proton Therapy. *J Appl Clin Med Phys* (2016) 17:368–78. doi: 10.1120/jacmp.v17i2.5795
37. Chang JY, Li H, Zhu XR, Liao Z, Zhao L, Liu A, et al. Clinical Implementation of Intensity Modulated Proton Therapy for Thoracic Malignancies. *Int J Radiat Oncol Biol Phys* (2014) 90:809–18. doi: 10.1016/j.ijrobp.2014.07.045
38. Yu J, Zhang X, Liao L, Li H, Zhu R, Park PC, et al. Motion-Robust Intensity-Modulated Proton Therapy for Distal Esophageal Cancer. *Med Phys* (2016) 43:1111–8. doi: 10.1118/1.4940789
39. Gorgisyan J, Perrin R, Lomax AJ, Persson GF, Josipovic M, Engelholm SA, et al. Impact of Beam Angle Choice on Pencil Beam Scanning Breath-Hold Proton Therapy for Lung Lesions. *Acta Oncol* (2017) 56:853–9. doi: 10.1080/0284186X.2017.1287950
40. Casares-Magaz O, Toftegaard J, Muren LP, Kallehauge JF, Bassler N, Poulsen PR, et al. A Method for Selection of Beam Angles Robust to Intra-Fractional Motion in Proton Therapy of Lung Cancer. *Acta Oncol* (2014) 53:1058–63. doi: 10.3109/0284186X.2014.927586
41. Zhang Y, Ho MW, Li Z. A Beam-Angle-Selection Method to Improve Inter-Fraction Motion Robustness for Lung Tumor Irradiation With Passive Proton Scattering. *Technol Cancer Res Treat* (2020) 19:1533033820948052. doi: 10.1177/1533033820948052
42. Mori S, Dong L, Starkschall G, Mohan R, Chen GT. A Serial 4DCT Study to Quantify Range Variations in Charged Particle Radiotherapy of Thoracic Cancers. *J Radiat Res* (2014) 55:309–19. doi: 10.1093/jrr/rrt114
43. Wang JZ, Li JB, Wang W, Qi HP, Ma ZF, Zhang YJ, et al. Changes in Tumour Volume and Motion During Radiotherapy for Thoracic Oesophageal Cancer. *Radiother Oncol* (2015) 114:201–5. doi: 10.1016/j.radonc.2014.12.010
44. Häfner MF, Sterzing F, Krug D, Körber SA, Jäkel O, Debus J, et al. Intrafractional Dose Variation and Beam Configuration in Carbon Ion Radiotherapy for Esophageal Cancer. *Radiat Oncol* (2016) 11:1–9. doi: 10.1186/s13014-016-0727-2
45. Zeng YC, Vyas S, Dang Q, Schultz L, Bowen SR, Shankaran V, et al. Proton Therapy Posterior Beam Approach With Pencil Beam Scanning for Esophageal Cancer. *Strahlenther Onkol* (2016) 192:913–21. doi: 10.1007/s00066-016-1034-4
46. Batista V, Richter D, Combs SE, Jäkel O. Planning Strategies for Inter-Fractional Robustness in Pancreatic Patients Treated With Scanned Carbon Therapy. *Radiat Oncol* (2017) 12:1–9. doi: 10.1186/s13014-017-0832-x
47. Dreher C, Habermehl D, Ecker S, Brons S, El-Shafie R, Jäkel O, et al. Optimization of Carbon Ion and Proton Treatment Plans Using the Raster-Scanning Technique for Patients With Unresectable Pancreatic Cancer. *Radiat Oncol* (2015) 10:237. doi: 10.1186/s13014-015-0538-x
48. Shiomi M, Mori S, Shinoto M, Nakayama Y, Kamada T, Yamada S. Comparison of Carbon-Ion Passive and Scanning Irradiation for Pancreatic Cancer. *Radiother Oncol* (2016) 119:326–30. doi: 10.1016/j.radonc.2016.04.026
49. Yang Z, Chang Y, Brock KK, Cazoulat G, Koay EJ, Koong AC, et al. Effect of Setup and Inter-Fraction Anatomical Changes on the Accumulated Dose in CT-Guided Breath-Hold Intensity Modulated Proton Therapy of Liver Malignancies. *Radiother Oncol* (2019) 134:101–9. doi: 10.1016/j.radonc.2019.01.028
50. Yokoyama A, Kubota Y, Kawamura H, Miyasaka Y, Kubo N, Sato H, et al. Impact of Inter-Fractional Anatomical Changes on Dose Distributions in Passive Carbon-Ion Radiotherapy for Prostate Cancer: Comparison of Vertical and Horizontal Fields. *Front Oncol* (2020) 10:1264. doi: 10.3389/fonc.2020.01264
51. Tang S, Both S, Bentefour H, Paly JJ, Tochner Z, Efstathiou J, et al. Improvement of Prostate Treatment by Anterior Proton Fields. *Int J Radiat Oncol Biol Phys* (2012) 83:408–18. doi: 10.1016/j.ijrobp.2011.06.1974
52. Moteabbed M, Trofimov A, Sharp GC, Wang Y, Zietman AL, Efstathiou JA, et al. Proton Therapy of Prostate Cancer by Anterior-Oblique Beams: Implications of Setup and Anatomy Variations. *Phys Med Biol* (2017) 62:1644–60. doi: 10.1088/1361-6560/62/5/1644
53. Ten Haken RK, Forman JD, Heimburger DK, Gerhardsson A, McShan DL, Perez-Tamayo C, et al. Treatment Planning Issues Related to Prostate Movement in Response to Differential Filling of the Rectum and Bladder. *Int J Radiat Oncol Biol Phys* (1991) 20:1317–24. doi: 10.1016/0360-3016(91)90244-X
54. Huang E, Dong L, Chandra A, Kuban DA, Rosen II, Evans A, et al. Intrafraction Prostate Motion During IMRT for Prostate Cancer. *Int J Radiat Oncol Biol Phys* (2002) 53:261–8. doi: 10.1016/S0360-3016(02)02738-4
55. Toramatsu C, Inaniwa T. Beam Angle Selection Incorporation of Anatomical Heterogeneities for Pencil Beam Scanning Charged-Particle Therapy. *Phys Med Biol* (2016) 61:8664–75. doi: 10.1088/1361-6560/61/24/8664
56. Gu W, Neph R, Ruan D, Zou W, Dong L, Sheng K. Robust Beam Orientation Optimization for Intensity-Modulated Proton Therapy. *Med Phys* (2019) 46:3356–70. doi: 10.1002/mp.13641
57. Wu RY, Liu AY, Sio TT, Blanchard P, Wages C, Amin MV, et al. Intensity-Modulated Proton Therapy Adaptive Planning for Patients With Oropharyngeal Cancer. *Int J Part Ther* (2017) 4:26–34. doi: 10.14338/IJPT-17-00010.1
58. Müller BS, Duma MN, Kampfer S, Nill S, Oelfke U, Geinitz H, et al. Impact of Interfractional Changes in Head and Neck Cancer Patients on the Delivered Dose in Intensity Modulated Radiotherapy With Protons and Photons. *Phys Med* (2015) 31:266–72. doi: 10.1016/j.ejmp.2015.02.007
59. Kim J, Park YK, Sharp G, Busse P, Winey B. Beam Angle Optimization Using Angular Dependency of Range Variation Assessed via Water Equivalent Path Length (WEPL) Calculation for Head and Neck Proton Therapy. *Phys Med* (2020) 69:19–27. doi: 10.1016/j.ejmp.2019.11.021
60. Fukumitsu N, Ishikawa H, Ohnishi K, Terunuma T, Mizumoto M, Numajiri H, et al. Dose Distribution Resulting From Changes in Aeration of Nasal Cavity or Paranasal Sinus Cancer in the Proton Therapy. *Radiother Oncol* (2014) 113:72–6. doi: 10.1016/j.radonc.2014.08.024
61. Shusharina N, Fullerton B, Adams JA, Sharp GC, Chan AW. Impact of Aeration Change and Beam Arrangement on the Robustness of Proton Plans. *J Appl Clin Med Phys* (2019) 20:14–21. doi: 10.1002/acm2.12503
62. Sharma MB, Argota Perez R, Holm AIS, Korreman SS, Jensen K, Elstrøm UV, et al. Air Variability in Maxillary Sinus During Radiotherapy for Sinonasal

Carcinoma. *Clin Transl Radiat Oncol* (2021) 27:36–43. doi: 10.1016/j.ctro.2020.12.007
63. Farace P, Bizzocchi N, Righetto R, Fellin F, Fracchiolla F, Lorentini S, et al. Supine Craniospinal Irradiation in Pediatric Patients by Proton Pencil Beam Scanning. *Radiother Oncol* (2017) 123:112–8. doi: 10.1016/j.radonc.2017.02.008
64. Schaffner B, Pedroni E, Lomax A. Dose Calculation Models for Proton Treatment Planning Using a Dynamic Beam Delivery System: An Attempt to Include Density Heterogeneity Effects in the Analytical Dose Calculation. *Phys Med Biol* (1999) 44:27–41. doi: 10.1088/0031-9155/44/1/004
65. Ammazzalorso F, Jelen U, Engenhart-Cabillic R, Schlegel W. Dosimetric Robustness Against Setup Errors in Charged Particle Radiotherapy of Skull Base Tumors. *Radiat Oncol* (2014) 9:279. doi: 10.1186/s13014-014-0279-2
66. Lassen-Ramshad Y, Vestergaard A, Muren LP, Høyer M, Petersen JB. Plan Robustness in Proton Beam Therapy of a Childhood Brain Tumour. *Acta Oncol* (2011) 50:791–6. doi: 10.3109/0284186X.2011.590149
67. Morávek Z, Rickhey M, Hartmann M, Bogner L. Uncertainty Reduction in Intensity Modulated Proton Therapy by Inverse Monte Carlo Treatment Planning. *Phys Med Biol* (2009) 54:4803–19. doi: 10.1088/0031-9155/54/15/011
68. Cao W, Lim GJ, Lee A, Li Y, Liu W, Ronald Zhu X, et al. Uncertainty Incorporated Beam Angle Optimization for IMPT Treatment Planning. *Med Phys* (2012) 39:5248–56. doi: 10.1118/1.4737870
69. Cao W, Lim GJ, Li Y, Zhu XR, Zhang X. Improved Beam Angle Arrangement in Intensity Modulated Proton Therapy Treatment Planning for Localized Prostate Cancer. *Cancers* (2015) 7:574–84. doi: 10.3390/cancers7020574
70. Ding X, Li X, Zhang JM, Kabolizadeh P, Stevens C, Yan D. Spot-Scanning Proton Arc (Sparc) Therapy: The First Robust and Delivery-Efficient Spot-Scanning Proton Arc Therapy. *Int J Radiat Oncol Biol Phys* (2016) 96:1107–16. doi: 10.1016/j.ijrobp.2016.08.049
71. Li X, Kabolizadeh P, Yan D, Qin A, Zhou J, Hong Y, et al. Improve Dosimetric Outcome in Stage III Non-Small-Cell Lung Cancer Treatment Using Spot-Scanning Proton Arc (SPArc) Therapy. *Radiat Oncol* (2018) 13:35. doi: 10.1186/s13014-018-0981-6
72. Ding X, Li X, Qin A, Zhou J, Yan D, Stevens C, et al. Have We Reached Proton Beam Therapy Dosimetric Limitations? - A Novel Robust, Delivery-Efficient and Continuous Spot-Scanning Proton Arc (SPArc) Therapy Is to Improve the Dosimetric Outcome in Treating Prostate Cancer. *Acta Oncol* (2018) 57:435–7. doi: 10.1080/0284186X.2017.1358463
73. Schreibmann E, Xing L. Feasibility Study of Beam Orientation Class-Solutions for Prostate IMRT. *Med Phys* (2004) 31:2863–70. doi: 10.1118/1.1797571

Conflict of Interest: The authors declare that the research was conducted in the absence of any commercial or financial relationships that could be construed as a potential conflict of interest.

Publisher's Note: All claims expressed in this article are solely those of the authors and do not necessarily represent those of their affiliated organizations, or those of the publisher, the editors and the reviewers. Any product that may be evaluated in this article, or claim that may be made by its manufacturer, is not guaranteed or endorsed by the publisher.

frontiers in Oncology

ORIGINAL RESEARCH
published: 22 September 2021
doi: 10.3389/fonc.2021.747532

Investigate the Dosimetric and Potential Clinical Benefits Utilizing Stereotactic Body Radiation Therapy With Simultaneous Integrated Boost Technique for Locally Advanced Pancreatic Cancer: A Comparison Between Photon and Proton Beam Therapy

Peilin Liu[1], Xian-shu Gao[1], Zishen Wang[2], Xiaomei Li[1], Xi Cao[1], Chenghao Jia[1], Mu Xie[1], Feng Lyu[1], Shiyu Shang[3] and Xuanfeng Ding[4]**

[1] Department of Radiation Oncology, Peking University First Hospital, Beijing, China, [2] Department of Radiation Oncology, Hebei Yizhou Tumor Hospital, Zhuozhou, China, [3] Department of Oncology, Hebei North University, Shijiazhuang, China, [4] Department of Radiation Oncology, Beaumont Health, Proton Beam Therapy Center, Royal Oak, MI, United States

OPEN ACCESS

Edited by:
Lanchun Lu,
The Ohio State University,
United States

Reviewed by:
Hualin Zhang,
Northwestern Medicine, United States
Carlos Perez-Torres,
Purdue University, United States

***Correspondence:**
Xuanfeng Ding
xuanfeng.ding@beaumont.edu
Xian-shu Gao
Doctorgaoxs@126.com

Specialty section:
This article was submitted to Cancer Imaging and Image-directed Interventions, a section of the journal Frontiers in Oncology

Received: 26 July 2021
Accepted: 30 August 2021
Published: 22 September 2021

Citation:
Liu P, Gao X-s, Wang Z, Li X, Cao X, Jia C, Xie M, Lyu F, Shang S and Ding X (2021) Investigate the Dosimetric and Potential Clinical Benefits Utilizing Stereotactic Body Radiation Therapy With Simultaneous Integrated Boost Technique for Locally Advanced Pancreatic Cancer: A Comparison Between Photon and Proton Beam Therapy. Front. Oncol. 11:747532. doi: 10.3389/fonc.2021.747532

Purpose: To investigate the potential clinical benefits of using stereotactic body radiation therapy (SBRT) with simultaneous integrated boost (SIB) technique for locally advanced pancreatic cancer (LAPC) among different treatment modalities and planning strategies, including photon and proton.

Method: A total of 19 patients were retrospectively selected in this study: 13 cases with the tumor located in the head of the pancreas and 6 cases with the tumor in the body of the pancreas. SBRT-SIB plans were generated using volumetric modulated arc therapy (VMAT), two-field Intensity Modulated Proton Therapy (IMPT), and three-field IMPT. The IMPT used the robust optimization parameters of ± 3.5% range and 5-mm setup uncertainties. Root-mean-square deviation dose (RMSD) volume histograms were used to evaluate the target coverage robustness quantitatively. Dosimetric metrics based on the dose-volume histogram (DVH), homogeneity index (HI), and normal tissue complication probability (NTCP) were analyzed to evaluate the potential clinical benefits among different planning groups.

Results: With a similar CTV and SIB coverage, two-field IMPT provided a lower maximum dose for the stomach (median: 18.6GyE, $p<0.05$) and duodenum (median: 32.62GyE, $p<0.05$) when the target was located in the head of the pancreas compared to VMAT and three-field IMPT. The risks of gastric bleed (3.42%) and grade ≥ 3 GI toxicity (4.55%) were also decreased. However, for the target in the body of the pancreas, VMAT showed a lower maximum dose for the stomach (median 30.93GyE, $p<0.05$) and toxicity of gastric

bleed (median: 8.67%, $p<0.05$) compared to two-field IMPT and three-field IMPT, while other maximum doses and NTCPs were similar. The RMSD volume histogram (RVH) analysis shows that three-field IMPT provided better robustness for targets but not for OARs. Instead, three-field IMPT increased the Dmean of organs such as the stomach, duodenum, and intestine.

Conclusion: The results indicated that the tumor locations could play a critical role in determining clinical benefits among different treatment modalities. Two-field IMPT could be a better option for LAPC patients whose tumors are located in the head of the pancreas. It provides lower severe toxicity for the stomach and duodenum. Nevertheless, VMAT is preferred for the body with better protection for the possibility of gastric bleed.

Keywords: normal tissue complication probability (NTCP), stereotactic body radiation therapy (SBRT), simultaneous integrated boost (SIB), pancreatic cancer, intensity modulated proton therapy (IMPT), volumetric modulated arc therapy (VMAT)

1 INTRODUCTION

Pancreatic cancer is a malignant tumor with a high mortality rate. It is the sixth leading cause of cancer death in China and the fourth leading cause of cancer death in the United States (1, 2). As of today, surgery remains the only treatment to achieve long-term survival. However, most patients are locally advanced and unresectable when first diagnosed (3). For the locally advanced pancreatic cancer (LAPC) patient population, stereotactic body radiation therapy (SBRT) is the first-line treatment recommended by the guidelines, providing better survival than chemotherapy alone or conventional-fraction radiation therapy (CFRT) (4–6). Although RT dosing for SBRT has not been specified in the guidelines, prescription doses of three fractions (total dose 30–45 Gy) or five fractions (total dose 25–45 Gy) have been applied in some clinical trials (6). In order to have better local control of the hypoxic region in the center of the tumor, simultaneous integrated boost (SIB) was proposed by escalating the dose in the central region (7). A stage I clinical trial proved the safety of delivering 36 Gy in three fractions to borderline resectable pancreatic cancer (BRPC), with a 9-Gy SIB to the positive posterior margins (PM) in patients whose tumor was at least 3 mm away from the duodenum (8). However, it is challenging to administrate such high doses (e.g., the biologically effective dose (BED) of 45 Gy is 85.5 Gy) with photon radiotherapy technique, e.g., volumetric modulated arc therapy (VMAT), when the tumor is adjacent to gastrointestinal (GI) tracts such as the stomach and duodenum with photon therapy. Surpassing dose tolerance to these structures could cause gastrointestinal perforation or ulceration, which could be fatal.

On the other hand, with the rapid development of proton beam technology over the last decades, intensity-modulated proton therapy (IMPT) based on the pencil beam scanning technique has shown potential dosimetric advantage and flexibility to improve organs at risk (OARs) sparing with a sharper fall-off of distal dose compared to photon therapy (9). Proton has proven the advantage to diminish acute toxicities in many diseases such as pediatric low-grade glioma, thymic tumor, and locally advanced non-small cell lung cancer (10–12). Previous studies have reported the potential dosimetric advantage to provide a lower dose for the adjacent GI organs in postoperative pancreatic cancer in comparison with VMAT and passive-scattering technique (13). However, due to the range uncertainties, the proton treatment plan normally enlarges the high dose zone at the distal end of the beam angle, in other words, less conformal to the target volume, in order to provide a robust coverage. Since most of the proton beam angles for LAPC were selected posteriorly, avoiding the bowel gas uncertainties (14), the margin taking into account the range uncertainty directly translated into the high dose spill to the GI organs is critical to the pancreatic SBRT. As a result, not all the studies found that proton beam therapy has the potential clinical advantage in the management of LAPC over photon therapy. For example, Thompson's study showed that with standard fractions, proton showed no dosimetric advantage in treating LAPC (14). Additionally, Raturi showed that the normal tissue complication probability (NTCP) is not statistically different between photon and proton planning groups. However, these studies did not consider the relationship between the OAR sparing, and the target location since the patient-specific geometry plays a key factor in proton planning (15). Additionally, the feasibility of proton SBRT-SIB for pancreatic tumor has not been addressed yet.

Thus, this study performs a quantitative and comprehensive dosimetric study based on the LAPC location and patient geometry to explore the feasibility and potential clinical benefits of utilizing SBRT-SIB among different treatment modalities and proton field arrangement, including VMAT, two-field IMPT, and three-field IMPT. Furthermore, the NTCP model is implemented to investigate the potential clinical benefits among these planning groups. To the best of our knowledge, this is the first investigation that evaluates the SBRT-SIB plan quality by using the NTCP model for LAPC patient population.

2 METHOD AND MATERIALS

2.1 Patient Section, Target Volume, and OAR Definition

Nineteen patients with LAPC who received 50.4 Gy in 1.8 Gy per fraction using the VMAT technique in our institution between

2016 and 2020 were selected in this study. All data of the 19 patients we used were approved by Peking University First Hospital Ethics Committee. Tumor location, the volume of the clinical target volume (CTV), planning target volume (PTV), and boost area were shown (**Table 1**). The patient groups were divided by the location of the tumor (head: 13 patients, body: 6 patients). Gross tumor volume (GTV) includes primary tumor and clinically apparent lymph nodes but does not include elective nodal regions (16). GTV to CTV uniform expansions of 0.5 cm were based on ESTRO guidelines (16). For photon therapy, PTV was the CTV plus a 0.5-cm uniform margin. The boost area was 1 cm contracted with CTV to avoid extra dose delivered to adjacent OARs (17). All patients were treated with breath-hold technique, controlling motion in order to assess the maximal potential benefit (18).

2.2 Treatment Planning

VMAT, robustness optimized two-field IMPT, and three-field IMPT were all generated on Raystation v 7.0 (RaySearch Laboratory AB, Stockholm). VMAT plans were generated using 6-MV beams with two full arcs, delivered by the Varian linear accelerator (Trilogy, Varian Medical System, Inc., Palo Alto, CA). A collapsed-cone convolution superposition (CCC) based algorithm was applied to calculate, and the dose grid used was 0.3*0.3*0.3 cm^3.

Proton planning uses CTV plus robustness optimization to take into account the setup and range uncertainties. The plan for IMPT-SIB was done using the single field optimization (SFO) method. Considering the sensitivity of proton beams to inhomogeneous materials and adjacent organs at risk, the directions of the two-field proton plan were posterior, right posterior oblique (19). For the three-field proton plan, the other posterior oblique beam angle was chosen. A CTV-based robust optimization was used, and the plan was evaluated using the worst-case scenario perturbed dose with setup uncertainties of ± 5 mm for x, y, z directions and ±3.5% range uncertainties. The dose calculation was done using the Monte Carlo dose calculation. Proton relative biological effectiveness (RBE) was assumed as 1.1 (20).

The prescription dose of the photon and proton was 30GyE/5f for the target and 45GyE/5f for the boost area. In each plan, 95% volume of the target was requested to receive 95% of the prescription dose. All plans V98 of CTV should reach 98% prescription dose at least, and D95 of the boost area should reach the prescription with the maximum dose limited to 107% prescription. All the treatment plan meets the normal tissues constraints, which were as follows: for the stomach, duodenum, and intestine Dmax (0.5 cm^3)<35 Gy; for the stomach PRV, duodenum PRV, and intestine PRV Dmax (0.5 cm^3)<38 Gy; for the spinal cord (0.03 cm^3)<25 Gy, combined kidneys V12<25 Gy (volume that received 12 Gy should be less than 50% of the volume) and liver V12<40 Gy (18).

2.3 Planning Quality Evaluation

To evaluate the dose metric of the photon and proton plans, target coverage and OARs were all compared. Besides, HI of the boost area was used to assess the homogeneity of the plan. HI was defined as follows:

$$HI = D_{95}/D_5,$$

where D_{95} represents the minimum dose in 5% of the target volume, and D_5 represents the minimum dose in 95% of the target volume. The closer the value to 1, the better the homogeneity of the target (21).

2.4 Evaluation of Proton Radiation Plan Robustness

The plan robustness was evaluated using the worst-case scenario perturbed dose with setup uncertainties of ±5 mm for x, y, z directions and ±3.5% range uncertainties. The root-mean-square

TABLE 1 | Patient characteristics.

Case	Gender (M/F)	Age (years)	Location	Stage	CTV volume (cc)	PTV volume (cc)	Boost area volume (cc)
1	M	57	head	T4N1M0	134.52	221.19	31.60
2	F	71	body	T3N0M0	29.92	61.52	2.49
3	M	71	head	T3N0M0	47.33	93.92	4.47
4	F	61	head	T4N0M0	55.49	104.62	6.05
5	M	85	head	T4N1M0	75.76	136.17	11.91
6	F	72	head	T4N1M0	143.91	247.22	29.38
7	F	67	body	T3N0M0	75.89	138.02	8.91
8	F	74	head	T4N0M0	46.63	92.90	2.64
9	M	64	head	T3N0M0	117.00	214.47	17.01
10	F	53	head	T3N0M0	73.47	135.98	9.28
11	F	27	body	T3N0M0	58.02	109.77	6.10
12	F	87	body	T4N1M0	57.85	107.57	9.24
13	M	53	body	T4N1M0	160.44	271.96	32.59
14	M	59	body	T4N0M0	85.43	147.31	16.15
15	F	64	head	T3N1M0	113.60	202.22	17.94
16	M	69	head	T3N0M0	69.88	126.23	9.73
17	M	67	head	T4N1M0	170.75	264.99	49.14
18	M	39	head	T3N1M0	65.13	124.91	6.38
19	M	61	head	T3N0M0	356.46	585.90	80.31

M, male; F, female; CTV, clinical target volume; PTV, planning target volume.

deviation doses (RMSD) volume histograms (RVHs) of all 21 scenarios were generated to evaluate plan robustness (22). The two-field IMPT-SIB plan and three-field IMPT-SIB plan were compared relatively with the area under the RVH curve (AUC) (23). The smaller value of the specific structures indicated that the plan had more robustness in the structure.

2.5 Evaluation of NTCP

The cumulative physical dose of all plans was exported from TPS and converted into an equivalent dose in 2 Gy per fraction (EQD2). The evaluation of NTCP was performed using the Lyman–Kutcher–Burman (LKB) NTCP model shown in the following equations (24):

$$NTCP = \frac{1}{\sqrt{2\pi}} \int_{-\infty}^{t} e^{-\frac{x^2}{2}} dx \tag{1}$$

where

$$t = \frac{EUD - TD_{50}}{mTD_{50}} \tag{2}$$

with

$$EUD = (\Sigma_i v_i D_i^{\frac{1}{n}})^n \tag{3}$$

TD_{50} is the tolerance dose with a 50% probability of complications in the organ; EUD is the equivalent uniform dose; v_i is the volume when a uniform dose D_i is received. Besides, the parameters m and n represent the slope of the dose-response curve and the volume dependence of the NTCP, respectively.

All NTCPs were calculated from converted DVH *via* an in-home program on Matlab version R2019b (MathWorks Inc., Natick, MA, USA). The reference LKB-NTCP parameters (n, m, and TD50), the corresponding endpoints, and the L-Q-model α/β parameter in the present work are shown in **Table 2**.

In this study, we analyzed the NTCP and compared the results between the two patient populations with tumors located in the head and body of the pancreas.

2.6 Statistical Analysis

Analyses were all performed using the SPSS version 24.0 software (IBM, Armonk, NY). Dosimetric outcomes and estimated NTCPs were compared by using Friedman's test and pairwise comparison with Bonferroni correction between VMAT photon plans and two proton-based plans (two-field IMPT and three-field IMPT). Besides, a two-sided Wilcoxon signed-ranked test was used to compare AUC between two-field IMPT and three-field IMPT. P<0.05 was considered statistically significant.

3 RESULTS

3.1 Planning Quality Evaluation

The detailed summary of target coverage and the dosimetric parameters of OARs are all shown in **Table 3**. Representative dose contributions are displayed in **Figure 1**, for two cases with different locations of the tumors. The corresponding DVHs are also shown in **Figure 2**.

3.1.1 Target Coverage

The targets of all treatment methods had reached clinical criteria. As we had observed, all D95 of the boost area reached 45GyE, and two proton plans had the higher D5. VMAT had a slight advantage in HI of the boost area when the tumor was at the head of the pancreas (median 1.03) compared to two-field IMPT (median 1.04, p=0.013) and three-field IMPT (median 1.04, p=0.018). The same HI value of the boost area was obtained for tumors located in the body of the pancreas compared to two-field IMPT and three-field IMPT (all p>0.05). No matter where the tumor was located, the HI of the two kinds of IMPT plans had no statistical significance (p>0.05).

3.1.2 Dose Sparing in OARs

With equivalent target coverage, the remarkable mean dose reductions in most OARs were observed in IMPT planning groups compared to the VMAT (**Table 3**). For the tumors located at the head of the pancreas, the maximum dose of the stomach was decreased from 21.82GyE with VMAT to 18.60GyE with two-field IMPT (p=0.001) and 17.85GyE with three-field IMPT (p=0.063). However, when the tumors were in the body of the pancreas, opposite results were observed. The maximum dose of the stomach in VMAT (median 30.93GyE) was increased with both two-field IMPT (median 33.08GyE, p=0.012) and three-field IMPT (median 32.06GyE, p=0.063).

3.2 Evaluation of Proton Radiation Plan Robustness

All the AUC values of target volumes and OARs from the 19 cases were evaluated and are presented in **Table 4**. The typical RVHs are shown in the **Figure 3** with the same patients. The targets showed better robustness when the tumor was at the head of the pancreas when compared to two-field IMPT. The targets include CTV (2.32 in three-field IMPT versus 2.48 in two-field IMPT, p=0.021) and the boost area (1.19 in three-field IMPT versus 1.32 in two-field IMPT, p=0.028). There is no statistical difference among the stomach, duodenum, intestine, liver, and kidneys (p>0.5). Similarly, for tumors located at the body of the

TABLE 2 | Reference LKB-NTCP model parameters (n, m, TD_{50}), the corresponding endpoints, and the L-Q-model α/β parameter in the present work.

OAR	n	m	TD_{50}(Gy)	α/β	Endpoint	Source
Intestine	0.15	0.79	55	4	Diarrhea	Reinartz. et al. (25)
Intestine	0.15	0.16	55	4	Ulceration/perforation	Burman. et al. (26)
Duodenum	0.193	0.51	299.1	4	Grade ≥3 GI toxicity	Holyoake. et al. (27)
Stomach	0.07	0.3	62	4	Gastric bleed	Pan. et al. (28)

LKB-NTCP model, Lyman–Kutcher–Burman model; OAR, organs at risk; TD_{50}, the tolerance dose with a 50% probability of complications in the organ.

TABLE 3 | Dosimetric parameters evaluation.

Dosimetric parameters	Treatment modality			P value		
	VMAT (median and IQR)	2-field IMPT (median and IQR)	3-field IMPT (median and IQR)	VMAT *vs* 2-field IMPT	VMAT vs 3-field IMPT	2-field IMPT *vs* 3-field IMPT
Boost area						
D5(GyE)						
Head	46.28 (46.26-46.47)	46.70 (46.60-46.86)	46.63 (46.54-46.74)			
Body	46.01 (45.85-46.18)	46.65 (46.46-46.74)	46.67 (46.59-46.78)			
D95(GyE)						
Head	45.00 (45.00-45.00)	45.00 (45.00-45.03)	45.00 (45.00-45.00)			
Body	45.00 (45.00-45.00)	45.01 (45.00-45.04)	45.00 (45.00-45.01)			
HI						
Head	1.03 (1.02-1.03)	1.04 (1.03-1.04)	1.04 (1.03-1.04)	0.013	0.018	1.000
Body	1.02(1.02-1.03)	1.04 (1.03-1.04)	1.04 (1.04-1.04)	0.250	0.091	1.000
Mean (GyE)						
Head	45.77 (45.65-45.83)	45.95 (45.88-46.06)	45.93 (45.87-45.99)			
Body	45.69 (45.53-45.71)	45.99 (45.88-46.00)	45.98 (45.86-46.02)			
CTV						
V98(%)						
Head	99.92 (99.84-99.98)	99.55 (99.08-99.83)	99.71 (99.57-99.90)			
Body	99.96 (99.95-99.99)	99.94 (99.88-100.00)	100.00 (99.97-100.00)			
Stomach						
Dmax (GyE)						
Head	21.82 (12.21-29.23)	18.60 (11.50-28.98)	17.85 (11.48-28.97)	0.001	0.003	1.000
Body	30.93 (27.13-32.48)	33.08 (32.30-34.56)	32.36 (31.21-35.06)	0.012	0.063	1.000
Mean (GyE)						
Head	4.01 (1.83-6.53)	0.49 (0.26-1.61)	0.70 (0.24-2.28)	<0.001	0.001	1.000
Body	9.87 (6.62-11.30)	3.07 (1.55-6.39)	5.62 (2.42-8.19)	0.007	0.091	1.000
Duodenum						
Dmax(GyE)						
Head	35.39 (34.16-35.87)	32.62 (31.77-32.83)	31.94 (31.24-32.85)	0.001	<0.001	1.000
Body	25.52 (19.46-31.58)	25.26 (14.23-31.25)	26.32 (14.79-31.65)	0.607	0.607	0.607
Mean(GyE)						
Head	21.14 (18.18-23.56)	17.23 (14.15-17.79)	16.19 (14.23-18.57)	<0.001	0.005	1.000
Body	6.65 (5.18-8.55)	2.79 (1.55-3.62)	3.35 (1.53-3.89)	0.063	0.012	1.000
Intestine						
Dmax(GyE)						
Head	33.11 (31.66-35.26)	32.90 (32.06-34.75)	33.52 (32.88-35.02)	0.775	0.775	0.775
Body	32.21 (29.78-34.14)	32.84 (30.83-34.20)	32.94 (32.38-34.35)	0.311	0.311	0.311
Mean(GyE)						
Head	8.71 (7.89-10.44)	1.83 (1.07-2.88)	2.57 (1.19-3.70)	<0.001	0.010	0.233
Body	5.05 (3.52-7.79)	1.49 (0.98-2.13)	1.56 (1.12-2.29)	0.003	0.182	0.447
Kidneys						
Mean (GyE)						
Head	5.67 (4.63-5.83)	4.10 (3.08-5.42)	4.14 (3.75-5.01)	0.199	0.199	0.199
Body	4.11 (3.12-5.13)	3.52 (3.22-3.93)	3.02 (2.49-4.12)	0.607	0.607	0.607
Liver						
Mean (GyE)						
Head	3.62 (2.39-3.82)	0.48 (0.12-0.98)	0.43 (0.12-1.13)	<0.001	<0.001	1.000
Body	2.89 (2.68-3.85)	0.30 (0.24-0.55)	0.32 (0.24-0.84)	0.007	0.091	1.000
Spinal Cord						
Dmax						
Head	19.28 (15.46-19.98)	22.25 (19.79-24.39)	21.50 (18.54-23.02)	0.002	0.043	0.980
Body	11.32 (9.37-14.82)	17.82 (16.01-19.30)	18.42 (13.80-18.58)	0.028	0.028	1.000

VMAT, volumetric modulated arc therapy; IMPT, intensity modulated proton therapy; Mean, mean dose; HI, homogeneity index.

pancreas, three-field IMPT improved robustness in CTV (2.32 in three-field IMPT versus 2.47 in two-field IMPT, p=0.028) and the boost area (1.19 in three-field IMPT versus 1.32 in two-field IMPT, p=0.028). There was no statistical significance between two-field IMPT and three-field IMPT in OARs (all p>0.05).

3.3 NTCP Analysis

NTCP values of the stomach, duodenum, and intestine for VMAT, two-field IMPT, and three-field IMPT plans are shown in **Table 5** and **Figure 4**. When the tumor was at the head of the pancreas, both two- and three-field IMPT plans provided lower

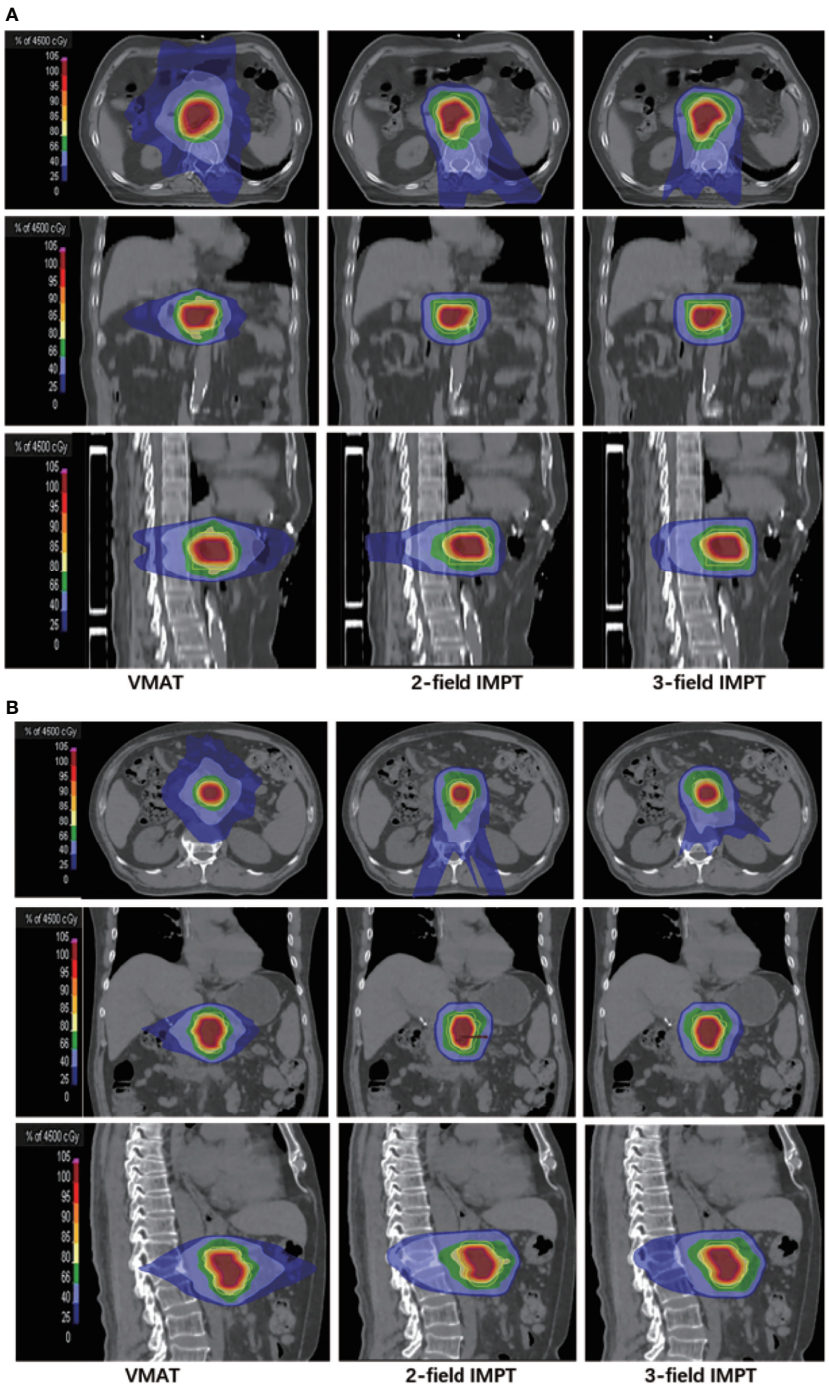

FIGURE 1 | Representative dose contributions for **(A)** tumor located in the head of the pancreas: left (VMAT), middle (two-field IMPT), right (three-field IMPT) patient #5; **(B)** tumor located in the body of the pancreas: left (VMAT), middle (two-field IMPT), right (three-field IMPT) in axial, sagittal, and coronal views, patient #14.

toxicity of gastric bleed for the stomach (median 2.68%, 1.62%) compared to VMAT (median 3.94%) (p=0.002 and p=0.001, respectively). The risk of grade ≥ 3 GI toxicity of the duodenum was also reduced from a median value of 4.61% with VMAT to 4.42% (two-field IMPT, p<0.001) and 4.38% (three-field IMPT, p=0.001). For the intestine, ulceration/perforation of the three treatment plans were 0.17, 0.10, and 0.18, respectively (all p>0.5). However, when the tumor was located in the body of the pancreas, VMAT provided a lower risk of gastric bleed for the stomach (median 8.67%) with two-field IMPT and three-field

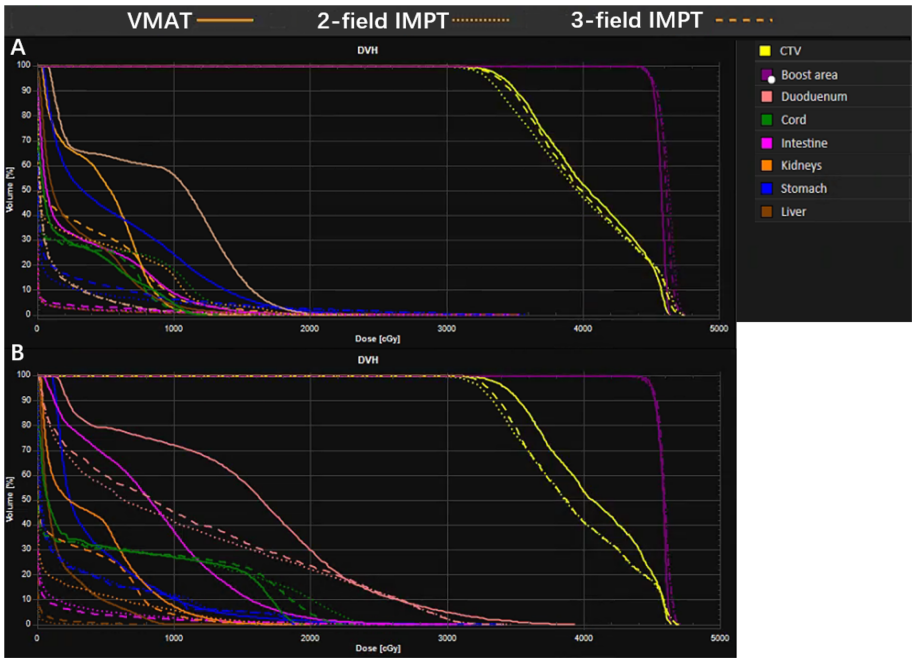

FIGURE 2 | A representative dose volume histogram (DVH) for VMAT, two-field IMPT, and three-field IMPT. **(A)** Tumor located in the head of the pancreas; data are from patient #5; **(B)** tumor located in the body of the pancreas; data are from patient #14.

TABLE 4 | Proton therapy robustness evaluation.

Structure	Target Location: Head of the pancreas			Target Location: Body of the pancreas		
	2-field IMPT AUC	3-field IMPT AUC	P value	2-field IMPT AUC	3-field IMPT AUC	P value
Boost area	1.25 (1.20-1.31)	1.02 (0.97-1.15)	0.021	1.32 (1.27-1.39)	1.19 (1.05-1.35)	0.028
CTV	2.48 (2.41-2.58)	2.32 (2.18-2.37)	0.002	2.47 (2.40-2.57)	2.32 (2.14-2.47)	0.028
Stomach	0.33 (0.20-0.63)	0.42 (0.21-0.73)	0.504	1.73 (1.06-2.71)	1.76 (1.20-2.64)	0.416
Duodenum	3.23 (0.47-1.12)	3.09 (2.94-3.18)	0.506	0.77 (0.75-0.87)	0.82 (0.78-0.89)	0.344
Intestine	0.88 (0.47-1.12)	0.92 (0.55-1.11)	0.239	0.55 (0.30-0.76)	0.57 (0.33-0.78)	0.104
Cords	0.81 (0.67-1.10)	0.70 (0.61-1.04)	0.009	0.58 (0.53-0.72)	0.52 (0.50-0.57)	0.131
Liver	0.10 (0.08-0.29)	0.10 (0.07-0.30)	0.859	0.17 (0.10-0.26)	0.18 (0.10-0.31)	0.343
Kidneys	0.73 (0.53-0.83)	0.71 (0.64-0.75)	0.754	0.58 (0.43-0.83)	0.59 (0.39-0.74)	0.917

IMPT, intensity modulated proton therapy; AUC, the area under root-mean-square deviation doses volume histograms curve; CTV, clinical target volume.

IMPT (median 12.83%, 16.32%), although statistical significance was not observed (all p>0.05). The risks of duodenum GI toxicity and ulceration/perforation of the intestine had no statistical significance between VMAT and two-field IMPT (all p>0.05). Besides, VMAT provided better NTCPs of ulceration/perforation (p=0.042) and diarrhea for the intestine (p=0.018). Comparing the two kinds of IMPT plans, all values of NTCP have nonexistent statistical significance (all p>0.05).

4 DISCUSSION

In the treatment of LAPC, the application of photon therapy is limited because sometimes it fails to deliver a high dose to the target due to the existence of many radiosensitive OARs around. Proton can address this problem due to its unique physical properties. Some studies have shown that proton therapy as part of CRT can achieve satisfying tumor control with low toxicity (29, 30). This study investigated the potential clinical benefits of utilizing the IMPT-SIB technique in the management of the LAPC population through a comprehensive dosimetric comparison among two- and three-field IMPT and VMAT. Under good CTV and boost area dose-coverage obtained from both the IMPT plans and the clinically used photon plans, the results showed that IMPT plans provided lower severe toxicity risks and maximum doses when the tumors were located in the head of the pancreas. However, when the target was located in the body of the pancreas, the clinical benefit of utilizing IMPT diminished due to range overshooting that resulted from the inferior dose conformality. More specifically, for the target located in the pancreatic head, two- or three-field IMPT-SIB reduced the

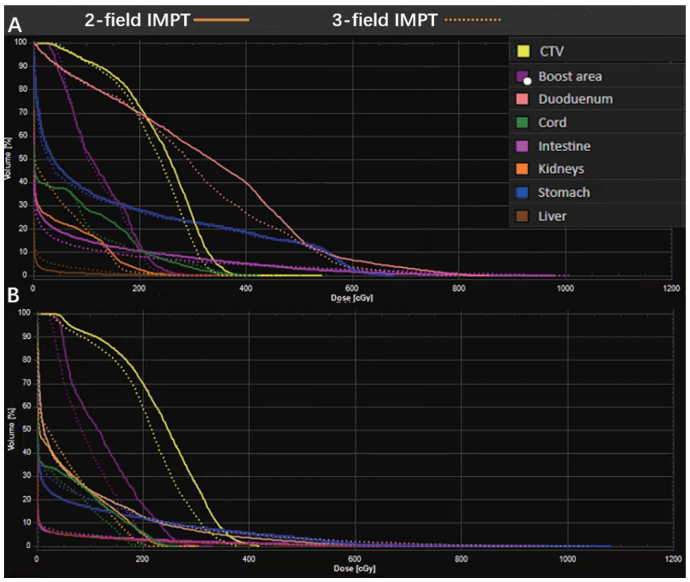

FIGURE 3 | A representative robustness evaluation using RVH: **(A)** tumor located in the head of the pancreas; data are for patient #5; **(B)** tumor located in the body of the pancreas; data are from patient #14.

TABLE 5 | NTCP value.

OAR	Endpoint	NTCP (%) [median and IQR]					
		Head of the pancreas			Body of the pancreas		
		VMAT	2-field IMPT	3-field IMPT	VMAT	2-field IMPT	3-field IMPT
Stomach	Gastric bleed	6.73 (0.70-14.83)	3.42 (0.54-11.98)†	2.59 (0.49-14.59)†	8.67 (5.13-11.34)	12.83 (9.93-16.10)	16.32 (11.58-18.50)
Duodenum	Grade ≥3 GI toxicity	4.88 (4.64-5.22)	4.55 (4.28-4.77)†	4.58 (4.45-4.71)†	3.58 (3.31-3.72)	3.56 (3.02-3.85)	3.50 (3.05-3.75)
Intestine	Ulceration/Perforation	0.56 (0.23-1.31)	0.27 (0.10-2.06)	0.35 (0.17-2.12)	0.05 (0.02-0.09)	0.05 (0.03-0.11)	0.10 (0.06-0.70)†
	Diarrhea	30.38 (26.52-32.37)	28.66 (26.48-33.88)	29.24 (27.50-33.99)	24.87 (23.47-26.17)	25.02 (24.36-26.7)	26.43 (25.73-30.44)†

OAR, organs at risk; IQR, Interquartile range; VMAT, volumetric modulated arc therapy; IMPT, intensity modulated proton therapy.
†Compare with VMAT p<0.05.

NTCPs of gastric bleed of the stomach and intestinal toxicity of grade 3 and above. For tumors located in the body of the pancreas, VMAT showed lower toxicity of the stomach while other NTCPs were similar. These findings indicated that the model-based approach for patient selection could be an option due to the complicated patient-specific anatomical position (31, 32).

Moreover, we investigated the impact of the beam number and arrangement on the quality of the proton treatment plan. As the degree of freedom increased, the three-field IMPT-SIB plan indeed improved the robustness of targets; but we found that for the OARs, for example, the Dmean of the stomach, intestine, and kidneys was increased due to more entrance dose, raising the chance for low-grade toxicities such as nausea and emesis using three-field IMPT-SIB (33, 34). These findings agreed with the study reported by Stefanowicz et al.; adding one to two beams had no profit in the Dmax and Dmean of OARs with two-field IMPT in pancreatic cancer (17). Adding more fields requires more delivery time and potentially introduces more intrafraction motion, which might undermine the accuracy of treatment delivery (35–37). It makes more fields of IMPT unfavorable or not clinically feasible. However, the recent breakthrough in the rotation arc treatment delivery or call spot-scanning arc therapy (SPArc) introduces more degrees of freedom while improving the treatment delivery efficiency, which is worthy of investigating in the management of LAPC (38). Such technique has shown to be potentially clinically beneficial to various disease sites, including prostate, lung, head, neck, and breast cancer (39).

The application of proton therapy in LAPC using SBRT still faces several challenges. Since organs such as the stomach and the small intestine have significant interfractionation uncertainties such as deformation and gas movement, the accuracy of beam delivery faces difficulties that are critical to the clinical implementation of SBRT (40). Thus, it limits the beam angle selection, which is mostly posterior or posterior oblique. Some portions of the intestine or the stomach are located behind the target, normally receiving a high dose due to the required margin to cover the range uncertainties. Dual-

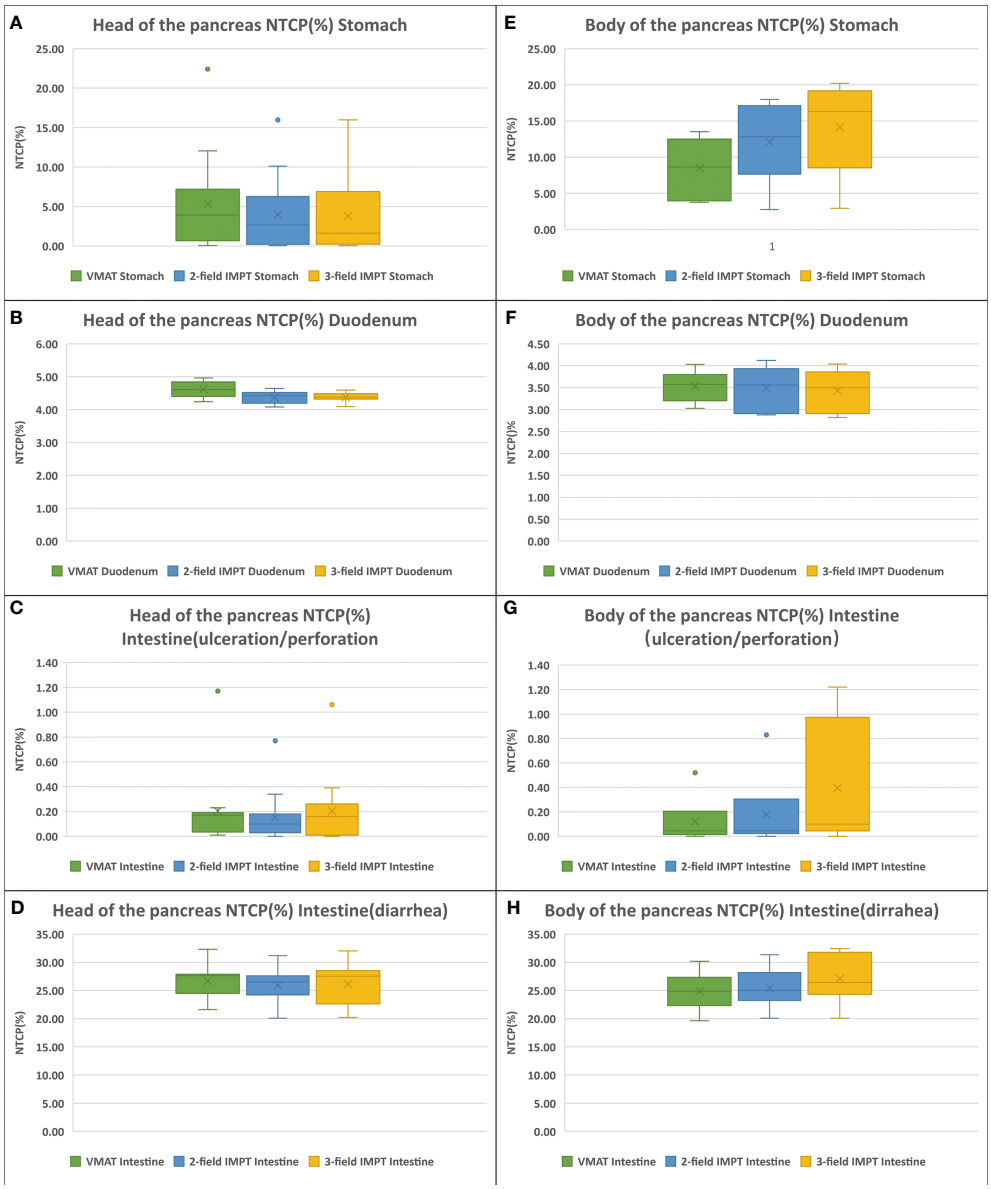

FIGURE 4 | NTCPs comparison of VMAT (green), two-field IMPT (blue), and three-field IMPT (yellow): **(A–D)** (the tumor located in the head of pancreas): ulceration/perforation for stomach, grade ≥ 3 GI toxicity for duodenum, gastric bleed for intestine, and diarrhea for intestine, respectively. **(E–H)** (the tumor located in the head of pancreas): the same order with **(A–D)**.

energy CT (DECT) might be able to help in reducing such range uncertainties and make the IMPT plan more conformal compared to the current limitation of using 3.5% range uncertainties (41). Motion mitigation strategies are also critical because the pancreas moves with breathing-induced motion (42). This study is based on the breath-hold technique, which effectively mitigates motion-induced uncertainties. However, such technique has its own limitation. For example, patient training might not work for the person who cannot stand with breath-hold or having an irregular respiratory rhythm that exceedingly prolongs treatment delivery. Gating and tracking would be a direction that we shall investigate in the treatment of LAPC (37). Furthermore, online adaptive MRI-guide radiotherapy will provide the possibility to control the dose distribution and migrate the dose to the OARs with diverse anatomical variations of GI organs such as the gas-filled intestine in the future (43).

Based on the study results, the potential future directions for proton application to LAPC might rely on the following two aspects. On one hand, maximum dose sparing for the stomach and bowel remains a challenge when using proton beam therapy, in which the target space between the intestine and tumors was

critical. It indicated that the application of the absorbable hydrogel spacer (TraceIT, Augmenix, Bedford, MA) to separate the head of the pancreas and duodenum could be useful in these cases (44). On the other hand, we should explore the feasibility of different-level dose escalation by increasing the probability of local target control while sparing the OARs utilizing new generation of treatment and planning techniques such as SPArc, minibeams, and functional image-guided dose painting (39, 45, 46).

There are still several potential limitations to our study. The RBE value we used was 1.1, which is the current clinical standard (20). However, recent studies implied that the value of RBE varied depending on the different positions of the SOBP. With the increasing linear energy transfer (LET), the RBE value could reach 1.15–1.7 at the distal edge of the Bragg peak, even 4–6 in the fall-off part (47). For the general anterior beam of the pancreatic cancer plan, the distal edge is generally near the intestine or the stomach. This uncertainty might affect the potential clinical benefits of utilizing the proton beam therapy. The outcomes of proton NTCPs may be reevaluated in the future. To mitigate such RBE uncertainty, the first step is to control better the LET distribution, which could lead to the clinical implementation of the LET optimization algorithm (48, 49).

Besides, the outcomes of our studies rely on the accuracy of the three NTCP models we applied. Please note that the absolute values of $\triangle$NTCPs for the duodenum (grade $\geq$ 3 GI toxicity) and the intestine (diarrhea) are small. These differences may not be observed in the clinical outcome study due to the uncertainties and variance of the NTCP model itself. However, the trend of the OAR protection from different treatment modalities and planning strategies might give clinical users a hint to further improve the dosimetric plan quality.

CONCLUSION

We have compared the SBRT-SIB plan quality and potential clinical benefits between VMAT, two-field IMPT, and three-field IMPT based on the NTCP model. In the current stage, two-field IMPT is a better option for LAPC patients whose tumor is located in the head. It could provide lower severe toxicity for the stomach and duodenum. However, VMAT is preferred for the body with better protection for the possibility of gastric bleed. Potentially, the model-based approach for patient selection could be an option due to the complicated patient-specific anatomical position.

DATA AVAILABILITY STATEMENT

The raw data supporting the conclusions of this article will be made available by the authors, without undue reservation.

ETHICS STATEMENT

Written informed consent was obtained from the individual(s) for the publication of any potentially identifiable images or data included in this article.

AUTHOR CONTRIBUTIONS

Study conception and design: X-SG, XD, and PLL. Data acquisition: MX, ZW, FL, SYS, and CHJ. Data and statistical analysis: PL and XD. Drafting of the manuscript: PL, XC, and XML. Critical editorial and writing contributions: XD, X-SG, and XC. All authors contributed to the article and approved the submitted version.

FUNDING

This work was supported by the China International Medical Foundation (Grant Number: 2019-N-11-07).

ACKNOWLEDGMENTS

We are grateful to the funding of China International Medical Foundation (Grant Number: 2019-N-11-07).

REFERENCES

1. Siegel RL, Miller KD, Jemal A. Cancer Statistics, 2020. *CA Cancer J Clin* (2020) 70(1):7–30. doi: 10.3322/caac.21590
2. Chen W, Zheng R, Baade PD, Zhang S, Zeng H, Bray F, et al. Cancer Statistics in China, 2015. *CA Cancer J Clin* (2016) 66(2):115–32. doi: 10.3322/caac.21338
3. Vincent A, Herman J, Schulick R, Hruban RH, Goggins M. Pancreatic Cancer. *Lancet* (2011) 378(9791):607–20. doi: 10.1016/s0140-6736(10)62307-0
4. Zhong J, Patel K, Switchenko J, Cassidy RJ, Hall WA, Gillespie T, et al. Outcomes for Patients With Locally Advanced Pancreatic Adenocarcinoma Treated With Stereotactic Body Radiation Therapy *Versus* Conventionally Fractionated Radiation. *Cancer* (2017) 123(18):3486–93. doi: 10.1002/cncr.30706
5. Tchelebi LT, Lehrer EJ, Trifiletti DM, Sharma NK, Gusani NJ, Crane CH, et al. Conventionally Fractionated Radiation Therapy Versus Stereotactic Body Radiation Therapy for Locally Advanced Pancreatic Cancer (CRiSP): An International Systematic Review and Meta-Analysis. *Cancer* (2020) 126 (10):2120–31. doi: 10.1002/cncr.32756
6. Tempero MA, Malafa MP, Al-Hawary M, Behrman SW, Benson AB, Cardin DB, et al. Pancreatic Adenocarcinoma, Version 2.2021, NCCN Clinical Practice Guidelines in Oncology. *J Natl Compr Canc Netw* (2021) 19 (4):439–57. doi: 10.6004/jnccn.2021.0017
7. Cellini F, Arcelli A, Simoni N, Caravatta L, Buwenge M, Calabrese A, et al. Basics and Frontiers on Pancreatic Cancer for Radiation Oncology: Target Delineation, SBRT, SIB Technique, MRgRT, Particle Therapy, Immunotherapy and Clinical Guidelines. *Cancers (Basel)* (2020) 12(7):1729. doi: 10.3390/cancers12071729
8. Shaib WL, Hawk N, Cassidy RJ, Chen Z, Zhang C, Brutcher E, et al. A Phase 1 Study of Stereotactic Body Radiation Therapy Dose Escalation for Borderline Resectable Pancreatic Cancer After Modified FOLFIRINOX (Nct01446458). *Int J Radiat Oncol Biol Phys* (2016) 96(2):296–303. doi: 10.1016/j.ijrobp.2016.05.010

9. Tobias CA, Blakely EA, Alpen EL, Castro JR, Ainsworth EJ, Curtis SB, et al. Molecular and Cellular Radiobiology of Heavy Ions. *Int J Radiat Oncol Biol Phys* (1982) 8(12):2109–20. doi: 10.1016/0360-3016(82)90554-5
10. Indelicato DJ, Rotondo RL, Uezono H, Sandler ES, Aldana PR, Ranalli NJ, et al. Outcomes Following Proton Therapy for Pediatric Low-Grade Glioma. *Int J Radiat Oncol Biol Phys* (2019) 104(1):149–56. doi: 10.1016/j.ijrobp.2019.01.078
11. Lidestahl A, Mondlane G, Gubanski M, Lind PA, Siegbahn A. An *in Silico* Planning Study Comparing Doses and Estimated Risk of Toxicity in 3D-CRT, IMRT and Proton Beam Therapy of Patients With Thymic Tumours. *Phys Med* (2019) 60:120–6. doi: 10.1016/j.ejmp.2019.03.028
12. Hoppe BS, Nichols RC, Flampouri S, Li Z, Morris CG, Pham DC, et al. Hypofractionated Proton Therapy With Concurrent Chemotherapy for Locally Advanced Non-Small Cell Lung Cancer: A Phase 1 Trial From the University of Florida and Proton Collaborative Group. *Int J Radiat Oncol Biol Phys* (2020) 107(3):455–61. doi: 10.1016/j.ijrobp.2020.03.015
13. Ding X, Dionisi F, Tang S, Ingram M, Hung CY, Prionas E, et al. A Comprehensive Dosimetric Study of Pancreatic Cancer Treatment Using Three-Dimensional Conformal Radiation Therapy (3DCRT), Intensity-Modulated Radiation Therapy (IMRT), Volumetric-Modulated Radiation Therapy (VMAT), and Passive-Scattering and Modulated-Scanning Proton Therapy (PT). *Med Dosim* (2014) 39(2):139–45. doi: 10.1016/j.meddos.2013.11.005
14. Thompson RF, Mayekar SU, Zhai H, Both S, Apisarnthanarax S, Metz JM, et al. A Dosimetric Comparison of Proton and Photon Therapy in Unresectable Cancers of the Head of Pancreas. *Med Phys* (2014) 41 (8):081711. doi: 10.1118/1.4887797
15. Raturi VP, Tochinai T, Hojo H, Rachi T, Hotta K, Nakamura N, et al. Dose-Volume and Radiobiological Model-Based Comparative Evaluation of the Gastrointestinal Toxicity Risk of Photon and Proton Irradiation Plans in Localized Pancreatic Cancer Without Distant Metastasis. *Front Oncol* (2020) 10:517061. doi: 10.3389/fonc.2020.517061
16. Brunner TB, Haustermans K, Huguet F, Morganti AG, Mukherjee S, Belka C, et al. ESTRO ACROP Guidelines for Target Volume Definition in Pancreatic Cancer. *Radiother Oncol* (2021) 154:60–9. doi: 10.1016/j.radonc.2020.07.052
17. Stefanowicz S, Stutzer K, Zschaeck S, Jakobi A, Troost EGC. Comparison of Different Treatment Planning Approaches for Intensity-Modulated Proton Therapy With Simultaneous Integrated Boost for Pancreatic Cancer. *Radiat Oncol* (2018) 13(1):228. doi: 10.1186/s13014-018-1165-0
18. Oar A, Lee M, Le H, Hruby G, Dalfsen R, Pryor D, et al. Australasian Gastrointestinal Trials Group (AGITG) and Trans-Tasman Radiation Oncology Group (TROG) Guidelines for Pancreatic Stereotactic Body Radiation Therapy (SBRT). *Pract Radiat Oncol* (2020) 10(3):e136–46. doi: 10.1016/j.prro.2019.07.018
19. Sawakuchi GO, Titt U, Mirkovic D, Mohan R. Density Heterogeneities and the Influence of Multiple Coulomb and Nuclear Scatterings on the Bragg Peak Distal Edge of Proton Therapy Beams. *Phys Med Biol* (2008) 53(17):4605–19. doi: 10.1088/0031-9155/53/17/010
20. Paganetti H, van Luijk P. Biological Considerations When Comparing Proton Therapy With Photon Therapy. *Semin Radiat Oncol* (2013) 23(2):77–87. doi: 10.1016/j.semradonc.2012.11.002
21. Semenenko VA, Reitz B, Day E, Qi XS, Miften M, Li XA. Evaluation of a Commercial Biologically Based IMRT Treatment Planning System. *Med Phys* (2008) 35(12):5851–60. doi: 10.1118/1.3013556
22. Liu W, Mohan R, Park P, Liu Z, Li H, Li X, et al. Dosimetric Benefits of Robust Treatment Planning for Intensity Modulated Proton Therapy for Base-of-Skull Cancers. *Pract Radiat Oncol* (2014) 4(6):384–91. doi: 10.1016/j.prro.2013.12.001
23. Liu W, Frank SJ, Li X, Li Y, Park PC, Dong L, et al. Effectiveness of Robust Optimization in Intensity-Modulated Proton Therapy Planning for Head and Neck Cancers. *Med Phys* (2013) 40(5):051711. doi: 10.1118/1.4801899
24. Kutcher GJ, Burman C. Calculation of Complication Probability Factors for non-Uniform Normal Tissue Irradiation: The Effective Volume Method. *Int J Radiat Oncol Biol Phys* (1989) 16(6):1623–30. doi: 10.1016/0360-3016(89)90972-3
25. Reinartz G, Baehr A, Kittel C, Oertel M, Haverkamp U, Eich HT. Biophysical Analysis of Acute and Late Toxicity of Radiotherapy in Gastric Marginal Zone Lymphoma-Impact of Radiation Dose and Planning Target Volume. *Cancers (Basel)* (2021) 13(6):1390. doi: 10.3390/cancers13061390
26. Burman C, Kutcher GJ, Emami B, Goitein M. Fitting of Normal Tissue Tolerance Data to an Analytic Function. *Int J Radiat Oncol Biol Phys* (1991) 21 (1):123–35. doi: 10.1016/0360-3016(91)90172-z
27. Holyoake DLP, Aznar M, Mukherjee S, Partridge M, Hawkins MA. Modelling Duodenum Radiotherapy Toxicity Using Cohort Dose-Volume-Histogram Data. *Radiother Oncol* (2017) 123(3):431–7. doi: 10.1016/j.radonc.2017.04.024
28. Pan CC, Dawson LA, McGinn CJ, Lawrence TS, Ten Haken RK. Analysis of Radiation-Induced Gastric and Duodenal Bleeds Using the Lyman-Kutcher-Burman Model. *Int J Radiat OncologyBiologyPhysics* (2003) 57(2):S217–S8. doi: 10.1016/s0360-3016(03)01031-9
29. Shimomura O, Oda T, Hashimoto S, Doi M, Hiroshima Y, Numajiri H, et al. Survival Impact on Triple-Modal Strategy Comprising Hyperthermia, External Radiation, and Chemotherapy for Unresectable Locally Advanced (UR-LA) Pancreatic Ductal Adenocarcinoma. *Surg Oncol* (2021) 37:101542. doi: 10.1016/j.suronc.2021.101542
30. Terashima K, Demizu Y, Hashimoto N, Jin D, Mima M, Fujii O, et al. A Phase I/II Study of Gemcitabine-Concurrent Proton Radiotherapy for Locally Advanced Pancreatic Cancer Without Distant Metastasis. *Radiother Oncol* (2012) 103(1):25–31. doi: 10.1016/j.radonc.2011.12.029
31. Gandhi SJ, Liang X, Ding X, Zhu TC, Ben-Josef E, Plastaras JP, et al. Clinical Decision Tool for Optimal Delivery of Liver Stereotactic Body Radiation Therapy: Photons Versus Protons. *Pract Radiat Oncol* (2015) 5(4):209–18. doi: 10.1016/j.prro.2015.01.004
32. Brodin NP, Kabarriti R, Pankuch M, Schechter CB, Gondi V, Kalnicki S, et al. A Quantitative Clinical Decision-Support Strategy Identifying Which Patients With Oropharyngeal Head and Neck Cancer May Benefit the Most From Proton Radiation Therapy. *Int J Radiat Oncol Biol Phys* (2019) 104(3):540–52. doi: 10.1016/j.ijrobp.2018.11.039
33. Kelly P, Das P, Pinnix CC, Beddar S, Briere T, Pham M, et al. Duodenal Toxicity After Fractionated Chemoradiation for Unresectable Pancreatic Cancer. *Int J Radiat Oncol Biol Phys* (2013) 85(3):e143–9. doi: 10.1016/j.ijrobp.2012.09.035
34. Nakamura A, Shibuya K, Matsuo Y, Nakamura M, Shiinoki T, Mizowaki T, et al. Analysis of Dosimetric Parameters Associated With Acute Gastrointestinal Toxicity and Upper Gastrointestinal Bleeding in Locally Advanced Pancreatic Cancer Patients Treated With Gemcitabine-Based Concurrent Chemoradiotherapy. *Int J Radiat Oncol Biol Phys* (2012) 84 (2):369–75. doi: 10.1016/j.ijrobp.2011.12.026
35. Seco J, Robertson D, Trofimov A, Paganetti H. Breathing Interplay Effects During Proton Beam Scanning: Simulation and Statistical Analysis. *Phys Med Biol* (2009) 54(14):N283–N94. doi: 10.1088/0031-9155/54/14/n01
36. Gorgisyan J, Munck Af Rosenschold P, Perrin R, Persson GF, Josipovic M, Belosi MF, et al. Feasibility of Pencil Beam Scanned Intensity Modulated Proton Therapy in Breath-Hold for Locally Advanced Non-Small Cell Lung Cancer. *Int J Radiat Oncol Biol Phys* (2017) 99(5):1121–8. doi: 10.1016/j.ijrobp.2017.08.023
37. Bert C, Durante M. Motion in Radiotherapy: Particle Therapy. *Phys Med Biol* (2011) 56(16):R113–44. doi: 10.1088/0031-9155/56/16/R01
38. Ding X, Zhou J, Li X, Blas K, Liu G, Wang Y, et al. Improving Dosimetric Outcome for Hippocampus and Cochlea Sparing Whole Brain Radiotherapy Using Spot-Scanning Proton Arc Therapy. *Acta Oncol* (2019) 58(4):483–90. doi: 10.1080/0284186X.2018.1555374
39. Ding X, Li X, Zhang JM, Kabolizadeh P, Stevens C, Yan D. Spot-Scanning Proton Arc (SPArc) Therapy: The First Robust and Delivery-Efficient Spot-Scanning Proton Arc Therapy. *Int J Radiat Oncol Biol Phys* (2016) 96 (5):1107–16. doi: 10.1016/j.ijrobp.2016.08.049
40. Kim TG, Kang KM, Park B, Park J, Song YG, Kim KM, et al. Interfractional Diaphragmatic Position Variation According to Stomach Volume Change During Respiratory-Gated Radiotherapy for Hepatocellular Carcinoma. *Med Phys* (2021). doi: 10.1002/mp.15055
41. Bär E, Lalonde A, Royle G, Lu H-M, Bouchard H. The Potential of Dual-Energy CT to Reduce Proton Beam Range Uncertainties. *Med Phys* (2017) 44 (6):2332–44. doi: 10.1002/mp.12215
42. Lens E, van der Horst A, Versteijne E, Bel A, van Tienhoven G. Considerable Pancreatic Tumor Motion During Breath-Holding. *Acta Oncol* (2016) 55 (11):1360–8. doi: 10.1080/0284186X.2016.1221532
43. Boldrini L, Cusumano D, Cellini F, Azario L, Mattiucci GC, Valentini V. Online Adaptive Magnetic Resonance Guided Radiotherapy for Pancreatic

Cancer: State of the Art, Pearls and Pitfalls. *Radiat Oncol* (2019) 14(1):71. doi: 10.1186/s13014-019-1275-3
44. Rao AD, Feng Z, Shin EJ, He J, Waters KM, Coquia S, et al. A Novel Absorbable Radiopaque Hydrogel Spacer to Separate the Head of the Pancreas and Duodenum in Radiation Therapy for Pancreatic Cancer. *Int J Radiat Oncol Biol Phys* (2017) 99(5):1111–20. doi: 10.1016/j.ijrobp.2017.08.006
45. Charyyev S, Artz M, Szalkowski G, Chang CW, Stanforth A, Lin L, et al. Optimization of Hexagonal-Pattern Minibeams for Spatially Fractionated Radiotherapy Using Proton Beam Scanning. *Med Phys* (2020) 47(8):3485–95. doi: 10.1002/mp.14192
46. Alber M, Thorwarth D. Multi-Modality Functional Image Guided Dose Escalation in the Presence of Uncertainties. *Radiother Oncol* (2014) 111 (3):354–9. doi: 10.1016/j.radonc.2014.04.016
47. Luhr A, von Neubeck C, Krause M, Troost EGC. Relative Biological Effectiveness in Proton Beam Therapy - Current Knowledge and Future Challenges. *Clin Transl Radiat Oncol* (2018) 9:35–41. doi: 10.1016/j.ctro.2018.01.006
48. Bertolet A, Cortes-Giraldo MA, Souris K, Carabe A. A Kernel-Based Algorithm for the Spectral Fluence of Clinical Proton Beams to Calculate Dose-Averaged LET and Other Dosimetric Quantities of Interest. *Med Phys* (2020) 47(6):2495–505. doi: 10.1002/mp.14108
49. Li X, Ding X, Zheng W, Liu G, Janssens G, Souris K, et al. Linear Energy Transfer Incorporated Spot-Scanning Proton Arc Therapy Optimization: A Feasibility Study. *Front Oncol* (2021) 11:698537. doi: 10.3389/fonc.2021.698537

Conflict of Interest: The authors declare that the research was conducted in the absence of any commercial or financial relationships that could be construed as a potential conflict of interest.

Publisher's Note: All claims expressed in this article are solely those of the authors and do not necessarily represent those of their affiliated organizations, or those of the publisher, the editors and the reviewers. Any product that may be evaluated in this article, or claim that may be made by its manufacturer, is not guaranteed or endorsed by the publisher.

frontiers in Oncology

ERRATUM
published: 04 January 2022
doi: 10.3389/fonc.2021.836410

Erratum: Investigate the Dosimetric and Potential Clinical Benefits Utilizing Stereotactic Body Radiation Therapy With Simultaneous Integrated Boost Technique for Locally Advanced Pancreatic Cancer: A Comparison Between Photon and Proton Beam Therapy

*Frontiers Production Office**

Frontiers Media SA, Lausanne, Switzerland

OPEN ACCESS

Approved by:
Frontiers Editorial Office, Frontiers Media SA, Switzerland

***Correspondence:**
Frontiers Production Office
production.office@frontiersin.org

Specialty section:
This article was submitted to Cancer Imaging and Image-directed Interventions, a section of the journal Frontiers in Oncology

Received: *15 December 2021*
Accepted: *15 December 2021*
Published: *04 January 2022*

Citation:
Frontiers Production Office (2022) Erratum: Investigate the Dosimetric and Potential Clinical Benefits Utilizing Stereotactic Body Radiation Therapy With Simultaneous Integrated Boost Technique for Locally Advanced Pancreatic Cancer: A Comparison Between Photon and Proton Beam Therapy. Front. Oncol. 11:836410. doi: 10.3389/fonc.2021.836410

Keywords: normal tissue complication probability (NTCP), stereotactic body radiation therapy (SBRT), simultaneous integrated boost (SIB), pancreatic cancer, intensity modulated proton therapy (IMPT), volumetric modulated arc therapy (VMAT)

An erratum on

Investigate the Dosimetric and Potential Clinical Benefits Utilizing Stereotactic Body Radiation Therapy With Simultaneous Integrated Boost Technique for Locally Advanced Pancreatic Cancer: A Comparison Between Photon and Proton Beam Therapy

By Liu P, Gao X-s, Wang Z, Li X, Xi C, Jia C, Xie M, Lyu F, Shang S and Ding X (2021) Front. Oncol. 11:747532. doi: 10.3389/fonc.2021.747532

Due to a production error, "Shiyu Shang" was not included as an author in the published article. The corrected affiliations appear below.

Peilin Liu[1], Xian-shu Gao[1*], Zishen Wang[2], Xiaomei Li[1], Xi Cao[1], Chenghao Jia[1], Mu Xie[1], Feng Lyu[1], Shiyu Shang[3] and Xuanfeng Ding[4*]

1 Department of Radiation Oncology, Peking University First Hospital, Beijing, China,

2 Department of Radiation Oncology, Hebei Yizhou Tumor Hospital, Zhuozhou, China,

3 Department of Oncology, Hebei North University, Shijiazhuang, China,

4 Department of Radiation Oncology, Beaumont Health, Proton Beam Therapy Center, Royal Oak, MI, United States

The corrected Author Contributions Statement appears below.

"Study conception and design: X-SG, XD, and PLL. Data acquisition: MX, ZW, FL, SYS, and CHJ. Data and statistical analysis: PL and XD. Drafting of the manuscript: PL, XC, and XML. Critical editorial and writing contributions: XD, X-SG, and XC. All authors contributed to the article and approved the submitted version."

Additionally, author Xi Cao was mistakenly captured as Cao Xi. This error has now been corrected.

The publisher apologizes for these mistakes. The original version of this article has been updated.

frontiers in Oncology

ORIGINAL RESEARCH
published: 25 January 2022
doi: 10.3389/fonc.2021.812993

Predicting Disease-Free Survival With Multiparametric MRI-Derived Radiomic Signature in Cervical Cancer Patients Underwent CCRT

Bing Liu[1†], Zhen Sun[2†], Zi-Liang Xu[1], Hong-Liang Zhao[1], Di-Di Wen[1], Yong-Ai Li[3], Fan Zhang[4], Bing-Xin Hou[5], Yi Huan[1], Li-Chun Wei[5*] and Min-Wen Zheng[1*]*

[1] Department of Radiology, Xijing Hospital, Airforce Military Medical University, Xi'an, China, [2] Department of Orthopaedics, Xijing Hospital, Airforce Military Medical University, Xi'an, China, [3] Department of Radiology, Jinshan Hospital, Fudan University, Shanghai, China, [4] Department of Radiology, Shanxi Traditional Chinese Medical Hospital, Taiyuan, China, [5] Department of Radiation Oncology, Xijing Hospital, Airforce Military Medical University, Xi'an, China

Prognostic biomarkers that can reliably predict the disease-free survival (DFS) of locally advanced cervical cancer (LACC) are needed for identifying those patients at high risk for progression, who may benefit from a more aggressive treatment. In the present study, we aimed to construct a multiparametric MRI-derived radiomic signature for predicting DFS of LACC patients who underwent concurrent chemoradiotherapy (CCRT).

Methods: This multicenter retrospective study recruited 263 patients with International Federation of Gynecology and Obetrics (FIGO) stage IB-IVA treated with CCRT for whom pretreatment MRI scans were performed. They were randomly divided into two groups: primary cohort (n = 178) and validation cohort (n = 85). The LASSO regression and Cox proportional hazard regression were conducted to construct the radiomic signature (RS). According to the cutoff of the RS value, patients were dichotomized into low- and high-risk groups. Pearson's correlation and Kaplan–Meier analysis were conducted to evaluate the association between the RS and DFS. The RS, the clinical model incorporating FIGO stage and lymph node metastasis by the multivariate Cox proportional hazard model, and a combined model incorporating RS and clinical model were constructed to estimate DFS individually.

Results: The final radiomic signature consisted of four radiomic features: $T2W_{\_wavelet\text{-}LH\_glszm\_Size\ Zone\ NonUniformity}$, $ADC_{\_wavelet\text{-}HL\text{-}first\ order\_\ Median}$, $ADC_{\_wavelet\text{-}HH\text{-}glrlm\_Long\ Run\ Low\ Gray\ Level\ Emphasis}$, and $ADC_{\_wavelet\ \_LL\_gldm\_Large\ Dependence\ High\ Gray\ Emphasis}$. Higher RS was significantly associated with worse DFS in the primary and validation cohorts (both $p<0.001$). The RS demonstrated better prognostic performance in predicting DFS than the clinical model in both cohorts (C-index, 0.736–0.758 for RS, and 0.603–0.649 for clinical model). However, the combined model showed no significant improvement (C-index, 0.648, 95% CI, 0.571–0.685).

OPEN ACCESS

Edited by:
Marco Durante, Helmholtz Association of German Research Centres (HZ), Germany

Reviewed by:
Beth Ann Erickson, Medical College of Wisconsin, United States
Valerio Gallotta, Agostino Gemelli University Polyclinic (IRCCS), Italy

***Correspondence:**
Yi Huan
huanyi3000@163.com
Li-Chun Wei
weilichun@fmmu.edu.cn
Min-Wen Zheng
zhengmw2007@fmmu.edu.cn

[†]These authors have contributed equally to this work

Specialty section:
This article was submitted to Cancer Imaging and Image-directed Interventions, a section of the journal Frontiers in Oncology

Received: *11 November 2021*
Accepted: *30 December 2021*
Published: *25 January 2022*

Citation:
Liu B, Sun Z, Xu Z-L, Zhao H-L, Wen D-D, Li Y-A, Zhang F, Hou B-X, Huan Y, Wei L-C and Zheng M-W (2022) Predicting Disease-Free Survival With Multiparametric MRI-Derived Radiomic Signature in Cervical Cancer Patients Underwent CCRT. Front. Oncol. 11:812993. doi: 10.3389/fonc.2021.812993

Conclusions: The present study indicated that the multiparametric MRI-derived radiomic signature could be used as a non-invasive prognostic tool for predicting DFS in LACC patients.

Keywords: locally advanced cervical cancer, concurrent chemoradiotherapy, multiparametric magnetic resonance imaging, disease-free survival, radiomics

INTRODUCTION

Cervical cancer is one of the most frequent malignancies in women, with over 604,000 new cases annually worldwide, associated with 342,000 deaths in 2020 (1). For patients diagnosed with locally advanced cervical cancer (LACC), concurrent chemoradiotherapy (CCRT) including pelvic external beam radiotherapy (EBRT), cisplatin-based chemotherapy, and brachytherapy, was the primary choice. However, about 1/3 patients suffer treatment failure; they experience unnecessary treatment-related complications and low locoreginal control rates, which worsen the prognosis (2). Usual clinical features and standard exploitation of imaging fail to deliver actionable predictive models with sufficient accuracy in cervical cancer (3, 4). Improving the patients' risk stratification in order to individualize the treatment or surveillance schemes in cervical cancer patients would fulfill an unmet clinical need.

Magnetic resonance imaging (MRI) is recognized as the first-line image modality for diagnosing, staging, treatment planning, treatment response evaluating, and monitoring during the whole process for LACC patients (5, 6). Radiomics is an emerging field that reflects spatial and temporal heterogeneity of tumors, *via* the extraction of high-dimensional quantitative features from clinically accessibly commonly performed medical images using automated data mining algorithms, with the aim to support clinical decision-making (7–9). Previous radiomic studies in cancer have shown the potential to discover hidden information that was inaccessible with single-parameter approaches (9). For early-stage cervical cancer patients who underwent radical hysterectomy, radiomic features could predict patients' survival with high accuracy (10). Nevertheless, whether the multiparametric MRI-derived radiomic features could be used to predict survival in LACC patients underwent CCRT remains uncertain.

Therefore, the aim of this study was to develop a radiomic signature by pretreatment MRI and evaluate the performance of different models to predict DFS in LACC patients.

Abbreviations: MRI, magnetic resonance imaging; DFS, disease-free survival; FIGO, International Federation of Gynecology and Obstetrics; LASSO, least absolute shrinkage and selection operator; PET/CT, positron emission tomography-computed tomography; T2W, T2-weighted; ADC, apparent diffusion coefficient; DWI, diffusion-weighted imaging; DICOM, Digital Imaging and Communications in Medicine; PACS, picture archiving and communication system; ROI, regions of interest; LACC, locally advanced cervical cancer; ROC, receiver-operating characteristic; AUC, area under the curve.

METHODS

Patients

The hospital ethics review board approved this study; written informed consent was not required for this retrospective study. All procedures performed in the study involving human participants were in accordance with the 1964 Helsinki declaration and its later amendments.

This retrospective study included patients with biopsy-confirmed locally advanced cervical cancer from three tertiary centers in different parts of China (Xijing Hospital, Shanxi Traditional Chinese Medical Hospital, and Jinshan Hospital) between October 1, 2014, and December 1, 2017. The patients' baseline demographics, laboratory test results, pretreatment MRI images, pathological results, and survival outcome were reviewed. All patients were enrolled with strict inclusion and exclusion criteria, which are shown as follows:

Inclusion criteria

1) primary cervical cancer confirmed *via* biopsy;

2) locally advanced disease (Federation of Gynecology and Obstetrics [FIGO] stage IB-IVA) determined based on pretreatment MRI of the pelvis;

3) patients underwent pelvic MRI scans within a 2-week period before CCRT started;

3) the largest diameter of the cervical mass was 1.0 cm or larger;

4) age of 18–75 years;

5) no other treatment before MRI scan;

6) finished the entire CCRT treatment.

Exclusion criteria

1) patients with a history of cancer <5 years;

2) patients with insufficient clinical and/or follow-up data.

Finally, 263 patients were recruited in this study. **Figure 1** displays the patient selection flowchart from the three hospitals. Eligible patients were randomly divided into a primary cohort (n = 178) and an independent validation cohort (n = 85) at a ratio of 2:1.

CCRT Treatments and Follow-Up

All patients were treated with a combination of external beam radiotherapy (EBRT) and intracavitary brachytherapy (ICBT). EBRT was delivered to the whole pelvis with 15-MV photon beams at a daily dose of 2 Gy, 5 times per week, for a total dose of 50 Gy. EBRT was accompanied by concurrent chemotherapy: six cycles of weekly cisplatin (30 mg/mm^2) in 30 patients and three cycles of 5-fluorouracil (1,000 mg/mm^2) plus cisplatin (60 mg/mm^2) at 3-week intervals in 18 patients. ICBT was delivered twice a week in 4 fractions with a fractional dose of 7 Gy at point A. the median overall treatment time was 59 days (range 45–71

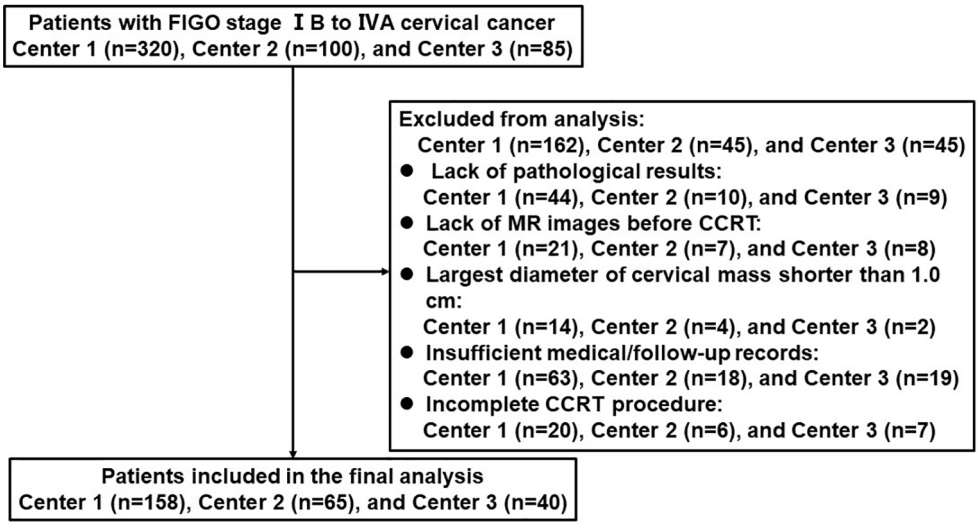

FIGURE 1 | Flow diagram of patient enrollment.

days). The selection of the chemotherapeutic regime was individualized according to local tumor extent, pelvic lymph node involvement, and general patient condition (11).

Regular follow-up was conducted every 3 months during the first 2 years after treatment, 2 times annually for 3–5 years, and once a year thereafter or as clinically indicated. The endpoint of our study was DFS, which is defined as the period from the date of CCRT completion to the date of the first locoregional recurrence, distant metastasis, death, or the last visit in follow-up. Locoregional recurrences and distant metastasis were confirmed by gynecological examination and imaging modalities such as CT, MRI, and PET/CT. Available information was collected from patients' medical records.

MR Image Acquisitions

Pelvic MRI scans were conducted before the biopsy to avoid the impact of inflammation. All patients underwent pelvic MRI protocol that include T2WI and DWI with two b values (0 and 800 s/mm^2). ADC maps were automatically generated and included both b values in a mono-exponential decay model. The MRI images were obtained by different MRI devices at three institutions. Detailed MRI acquisition parameters are presented in **Supplementary Methods 1**.

Radiomic Analyses

The radiomic analysis workflow included five steps as illustrated in **Figure 2**: tumor image segmentation, radiomic feature extraction, feature selection, radiomic signature construction, and validation.

Tumor Image Segmentation

The open-source ITK-SNAP software was used for three-dimensional manual segmentation. The regions of interest (ROIs) were delineated manually on each slice obtained in T2WI and ADC (delineated on DWI images with a b value of 800 s/mm2 and then copied to the corresponding ADC maps). Three radiologists with at least 3 years' experience in gynecological MR imaging interpretation were chiefly responsible for the evaluation of tumor masking. To ensure reproducibility, each radiologist repeated the tumor segmentation and generation of radiomic features twice with an interval of at least 1 month, following the same procedure. To ensure the accuracy of tumor segmentation, the tumor masks were validated by a senior radiologist with 10 years of experience in segmentation result validation.

Radiomic Feature Extraction

All images of each MRI scan for each patient were normalized separately using Z-scores to obtain a standard and normal distribution of image intensity. Then, we extracted radiomic features from T2WI and ADC respectively through an open-source package PyRadiomics, to extract 120 dimensional radiomic features of the segmented lesions. We extracted the following radiomics features: 19 first-order statistics features, 16 shape-based 3D features, 10 shape-based 2D features, 24 gray-level co-occurrence features, 16 gray-level run-length features, 16 gray-level size zone features, five neighboring gray tone difference features, and 14 gray-level dependence features. Details of the feature extraction are presented on the webpage of PyRadiomics (12). These features described the tumor information from multiscale space which incorporate the very detailed and macroscopic tumor texture patterns.

Radiomic Signature Construction and Validation

The radiomic signature was constructed with multiparametric MRI (T2WI and ADC) based on the primary cohort. The imaging

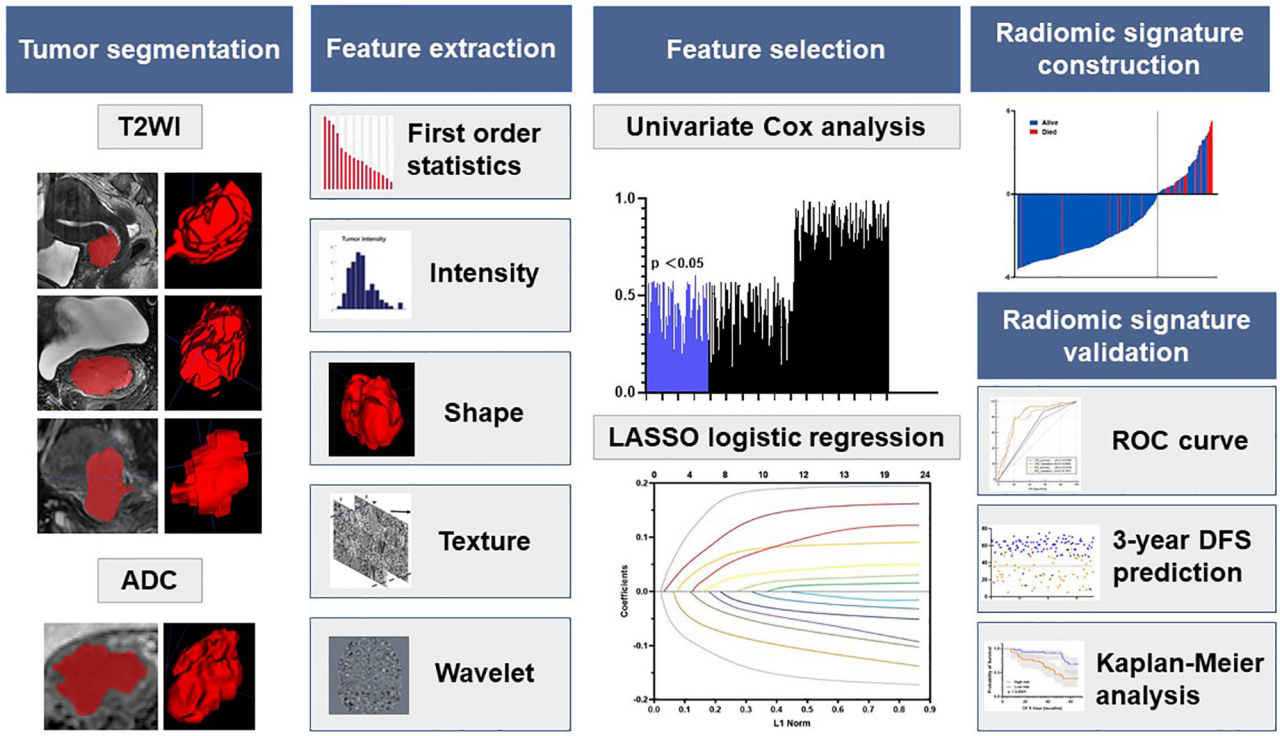

FIGURE 2 | Radiomics framework of predicting the DFS of LACC patients. DFS represents disease-free survival; LACC represents locally advanced cervical cancer; ROC represents receiver operating curves.

features were first normalized, and then a coarse-to-fine feature selection strategy was used to reduce the risk of bias and potential overfitting. Then, we conducted a three-step feature selection method to retain only the most robust features that are significantly associated with DFS. First, univariate Cox analysis was used to detect the associations between each feature and the DFS. All features were then ranked in ascending order according to the Cox p value, and the top 20% of the features with $p<0.1$ was used for the next step. Second, among these features, the Pearson correlation coefficients for each feature were then calculated. Features with $|r|>0.6$ were selected for the next step. Finally, the LASSO algorithm with Cox analysis was used to identify the most useful prognostic features for constructing the radiomic signature.

The potential association between the radiomic signature and DFS was initially assessed in the primary cohort and then validated in the validation cohort based on Kaplan–Meier survival analysis. The median value for the radiomic signature in the primary cohort was used as the cutoff for dividing patients into groups with high- or low-risk groups. The same cutoff value was applied to the validation cohort. The receiver-operating characteristic (ROC) curves for 1-, 2-, and 3-year DFS were plotted for each cohort, and the AUCs were quantified. Kaplan–Meier survival analysis was also performed to explore whether the radiomic signature was associated with DFS within FIGO stage subgroups for each cohort.

Development and Validation of the Clinicopathological Model and Radiomic Signature on DFS Prediction

Among the clinicopathological factors, we firstly conducted the univariate Cox proportional hazard model to select the significant prognostic factors in the primary cohort. Then, significant factors were included in the multivariate Cox model to build a clinical model for DFS prediction.

We also evaluated whether the radiomic signature showed a superior value than the clinical model for predicting DFS in cervical cancer patients. These models were tested in the primary and validation cohorts. The prognostic performance of each model in predicting 3-year DFS was evaluated based on Harrell's concordance index (C-index) and ROC analysis.

Statistical Analysis

All the statistical analyses in this study were performed with SPSS v.22.0 (IBM; Armonk, NY) and R software v.4.1 (R Foundation for Statistical Computing, Vienna, Austria). Descriptive statistics were summarized as mean ± SD. Comparisons between groups were made with the t test or Mann–Whitney U test, when appropriate, for quantitative variables and with the X^2 test or Fisher's test for qualitative variables. The interobserver agreement of feature extraction was calculated by ICC from the different radiologists' tumor segmentation of the three

radiologists. The AUC, ACC, specificity, and sensitivity with the cutoff of 0.5 and the 95% CI by the DeLong (13) method were used to assess the ability of different models to predict DFS. The Kaplan–Meier survival curve method and Cox proportional hazard model were used to analyze DFS. All tests were two-sided, and results were considered significant at $p<0.05$.

RESULTS

Patient Characteristics

A total of 263 patients were included from three centers. The patient characteristics are displayed in **Table 1**. The mean age of the patients was 53.77 ± 8.93 years. The median follow-up time was 45.0 months (interquartile range [IQR]: 32.2–56.7 months) in the primary cohort, 43.2 months (interquartile range [IQR]: 28.6–58.5 months) in the validation cohort. The comparisons between the two cohorts showed no significant difference (p = 0.099–0.984).

Satisfactory inter- and intraobserver reproducibility was observed for the tumor segmentation and radiomic feature extraction (ICC>0.60) (14) when we compared results for three radiologists and results from the same radiologist at baseline and at least 1 month later.

Radiomic Signature Construction and Validation

A total of 4 radiomic features were selected for the RS construction (**Supplementary Table 1**). The selected features were combined into a LASSO-Cox regression model to define the radiomic signature (RS) (**Supplementary Figure 1**). For the primary cohort and the validation cohorts, patients were dichotomized into high- and low-risk groups based on the median RS of the primary cohort as the cutoff value for further analyses. **Figure 3** shows two representative patients with similar clinicopathological features, but distinctively different DFS time, due to the different risk stratification by the radiomic signature.

The Kaplan–Meier survival curves confirmed a significant difference in DFS between the high- and low-RS groups ($p<0.0001$) (**Figure 4**, upper), with relatively high hazard ratios (HRs = 10.688) in the primary cohort (**Table 2**). In the primary cohort, the RS showed good performance on DFS prediction (C-index, 0.758; 95% CI: 0.691–0.815). In the validation cohort, the performance of the radiomic score was further confirmed (C-index, 0.736; 95% CI: 0.673–0.800) (**Table 3**). The areas under the curve (AUCs) at different follow-up times (1, 2, and 3 years) also confirmed that the RS had good prognostic accuracy in the primary and validation cohorts (**Figure 4**, lower). The hazard ratio (HR) for RS was 10.688 ($p<0.001$, 95% CI: 6.605–17.294) in the primary cohort and 10.880 ($p<0.001$, 95% CI: 6.660–17.774) in the validation cohort.

Subgroup analyses further confirmed that the RS could predict prognosis according to the FIGO stage from primary and validation cohorts (**Figure 5**). These results confirmed the high prognostic accuracy of the RS.

Performance and Validation of the Clinical Model on DFS Prediction

Only two clinical features (FIGO stage and lymph node metastasis) were selected to create a clinicopathological model

TABLE 1 | Characteristics of the patients at baseline.

Characteristics	Primary cohort (n = 178)	Validation cohort (n = 85)	p value
Age (years, mean ± SD)	54.28 ± 9.40	53.17 ± 9.36	0.843
SCC (ng/ml)	8.98 ± 12.10	8.74 ± 11.83	0.766
FIGO stage			0.984
IB	3 (1.69%)	1 (1.18%)	
IIA	8 (4.49%)	4 (4.71%)	
IIB	112 (62.92%)	56 (65.88%)	
IIIA	8 (4.49%)	3 (3.53%)	
IIIB	18 (10.11%)	8 (9.41%)	
IIIC	9 (5.06%)	4 (4.70%)	
IVA	20 (11.24%)	9 (10.59%)	
Histology			0.449
Squamous cell carcinoma	136 (76.41%)	61 (71.76%)	
Adenocarcinoma	34 (19.10%)	17 (20.00%)	
Adenosquamous carcinoma	8 (4.49%)	7 (8.24%)	
Tumor size			0.099
≤4 cm	107 (60.11%)	60 (70.59%)	
>4 cm	71 (39.89%)	25 (29.41%)	
Differentiation			0.797
Well	85 (47.75%)	41 (48.24%)	
Moderate	40 (22.47%)	21 (24.70%)	
Poor	53 (29.78%)	23 (27.06%)	
Lymph node metastases			0.611
Positive	45 (25.28%)	24 (28.24%)	
Negative	133 (74.72%)	61 (71.76%)	
Mean DFS time (months, mean ± SD)	42.82 ± 16.40	40.76 ± 20.17	0.452

SCC, squamous cell carcinoma antigen; FIGO, Federation of Gynecology and Obstetrics; DFS, disease-free survival.

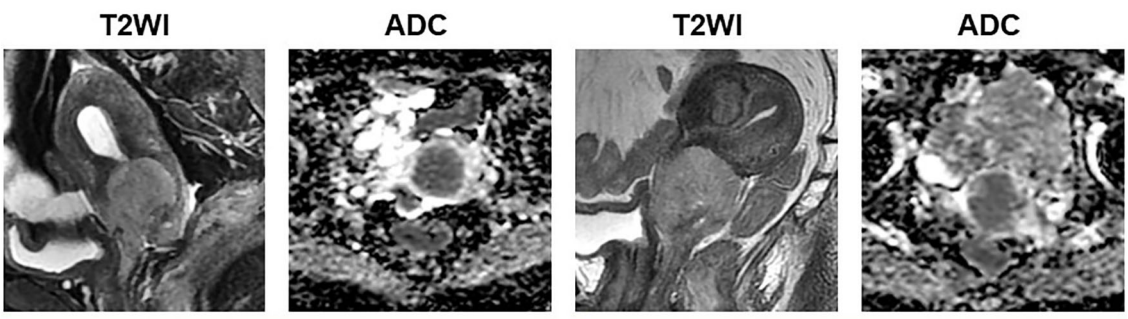

Patient 1	
Age:	41 years
Histological type:	Squamous cell carcinoma
FIGO stage:	IIB
Differentiation:	Middle-grade
Lymph node metastasis:	Positive
DFS:	16 months
The radiomic signature:	2.566

Patient 2	
Age:	57 years
Histological type:	Squamous cell carcinoma
FIGO stage:	IIB
Differentiation:	Middle-grade
Lymph node metastasis:	Positive
DFS:	64 months
The radiomic signature:	0.315

FIGURE 3 | MR images of two patients with similar clinicopathological features but significantly different DFS time. DFS, disease-free survival.

(**Table 2**). This model achieved a poor performance in DFS estimation, with a C-index of 0.631 (95% CI: 0.562–0.691) in the primary cohort and 0.603 (95% CI: 0.530–0.669) in the validation cohort (**Table 3**). The combined model incorporating the RS and clinicopathological features showed no improvement in both cohorts (primary cohort, C-index: 0.648, 95% CI: 0.571–0.685; validation cohort, C-index: 0.585, 95% CI: 0.511–0.637) when compared with RS.

3-Year DFS Probability Prediction of Clinical Model and the RS

For 3-year DFS probability prediction, the clinical model achieved an AUC of 0.608 (95% CI: 0.533–0.681), sensitivity of 0.504 (95% CI: 0.353–0.642), specificity of 0.715 (95% CI: 0.638–0.778), and accuracy of 0.610 (95% CI: 0.540–0.671) in the validation cohort (**Figure 6A** and **Table 3**). The RS yielded an AUC of 0.787 (95% CI: 0.687–0.839), sensitivity of 0.771 (95% CI: 0.627–0.880), specificity of 0.762 (95% CI:0.679–0.832), and accuracy of 0.767 (95% CI: 0.687–0.839) in the validation cohort (**Figure 6A** and **Table 3**). The RS showed significant difference between patients with DFS time >3 years and <3 years (**Figure 6B**).

DISCUSSION

In this study, we developed and validated the prognostic value of multiparametric MR-derived radiomic features on LACC patients underwent CCRT. The results showed that LASSO-Cox-based RS had favorable predictive performance in DFS estimation than the traditional clinical model. The higher value of the RS was associated with worse outcomes, confirming that more heterogeneous tumors tended to have a poorer prognosis. Our study would help to determine whether more intensive surveillance and aggressive treatment regimens should be administered to patients with worse DFS, to assist clinical treatment and healthcare decisions.

Radiomics provided a non-invasive technique to obtain essential information of "macro-heterogeneity" underlying diagnostic, therapeutic, and prognostic information by non-invasively extracting useful imaging features from medical images (15). Radiomic biomarkers may eventually complement existing genomic and proteomic biomarkers to form a unique patient profile that informs personalized care strategies. Radiomics has been proposed for characterizing cervical cancer subtypes (16), predicting tumor staging (17), histological grading (18), and lymph node metastasis (19–21) and predicting the

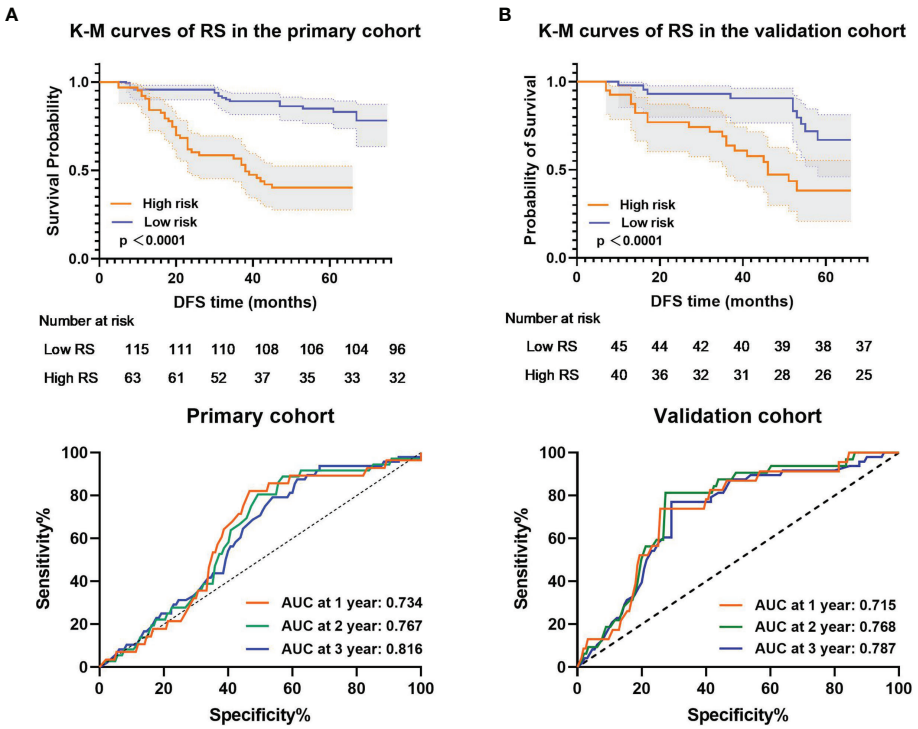

FIGURE 4 | Kaplan–Meier analysis and time-dependent ROC curves of the radiomic signature. p values were calculated using a two-sided log-rank test, and AUCs at 1, 2, and 3 years were calculated to assess the prognostic accuracy within the **(A)** primary cohort (n = 178) and **(B)** validation cohort (n = 85). Shadows represent 95% CI. DFS represents disease-free survival. CI represents confidence interval.

TABLE 2 | Univariate and multivariable analyses between DFS, RS, and clinicopathological features in the primary cohort.

Variables	Univariate Cox regression		Multivariable Cox regression	
	HR (95% CI)	p value	HR (95% CI)	p value
Radiomic signature	10.688 (6.605–17.294)	<0.001	10.880 (6.660–17.774)	<0.001
Age	1.002 (0.974–1.032)	0.877		
FIGO stage				
I–II	–	–		
III	0.931 (0.522–1.660)	0.808	0.793 (0.432–1.455)	0.453
IVa	2.014 (1.015–3.994)	0.005	1.582 (0.566–2.971)	0.046
Histological type				
Squamous cell carcinoma	–	–		
Adenocarcinoma	3.030 (0.413–22.214)	0.276		
Adenosquamous carcinoma	1.929 (0.603–6.173)	0.269		
Differentiation				
Well	–	–		
Moderate	0.977 (0.567–1.684)	0.933		
Poor	1.520 (0.539–4.288)	0.429		
Lymph node metastases				
Negative	–	–		
Positive	2.007 (1.098–3.666)	0.002	1.599 (1.050–2.976)	0.033
SCC	1.015 (0.998–1.031)	0.088		
CA 125	1.007 (0.999–1.016)	0.088		
CEA	0.999 (0.958–1.042)	0.972		
Tumor size	1.010 (0.847–1.204)	0.914		

FIGO, Federation of Gynecology and Obstetrics; SCC, squamous cell carcinoma antigen; CEA, carcinoembryonic antigen.

TABLE 3 | Model performance on predicting DFS and 3-year DFS probability.

Models	Cohorts	C-index (95% CI)	AUC (95% CI)	ACC (95% CI)	Sensitivity (95% CI)	Specificity (95% CI)
Clinical model	Primary	0.631 (0.562–0.691)	0.649 (0.574–0.719)	0.644 (0.574–0.702)	0.588 (0.437–0.713)	0.700 (0.621–0.765)
	Validation	0.603 (0.530–0.669)	0.608 (0.533–0.681)	0.610 (0.540–0.671)	0.504 (0.353–0.642)	0.715 (0.638–0.778)
Radiomic signature	Primary	0.758 (0.691–0.815)	0.816 (0.751–0.870)	0.792 (0.691–0.878)	0.792 (0.650–0.895)	0.792 (0.712–0.858)
	Validation	0.736 (0.673–0.800)	0.787 (0.726–0.845)	0.767 (0.687–0.839)	0.771 (0.627–0.880)	0.762 (0.679–0.832)
Combined model	Primary	0.648 (0.571–0.685)	0.683 (0.609–0.751)	0.682 (0.605–0.744)	0.958 (0.857–0.995)	0.407 (0.322–0.497)
	Validation	0.585 (0.511–0.637)	0.612 (0.536–0.684)	0.612 (0.533–0.679)	0.854 (0.722–0.939)	0.369 (0.286–0.458)

CI represents confidence interval. C-index represents Harrell's concordance index, which measures the performance of the DFS prediction. AUC represents the area under the receiver operating characteristic curve, and ACC represents accuracy. AUC and ACC evaluate the performance of the 3-year DFS prediction.

response to treatment either by CT, MRI alone or in combination with PET/CT (22–26).

Treatment response of cervical cancer patients varied, even patients with the same disease stage, which makes accurate prognostication essential for treatment selection (27). In the current study, we confirmed that RS was a robust predictor of DFS from a multicenter study. Furthermore, we also showed that RS was a better predictor of DFS with superior predictive potency than traditional clinicopathological features, based on larger C-index and AUCs in primary and validation cohorts. This may be because clinicopathological factors only reflect specific tumor characteristics, while radiomics based on multiparametric MRI can comprehensively and quantifiably characterize the tumor phenotype (28, 29). It is also possible that high-dimensional imaging features provide additional information, allowing radiomics to be less affected by patient distribution. Fang et al. investigated the potency of radiomic biomarkers in DFS prediction with early-stage (IB-IIA) cervical cancer patients who underwent hysterectomy by contrast-enhanced T1WI and T2WI and reported AUCs of radiomic score as 0.816 in the training cohort and 0.822 in the validation cohort (10), which was consistent and similar to our results. Sun et al. adopted T1WI- and T2WI-derived radiomic features for treatment response prediction in cervical cancer patients who underwent chemoradiotherapy; the combined model yielded an AUC of 0.998

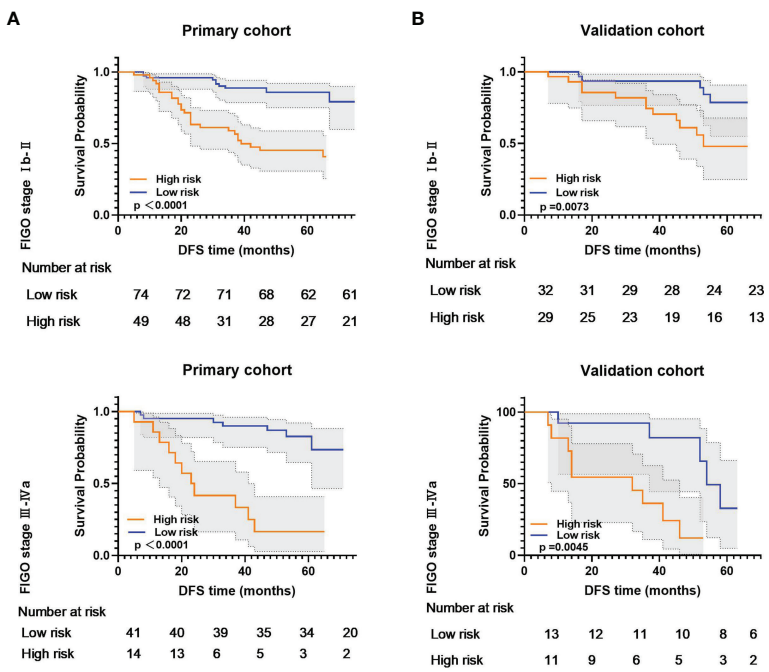

FIGURE 5 | Kaplan-Meier analysis according to the radiomic signature among locally advanced cervical cancer patient subgroups in **(A)** primary cohort and **(B)** validation cohort.

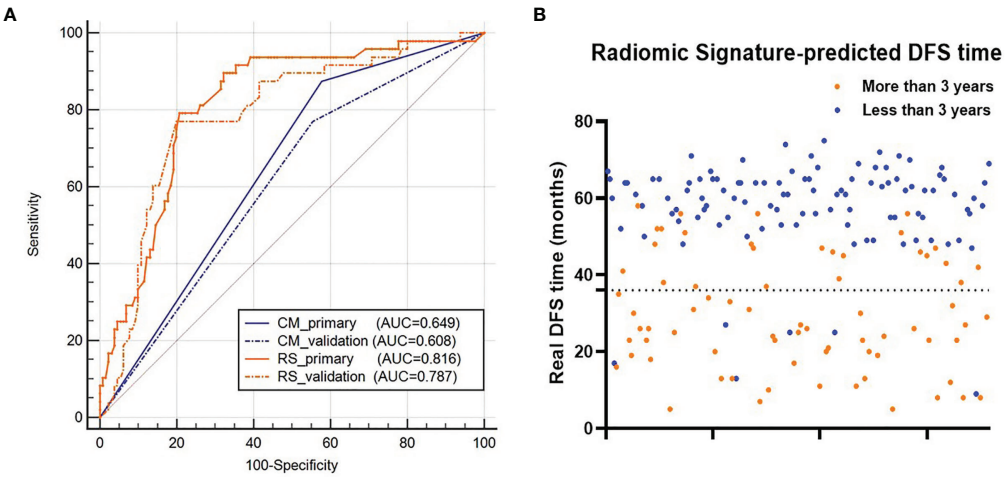

FIGURE 6 | **(A)** ROC curves of the two models for 3-year DFS probability prediction. **(B)** Distribution of the DFS time for patients. The orange dots represent patients who are predicted to have DFS time longer than 3 years by the RS, and the blue dots represent patients who are predicted to have DFS time less than 3 years by the RS. RS represents radiomic signature; CM represents clinical model; ROC represents receiver-operating characteristics; DFS represents disease-free survival.

and 0.999 in the training and validation cohorts, respectively, showing the prominent potential for treatment response evaluation and prediction of radiomic features (30). However, the AUCs in our study were 0.816 in the primary cohort and 0.787 in the training cohort, which was significantly lower than theirs. This may be caused by the different endpoints of the two studies; they defined responders as complete response or partial response within two cycles of chemotherapy regardless of the response after the final chemotherapy cycle, while we chose DFS as the endpoint of our study, which was sophisticatedly impacted by various factors. Thus, the RS constructed in our study might be better instructing personalized treatment, and the radiomic model they built was more valuable in early treatment evaluation and prediction. Although many features in MRI were significantly associated with DFS, we selected the smallest subsets of features available to achieve high accuracy for the clinical endpoint.

With excellent space definition and multiple functional imaging modalities, MRI has become the prior imaging examination in cervical cancer during the whole CCRT procedure. The clinical advantage of the extraction of MRI-derived radiomic features is that it exploits diagnostic images that are available already, so it does not require additional examinations. Moreover, extracting the RS is non-invasive and can be repeated at different time points during the whole treatment procedure. The RS provides a high-dimensional description of the intra-tumor heterogeneity. Interestingly, the ADC sequence appears to be important, as three of the four radiomic features of the RS were from ADC maps, which is consistent with previous results that ADC maps were valuable for evaluating the treatment response of various cancer types (29, 31), which also supported the indication that RS is a fairly reliable marker. Bourbonne et al. (32) and Lucia et al. (24) conducted an external validation of a multicenter study confirming the good prognostic predictive ability of ADC-derived radiomic features in prostate cancer and cervical cancer, which supported our results.

The present study has some limitations that merit consideration. Firstly, this was a retrospective study with limited sample size, and a larger prospective validation study should be conducted. The accumulation of additional patients will also allow for the collection of more information from various aspects, which can make the RS more stable and accurate. Secondly, whether imaging-derived digital biopsy features correlated with pathological biopsy results and genomic sequencing remained undefined, and molecular biology experiments should be conducted. Thirdly, although the segmentation of all images was processed by expertly trained radiologists, the use of semiautomatic segmentation tools should reduce the user dependency.

In conclusion, this present study provided a multiparametric MRI-derived radiomic signature that effectively predicted DFS in LACC patients who underwent CCRT and the RS showed superior performance than the traditional clinical model. Non-invasive MRI-derived RS showed prominent ability in risk stratification of cervical cancer patients, thus allowing radiation oncologists to select more personalized treatment regimens.

DATA AVAILABILITY STATEMENT

The raw data supporting the conclusions of this article will be made available by the authors, without undue reservation.

ETHICS STATEMENT

The studies involving human participants were reviewed and approved by the ethics review board of Xijing Hospital. The patients/participants provided their written informed consent to participate in this study.

AUTHOR CONTRIBUTIONS

Conception and design: L-CW, YH, M-WZ. Collection and assembly of data: BL, ZS, FZ, Y-AL, B-XH. Data analysis and interpretation: BL, Z-LX, H-LZ, D-DW. Manuscript writing: BL, ZS, YH, M-WZ. Final approval of manuscript: all authors. All authors contributed to the article and approved the submitted version.

FUNDING

We acknowledge financial support from the National Nature Science Foundation of China (Grant Numbers 81471663, 82002348) and the Key Research and Development Plan of Shaanxi Province (Grant Number: 2020ZDLSF01-01). The funders had no role in the study design, data collection, data analysis, interpretation, or writing.

ACKNOWLEDGMENTS

The authors would like to thank all staff from the department of radiology and radiation oncology for their hard work and invaluable support for this study.

SUPPLEMENTARY MATERIAL

The Supplementary Material for this article can be found online at: https://www.frontiersin.org/articles/10.3389/fonc.2021.812993/full#supplementary-material

REFERENCES

1. Sung H, Ferlay J, Siegel RL, Laversanne M, Soerjomataram I, Jemal A, et al. Global Cancer Statistics 2020: GLOBOCAN Estimates of Incidence and Mortality Worldwide for 36 Cancers in 185 Countries. *CA: Cancer J Clin* (2021) 71:209–49. doi: 10.3322/caac.21660
2. Katsumata N, Yoshikawa H, Kobayashi H, Saito T, Kuzuya K, Nakanishi T, et al. Phase III Randomised Controlled Trial of Neoadjuvant Chemotherapy Plus Radical Surgery vs Radical Surgery Alone for Stages IB2, IIA2, and IIB Cervical Cancer: A Japan Clinical Oncology Group Trial (JCOG 0102). *Brit J Cancer* (2013) 108:1957–63. doi: 10.1038/bjc.2013.179
3. Rose PG, Java J, Whitney CW, Stehman FB, Lanciano R, Thomas GM, et al. Nomograms Predicting Progression-Free Survival, Overall Survival, and Pelvic Recurrence in Locally Advanced Cervical Cancer Developed From an Analysis of Identifiable Prognostic Factors in Patients From NRG Oncology/Gynecologic Oncology Group Randomized Trials of Chemoradiotherapy. *J Clin Oncol: Off J Am Soc Clin Oncol* (2015) 33:2136–42. doi: 10.1200/JCO.2014.57.7122
4. Kristensen GB, Abeler VM, Risberg B, Trop C, Bryne M. Tumor Size, Depth of Invasion, and Grading of the Invasive Tumor Front are the Main Prognostic Factors in Early Squamous Cell Cervical Carcinoma. *Gynecol Oncol* (1999) 74:245–51. doi: 10.1006/gyno.1999.5420
5. Ward ZJ, Grover S, Scott AM, Woo S, Salama DH, Jones EC, et al. The Role and Contribution of Treatment and Imaging Modalities in Global Cervical Cancer Management: Survival Estimates From a Simulation-Based Analysis. *Lancet Oncol* (2020) 21:1089–98. doi: 10.1016/S1470-2045(20)30316-8
6. Westerveld H, Nesvacil N, Fokdal L, Chargari C, Schmid MP, Milosevic M, et al. Definitive Radiotherapy With Image-Guided Adaptive Brachytherapy for Primary Vaginal Cancer. *Lancet Oncol* (2020) 21:e157–67. doi: 10.1016/S1470-2045(19)30855-1
7. Lambin P, Rios-Velazquez E, Leijenaar R, Carvalho S, van Stiphout RGPM, Granton P, et al. Radiomics: Extracting More Information From Medical Images Using Advanced Feature Analysis. *Eur J Cancer* (2012) 48(4):441–6. doi: 10.1016/j.ejca.2011.11.036
8. Aerts HJWL, Velazquez ER, Leijenaar RTH, Parmar C, Grossmann P, Carvalho S, et al. Decoding Tumour Phenotype by Noninvasive Imaging Using a Quantitative Radiomics Approach. *Nat Commun* (2014) 5:4006. doi: 10.1038/ncomms5006
9. Lambin P, Leijenaar RTH, Deist TM, Peerlings J, de Jong EEC, van Timmeren J, et al. Radiomics: The Bridge Between Medical Imaging and Personalized Medicine. *Nat Rev Clin Oncol* (2017) 14:749–62. doi: 10.1038/nrclinonc.2017.141
10. Fang J, Zhang B, Wang S, Jin Y, Wang F, Ding Y, et al. Association of MRI-Derived Radiomic Biomarker With Disease-Free Survival in Patients With Early-Stage Cervical Cancer. *Theranostics* (2020) 10:2284–92. doi: 10.7150/thno.37429
11. Liu B, Sun Z, Ma W, Ren J, Zhang G, Wei M, et al. DCE-MRI Quantitative Parameters as Predictors of Treatment Response in Patients With Locally Advanced Cervical Squamous Cell Carcinoma Underwent CCRT. *Front Oncol* (2020) 10:585738. doi: 10.3389/fonc.2020.585738
12. van Griethuysen JJM, Fedorov A, Parmar C, Hosny A, Aucoin M, Narayan NV, et al. Computational Radiomics System to Decode the Radiographic Phenotype. *Cancer Res* (2017) 77:e104–7. doi: 10.1158/0008-5472.CAN-17-0339
13. DeLong ER, DeLong DM, Clarke-Pearson DL. Comparing the Areas Under Two or More Correlated Receiver Operating Characteristic Curves: A Nonparametric Approach. *Biometrics* (1988) 44:837–45. doi: 10.2307/2531595
14. Landis JR, Koch GG. The Measurement of Observer Agreement for Categorical Data. *Biometrics* (1977) 33:159–74. doi: 10.2307/2529310
15. Gillies RJ, Kinahan PE, Hricak H. Radiomics: Images are More Than Pictures, They are Data. *Radiology* (2016) 278:563–77. doi: 10.1148/radiol.2015151169
16. Tsujikawa T, Rahman T, Yamamoto M, Yamada S, Tsuyoshi H, Kiyono Y, et al. (18)F-FDG PET Radiomics Approaches: Comparing and Clustering Features in Cervical Cancer. *Ann Nucl Med* (2017) 31:678–85. doi: 10.1007/s12149-017-1199-7
17. Mu W, Chen Z, Liang Y, Shen W, Yang F, Dai R, et al. Staging of Cervical Cancer Based on Tumor Heterogeneity Characterized by Texture Features on (18)F-FDG PET Images. *Phys Med Biol* (2015) 60:5123–39. doi: 10.1088/0031-9155/60/13/5123
18. Liu Y, Zhang Y, Cheng R, Liu S, Qu F, Yin X, et al. Radiomics Analysis of Apparent Diffusion Coefficient in Cervical Cancer: A Preliminary Study on Histological Grade Evaluation. *J Magn Reson Imaging: JMRI* (2019) 49:280–90. doi: 10.1002/jmri.26192
19. Song J, Hu Q, Ma Z, Zhao M, Chen T, Shi H. Feasibility of T(2)WI-MRI-Based Radiomics Nomogram for Predicting Normal-Sized Pelvic Lymph Node Metastasis in Cervical Cancer Patients. *Eur Radiol* (2021) 31:6938–48. doi: 10.1007/s00330-021-07735-x
20. Hou L, Zhou W, Ren J, Du X, Xin L, Zhao X, et al. Radiomics Analysis of Multiparametric MRI for the Preoperative Prediction of Lymph Node Metastasis in Cervical Cancer. *Front Oncol* (2020) 10:1393. doi: 10.3389/fonc.2020.01393
21. Dong T, Yang C, Cui B, Zhang T, Sun X, Song K, et al. Development and Validation of a Deep Learning Radiomics Model Predicting Lymph Node Status in Operable Cervical Cancer. *Front Oncol* (2020) 10:464. doi: 10.3389/fonc.2020.00464
22. Lucia F, Visvikis D, Desseroit M, Miranda O, Malhaire J, Robin P, et al. Prediction of Outcome Using Pretreatment (18)F-FDG PET/CT and MRI Radiomics in Locally Advanced Cervical Cancer Treated With Chemoradiotherapy. *Eur J Nucl Med Mol I* (2018) 45:768–86. doi: 10.1007/s00259-017-3898-7
23. Bowen SR, Yuh WTC, Hippe DS, Wu W, Partridge SC, Elias S, et al. Tumor Radiomic Heterogeneity: Multiparametric Functional Imaging to Characterize

Variability and Predict Response Following Cervical Cancer Radiation Therapy. *J Magn Reson Imaging: JMRI* (2018) 47:1388–96. doi: 10.1002/jmri.25874
24. Lucia F, Visvikis D, Vallières M, Desseroit M, Miranda O, Robin P, et al. External Validation of a Combined PET and MRI Radiomics Model for Prediction of Recurrence in Cervical Cancer Patients Treated With Chemoradiotherapy. *Eur J Nucl Med Mol I* (2019) 46:864–77. doi: 10.1007/s00259-018-4231-9
25. Ferreira M, Lovinfosse P, Hermesse J, Decuypere M, Rousseau C, Lucia F, et al. [(18)F]FDG PET Radiomics to Predict Disease-Free Survival in Cervical Cancer: A Multi-Scanner/Center Study With External Validation. *Eur J Nucl Med Mol I* (2021) 48:3432–43. doi: 10.1007/s00259-021-05303-5
26. Li H, Zhu M, Jian L, Bi F, Zhang X, Fang C, et al. Radiomic Score as a Potential Imaging Biomarker for Predicting Survival in Patients With Cervical Cancer. *Front Oncol* (2021) 11:706043. doi: 10.3389/fonc.2021.706043
27. Kato S, Ohno T, Thephamongkhol K, Chansilpa Y, Cao J, Xu X, et al. Long-Term Follow-Up Results of a Multi-Institutional Phase 2 Study of Concurrent Chemoradiation Therapy for Locally Advanced Cervical Cancer in East and Southeast Asia. *Int J Radiat Oncol Biol Phys* (2013) 87:100–5. doi: 10.1016/j.ijrobp.2013.04.053
28. Aerts HJWL. The Potential of Radiomic-Based Phenotyping in Precision Medicine: A Review. *JAMA Oncol* (2016) 2:1636–42. doi: 10.1001/jamaoncol.2016.2631
29. Liu Z, Meng X, Zhang H, Li Z, Liu J, Sun K, et al. Predicting Distant Metastasis and Chemotherapy Benefit in Locally Advanced Rectal Cancer. *Nat Commun* (2020) 11:4308. doi: 10.1038/s41467-020-18162-9
30. Sun C, Tian X, Liu Z, Li W, Li P, Chen J, et al. Radiomic Analysis for Pretreatment Prediction of Response to Neoadjuvant Chemotherapy in Locally Advanced Cervical Cancer: A Multicentre Study. *Ebiomedicine* (2019) 46:160–9. doi: 10.1016/j.ebiom.2019.07.049
31. Liu Z, Li Z, Qu J, Zhang R, Zhou X, Li L, et al. Radiomics of Multiparametric MRI for Pretreatment Prediction of Pathologic Complete Response to Neoadjuvant Chemotherapy in Breast Cancer: A Multicenter Study. *Clin Cancer Res: an Off J Am Assoc Cancer Res* (2019) 25:3538–47. doi: 10.1158/1078-0432.CCR-18-3190
32. Bourbonne V, Fournier G, Vallières M, Lucia F, Doucet L, Tissot V, et al. External Validation of an MRI-Derived Radiomics Model to Predict Biochemical Recurrence After Surgery for High-Risk Prostate Cancer. *Cancers* (2020) 12. doi: 10.3390/cancers12040814

Conflict of Interest: The authors declare that the research was conducted in the absence of any commercial or financial relationships that could be construed as a potential conflict of interest.

Publisher's Note: All claims expressed in this article are solely those of the authors and do not necessarily represent those of their affiliated organizations, or those of the publisher, the editors and the reviewers. Any product that may be evaluated in this article, or claim that may be made by its manufacturer, is not guaranteed or endorsed by the publisher.

frontiers in Oncology

ORIGINAL RESEARCH
published: 25 March 2022
doi: 10.3389/fonc.2022.830080

Experimental Comparison of Fiducial Markers Used in Proton Therapy: Study of Different Imaging Modalities and Proton Fluence Perturbations Measured With CMOS Pixel Sensors

Claire-Anne Reidel[1], Felix Horst[1], Christoph Schuy[1], Oliver Jäkel[2,3], Swantje Ecker[3], Katrin Henkner[3], Stephan Brons[3], Marco Durante[1,4] and Uli Weber[1]*

[1] Biophysics Department, GSI Helmholtzzentrum für Schwerionenforschung GmbH, Darmstadt, Germany, [2] Division of Medical Physics in Radiation Oncology, German Cancer Research Center (DKFZ), Heidelberg, Germany, [3] Heidelberg Ion Beam Therapy Center (HIT), Heidelberg, Germany, [4] Institut für Physik Kondensierter Materie, Technische Universität Darmstadt, Darmstadt, Germany

OPEN ACCESS

Edited by:
John C. Roeske, Loyola University Medical Center, United States

Reviewed by:
Mark Pankuch, Northwestern Medicine Chicago Proton Center, United States
Erik Tryggestad, Mayo Clinic, United States

***Correspondence:**
Christoph Schuy
c.schuy@gsi.de

Specialty section:
This article was submitted to Cancer Imaging and Image-directed Interventions, a section of the journal Frontiers in Oncology

Received: *06 December 2021*
Accepted: *23 February 2022*
Published: *25 March 2022*

Citation:
Reidel C-A, Horst F, Schuy C, Jäkel O, Ecker S, Henkner K, Brons S, Durante M and Weber U (2022) Experimental Comparison of Fiducial Markers Used in Proton Therapy: Study of Different Imaging Modalities and Proton Fluence Perturbations Measured With CMOS Pixel Sensors. Front. Oncol. 12:830080. doi: 10.3389/fonc.2022.830080

Fiducial markers are used for image guidance to verify the correct positioning of the target for the case of tumors that can suffer interfractional motion during proton therapy. The markers should be visible on daily imaging, but at the same time, they should produce minimal streak artifacts in the CT scans for treatment planning and induce only slight dose perturbations during particle therapy. In this work, these three criteria were experimentally investigated at the Heidelberg Ion Beam Therapy Center. Several small fiducial markers with different geometries and materials (gold, platinum, and carbon-coated ZrO_2) were evaluated. The streak artifacts on treatment planning CT were measured with and without iMAR correction, showing significantly smaller artifacts from markers lighter than 6 mg and a clear improvement with iMAR correction. Daily imaging as X-ray projections and in-room mobile CT were also performed. Markers heavier than 6 mg showed a better contrast in the X-ray projections, whereas on the images from the in-room mobile CT, all markers were clearly visible. In the other part of this work, fluence perturbations of proton beams were measured for the same markers by using a tracker system of several high spatial resolution CMOS pixel sensors. The measurements were performed for single-energy beams, as well as for a spread-out Bragg peak. Three-dimensional fluence distributions were computed after reconstructing all particle trajectories. These measurements clearly showed that the ZrO_2 markers and the low-mass gold/platinum markers (0.35mm diameter) induce perturbations being 2–3 times lower than the heavier gold or platinum markers of 0.5mm diameter. Monte Carlo simulations, using the FLUKA code, were used to compute dose distributions and showed good agreement with the experimental data after adjusting the phase space of the simulated proton beam compared to the experimental beam.

Keywords: fiducial marker, dose perturbation, proton therapy, CMOS pixel sensor, image guidance, streak artifacts, Monte Carlo simulation

1 INTRODUCTION

Over the last years, innovative techniques for particle therapy were developed in order to deliver a more conformal dose to the tumor and better spare healthy tissues. A mispositioning of the patient can lead to severe under- and overdosage, especially for proton and ion beams where high doses are delivered at the end of their range (1, 2).

During radiation therapy, the positioning of the patient is ensured by daily imaging, usually performed by X-ray projections, cone beam computed tomography (CBCT), or in-room mobile CT. In most cases, a patient is aligned to the absolute coordinate system of the treatment room by matching its bony structure, visible on the daily image, to the one reconstructed from the treatment planning CT. In the case of interfractional motion due to anatomical changes, e.g., prostate cancer, the tumor can move in the range 0–2 cm due to the filling of the bladder and rectum (3–5). Therefore, fiducial markers are implanted inside or nearby the tumor before the treatment and are used for image guidance during radiation therapy (6, 7) since the alignment with the bony structure of the patient is not reliable for tumor position in some regions. Their position on the daily image is compared to the one from the treatment planning CT, and the consistency of the tumor position is assessed to decide if the treatment can be performed or if corrections are necessary.

Several criteria are to be considered for the fiducial markers. Three important ones were evaluated in this study: low streak artifacts on the treatment planning CT, good visibility on the daily images, and low perturbation of the dose distribution during particle therapy. For a good visibility on the daily image, the markers are generally composed of high density and high atomic number materials such as gold or platinum, but also fiducial markers with lower-density material such as zirconium dioxide (ZrO_2) were considered (8–10). However, due to their high atomic number and density, metallic markers induce streak artifacts on the treatment planning CT and may cause errors in the dose calculation during treatment planning (11). Several studies have been performed to evaluate the visibility of different markers and the streak artifacts that they produce, showing that high-density markers are necessary in order to be visible on X-ray projections (8, 9). In addition to streak artifacts, high-density fiducial markers induce dose perturbations and additional range uncertainties during particle therapy, due to inhomogeneous scattering through high-density gradient edges and their different stopping power relative to water, respectively. The multiple Coulomb scattering depends on the projectile species and energy, as well as the material dimensions and composition, and can be estimated by the Highland formula (12, 13). In previous studies, the severeness of this effect was evaluated for different markers by Monte Carlo simulations (14–16) and/or by measurements with radiochromic films (17–19). Another experimental study, conducted by our group, quantified the fluence perturbation of carbon ions for different fiducial markers with an advanced measurement technique, using CMOS pixel sensors (20). These studies showed that the strength of the perturbation mostly depends on the size and density of the fiducial marker. The ZrO_2 marker showed less perturbation than did gold markers of comparable size. On the other hand, this marker was less visible on the daily X-ray projection imaging. The present work intends to investigate these effects and to discuss the trade-off between the visibility versus the dose perturbations during proton therapy, which is more frequently used than carbon ion therapy. Moreover, perturbations are larger for protons than carbon ions due to the stronger multiple Coulomb scattering, which gives an additional motivation for this work.

In the present work, a comprehensive study, including imaging, experimental measurements for proton beams, and Monte Carlo simulations, was performed for various fiducial markers made of different materials and geometries. In a first part, an imaging study was carried out to evaluate the streak artifacts on the treatment planning CT, and the visibility on X-ray projections and on the images taken with an in-room mobile CT. In a second part, fluence perturbations of proton beams due to fiducial markers were measured with CMOS pixel sensors, where the maximum perturbation and its position along the beam axis were quantified. Both experimental parts were conducted at the Heidelberg Ion Beam Therapy Center (HIT) (21). For the fluence perturbation measurements, a set of high spatial resolution Mimosa-28 pixel sensors was used (22), as in our previous work (20). In a last part, Monte Carlo simulations, performed with the FLUKA code (23–25), were compared against the experimental results, and dose perturbations in a spread-out Bragg peak (SOBP) were computed for the same markers and proton beams as in the experiment.

2 MATERIALS AND METHODS

2.1 Fiducial Markers

The experimental study was performed for 8 fiducial markers clinically in use, with their properties listed in **Table 1**. The folded Gold Anchor markers were evaluated during the imaging study only, while the linear Gold Anchor was used during the proton beam experiment because of its more defined geometry. All the other listed markers were used in both experiments. In the case of the Visicoil markers, the length and diameter were given by the manufacturer and each marker was weighted. The inner diameter, referred in **Table 1**, was calculated and adjusted compared to the mass of the marker.

2.2 Imaging Study

The imaging was performed for 7 fiducial markers [all markers listed in **Table 1**, except the linear Gold Anchor (5)]. This study was conducted at HIT, using the treatment planning CT, the recently installed in-room mobile CT, and the standard X-ray projection method for daily imaging (see specifications in the sections below). The fiducial markers were inserted in a container of around 30 cm diameter, filled with a homogeneous gelatin solution. To obtain a more realistic case, two bone-like slabs of different density, manufactured by GAMMEX, were placed at one side of the phantom. The X-ray images were performed using two projections, one traversing the

TABLE 1 | Properties of all fiducial markers used in this study for the imaging and proton beam experiments.

Marker number	Name	Manufacturer	Material	Shape	Length (mm)	Diameter (mm)	Mass (mg)
1	Visicoil	RadioMed	Gold	Coiled	5	0.35[a]	3.8
2	Visicoil	RadioMed	Gold	Coiled	5	0.5[b]	10.8
3	Visicoil	RadioMed	Platinum	Coiled	5	0.35[c]	3.6
4	Visicoil	RadioMed	Platinum	Coiled	5	0.5[d]	12.6
	Gold Anchor	Naslund Medical AB	Gold	Linear	15	0.28	12.3
6	Gold Anchor	Naslund Medical AB	Gold	Folded	10	0.28	7.3
7	Gold Anchor	Naslund Medical AB	Gold	Folded	20	0.28	14.2
8	Acculoc Carbon marker	Carbon Medical Technologies	ZrO_2 (carbon-coated)	Bone	3	1	5.5

Inner diameter calculated according to the mass (mm).
[a]0.27, [b]0.33, [c]0.28, [d]0.32.

bone materials that shadowed the markers, and a second offset by 90° where the bone material does not shadow the markers. Therefore, it was possible to compare the X-ray projections with and without bone slabs in front of the markers. A schematic of the phantom used for the imaging study is sketched in **Figure 1**.

2.2.1 Streak Artifacts on Treatment Planning CT

The CT scans were acquired by a SOMATOM Confidence® scanner (Siemens, Erlangen, Germany), using the standard protocol for head planning CT at HIT, with 120 kVP, 255 mAs, and 500 mm field of view. The transversal pixel resolution was 0.977 mm, and the scans were performed with 0.5 and 1mm slice thicknesses, with and without applying an iterative metal artifact reduction (iMAR) correction in the reconstruction. The images were later analyzed with the software ImageJ (26). A square of 2mm length was drawn at the marker position where the Hounsfield value was maximum. Square-shaped rings with a thickness of one pixel (~1 mm) and with an inner length as the one of the previous ring were then drawn around the marker (see **Figure 3C**). The streak artifacts, defined as the maximum and minimum values inside the different square-shaped rings, were computed as a function of the distance from the marker position.

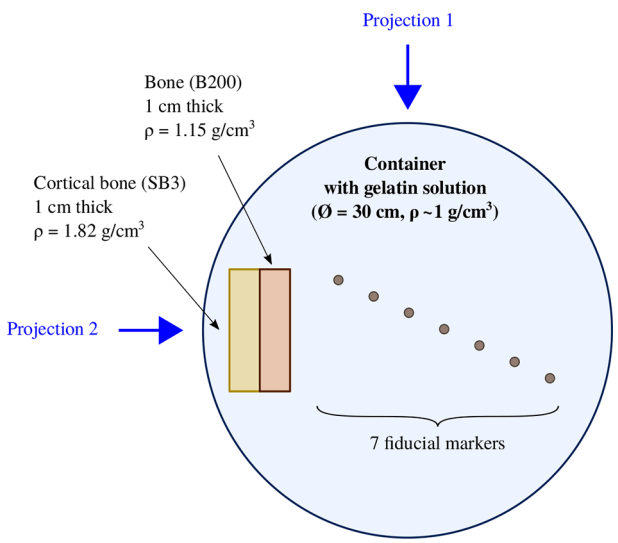

FIGURE 1 | Phantom used for the imaging study where 7 fiducial markers were inserted inside a gelatin solution. Two bone-like slabs were placed on one side of the phantom.

2.2.2 Visibility on X-Ray Projections and In-Room Mobile CT Images

A qualitative comparison of the visibility from the different fiducial markers on X-ray projections was performed with an AXIOM Artis (Siemens) robotic arm, installed in the treatment room at HIT (8). This on-board imaging device is used for patient position verification prior to the treatment. In this study, imaging was performed with and without collimation, and with and without the bone slabs in front of the markers. The settings of the X-ray machine for the different acquisitions are listed in **Table 2**.

The images analysis was then performed with the software ImageJ (26). A rectangular window of 3mm height and 6mm width was drawn perpendicularly to each marker placed in vertical position. The profile was integrated within this window, and the maximum value I_{max} was extracted from the profile. In order to evaluate the background, a window of identical size as the previous one was drawn close to the marker position. In this work, the background I_b was computed as the mean value of the integrated window, while the pixel noise was defined as the standard deviation σ. The errors on I_{max} and I_b were considered the same, and the contrast C was then computed as

$$C = |I_{\max} - I_b| \pm \sigma \sqrt{2/N}, \quad (1)$$

where N is the sample number in the window area.

The in-room mobile CT images were obtained with an AIRO (Mobius Imaging, LLC), which is the in-room mobile CT

TABLE 2 | Settings of the X-ray machine for the different acquisitions of fiducial marker images at HIT.

In-line bone	kVP	Current time product (mAs)	Exposure time (ms)	Collimation
No	69	172	59	No
No	69	254	94	Yes
Yes	69	176	61	No
Yes	69	279	105	Yes

installed in one of the treatment rooms at HIT. The scans were performed with 120 kVP, 80 mAs, and 493 mm field of view. The transversal pixel resolution was 0.963 mm for a slice thickness of 1 mm.

2.3 Fluence Perturbation Measurements

2.3.1 Mimosa-28 Pixel Sensor and Software Analysis

The Mimosa-28 (Minimum Ionizing MOS Active pixel sensor) detector, based on CMOS technology, is a high spatial resolution pixel sensor (22). The sensor has an active area of ~ 2 × 2 cm^2 and is composed of 928 rows × 960 columns with squared pixels of 20.7μm length. The total thickness of the sensor is 50 μm, with an epitaxial layer of 14 μm. Each pixel delivers a binary output after discrimination of the signal, and the sensor has a readout time of 186.5 μs (~5 kHz frame rate).

When a particle passes through the sensor, charges produced by ionization are collected by a certain number of pixels in the sensor. The analysis software Qapivi (27), based on the Root (28) and Geant4 (29) libraries, reconstructs the groups of fired pixels, referred to as clusters. The cluster position is defined as the center of mass of the group of fired pixels, and a straight line (called track) matching the clusters in the different sensors is reconstructed. The tracking procedure was performed with the implemented algorithm based on multiple Coulomb scattering. The resolution of a single track is better than 10 μm, and the performance of the algorithms is described in the study from (30). In order to reach a high track resolution, it is necessary to align the sensors using a dedicated no-target run to compensate mechanical mispositioning of the sensors *via* a software alignment procedure (31).

2.3.2 Experimental Setup

The fluence perturbation measurements of proton beams due to fiducial markers were conducted in the experimental room at HIT, placing a tracker system of 7 Mimosa-28 pixel sensors along the beam axis. The experimental setup was similar to the one used in our previous work (20). A water aquarium of 4cm length, representing the tumor volume, was positioned in between two sets of three sensors. To improve their handling, the markers were glued to a thin polymethyl methacrylate (PMMA) plate of 1mm thickness and 1.18g/cm^3 density. The markers were positioned along the vertical axis perpendicular to the beam at the isocenter of the experimental room. The PMMA plate, including the marker, was glued behind the water aquarium. In our last study with carbon ion beams, the marker was immersed in the water aquarium. However, the maximum perturbation of proton beams was expected to be closer to the marker; therefore, their position was adjusted in order to place the tracker system closer to the marker. The markers were surrounded by a thin layer of gelatin solution to have a more realistic setup where the edges of the marker were surrounded by tissue-like material. In addition, a polyethylene (PE) block of 9cm length was placed in front of the first set of three sensors to simulate the healthy tissues of a patient. Another sensor was positioned in front of the PE block in order to monitor the stability of the beam profile between different measurements, and a 5mm plastic scintillator (BC-400) monitored the beam intensity by counting the incoming particles. A range modulator (2D RM) (32) was placed in front of the first Mimosa-28 sensor. The modulator used in the present work was optimized for a proton SOBP of 5 cm and is composed of 13 × 13 pins within an area of around 4 × 4 cm^2. The pin length is 5 cm, and the modulator is composed of Rigur, which is a polypropylene-like material for 3D printing. The experimental setup is depicted in **Figure 2A**.

The beam time campaign was divided in several parts. First, the runs were performed only with the 7 Mimosa-28 sensors and the plastic scintillator in order to properly align the sensors and tune the initial beam parameters for the Monte Carlo simulations. Second, the measurements were performed with the PE block and the water aquarium to obtain a reference measurement without marker. In a next step, the fiducial markers were placed behind the water aquarium, as explained above. These measurements were performed with two single-energy proton beams (142.10 and 169.02 MeV), which were chosen to have a range difference of 5 cm. In a last step, the 2D RM was positioned in front of the first sensor and the measurements were performed with the PE block and the water aquarium, with and without fiducial marker. For this set of measurements, a single proton energy of 170.05 MeV together with the 2D RM was used to produce a 5cm SOBP. The primary energy was chosen slightly higher than 169.02 MeV because of the additional base plate of the 2D RM. The primary beam energies, their full width half maximum (FWHM), and their range in water are listed in **Table 3**. The energies and FWHM at isocenter position were assumed as the nominal values from HIT (ensured by the regular QA), while the ranges were calculated with LISE++ (33). In **Figure 2B**, the depth–dose profiles in water equivalent are shown for 142 and 169MeV protons, as well as the SOBP produced by the 2D RM for a primary beam of 170MeV protons. The PE block, the water aquarium, and the positions of the fiducial marker and of the last sensor S7 are also indicated. The total range of the different proton beams used in the experiment was chosen to have enough energy to pass through the PE block, the water aquarium, and the sensors placed behind the water aquarium.

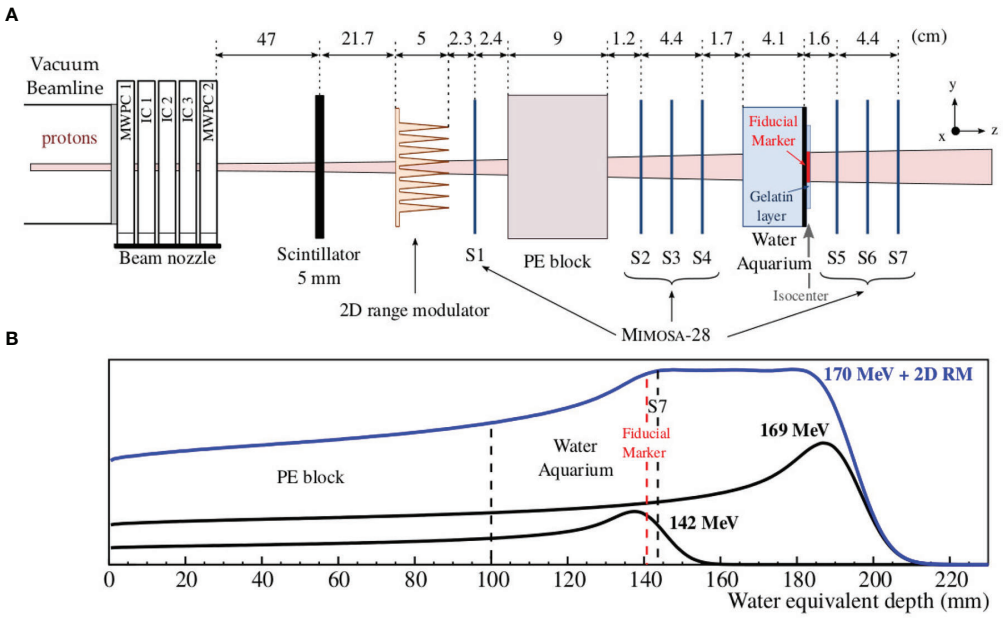

FIGURE 2 | **(A)** Experimental setup for fluence perturbation of proton beams due to fiducial markers, measured with 7 MIMOSA-28 pixel sensors. **(B)** The depth–dose profiles in water equivalent are shown for 142 and 169MeV protons, as well as for the 170-MeV proton beams modulated by a 2D RM. The depth–dose profiles were laterally integrated and obtained with the Monte Carlo code FLUKA (23-25). In this panel, the PE block, the water aquarium, and the positions of the fiducial marker and of the last sensor S7 are also indicated.

2.3.3 Beam Profile Analysis

The beam profiles, measured with the MIMOSA-28 pixel sensors, were used to validate the Monte Carlo simulations. The beam profiles were extracted from the cluster maps, defined by the position of all clusters in x and y, for all 7 CMOS pixel sensors placed at different positions along the z-axis (see **Figure 2A** for the coordinate system). The beam profiles in x and y were obtained after integrating (averaging) the cluster maps over the perpendicular directions y and x, respectively. The profiles were used to adjust the initial beam parameters of the Monte Carlo simulations for 142.10 and 170.05 MeV. In a next step, the beam profiles were computed with the fiducial markers. For this, the profiles were obtained after integrating the cluster maps over a given window along the y-axis that was chosen according to the marker length.

2.3.4 Fluence Distribution Analysis

This study aims at determining the maximum perturbation and its position along the beam axis with high spatial resolution. For this, a three-dimensional (3D) fluence distribution was computed after reconstructing the trajectory of each particle crossing the tracker system. This distribution was computed from all tracks, which are defined by 3D vectors, reconstructed with the tracker placed behind the aquarium (sensors S5–S7 in **Figure 2A**), and extrapolated to the fiducial marker position. Voxels of $20 \times 20 \times 200$ m^3 were defined, and the fluence in each voxel was determined as the sum of all the tracks passing through this voxel. Therefore, the 3D fluence distribution scores the total number of intersections between the reconstructed tracks and the voxels. The 2D fluence distributions (referred to as fluence maps), extracted from the 3D fluence distributions, are presented in this study to quantify the propagation of the perturbation in the (x,z) plane. The fluence map was computed by integrating the tracks over a given window along the y-axis that was chosen according to the marker length. From the integrated fluence map, the perturbation at any position along the beam axis can be assessed. The fluence maps with and without marker were reconstructed, and the beam profiles were extracted at the position along the beam where the perturbation was maximum. The maximum fluence perturbation was then quantified by comparing the beam profiles (x,y) with and without marker. The fluence maps were computed for the case

TABLE 3 | Primary beam energy, FWHM at the isocenter, and range in water (calculated with LISE++) of the proton beams used for the measurements.

Energy (MeV)	FWHM (mm)	Range in water (mm)
142.10	11.7	143.6
169.02	10.0	194.3
170.05	10.0	196.4

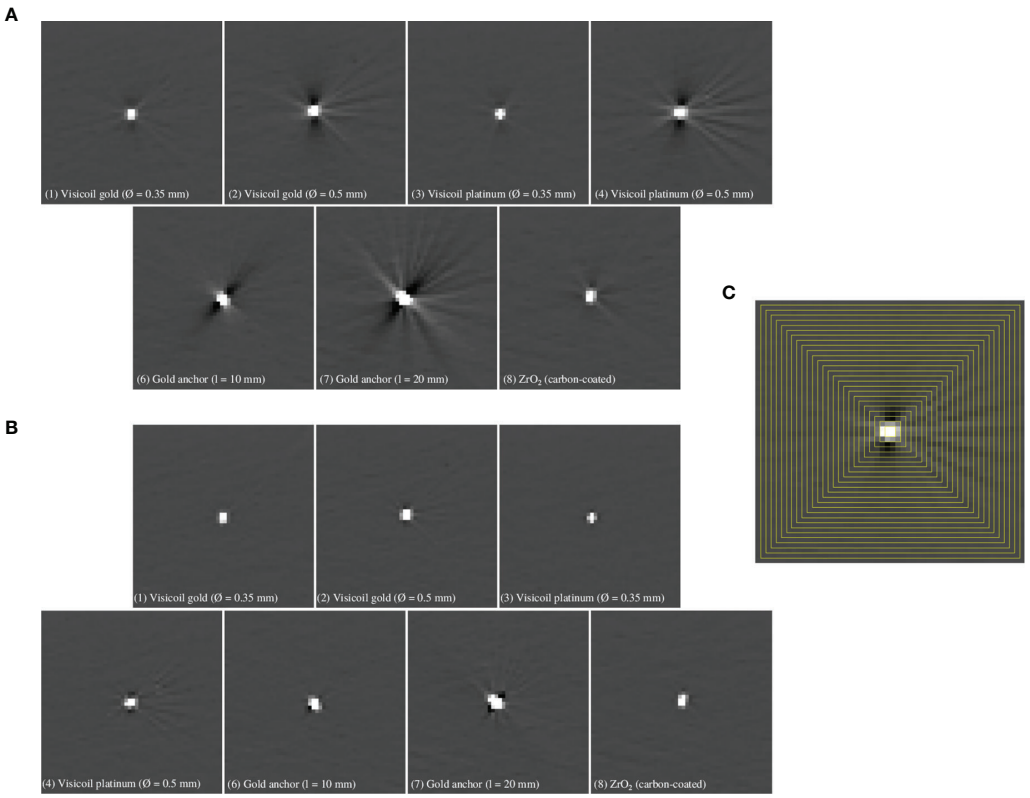

FIGURE 3 | Reconstructed images for conventional treatment planning CT **(A)** and with iMAR correction **(B)** of 0.5mm slice thickness for 7 different fiducial markers (**Table 1**). **(C)** Square-shaped rings (yellow lines) used to determine the minimum and maximum values as a function of the distance from the marker, as explained in *Section 2.2.1*.

of single-energy beams and for the modulated beam by the 2D RM. It is important to note that during the experiment the beam moved due to unintended drift effects of the ion optics, which made it difficult to use the reference measurement, in particular for the 2D RM case. Therefore, the beam profile from the reference measurement could not be used to quantify the perturbation. For this case, the beam profile of the corresponding maximum perturbation was computed, and the reference was defined as the fit of the profile without taking into account the perturbation. Since the beam was slightly shifted and tilted compared to the tracker system, the beam profiles obtained after the tracking were not perfectly Gaussian-like. Therefore, they were fitted by convoluting three Gaussian functions. This method was verified and validated on the beam profiles with a single energy, where the reference measurement could be used properly.

2.4 Monte Carlo Simulations

The Monte Carlo simulations were performed with the FLUKA2020 code version 0.10 (23–25). The default PRECISIO settings were used. In FLUKA, single Coulomb scattering events are condensed in a multiple scattering algorithm. Fluence and dose profiles were calculated using the USRBIN scorer.

2.4.1 Setup Geometry

The setup geometry of the FLUKA simulations reproduced the one used during the experiment. For this, several layers of different thicknesses and materials were placed along the beam axis. The beam nozzle, which is composed of several detectors and air gaps, was simulated by a water volume of 320mm length and 0.0115 g/cm^3. The Mimosa-28 sensors were simulated by a silicon volume of 50µm thickness, and the scoring volume was defined as the sensitive layer of the sensor of 14-µm thickness. The sensor is surrounded by a printed circuit board (PCB) of 1.7mm thickness. The PCB of the sensor was also implemented in the simulation since low-energy particles can be stopped in this material layer. The primary energy of the proton beams was chosen as the ones used during the experimental campaign (see **Table 3**). The simulations were also performed for an initial beam shift (and tilt), which means that the beam position and divergence in front of the exit window were set as the ones obtained from the CMOS measurements. The fiducial markers were designed as tubes for the 4 Visicoil markers and as cylinders for the Gold Anchor and the ZrO_2 markers. The approximations of the markers as cylinder/tube neglect the helical structure of the Visicoil and the bone shape of the ZrO_2 markers. Considering the size of these fine structures compared to the resolution of the

scoring grid, those assumptions are believed to be reasonable. The dimensions used for the Monte Carlo simulations are indicated in **Table 1**.

2.4.2 Benchmarking

To benchmark the Monte Carlo code FLUKA against the MIMOSA-28 pixel sensor measurements, the optical beam parameters (FWHM and divergence) were tuned to reproduce the measured lateral beam spread along the beam axis. The transport code SCATTMAN (1, 34) was used to extract the ion optical parameters (phase space), in particular the beam width and divergence in front of the vacuum exit window. The parameters were obtained based on the measured beam profiles and were used as initial parameters for the Monte Carlo simulations. The beam profiles from the Monte Carlo simulations were computed in the scoring volume, which represents the CMOS sensors, at different positions along the beam axis. First, the simulated beam profiles were compared to the measured ones on one hand without any target and on the other hand with the PE block and the water aquarium. Second, the simulations were performed with the PE block, the water aquarium, and the fiducial marker. For these simulations, the PCB of the sensor and the initial beam tilt and shift were also implemented. In addition, the primary beam energy of the Monte Carlo simulations was verified to the one calculated from the energy loss estimation in the sensors (35). To compare the perturbation from the fiducial markers, the 2D beam profiles were extracted at each sensor position for the simulated and experimental results. The beam profiles were then computed after integration over a given window along the *y*-axis that was chosen according to the marker length. The perturbations were quantified by comparing the beam profiles with and without fiducial markers.

2.4.3 Dose Distribution

The dose distributions were computed with a simple setup composed of a water phantom and the fiducial markers implanted at 15cm depth. A 5cm length SOBP from 14 to 19 cm (lateral extensions 5 × 5 cm^2) was simulated with several proton pristine Bragg peaks. The lowest and highest energies were set to 142 and 169 MeV as the ones used during the experiment, respectively. The dose distributions in the water phantom were scored as 2D maps to quantify the cold spots. The resolution of the 2D maps was 0.02 mm in *x* and 0.4 mm in *z*, after integrating over the length of the marker in *y*. A reference simulation without marker was also performed to quantify the cold spot. The maximum cold spot and its position along the beam axis could then be evaluated.

3 RESULTS

3.1 Imaging Study

3.1.1 Treatment Planning CT Streak Artifacts

The images from the treatment planning CT of 0.5mm slice thickness with and without iMAR correction are presented in **Figure 3** for 7 different markers (see **Table 1**). It is important to note that the markers are smaller than one voxel in the reconstruction. Therefore, the maximum HU values are determined by the marker density and partial volume effects.

The maximum and minimum gray levels of the recorded images with the treatment planning CT were computed for 7 fiducial markers, as described in Section 2.2.1. In **Figure 4**, the minimum and maximum values in Hounsfield units (HU) are shown as a function of the distance to the fiducial marker for the conventional planning CT and the one with iMAR correction.

For all fiducial markers, the maximum value reaches 3060 in the marker area, while for the Gold Anchor also -1024 is reached, even if the markers fill only a partial volume of the reconstructed voxels. Before treatment planning, these saturated voxels need to be overwritten by a realistic value. In **Table 4**, the distance from the fiducial marker position, at which the maximum and minimum values of the streak artifacts become lower than 3% of the background level, is summarized for the 7 fiducial markers for the conventional treatment planning CT and the one with iMAR correction. The folded Gold Anchor of 20mm length (7), which is also the heaviest marker, shows the strongest streak artifacts. The Visicoil markers (1) and (3) of 0.35mm diameter (gold and platinum) and the ZrO_2 marker (8), which are the

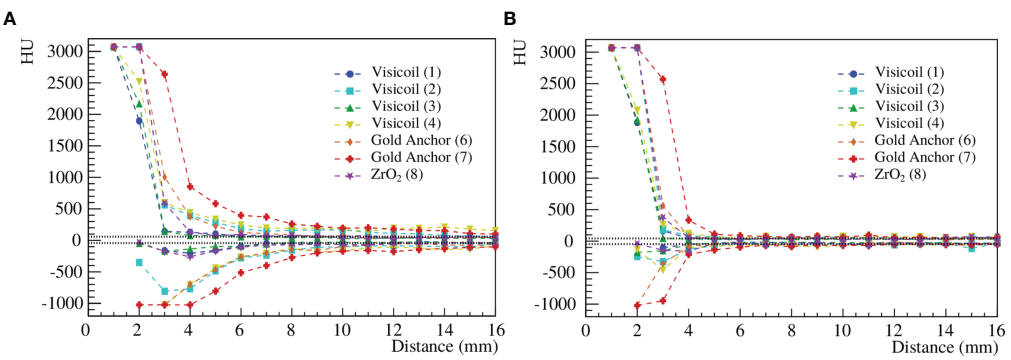

FIGURE 4 | Maximum and minimum HU as a function of the distance to the fiducial marker for the conventional treatment planning CT **(A)** and with iMAR correction **(B)** for 7 fiducial markers (**Table 1**).

TABLE 4 | Distance from the fiducial marker position, at which the streak artifacts become lower than 3% of the background level for 7 fiducial markers (**Table 1**), for the conventional treatment planning CT and the one with iMAR correction.

Marker number	1	2	3	4	6	7	8
CT distance artifacts (mm)	7	16	7	19	11	18	7
CT distance artifacts iMAR (mm)	4	5	4	5	5	6	5

lighter studied markers, are the ones producing less intense streak artifacts. The Viscoil markers (2) and (4) of 0.5mm diameter and the Gold Anchor of 10mm length (6) show similar values. **Figure 4B** shows that streak artifacts are significantly reduced when using an iMAR correction. The HU drops down to the background level around the marker, while for the conventional treatment planning CT, the artifacts propagate at further distances from the marker. Therefore, the application of an iMAR correction could significantly reduce the errors in dose calculation due to fiducial markers and should be investigated further in the future.

3.1.2 X-Ray Visibility

The images acquired during the X-ray measurements are shown in **Figure 5** for the different scenarios with and without collimation, as well as with and without bone slabs placed in front of the markers. The contrast of the different fiducial markers was computed as described in Section 2.2.2. In **Figure 6**, the contrast of 7 fiducial markers is shown for the X-ray imaging with the 4 different scenarios.

Figure 6 shows that the contrast is significantly improved when a collimation is applied during the imaging, which is the common practice in order to reduce the patient exposure. In a more realistic case, where a bone slab was placed in front, the contrast decreases. The heavier markers, with high-density materials and a mass larger than 10 mg, such as the Gold Anchor (7) and the two Visicoil markers of 0.5mm diameter (2) and (4), show a contrast of around 400. For the Gold Anchor (6) and the ZrO_2 (8) of mass between 5 and 10 mg, the contrast is around 300. For the smaller Visicoil markers (1) and (3) of mass lower than 5 mg, the contrast is around 200. However, all markers are visible on the images. The images from the in-room mobile CT study are shown in **Figure 7** for 7 fiducial markers. All markers are clearly visible with this imaging method. Streak artifacts are also present, but not particularly important when the images are not used for dose calculation.

3.2 Fluence Perturbation: CMOS Measurements

Fluence perturbations due to the fiducial markers are induced by multiple Coulomb scattering, which means that the perturbation varies along the beam axis. In addition, for low-energy beams, fiducial markers can also create considerable range shifts due to energy losses in the markers. In this section, the results of the maximum perturbation due to the fiducial markers were computed from the fluence map of all reconstructed tracks, as explained in *Section 2.3.4*.

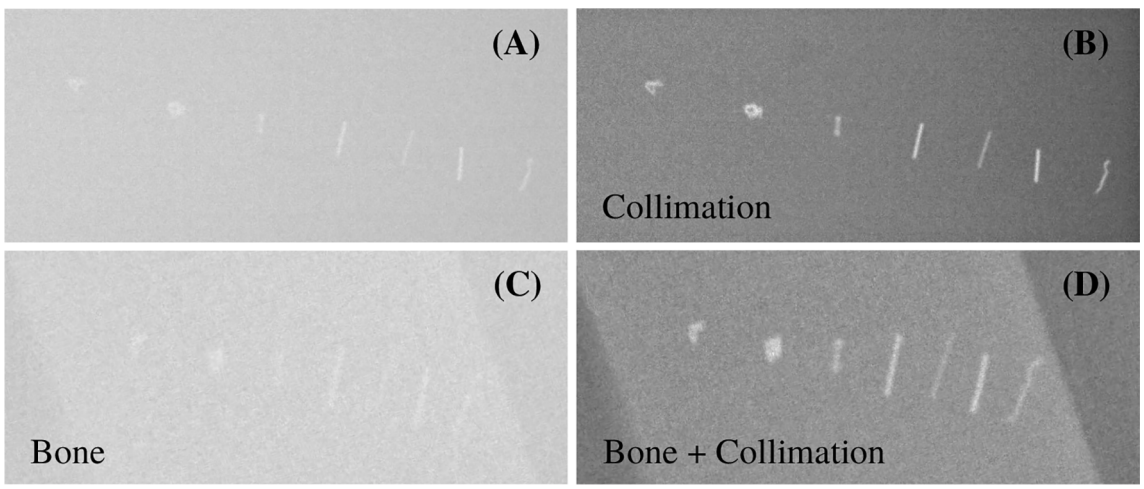

FIGURE 5 | X-ray images of 7 different fiducial markers for the different settings described in **Table 2**. From left to right: Gold Anchor (6), Gold Anchor (7), ZrO_2 (8), Viscoil (2), Visicoil (3), Visicoil (4), and Visicoil (1), listed in **Table 1**. **(A, B)** show the images without and with collimation. **(C, D)** show the images with the bone slabs in front of the markers without and with collimation, respectively.

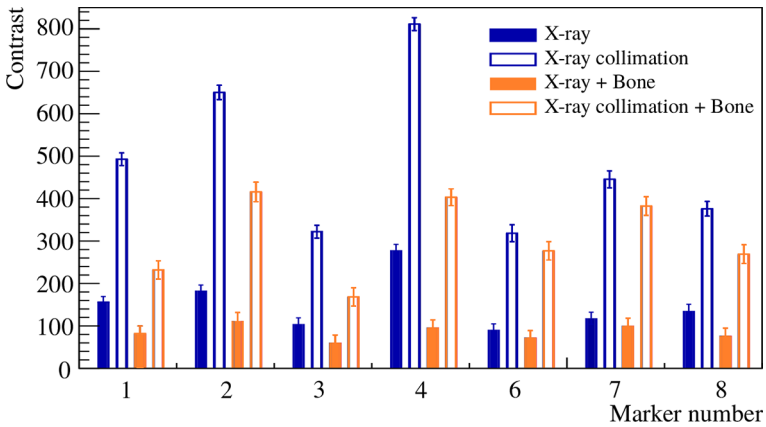

FIGURE 6 | Contrast of different fiducial markers (listed in **Table 1**) from the X-ray imaging study for the different settings of **Table 2**.

3.2.1 Single-Energy Proton Beam

In this study, the perturbation of proton beams was measured for 6 fiducial markers and two different energy proton beams of 142.10 and 169.02 MeV. To determine the maximum perturbation, the beam profile with marker was compared to the beam profile without marker for the same integrated window at the same position along the beam axis. In **Figure 8**, an example of fluence maps and the corresponding profiles from the maximum fluence perturbations are shown for 4 fiducial markers and different energy proton beams. The zero positions in x and z are the coordinates of the fiducial marker position. The statistical uncertainties on the maximum perturbation values were calculated as the quadratic sum of the uncertainty on the beam profiles with and without marker. The uncertainty on the z position, where the maximum perturbation is present, was determined as 1.5 mm, comprising the uncertainty of the sensor positioning and the uncertainty of the reconstructed track. A summary of the maximum fluence perturbation values from the fiducial markers and their corresponding position along the beam axis is listed in **Table 5**. These values were obtained from the back-projected tracks to the marker position, measured in air (see experimental setup in **Figure 2A**). The maximum

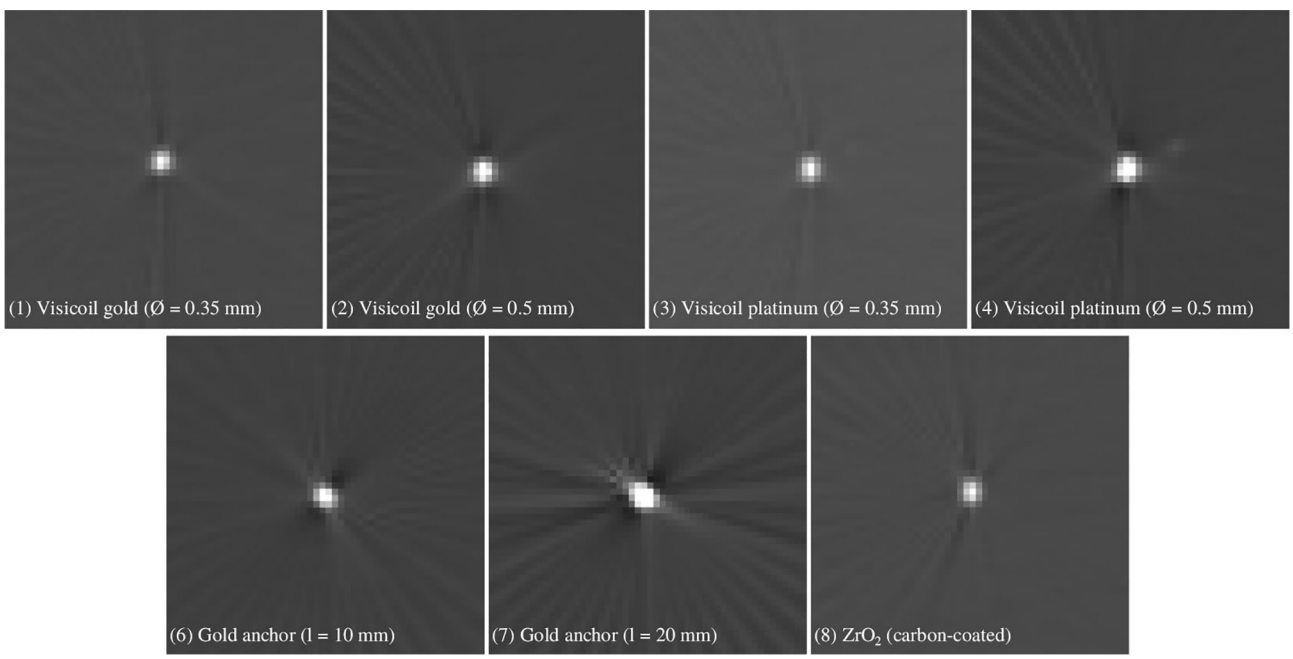

FIGURE 7 | In-room mobile CT images of 7 different fiducial markers listed in **Table 1**.

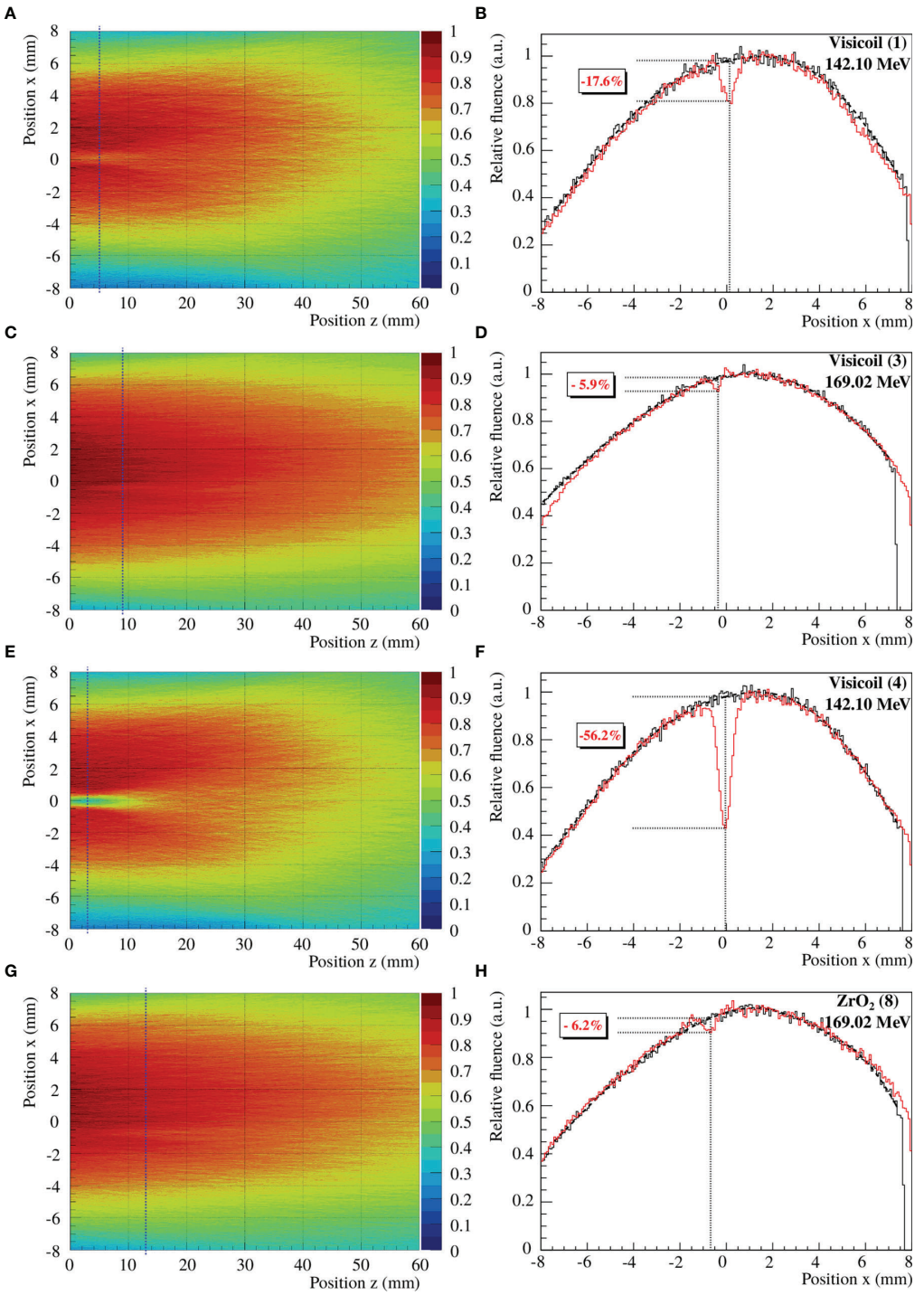

FIGURE 8 | Measured fluence maps and beam profiles of 142.10 and 169.02MeV proton beams through Visicoil (1), Visicoil (3), Visicoil (4), and ZrO_2 (8), placed at position zero along the *z*-axis and *x*-axis. **(A, C, E, G)** show the fluence maps reconstructed from all tracks. **(B, D, F, H)** show their corresponding profile at the *z* position where the perturbation is the strongest. The black vertical dash-dotted line on the fluence map represents the corresponding position along the beam axis where the fluence perturbation is maximum. In **(B, D, F, H)**, the red line shows the profile at this position with the marker, while the black line shows the profile without marker for the same *z* position. In the same panels, the vertical dotted line indicates the position in *x* of the maximum perturbation while the dotted horizontal lines quantify the strength of the perturbation.

TABLE 5 | Maximum fluence perturbation values and their position along the beam axis for the different fiducial markers for 142.10 and 169.02 MeV proton beams.

Marker	142.10 MeV protons		169.02 MeV protons	
	Perturbation (%)	*z* position (mm)	Perturbation (%)	*z* position (mm)
Visicoil (1)	17.6 ± 1.3	5 ± 1.5	3.1 ± 1.4	9 ± 1.5
Visicoil (2)	52.5 ± 1.2	3 ± 1.5	14.5 ± 1.3	8 ± 1.5
Visicoil (3)	20.2 ± 1.3	5 ± 1.5	5.9 ± 1.4	9 ± 1.5
Visicoil (4)	56.2 ± 1.2	3 ± 1.5	15.4 ± 1.4	9 ± 1.5
Gold Anchor (5)	17.1 ± 1.3	2 ± 1.5	7.3 ± 1.4	7 ± 1.5
ZrO_2 (8)	58.5 ± 1.1	3 ± 1.5	6.2 ± 1.4	13 ± 1.5

The given error on the perturbation value is the statistical uncertainty.

perturbations and their position vary as a function of the markers and the primary beam energy. The lower the energy is, the stronger is the effect induced by the marker. Moreover, markers with high density and high atomic number create stronger and larger perturbations. For 142.10MeV protons, the perturbation is significantly higher for the fiducial markers with diameter ≥ 0.5 mm, which additionally stop the low-energy particles and induce a significant range shift.

3.2.2 2D Range Modulator

In this study, the perturbation of proton beams was measured for 4 fiducial markers, and the fluence maps were reconstructed for a 170.05MeV proton beam modulated by a 2D RM in order to obtain a more realistic case (see **Figure 2B** for the position of the marker). To determine the maximum fluence perturbation, the beam profile with the marker was computed for a certain integrated window. As explained in *Section 2.3.4*, the reference measurement was considered as the fit of the beam profile without taking into account the perturbation. In **Figure 9**, the fluence maps and the corresponding profiles of the maximum fluence perturbations are shown for the studied fiducial markers. The uncertainties were computed as the ones obtained for the single-energy beams. A summary of the maximum perturbation values of the fiducial markers and their corresponding position along the beam axis are listed in **Table 6**. As for the single-energy beams, these values were obtained from the back-projected tracks to the marker position, measured in air (see experimental setup in **Figure 2A**).

3.3 Monte Carlo Simulations

3.3.1 Initial Beam Parameter Tuning

Monte Carlo simulations were performed with the FLUKA code (23–25), as described in Section 2.4. The initial beam optics were tuned to reproduce the experimental data as explained in Section 2.4.2. In **Table 7**, the initial beam width and beam divergence, extracted from SCATTMAN (1, 34) and introduced in the FLUKA simulations, are listed for 142 and 170 MeV. The initial beam optics for 169 and 170 MeV were found to be the same.

In **Figure 10**, the beam width as a function of the distance to the vacuum exit window was computed for 142 and 170 MeV with the initial ion beam optics listed in **Table 7**. The results are shown for the SCATTMAN code, as well as for the CMOS measurements and the FLUKA simulations. The Monte Carlo simulations were performed with and without including the initial beam shift (and tilt) and the PCB of the sensors (as explained in Section 2.4.1).

In all cases, the beam width of the FLUKA simulations and the CMOS measurements are in good agreement. The good agreement between SCATTMAN and the measurements were expected since the ion optical parameters in the SCATTMAN model were adapted from the CMOS measurements. In **Figure 10C**, deviations can be observed between the FLUKA simulations and the CMOS measurements. However, these deviations are significantly reduced when the simulation takes into account the PCB layer and the initial beam tilt. For 142 MeV with the PE block and the water aquarium, the proton beam has an energy of around 8 MeV in the last sensor, which is equivalent to around 2mm range in water. Therefore, the PCB of the first set of sensors plays a role in the energy loss, and this effect becomes significant only for low-energy beams.

3.3.2 Fluence Perturbation Comparison With Marker

The FLUKA simulations with fiducial markers were compared to the CMOS measurements following the simulated setup described in *Section 2.4.1*. The beam profiles were obtained with the Monte Carlo simulations and the CMOS measurements as explained in *Section 2.4.2*. In **Figure 11**, the beam profiles at sensor 5 position (see **Figure 2A**) are shown for the Visicoil (3) for 142MeV protons and for the Visicoil (2) for 169MeV protons.

In **Tables 8**, **9**, the fluence perturbation values are compared for the FLUKA simulations and the CMOS measurements for 142 and 169MeV protons, respectively. The fluence perturbations were computed for several positions (sensor 5, sensor 6, and sensor 7) to compare its propagation along the beam axis.

The results show a good agreement between the Monte Carlo simulations and the CMOS measurements within the uncertainties. For 142MeV protons, the deviations are bigger than for 169 MeV. This was expected since the primary protons of 142 MeV have an energy of around 10 MeV behind the water aquarium, compared to around 80 MeV in the case of the 169MeV primary proton beam. This means that small variations of the layer thicknesses of the simulated geometry, in the case of 142MeV protons, lead to larger fluctuations of the energy losses compared to the 169MeV proton beam. Therefore, small geometrical uncertainties in the simulated setup have a stronger impact on the perturbation values for low-energy beams. However, the results from both the simulations and the

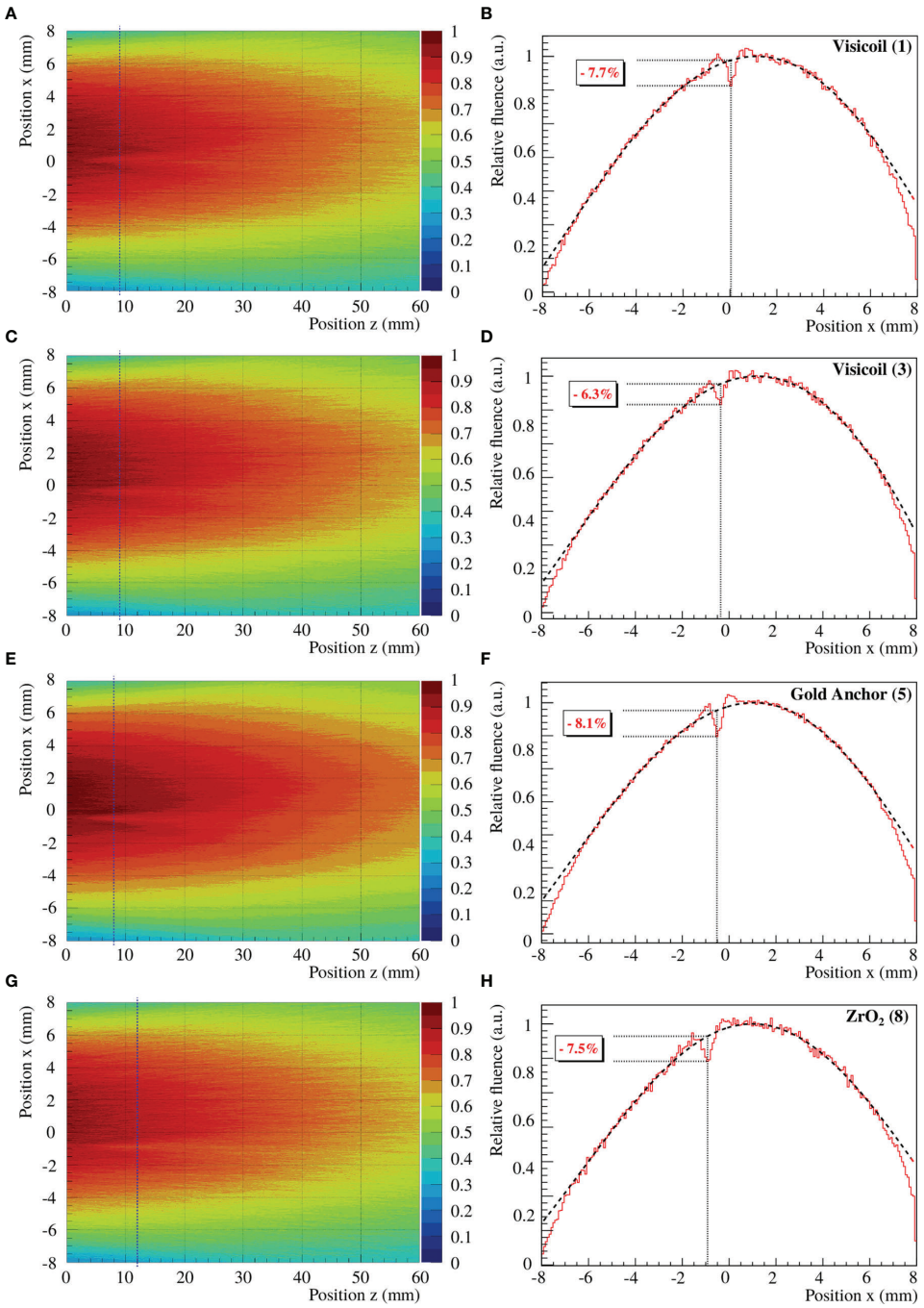

FIGURE 9 | **(A, C, E, G)** show the fluence maps reconstructed from all tracks. **(B, D, F, H)** show their corresponding profile at the z position where the perturbation is the strongest. The black vertical dash-dotted line on the fluence map represents the corresponding position along the beam axis where the fluence perturbation is maximum. In **(B, D, F, H)**, the red line shows the profile at this position with the marker, while the black line shows the profile without marker for the same z position. In the same panels, the vertical dotted line indicates the position in x of the maximum perturbation while the dotted horizontal lines quantify the strength of the perturbation.

experiments are in good agreement, showing the same tendencies. The Monte Carlo simulations could reproduce correctly the perturbation and its propagation along the beam axis.

3.3.3 Dose Perturbation: FLUKA Simulations

Compared to our previous work (20), where only fluence measurements were performed, dose distributions were also simulated in the present work. The dose distributions were

TABLE 6 | Maximum fluence perturbation values and their position along the beam axis for the different fiducial markers for the 170.05MeV proton beam modulated by a 2D RM.

Marker	Perturbation (%)	*z* position (mm)
Visicoil (1)	7.7 ± 1.4	9 ± 1.5
Visicoil (3)	6.3 ± 1.4	9 ± 1.5
Gold Anchor (5)	8.1 ± 1.3	8 ± 1.5
ZrO_2 (8)	7.5 ± 1.3	12 ± 1.5

The given error on the perturbation value is the statistical uncertainty.

computed following the description in **Section 2.4.3**, where a 5cm SOBP was created with protons and the fiducial markers were placed at the beginning of the SOBP at the 15cm depth. The simulated depth–dose profiles showed a very similar distribution to the measured ones from other experiments (32). In **Figure 12**, the dose maps are shown for the gold Visicoil (∅ = 0.35 mm) and the platinum Visicoil (∅ = 0.5 mm).

In **Figure 13**, the depth–dose profiles in the central line obtained from the dose maps are presented for all the studied markers. A reference simulation without marker is also shown in the same figure. The maximum perturbations and their position behind the fiducial marker along the beam axis are listed in **Table 10** for 6 fiducial markers. The two Visicoil markers of 0.5mm diameter (2) and (4), which are the heaviest markers used in this study, show the strongest perturbation of around 8%. The Gold Anchor (5) shows a maximum cold spot of around 6%, while the other lighter markers (1), (3), and (8) produce a perturbation of around 3–4%. The dose perturbations presented in this section show the same tendency as for the fluence measurements presented in *Section 3.2.2*.

4 DISCUSSION

In this work, a comprehensive study was performed for fiducial markers used for image guidance in proton beam therapy. Three main criteria for these markers, which are streak artifacts on treatment planning CT, visibility on daily imaging methods, and dose perturbations during particle therapy, were evaluated. Fiducial markers composed of different materials (gold, platinum, and ZrO_2) and with different geometries were studied. The markers of high-density materials (such as gold and platinum) had a diameter ≤0.5 mm, which is recommended for particle therapy (8, 20).

The streak artifacts on treatment planning CT, reconstructed with and without iMAR correction, were quantified for 7 fiducial markers. The maximum and minimum HU were computed as a function of the distance to the fiducial markers. The gold and platinum Visicoil of 0.5mm diameter and the two Gold Anchor markers, which have a mass bigger than 6 mg, were the ones inducing the strongest streak artifacts. The distance at which the streak artifacts were lower than 3% of the background level was found to be bigger than 10 mm for these markers, and 7 mm for the gold and platinum Visicoil of 0.35mm diameter and the ZrO_2 markers, which were lighter than 6 mg. For the case of treatment planning CT with iMAR correction, the streak artifacts are significantly reduced. The distance at which they are lower than 3% of the background level is reduced by a factor 2 compared to the conventional treatment planning CT in all cases. However, the iMAR correction would need to be further investigated to be applied for clinical treatment planning. It is important to note that the markers are smaller than a CT voxel; however, they appear in up to 4 neighboring voxels. Before treatment planning, the voxels need to be overwritten by a realistic value, considering the partial volumes and the stopping power of the marker material relative to water. This could lead to inaccurate range predictions around the marker.

The visibility of fiducial markers on X-ray projections was measured in 4 different scenarios with and without collimation, as well as with and without bone slabs in front of the markers. As expected, the contrast of the fiducial markers with bone slabs is significantly reduced. In a realistic case, with bone slabs and collimation, the heavier the marker is and higher is its density, the stronger the contrast is. However, all markers were visible in all cases.

The fluence perturbation from different fiducial markers was measured for proton beams with an advanced technique by using high resolution CMOS pixel sensors. With this method, 3D fluence distributions could be computed after reconstructing the trajectory of each particle. The measurements were performed with two single-energy beams and with a modulated beam using a 2D range modulator, producing an SOBP of 5cm length. The maximum fluence perturbation, created behind the fiducial marker and its position along the beam axis, was quantified, using the 2D fluence map. As in our previous study (20), the perturbations creating a small overdosage were not reported since it is less critical than a local underdosage that could cause a recurrence of the tumor. The created fluence perturbations can be caused by edge scattering but also due to particles stopping in the marker when the particle beam is at the end of its range. Both phenomena were observed in this study for the single-beam energy experiments, using 142.10 and 169.02MeV protons. For fiducial markers of diameter smaller than 0.5 mm, the perturbations were found to be lower than 8%, while the two Visicoil markers of 0.5 mm showed a maximum perturbation of around 15% for 169.02MeV protons. In the case of the lower energy proton beam, the maximum fluence perturbation was found to be around 50% for the markers thicker than 0.5 mm. These strong perturbations were due to high-energy losses in the fiducial markers, which fully stopped the low-energy proton beam. The perturbations induced by the Visicoil markers of 0.35mm diameter, the Gold Anchor, and the ZrO_2 marker were also measured for a modulated beam. These measurements provided a more realistic situation of a mixed beam, where the markers were positioned at the entrance of a 5cm SOBP.

TABLE 7 | Initial ion beam optics (FWHM and divergence at the vacuum exit window) used for the Monte Carlo simulations for 142 and 170 proton beams.

Energy (MeV)	FWHM (mm)	Divergence (mrad)
142	3.5	7.0
170	3.5	7.5

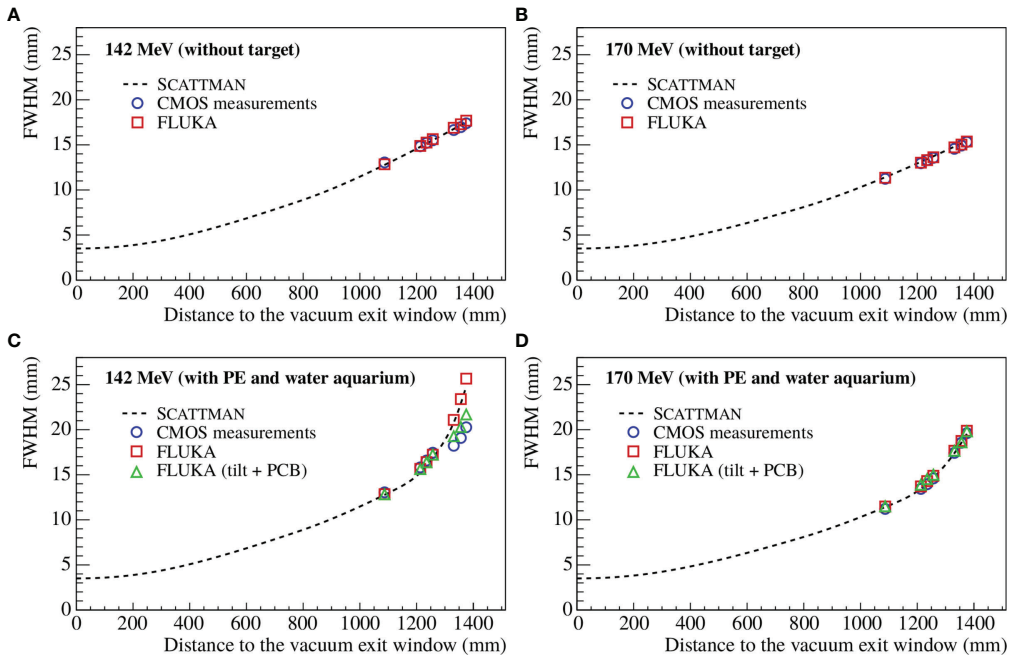

FIGURE 10 | Beam width as a function of the distance to the vacuum exit window for 142 MeV **(A, C)** and 170 MeV **(B, D)** with the initial beam optics from **Table 7**. The beam width was computed for SCATTMAN, the CMOS measurements, and the FLUKA simulation without target **(A, B)** and with the PE block and the water aquarium **(C, D)**. The Monte Carlo simulations were performed with and without including the initial beam tilt and the PCB of the sensors.

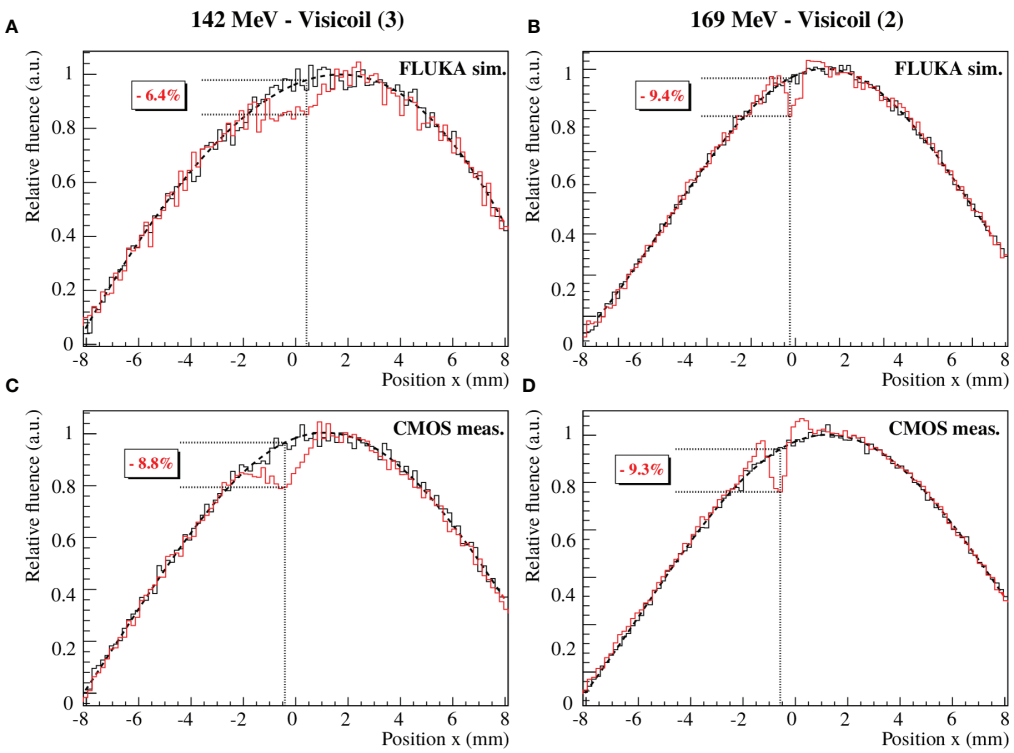

FIGURE 11 | Beam profile comparison between the FLUKA simulations **(A, B)** and the CMOS measurements **(C, D)** for 142MeV protons passing through the Visicoil (3) **(A, C)** and 169MeV protons passing through the Visicoil (2) **(B, D)**. The red and black lines show the beam profiles with and without marker, respectively.

TABLE 8 | Comparison of the fluence perturbation values at several positions (sensor 5, sensor 6, and sensor 7) between the FLUKA simulations (Sim.) and the CMOS measurements (Meas.) for the different fiducial markers for the 142MeV proton beam.

Marker	Perturbation on S5 (%)		Perturbation on S6 (%)		Perturbation on S7 (%)	
	Sim.	Meas.	Sim.	Meas.	Sim.	Meas.
Visicoil (1)	8.2 ± 1.4	9.0 ± 1.4	3.4 ± 1.4	4.2 ± 1.4	1.8 ± 1.4	3.7 ± 1.4
Visicoil (2)	15.8 ± 1.3	19.1 ± 1.3	8.0 ± 1.4	7.2 ± 1.4	4.1 ± 1.4	4.7 ± 1.4
Visicoil (3)	6.4 ± 1.4	8.8 ± 1.4	3.4 ± 1.4	5.0 ± 1.4	3.1 ± 1.4	3.1 ± 1.4
Visicoil (4)	17.2 ± 1.3	21.4 ± 1.3	6.8 ± 1.4	8.3 ± 1.4	3.8 ± 1.4	3.9 ± 1.4
Gold Anchor (5)	9.4 ± 1.4	11.3 ± 1.3	3.8 ± 1.4	5.2 ± 1.4	2.4 ± 1.4	3.0 ± 1.4
ZrO_2 (8)	14.0 ± 1.4	24.9 ± 1.3	6.4 ± 1.4	9.7 ± 1.4	3.8 ± 1.4	2.4 ± 1.4

The given error on the perturbation value is the statistical uncertainty.

The created fluence perturbations were found to be between 6% and 8% in all cases, which is closer to the perturbations created for 169.02MeV protons. This was expected since the marker was positioned in the plateau region of the pristine Bragg peak with the higher weight in the SOBP. The maximum perturbation depends on the position of the fiducial marker. The closer the marker is to the end of the SOBP, the bigger the perturbation is due to the stronger scattering and higher energy losses of the protons with the higher weighted pristine Bragg peak (36).

In addition, Monte Carlo simulations were performed with FLUKA (25) to compute a 5cm length SOBP, from 14 to 19 cm, created with protons in a water target. Dose perturbations induced by the fiducial marker were computed, and the created cold spots were quantified. The simulations, with and without fiducial marker, were first validated against the experimental measurements performed with the CMOS sensors. The FLUKA simulations and CMOS measurements were in good agreement. The perturbation of the different fiducial markers was computed for a marker placed at 15cm depth at the beginning of the SOBP. The maximum cold spot was found to be around 8% for the heaviest markers and around 4% for the smallest ones.

In this work, the perturbations were measured and simulated for a single field. However, in a realistic case, a patient would be treated with multiple fields, partly compensating the perturbation from one field to another (37). Moreover, daily alignment, which is generally performed with the bony structure of the patient, can be performed with an accuracy of only 0.5 cm. This would also blur out the effect during the particle therapy treatment between different fractions. However, the perturbations remain the same in the tissue for every fraction.

5 CONCLUSIONS

In this work, streak artifacts on treatment planning CT, visibility on daily imaging, and dose perturbations during proton therapy were studied for different fiducial markers that are used for image guidance in radiotherapy. The markers of different geometries were composed of different materials such as gold, platinum, and ZrO_2. The streak artifacts on a treatment planning CT were found to be the lowest for fiducial markers with a mass lower than 6 mg. However, the treatment planning CT reconstructed with iMAR correction showed a significant reduction of the streak artifacts for all markers. Visibility on X-ray projections was also evaluated, and a better contrast for heavier markers was found. However, all markers were visible in all studied scenarios. Imaging with in-room mobile CT was also performed showing a clear visibility from all markers. An advanced measurement method was used to quantify fluence perturbations due to fiducial markers in proton therapy, using high resolution CMOS pixel sensors. Based on the fluence maps, the measurements showed that the perturbations due to fiducial markers are reduced for small and low-density markers of mass lower than 6 mg. Monte Carlo simulations were performed with a comparable setup as the one used during the experiments. The simulations were validated against the experiments with and without fiducial marker, showing good agreement with the experimental data after adjusting properly the ion optical parameters (beam width and divergence). Dose maps were simulated for an SOBP in water created with protons, where the fiducial marker was positioned at the beginning of the SOBP. From this work, fiducial markers with a low mass, such as the gold and platinum Visicoil of 0.35mm diameter as well as ZrO_2 (carbon-

TABLE 9 | Comparison of the fluence perturbation values at several positions (sensor 5, sensor 6, and sensor 7) between the FLUKA simulations (Sim.) and the CMOS measurements (Meas.) for the different fiducial markers for the 169MeV proton beam.

Marker	Perturbation on S5 (%)		Perturbation on S6 (%)		Perturbation on S7 (%)	
	Sim.	Meas.	Sim.	Meas.	Sim.	Meas.
Visicoil (1)	4.6 ± 1.4	3.7 ± 1.4	2.0 ± 1.4	2.5 ± 1.4	2.2 ± 1.4	1.6 ± 1.4
Visicoil (2)	9.4 ± 1.4	9.3 ± 1.4	4.6 ± 1.4	4.0 ± 1.4	3.6 ± 1.4	3.3 ± 1.4
Visicoil (3)	5.2 ± 1.4	4.6 ± 1.4	2.5 ± 1.4	2.8 ± 1.4	2.1 ± 1.4	2.5 ± 1.4
Visicoil (4)	12.3 ± 1.4	12.1 ± 1.4	5.4 ± 1.4	6.9 ± 1.4	3.9 ± 1.4	4.6 ± 1.4
Gold Anchor (5)	5.2 ± 1.4	4.2 ± 1.4	2.1 ± 1.4	2.4 ± 1.4	1.5 ± 1.4	1.6 ± 1.4
ZrO_2 (8)	6.1 ± 1.4	5.3 ± 1.4	3.1 ± 1.4	3.2 ± 1.4	2.9 ± 1.4	2.5 ± 1.4

The given error on the perturbation value is the statistical uncertainty.

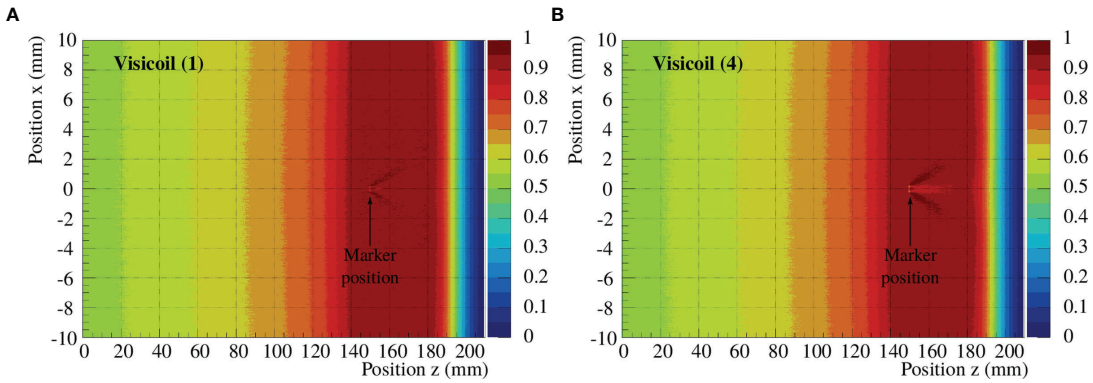

FIGURE 12 | Dose maps for an SOBP created with protons in water, covering 5 cm in depth. The pristine Bragg curves were generated with the Monte Carlo code FLUKA and superimposed to obtain the SOBP. The dose maps are shown for the Visicoil (1) **(A)** and the Visicoil (3) **(B)**, placed at 15 cm depth.

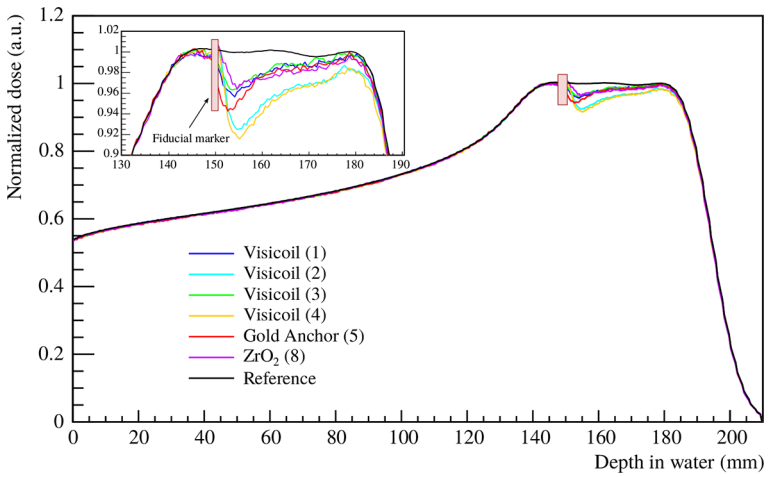

FIGURE 13 | SOBP created with protons in water, covering 5 cm in depth. The depth–dose profiles were extracted from the central line of the dose maps. The black line shows the reference measurement without marker, while the colored lines show the SOBP with a fiducial marker placed at 15cm depth. The FLUKA simulations were performed for 6 fiducial markers (**Table 1**).

TABLE 10 | Maximum cold spot values and their position behind the fiducial marker along the beam axis for 6 different markers (**Table 1**), computed with FLUKA simulations.

Marker	Cold spot (%)	*z* position (mm)
Visicoil (1)	4.3 ± 1.4	4.1 ± 0.5
Visicoil (2)	7.5 ± 1.4	4.6 ± 0.5
Visicoil (3)	3.6 ± 1.4	3.6 ± 0.5
Visicoil (4)	8.4 ± 1.4	5.1 ± 0.5
Gold Anchor (5)	5.7 ± 1.4	2.6 ± 0.5
ZrO_2 (8)	3.4 ± 1.4	4.6 ± 0.5

The given error on the cold spot value is the statistical uncertainty.

coated), can be recommended for image guidance in proton therapy since they provide a good trade-off between visibility versus dose perturbation. In principle, even smaller markers could be used as long as they are still visible on the daily imaging method.

DATA AVAILABILITY STATEMENT

The original contributions presented in the study are included in the article/supplementary material. Further inquiries can be directed to the corresponding author.

AUTHOR CONTRIBUTIONS

Conceptualization and methodology: C-AR, FH, CS, and UW. Investigation: C-AR, FH, and CS. Resources: OJ, SE, KH, and SB. Project administration, OJ, SE, KH, SB, MD, and UW. Original draft of the manuscript: C-AR. All authors contributed to the article and approved the submitted version.

ACKNOWLEDGMENTS

We would like to thank the Heidelberg Ion Therapy Center (HIT) for providing the beam to perform several measurements. We thank RadioMed, an IZI Medical company, for providing the Visicoil fiducial markers studied in this work. We also want to thank the mechanical workshop at GSI for their help for building many mechanical parts to improve the experimental setup. We would like to thank Dr. Lennart Volz for the fruitful explanations about imaging.

REFERENCES

1. Schardt D, Elsässer T, Schulz-Ertner D. Heavy-Ion Tumor Therapy: Physical and Radiobiological Benefits. *Rev Mod Phys* (2010) 82:383. doi: 10.1103/RevModPhys.82.383
2. Durante M, Orecchia R, Loeffler JS. Charged-Particle Therapy in Cancer: Clinical Uses and Future Perspectives. *Nat Rev Clin Oncol* (2017) 14:483. doi: 10.1038/nrclinonc.2017.30
3. Balter JM, Sandler HM, Lam K, Bree RL, Lichter AS, Haken RKT. Measurement of Prostate Movement Over the Course of Routine Radiotherapy Using Implanted Markers. *Int J Radiat Oncol Biol Phys* (1995) 31:113–8. doi: 10.1016/0360-3016(94)00382-U
4. Crook J, Raymond Y, Salhani D, Yang H, Esche B. Prostate Motion During Standard Radiotherapy as Assessed by Fiducial Markers. *Radiother Oncol* (1995) 37:35–42. doi: 10.1016/0167-8140(95)01613-L
5. Haken RT, Forman J, Heimburger D, Gerhardsson A, McShan D, Perez-Tamayo C, et al. Treatment Planning Issues Related to Prostate Movement in Response to Differential Filling of the Rectum and Bladder. *Int J Radiat Oncol Biol Phys* (1991) 20 6:1317–24. doi: 10.1016/0360-3016(91)90244-X
6. Coronel E, Cazacu I, Sakuraba A, Luzuriaga Chavez A, Uberoi A, Geng Y, et al. EUS-Guided Fiducial Placement for GI Malignancies: A Systematic Review and Meta-Analysis. *Gastrointest Endosc* (2019) 89:659–70.e18. doi: 10.1016/j.gie.2018.10.047
7. Bhutani MS, Herman JM. Endoscopic Ultrasound–Guided Fiducial Placement for Gastrointestinal Malignancies. *Gastroenterol Hepatol* (2019) 15:167.
8. Habermehl D, Henkner K, Ecker S, Jäkel O, Debus J, Combs SE. Evaluation of Different Fiducial Markers for Image-Guided Radiotherapy and Particle Therapy. *J Radiat Res* (2013) 54:i61–8. doi: 10.1093/jrr/rrt071
9. Handsfield LL, Yue NJ, Zhou J, Chen T, Goyal S. Determination of Optimal Fiducial Marker Across Image-Guided Radiation Therapy (IGRT) Modalities: Visibility and Artifact Analysis of Gold, Carbon, and Polymer Fiducial Markers. *J Appl Clin Med Phys* (2012) 13:181–9. doi: 10.1120/jacmp.v13i5.3976
10. Slagowski JM, Colbert LE, Cazacu IM, Singh BS, Martin R, Koay EJ, et al. Evaluation of the Visibility and Artifacts of 11 Common Fiducial Markers for Image Guided Stereotactic Body Radiation Therapy in the Abdomen. *Pract Radiat Oncol* (2020) 10:434–42. doi: 10.1016/j.prro.2020.01.007
11. Huang JY, Kerns JR, Nute JL, Liu X, Balter PA, Stingo FC, et al. An Evaluation of Three Commercially Available Metal Artifact Reduction Methods for CT Imaging. *Phys Med Biol* (2015) 60:1047–67. doi: 10.1088/0031-9155/60/3/1047
12. Highland VL. Some Practical Remarks on Multiple Scattering. *Nucl Instrum Meth* (1975) 129:497–9. doi: 10.1016/0029-554X(75)90743-0
13. Highland. Erratum. *Nucl Instrum Meth* (1979) 161:171. doi: 10.1016/0029-554X(79)90379-3
14. Newhauser W, Fontenot J, Koch N, Dong L, Lee A, Zheng Y, et al. Monte Carlo Simulations of the Dosimetric Impact of Radiopaque Fiducial Markers for Proton Radiotherapy of the Prostate. *Phys Med Biol* (2007) 52:2937. doi: 10.1088/0031-9155/52/11/001
15. Giebeler A, Fontenot J, Balter P, Ciangaru G, Zhu R, Newhauser W. Dose Perturbations From Implanted Helical Gold Markers in Proton Therapy of Prostate Cancer. *J Appl Clin Med Phys* (2009) 10:63–70. doi: 10.1120/jacmp.v10i1.2875
16. Herrmann R, Carl J, Jäkel O, Bassler N, Petersen JB. Investigation of the Dosimetric Impact of a Ni-Ti Fiducial Marker in Carbon Ion and Proton Beams. *Acta Oncol* (2010) 49:1160–4. doi: 10.3109/0284186X.2010.505934
17. Cheung J, Kudchadker RJ, Zhu XR, Lee AK, Newhauser WD. Dose Perturbations and Image Artifacts Caused by Carbon-Coated Ceramic and Stainless Steel Fiducials Used in Proton Therapy for Prostate Cancer. *Phys Med Biol* (2010) 55:7135. doi: 10.1088/0031-9155/55/23/s13
18. Huang JY, Newhauser WD, Zhu XR, Lee AK, Kudchadker RJ. Investigation of Dose Perturbations and the Radiographic Visibility of Potential Fiducials for Proton Radiation Therapy of the Prostate. *Phys Med Biol* (2011) 56:5287. doi: 10.1088/0031-9155/56/16/014
19. Gleeson FC, Tryggestad EJ, Remmes NB, Beltran CJ, Kruse JJ, Haddock MG, et al. Knowledge of Endoscopic Ultrasound-Delivered Fiducial Composition and Dimension Necessary When Planning Proton Beam Radiotherapy. *Endosc Int Open* (2018) 6:E766–8. doi: 10.1055/a-0588-4800
20. Reidel CA, Schuy C, Horst F, Ecker S, Finck C, Durante M, et al. Fluence Perturbation From Fiducial Markers Due to Edge-Scattering Measured With Pixel Sensors for ^{12}C Ion Beams. *Phys Med Biol* (2020) 65(8):085005. doi: 10.1088/1361-6560/ab762f
21. Haberer T, Debus J, Eickhoff H, Jäkel O, Schulz-Ertner D, Weber U. The Heidelberg Ion Therapy Center. *Radiother Oncol* (2004) 73:S186–90. doi: 10.1016/S0167-8140(04)80046-X
22. Valin I, Hu-Guo C, Baudot J, Bertolone G, Besson A, Colledani C, et al. A Reticle Size CMOS Pixel Sensor Dedicated to the STAR HFT. *J Instrum* (2012) 7:C01102. doi: 10.1088/1748-0221/7/01/C01102
23. Ferrari A, Sala PR, Fasso A, Ranft J. Fluka: A Multi-Particle Transport Code. (2005) CERN-2005-10. doi: 10.2172/877507
24. Böhlen T, Cerutti F, Chin M, Fassò A, Ferrari A, Ortega P, et al. The FLUKA Code: Developments and Challenges for High Energy and Medical Applications. *Nucl Data Sheets* (2014) 120:211–4. doi: 10.1016/j.nds.2014.07.049
25. Battistoni G, Bauer J, Boehlen TT, Cerutti F, Chin MPW, Dos Santos Augusto R, et al. The FLUKA Code: An Accurate Simulation Tool for Particle Therapy. *Front Oncol* (2016) 6:116. doi: 10.3389/fonc.2016.00116
26. Schneider CA, Rasband WS, Eliceiri KW. NIH Image to Imagej: 25 Years of Image Analysis. *Nat Methods* (2012) 9:671. doi: 10.1038/nmeth.2089
27. Finck C, Karakaya Y, Reithinger V, Rescigno R, Baudot J, Constanzo J, et al. Study for Online Range Monitoring With the Interaction Vertex Imaging Method. *Phys Med Biol* (2017) 62:9220. doi: 10.1088/1361-6560/aa954e
28. Brun R, Rademakers F. ROOT – an Object Oriented Data Analysis Framework. *Nucl Instrum Meth A* (1997) 389:81–6. doi: 10.1016/S0168-9002(97)00048-X
29. Agostinelli S, Allison J, Amako K, Apostolakis J, Araujo H, Arce P, et al. Geant4—A Simulation Toolkit. *Nucl Instrum Meth A* (2003) 506:250 – 303. doi: 10.1016/S0168-9002(03)01368-8
30. Rescigno R, Finck C, Juliani D, Spiriti E, Baudot J, Abou-Haidar Z, et al. Performance of the Reconstruction Algorithms of the FIRST Experiment Pixel Sensors Vertex Detector. *Nucl Instrum Meth A* (2014) 767:34–40. doi: 10.1016/j.nima.2014.08.024
31. Reidel CA, Finck C, Schuy C, Rovituso M, Weber U. Alignment Procedure of Silicon Pixel Detectors for Ion-Beam Therapy Applications. *Nucl Instrum Meth A* (2019) 931:142–50. doi: 10.1016/j.nima.2019.03.042
32. Simeonov Y, Weber U, Schuy C, Engenhart-Cabillic R, Penchev P, Durante M, et al. Monte Carlo Simulations and Dose Measurements of 2D Range-Modulators for Scanned Particle Therapy. *Z Med Phys* (2020) 31:203–4. doi: 10.1016/j.zemedi.2020.06.008
33. Tarasov O, Bazin D. LISE++: Radioactive Beam Production With in-Flight Separators. *Nucl Instrum Meth B* (2008) 266:4657–64. doi: 10.1016/j.nimb.2008.05.110
34. Weber U. *Volumenkonforme Bestrahlung Mit Kohlenstoff-Ionen Zur Vorbereitung Einer Strahlentherapie. Ph.D. Thesis*. Universität Kassel (1996).
35. Reidel CA, Schuy C, Finck C, Horst F, Boscolo D, Baudot J, et al. Response of the Mimosa-28 Pixel Sensor to a Wide Range of Ion Species

and Energies. *Nucl Instrum Meth A* (2021) 1017:165807. doi: 10.1016/j.nima.2021.165807
36. Newhauser WD, Koch NC, Fontenot JD, Rosenthal SJ, Gombos DS, Fitzek MM, et al. Dosimetric Impact of Tantalum Markers Used in the Treatment of Uveal Melanoma With Proton Beam Therapy. *Phys Med Biol* (2007) 52:3979. doi: 10.1088/0031-9155/52/13/021
37. Matsuura T, Maeda K, Sutherland K, Takayanagi T, Shimizu S, Takao S, et al. Biological Effect of Dose Distortion by Fiducial Markers in Spot-Scanning Proton Therapy With a Limited Number of Fields: A Simulation Study. *Med Phys* (2012) 39:5584–91. doi: 10.1118/1.4745558

Conflict of Interest: The authors declare that the research was conducted in the absence of any commercial or financial relationships that could be construed as a potential conflict of interest.

Publisher's Note: All claims expressed in this article are solely those of the authors and do not necessarily represent those of their affiliated organizations, or those of the publisher, the editors and the reviewers. Any product that may be evaluated in this article, or claim that may be made by its manufacturer, is not guaranteed or endorsed by the publisher.

frontiers | Frontiers in Oncology

ORIGINAL RESEARCH
published: 05 April 2022
doi: 10.3389/fonc.2022.830981

Evaluating Proton Dose and Associated Range Uncertainty Using Daily Cone-Beam CT

Heng Li, William T. Hrinivich, Hao Chen, Khadija Sheikh, Meng Wei Ho, Rachel Ger, Dezhi Liu, Russell Kenneth Hales, Khinh Ranh Voong, Aditya Halthore and Curtiland Deville*

Radiation Oncology and Molecular Radiation Sciences, Johns Hopkins University School of Medicine, Baltimore, MD, United States

OPEN ACCESS

Edited by:
Dandan Zheng, University of Nebraska Medical Center, United States

Reviewed by:
Mengying Shi, University of Massachusetts Lowell, United States
Dongxu Wang, Memorial Sloan Kettering Cancer Center, United States

****Correspondence:***
Heng Li
hengli@jhu.edu

Specialty section:
This article was submitted to Cancer Imaging and Image-directed Interventions, a section of the journal Frontiers in Oncology

Received: *07 December 2021*
Accepted: *02 March 2022*
Published: *05 April 2022*

Citation:
Li H, Hrinivich WT, Chen H, Sheikh K, Ho MW, Ger R, Liu D, Hales RK, Voong KR, Halthore A and Deville C (2022) Evaluating Proton Dose and Associated Range Uncertainty Using Daily Cone-Beam CT. Front. Oncol. 12:830981. doi: 10.3389/fonc.2022.830981

Purpose: This study aimed to quantitatively evaluate the range uncertainties that arise from daily cone-beam CT (CBCT) images for proton dose calculation compared to CT using a measurement-based technique.

Methods: For head and thorax phantoms, wedge-shaped intensity-modulated proton therapy (IMPT) treatment plans were created such that the gradient of the wedge intersected and was measured with a 2D ion chamber array. The measured 2D dose distributions were compared with 2D dose planes extracted from the dose distributions using the IMPT plan calculated on CT and CBCT. Treatment plans of a thymoma cancer patient treated with breath-hold (BH) IMPT were recalculated on 28 CBCTs and 9 CTs, and the resulting dose distributions were compared.

Results: The range uncertainties for the head phantom were determined to be 1.2% with CBCT, compared to 0.5% for CT, whereas the range uncertainties for the thorax phantom were 2.1% with CBCT, compared to 0.8% for CT. The doses calculated on CBCT and CT were similar with similar anatomy changes. For the thymoma patient, the primary source of anatomy change was the BH uncertainty, which could be up to 8 mm in the superior–inferior (SI) direction.

Conclusion: We developed a measurement-based range uncertainty evaluation method with high sensitivity and used it to validate the accuracy of CBCT-based range and dose calculation. Our study demonstrated that the CBCT-based dose calculation could be used for daily dose validation in selected proton patients.

Keywords: dose calculation, CBCT, radiation measurement, radiation therapy, proton radiation therapy (PBT)

INTRODUCTION

The use of daily cone-beam CT (CBCT) guidance has improved patient setup accuracy and precision in various radiotherapy delivery modalities, including proton therapy (1, 2). Since the proton range, and hence the proton dose distribution, is sensitive toward any density change along the beam path, CBCT can provide an additional benefit of verifying proton range and dose

distribution, complementing the geometrical verification of the patient anatomy daily (3–5). However, the Hounsfield unit (HU) accuracy and image quality of the CBCT images are inferior to those of regular CT and often considered inadequate for proton dose calculation without correction. Methods to correct the HU of CBCT and generate synthetic CT from CBCT images using regular CT images as *a priori* information have been extensively studied (6–8). However, problems arise when there is a difference between CBCT and regular CT. The CBCT data could be skewed and biased toward the regular CT, masking the very information we seek from CBCT. For example, Veiga et al. proposed to use deformable image registration (DIR) to create virtual CT (vCT) from CBCT and planning CT (pCT) (8–10). However, an additional correction step, which has an unknown impact on the final result, was necessary because the DIR process could artificially change the patient's anatomy as observed on CBCT (8). In general, when *a priori* information such as pCT was used, the bias it introduced and its impact on the range and dose distribution would compound with the actual anatomy change of the patient and could not be adequately quantified. On the other hand, previous studies have shown that using CBCT HU to density table (HU-D table) could produce mass density and dose calculation results with accuracy on the order of 1% for intensity-modulated radiation (photon) therapy (IMRT) treatments, even with inferior HU accuracy compared to CT (11). However, for proton radiotherapy, the proton range uncertainty arising from CBCT images with HU to density conversion instead of HU correction, and its impact on dose calculation, has not been quantitatively studied (12).

This study proposes using a measurement-based technique to quantify the proton range uncertainties arising from CBCT HU to density conversion, as compared to helical CT. We will also demonstrate the feasibility of CBCT-based daily dose validation without HU correction using a patient case.

MATERIALS AND METHODS

Imaging Systems and Proton Dose Calculation

The RayStation treatment planning system (versions 9A/10A, RaySearch Laboratories, Stockholm, Sweden) was used for this study. Proton dose engines in RayStation require a complete description of the material composition, including mass density, mass fraction of atomic elements, and mean ionization energy for each voxel of the patient. With the use of CT images as input, this was implemented by converting HU to mass density with the HU-D table. Then, the mass fraction of atomic elements and mean ionization energy of the voxel were determined from a number of well-established core materials through the interpolation of mass density (13).

A stoichiometric calibration method (14, 15) was used to establish the HU-D table for the CT simulator used in this study (Siemens SOMATOM Definition Edge plus, Siemens Healthcare, Forchheim, Germany). Separately, a patient group-based method (11) was used to create the HU-D table for the CBCT system used in this study (integrated into the Hitachi Probeat CR proton delivery system, Hitachi, Ltd., Tokyo, Japan). CT and CBCT image datasets of brain, head and neck, and thorax patients were used to establish the HU-D relationship on the CBCT images for typical materials such as air, brain, bone, or lung. The HU-D tables for CT and CBCT were then used for proton dose calculation on images acquired with respective modalities.

Phantom Imaging

A CT electron density phantom with inserts of known density (Gammex Inc., Middleton, WI, USA) and two anthropomorphic phantoms (Radiological Support Devices Inc., Long Beach, CA, USA) (one head phantom and one thorax phantom) were used in this study. **Figure 1A** shows the CT electron density phantom, **Figure 1B** shows the head and thorax phantoms put together on the simulator, **Figure 1C** shows the head phantom on top of a solid water slab at the simulator, and **Figure 1D** shows the head phantom on top of a solid water slab and a 2D ion chamber array (Octavius, PTW, Freiburg, Germany) at the treatment position ready for CBCT.

Phantom Treatment Planning

The pCT images were sent to RayStation. A solid water "Base" support was inserted posterior to the phantom, as it would be placed on top of the detector array during delivery. A wedge-shaped clinical target volume (CTV) was added posterior to the head such that the gradient of the wedge intersected the solid water slabs, as shown in **Figure 2**. This target design was chosen so that range error could be estimated from the gradient region of the wedge structure as measured using the detector array. For example, if the gradient edge was measured further laterally than computed by the TPS, this would indicate a measurement range deeper than the TPS predicted. A single anterior–posterior (AP) beam was optimized to deliver a homogeneous dose of 200 cGy (relative biological effectiveness (RBE)) to the wedge target, with robust optimization parameters of 0-mm setup uncertainties and 3.5% range uncertainties. The final dose was computed using a Monte Carlo proton dose engine with a 1-mm isotropic dose grid and exported in RT DICOM format to the Oncology Information System (OIS, Mosaiq, Elekta, Crawley, UK).

Phantom Setup and Cone-Beam CT Imaging

The head phantom was then set up to the "treatment" position, as shown in **Figure 1C** with laser, followed by shifts guided by a 3D–3D rigid registration between the CBCT and the plan CT. The CBCT images and the rigid registration were sent to OIS and RT PACS (Evercore DICOM RT archive, TeraMedica, Milwaukee, WI, USA).

Phantom Measurement

The treatment plan was then delivered using the proton treatment delivery system. A 2D plane of the delivered dose was measured using the 2D ion chamber array. A single 1-cm slab of solid water was placed between the phantom headrest and the detector array to ensure that the gradient region of the wedge intersected the detector array, as shown in **Figure 1C**.

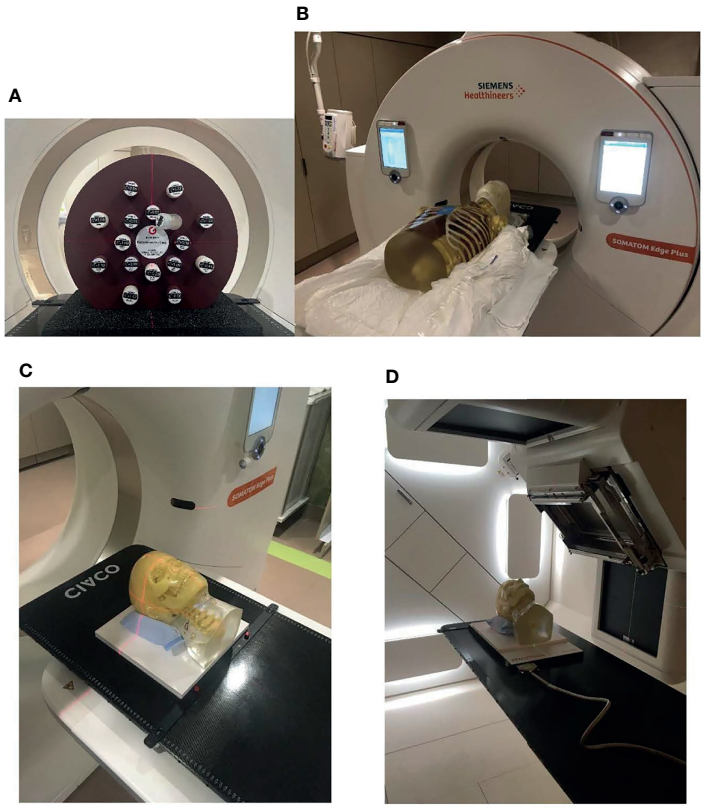

FIGURE 1 | Phantoms that were used in the study. **(A)** CT density phantom, **(B)** head and thorax phantoms put together on the simulator, **(C)** the head phantom on top of a solid water slab at the simulator, and **(D)** the head phantom on top of a solid water slab and a 2D ion chamber array at the treatment position ready for cone-beam CT (CBCT).

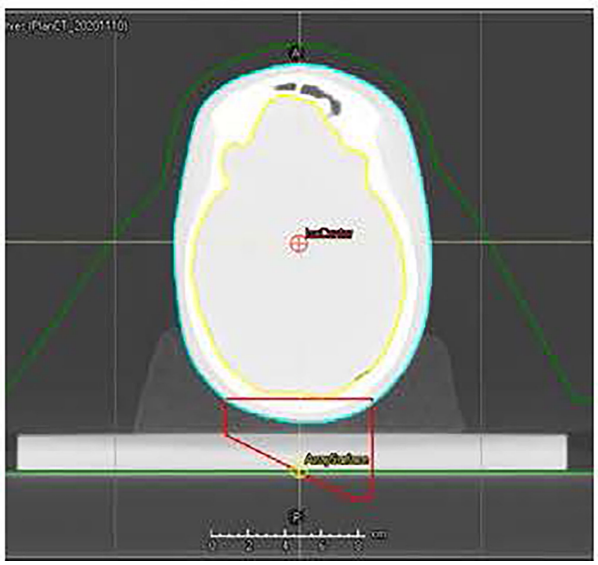

FIGURE 2 | CT image of the head phantom with a wedge-shaped target.

Hounsfield Unit Difference Between CT and Cone-Beam CT Images

The HUs of the CT and CBCT images for CT density inserts and patient images were compared. The difference of HU for the same material on the CT and CBCT images leads to different HU-D calibrations for the two different modalities.

Phantom Cone-Beam CT-Based Dose Calculation

The acquired CBCT images and the rigid registration were sent to the TPS from PACS. The proton plan was recalculated on CBCT with the isocenter placed using the registration.

Phantom Quantification of Range Uncertainties From CT and Cone-Beam CT

The proton dose distribution calculated on CT and CBCT was exported from the TPS. The measured 2D dose planes with the CT and CBCT doses were compared using Matlab (MathWorks, Inc., Natick, MA, USA). The measurement plane was determined on CT and CBCT, respectively. The corresponding dose planes on CT and CBCT were extracted and compared with the 2D

measurement by calculating the gamma indexes with criteria of 3 mm/3%. Because of the range uncertainties associated with the HU-D-proton stopping power conversion process, the measured dose plane may be shifted only on the range direction, assuming no geometrical uncertainties. Therefore, the range uncertainties between the calculated dose and the measurement could be quantified by the difference between the calculated measurement depth and the actual measurement depth. The actual measurement depth could be determined by comparing various dose planes extracted from the 3D dose calculated on CT/CBCT with the measured 2D dose plane.

Determination of the range uncertainties from CT and CBCT was repeated for head and thorax phantoms.

Workflow of Cone-Beam CT-Based Dose Verification

Figure 3 shows the workflow of using CBCT for patient dose verification. Black lines represent the data transfer of pCT and the treatment plan, the blue line represents the data transfer of CBCT, and the orange line represents the data transfer of rigid registration. The workflow is similar to the phantom validation workflow described above, and a large part of the workflow could be automated through scripting.

Patient Case Study

A patient with thymoma treated with active breathing control (ABC) (16), which is a breath-hold (BH) technique, and daily CBCT-guided intensity-modulated proton therapy (IMPT) was retrospectively studied. Three consecutive BH CT scans were acquired during patient simulation for treatment planning. Additionally, the patient acquired two additional sets of repeated CTs throughout the treatment, each consisting of three consecutive BH scans. The patient was given a total dose to CTV of 5,400-cGy RBE in 27 fractions. The patient went through CBCT imaging the first day on the treatment machine without actual treatment delivery, followed by daily CBCT-guided proton therapy, resulting in an additional set of CBCT images. For daily CBCT acquired with BH, the patient held their breath for ~25 s for each BH, and each full scan of CBCT acquisition required ~3–4 BH. In summary, there were 9 CTs and 28 CBCTs available for the patient.

Two treatment plans were created for the patient with robustly optimized IMPT using a spot scanning technique (17, 18). The first plan was created with only one of the planning BH CTs (19), whereas the second plan used all three planning BH CTs with multiple-CT optimization (20, 21). With the IMPT technique, all surrounding organs at risk (OARs), including the lung and the heart, received doses well below clinical tolerance in both plans. The main challenge was maintaining target coverage with the intra-fractional and inter-fractional motions of the patient. The proton plans were recalculated on all 9 CT and 28 CBCT scans to monitor and evaluate the impact of the motion. The target coverage along with heart and lung doses on each scan was evaluated.

RESULTS

Phantom Study

Figure 4 shows the comparison between HU from CT and CBCT for the same materials. The figure shows the HUs for inserts in the CT electron density phantom with known densities, extracted from CT images (x-axis) and CBCT images (y-axis). It also shows the HUs of volumes of interest (VOI) with nearly homogenous densities on the reference CT and the daily CBCT images (11), along with the HU-D curves for CT and CBCT modalities. There is a substantial difference between HUs from CT and CBCT for lung and soft tissue materials.

Figure 5 shows the proton dose distribution calculated on pCT (**Figure 5A**) and CBCT (**Figure 5B**) for the head phantom.

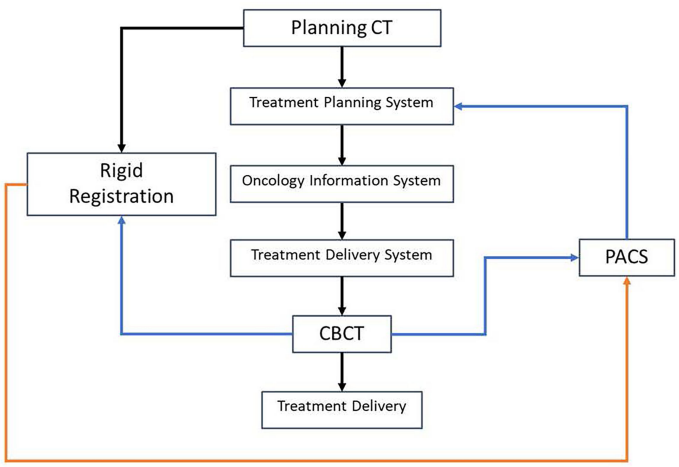

FIGURE 3 | Workflow of using cone-beam CT (CBCT) for patient dose verification. The black lines represent the data transfer of planning CT and the treatment plan, the blue line represents the data transfer of CBCT, and the orange line represents the data transfer of rigid registration.

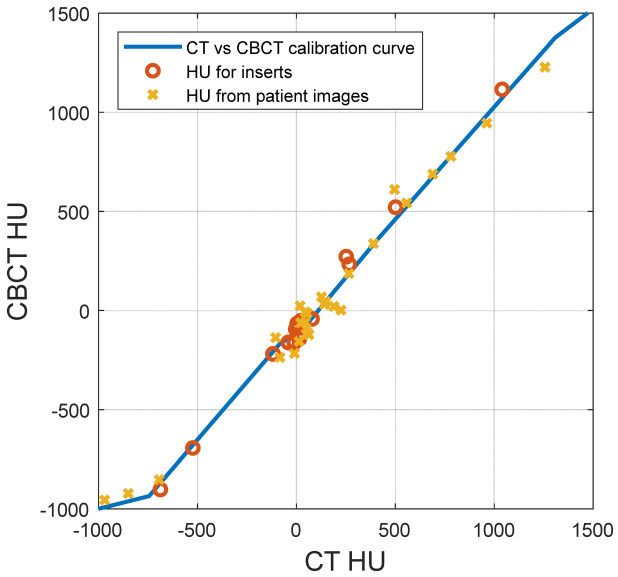

FIGURE 4 | Hounsfield unit (HU) comparison between CT and cone-beam CT (CBCT) for the same materials. The solid line represents the HU-D calibration curve, the circles represent inserts on the CT density phantom with known densities, and the crosses represent volumes of interest with nearly homogenous density on patient images.

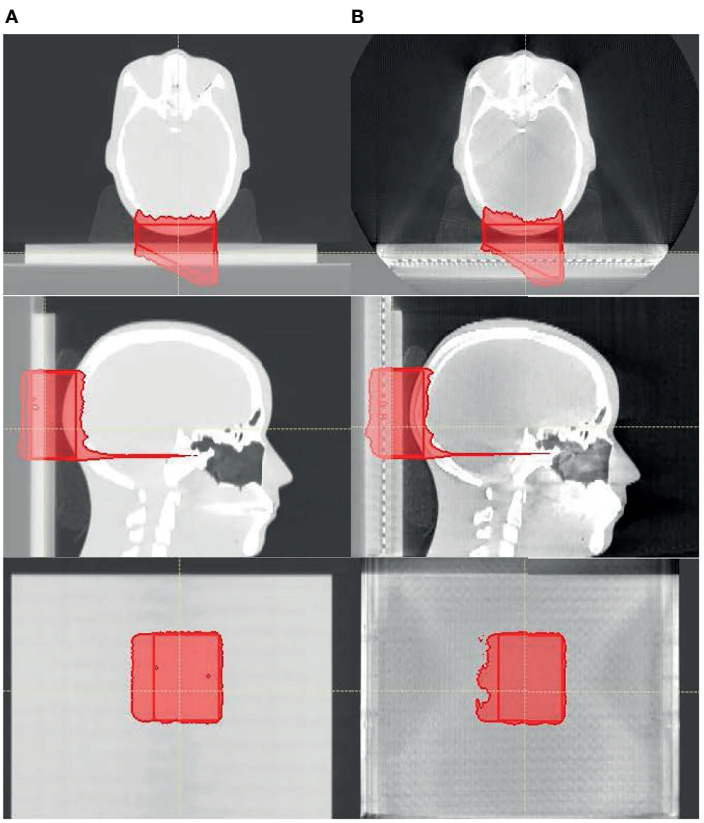

FIGURE 5 | The proton dose distribution calculated on **(A)** planning CT and **(B)** cone-beam CT (CBCT) for the head phantom. Only the prescription dose of 200 cGy is shown in the red color wash, and the red contour represents the target.

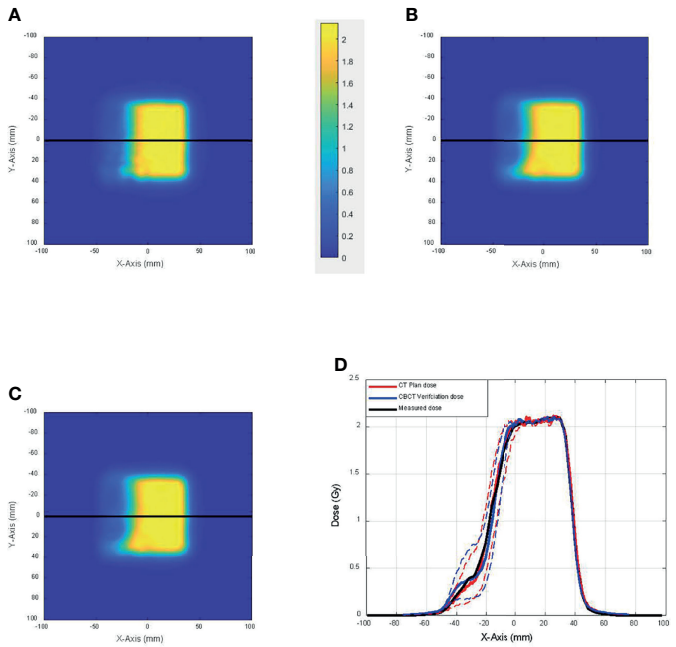

FIGURE 6 | The comparison among 2D planes extracted from the 3D dose calculated on **(A)** CT and **(B)** cone-beam CT (CBCT) that best match **(C)** the 2D plane measurement. **(D)** Dose profile of panels A–C (solid lines) and dose profiles from CT and CBCT dose planes that were 3 mm proximal and distal toward the best-matched dose planes (dashed lines).

The prescription dose of 200-cGy RBE is shown in the red color wash, and the red contour represents the target. As shown in the figures, since zero setup uncertainties were used in treatment planning, the prescription dose highly conformed to the target contour on lateral directions of the beam. Since 3.5% range uncertainties were used, there were margins on the proximal and distal directions of the beam between the prescription dose and the target. The 2D detector array could be easily identified from the CBCT. Since the entire base was overridden as solid water (shown in the figures as gray blocks), the material composition difference between CT and CBCT was not of concern.

As described in the *Materials and Methods* section, 2D dose planes from the 3D dose on CT and CBCT were extracted in 1-mm spacing and compared with the measured 2D plane dose. **Figure 6** shows the comparison among 2D planes extracted from the 3D dose calculated on CT (**Figure 6A**) and CBCT (**Figure 6B**) that best matches the 2D plane measurement (**Figure 6C**). **Figure 6D** shows the dose profile of **Figures 6A–C**, which were again the 2D array measurement along with the best-matched dose planes from dose calculation using CT and CBCT (solid lines). Also shown in the figure, in dashed lines, are the dose profiles from CT and CBCT dose planes that were 3 mm proximal and distal toward the best-matched dose planes. This figure demonstrates the geometric accuracy of the comparison and the sensitivity of the test toward range uncertainties.

Figure 7 shows the proton dose distribution calculated on pCT (**Figure 7A**) and CBCT (**Figure 7B**) for the thorax phantom. **Figure 8** shows the 2D gamma passing rate with a criterion of 3 mm/3% as a function of percentage range error, comparing the 2D measurement and 2D dose planes from CT or CBCT dose, for the head phantom (**Figure 8A**) and the thorax phantom (**Figure 8B**), respectively. The range error from CT was 0.5% and 0.8%, whereas the range error from CBCT was 1.2% and 2.1% for the head and thorax phantoms, respectively.

Patient Study

Two treatment plans were based on one ABC BH CT and on multiple (three) ABC BH scans. The first column of **Figures 9A, B** shows the dose distribution on the single pCT and multiple BH CTs, respectively. In the figures, only the dose cloud of the prescription dose (5,400-cGy RBE, red) and 50% (2,700-cGy RBE, green) are shown along with the CTV (yellow contour). The plan was recalculated on all 9 CTs and 28 CBCTs. The middle and right columns of **Figures 9A, B** show the dose distributions on CBCT and CT with the worst CTV coverage, respectively. As observed from CBCT and CT, the BH uncertainty was the primary source of anatomy change in the patient. The BH level could differ up to 8 mm in the superior–inferior (SI) direction. Red arrows in **Figure 9A** point to areas where target coverage was reduced on the daily CBCT or repeated CT. The treatment plan based on a single BH CT could not account for the anatomy change in the worst-case CBCT and CT; both result in loss of tumor dose coverage, whereas the dose coverage was maintained for the multiple BH CT plan. These results suggest that CBCT could provide similar information as repeated CT to support the clinical decision on adaptation.

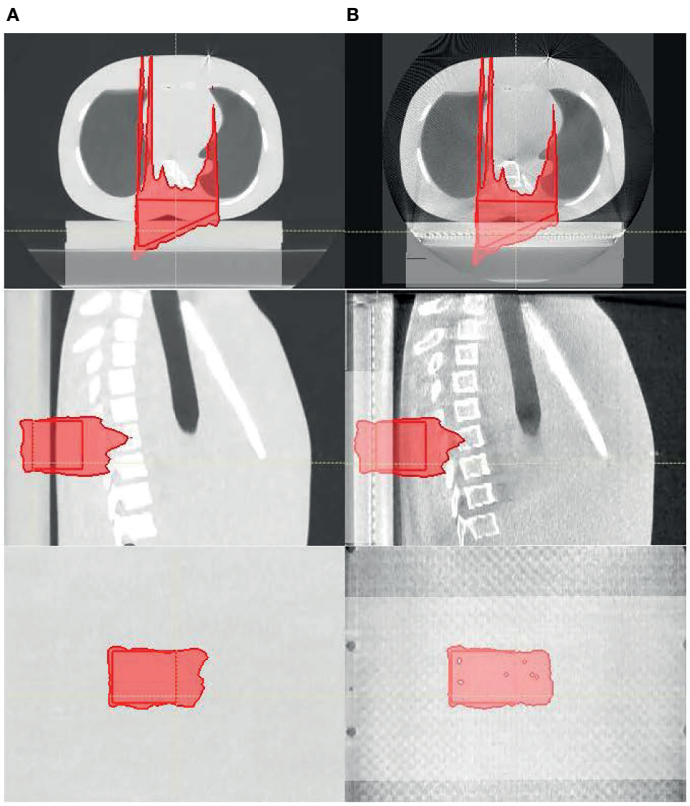

FIGURE 7 | The proton dose distribution calculated on **(A)** planning CT and **(B)** cone-beam CT (CBCT) for the thorax phantom.

Figure 10 shows CTV, and heart and lung dose–volume histograms (DVHs) for the single CT (**Figure 10A**) and multiple CT (**Figure 10B**) plans, calculated on all CTs and CBCTs, respectively. The solid line represents DVHs on pCT, the dashed lines represent DVHs on all CTs, and the bands represent DVHs on all CBCTs. The figure shows that V100% from the single CT plan dropped to 95.0% and 94.5%, in the worst case on CTs and CBCTs, respectively. The V100% for the multiple CT plan dropped to 98.4% for both CTs and CBCTs. Both plans' heart and lung doses remained excellent on all CTs and CBCTs.

DISCUSSION

In this study, we quantified the proton range uncertainties and their impact on dose calculation arising from CBCT images with HU to density calibration for the first time. The range uncertainties for the head phantom were determined to be 1.2% with CBCT, compared to 0.5% for CT, whereas the range uncertainties for the thorax phantom were 2.1% with CBCT, compared to 0.8% for CT. The profile comparison in **Figure 6D** and the gamma index comparison in **Figure 8** both showed excellent resolution of the measurement-based technique, in

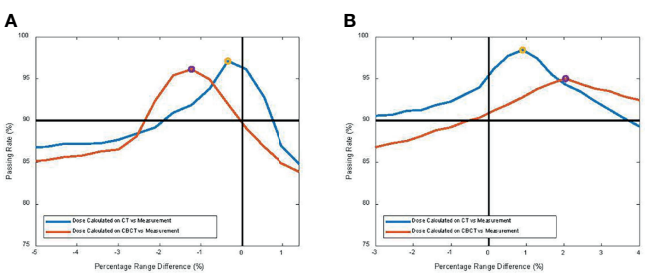

FIGURE 8 | 2D gamma passing rate with criterion of 3 mm/3% as a function of percentage range error, comparing the 2D measurement and 2D dose planes from CT or cone-beam CT (CBCT) dose for **(A)** the head phantom and **(B)** the thorax phantom, respectively.

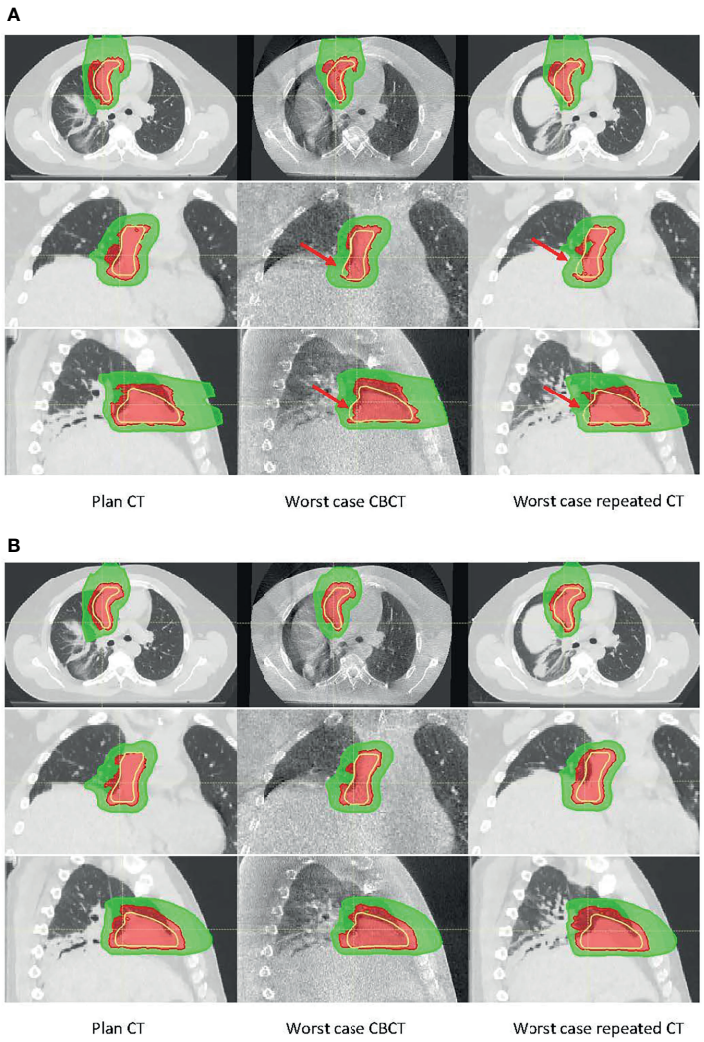

FIGURE 9 | Dose distribution calculated on planning CT (left), worst-case cone-beam CT (CBCT) (middle), and worst-case repeated CT (right) for **(A)** the single breath-hold BH CT plan and **(B)** multiple BH CT plan. There were ~8-mm superior–inferior (SI) BH uncertainties between the planning CT and the worst-case CBCT or CT. Red arrows in panel A point to the area where target coverage was reduced.

terms of both general geometric accuracy and the determination of range uncertainties based on dose gradient. These results are comparable with synthetic CT techniques for head (22) and thorax (8) studies.

One notable difference between the current and previous studies is that measurement was used as the baseline for our study. Much of the literature investigating CBCT-based proton dose calculation converted CBCT HU to CT HU and then used CT HU for proton dose calculation (3, 23–27). However, as mentioned above and demonstrated in this study, using CT as the baseline would introduce the inherent range uncertainties associated with the CT HU-D-stopping power conversion, which could potentially be removed by direct CBCT HU-D-stopping power conversion. Many HU correction techniques also use CT as *a priori* information that, as previously discussed, could introduce bias and geometrical uncertainties, which could compound with the actual patient anatomy change. Since the uncertainties could not be adequately quantified, one of the major benefits of CBCT images (i.e., its excellent geometrical accuracy) would be negated. **Figure 11** demonstrates an example of geometric uncertainties from the DIR-based HU correction techniques. In the figure, the planning ABC CT (left) used *a priori* information to correct the CBCT images (center) using deformation registration to create the synthetic CT images (right) on two consecutive days at day 5 (**Figure 11A**) and day 6 (**Figure 11B**), respectively (8). While the HU accuracy was generally improved on the synthetic CT compared to CBCT, the diaphragm was displaced in the synthetic CT on day 6. Since pCT is not the ground truth for daily patient data, the magnitude of the geometrical distortion in the synthetic CT could not be adequately quantified. This observation is consistent with previous publications (8–10). Advanced techniques for CBCT HU to density conversion without distorting the patient geometry could further improve the accuracy of the CBCT-based

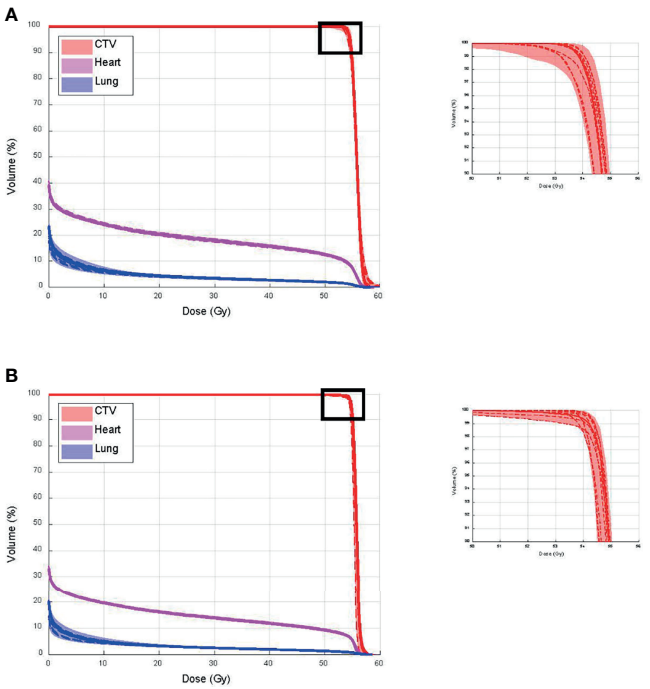

FIGURE 10 | Clinical target volume (CTV), and heart and lung dose–volume histograms (DVHs) for **(A)** single CT and **(B)** multiple CT plans, calculated on all CTs and cone-beam CTs (CBCTs), respectively.

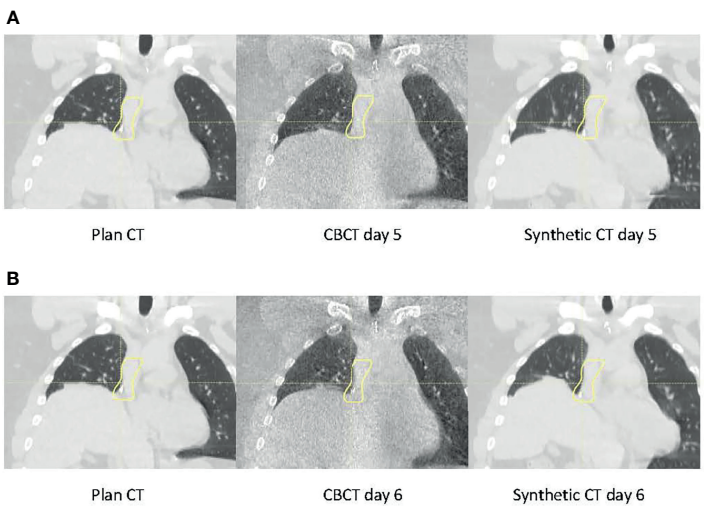

FIGURE 11 | Planning CT (left), daily cone-beam CT (CBCT (middle), and synthetic CT (right) for the same patient on **(A)** day 5 and **(B)** day 6.

dose calculation. For example, Spadea et al. and Thummerer et al. (22, 28) proposed a deep convolutional neural network based on CBCT HU to CT HU mapping to create synthetic CT without introducing geometry distortion.

We compared the dose calculated on CBCTs with CTs for an ABC BH patient as a feasibility study. The results showed that the CBCT calculated dose was consistent with CT calculated dose when there were similar BH-induced uncertainties. These results suggest that with a simple workflow, CBCT-based dose validation could be unbiased with excellent geometrical accuracy, and acceptable accuracy range determination, and may be an alternative to synthetic CT-based dose validation for selected proton patients.

In addition to the inferior image quality, CBCT also has other inherent problems that could limit the use of CBCT directly for dose calculation. For example, CBCT image quality could deteriorate with artifacts from metal or motion. One of the other major limitations of CBCT is the limited field of view (FOV). For accurate proton dose calculation, the entire beam path that transverses the patient and any supporting devices need to be included in the FOV of the images, which may not be feasible for many patients with pelvic targets. In addition, the HU accuracy of CBCT images is known to deteriorate with patient size. Therefore, we limited our investigation to head and thorax phantoms in this study. We do not expect to use CBCT directly for dose calculation in large patients where the FOV could not cover the entire patient.

CONCLUSION

We developed a measurement-based range uncertainty evaluation method with high sensitivity and used it to validate the accuracy of CBCT-based range and dose calculation. Our study demonstrated that the CBCT-based dose calculation could be used for daily dose validation in selected proton patients.

DATA AVAILABILITY STATEMENT

The raw data supporting the conclusions of this article will be made available by the authors, without undue reservation.

ETHICS STATEMENT

The retrospective study was based on patient data with Johns Hopkins Medicine IRB approval.

AUTHOR CONTRIBUTIONS

HL, WH, and HC conceptualized the design and experiments. HL and WH drafted the manuscript. HC, WH, and KS contributed to acquiring, analyzing, and interpreting the data. MH and DL contributed to the coding of the analysis. RH, KV, and AH provided recommendations on the clinical perspective of the study. RG and CD reviewed and edited the manuscript. All authors read and approved the final manuscript.

REFERENCES

1. Hua C, Yao W, Kidani T, Tomida K, Ozawa S, Nishimura T, et al. A Robotic C-Arm Cone Beam CT System for Image-Guided Proton Therapy: Design and Performance. *Br J Radiol* (2017) 90:20170266. doi: 10.1259/bjr.20170266
2. MacFarlane MJ, Jiang K, Mundis M, Nichols E, Gopal A, Chen S, et al. Comparison of the Dosimetric Accuracy of Proton Breast Treatment Plans Delivered With SGRT and CBCT Setups. *J Appl Clin Med Phys* (2021) 22:153–8. doi: 10.1002/acm2.13357
3. Park YK, Sharp GC, Phillips J, Winey BA. Proton Dose Calculation on Scatter-Corrected CBCT Image: Feasibility Study for Adaptive Proton Therapy. *Med Phys* (2015) 42:4449–59. doi: 10.1118/1.4923179
4. Nesteruk KP, Bobić M, Lalonde A, Winey BA, Lomax AJ, Paganetti H. CT-on-Rails Versus in-Room CBCT for Online Daily Adaptive Proton Therapy of Head-and-Neck Cancers. *Cancers* (2021) 13:5991. doi: 10.3390/cancers13235991
5. Paganetti H, Botas P, Sharp GC, Winey B. Adaptive Proton Therapy. *Phys Med Biol* (2021) 66:22TR01. doi: 10.1088/1361-6560/ac344f
6. Landry G, Dedes G, Zöllner C, Handrack J, Janssens G, De Xivry JO, et al. Phantom Based Evaluation of CT to CBCT Image Registration for Proton Therapy Dose Recalculation. *Phys Med Biol* (2014) 60:595. doi: 10.1088/0031-9155/60/2/595
7. Landry G, Nijhuis R, Dedes G, Handrack J, Thieke C, Janssens G, et al. Investigating CT to CBCT Image Registration for Head and Neck Proton Therapy as a Tool for Daily Dose Recalculation. *Med Phys* (2015) 42:1354–66. doi: 10.1118/1.4908223
8. Veiga C, Janssens G, Teng C-L, Baudier T, Hotoiu L, Mcclelland JR, et al. First Clinical Investigation of Cone Beam Computed Tomography and Deformable Registration for Adaptive Proton Therapy for Lung Cancer. *Int J Radiat Oncol Biol Phys* (2016) 95:549–59. doi: 10.1016/j.ijrobp.2016.01.055
9. Veiga C, Janssens G, Baudier T, Hotoiu L, Brousmiche S, Mcclelland J, et al. A Comprehensive Evaluation of the Accuracy of CBCT and Deformable Registration Based Dose Calculation in Lung Proton Therapy. *Biomed Phys Eng Express* (2017) 3:015003. doi: 10.1088/2057-1976/3/1/015003
10. Veiga C, Alshaikhi J, Amos R, Lourenço AM, Modat M, Ourselin S, et al. Cone-Beam Computed Tomography and Deformable Registration-Based "Dose of the Day" Calculations for Adaptive Proton Therapy. *Int J Particle Ther* (2015) 2:404–14. doi: 10.14338/IJPT-14-00024.1
11. Richter A, Hu Q, Steglich D, Baier K, Wilbert J, Guckenberger M, et al. Investigation of the Usability of Conebeam CT Data Sets for Dose Calculation. *Radiat Oncol* (2008) 3:1–13. doi: 10.1186/1748-717X-3-42
12. Giacometti V, Hounsell AH, McGarry CK. A Review of Dose Calculation Approaches With Cone Beam CT in Photon and Proton Therapy. *Physica Med* (2020) 76:243–76. doi: 10.1016/j.ejmp.2020.06.017
13. Raysearch Laboratories. *RSL-D-RS-9A-REF-EN-1.0-2019-06-20 Raystation 9A Reference Manual*. Stockholm, Sweden: Raysearch Laboratories AB (2019).
14. Schneider U, Pedroni E, Lomax A. The Calibration of CT Hounsfield Units for Radiotherapy Treatment Planning. *Phys Med Biol* (1996) 41:111. doi: 10.1088/0031-9155/41/1/009
15. Schneider W, Bortfeld T, Schlegel W. Correlation Between CT Numbers and Tissue Parameters Needed for Monte Carlo Simulations of Clinical Dose Distributions. *Phys Med Biol* (2000) 45:459. doi: 10.1088/0031-9155/45/2/314
16. Wong JW, Sharpe MB, Jaffray DA, Kini VR, Robertson JM, Stromberg JS, et al. The Use of Active Breathing Control (ABC) to Reduce Margin for Breathing Motion. *Int J Radiat Oncol Biol Phys* (1999) 44:911–9. doi: 10.1016/S0360-3016(99)00056-5
17. Li H, Zhang X, Park P, Liu W, Chang J, Liao Z, et al. Robust Optimization in Intensity-Modulated Proton Therapy to Account for Anatomy Changes in Lung Cancer Patients. *Radiother Oncol* (2015) 114:367–72. doi: 10.1016/j.radonc.2015.01.017
18. Chang JY, Li H, Zhu XR, Liao Z, Zhao L, Liu A, et al. Clinical Implementation of Intensity Modulated Proton Therapy for Thoracic Malignancies. *Int J Radiat Oncol Biol Phys* (2014) 90:809–18. doi: 10.1016/j.ijrobp.2014.07.045
19. Yang Z, Chang Y, Brock KK, Cazoulat G, Koay EJ, Koong AC, et al. Effect of Setup and Inter-Fraction Anatomical Changes on the Accumulated Dose in CT-Guided Breath-Hold Intensity Modulated Proton Therapy of Liver Malignancies. *Radiother Oncol* (2019) 134:101–9. doi: 10.1016/j.radonc.2019.01.028
20. Yang Z, Zhang X, Wang X, Zhu XR, Gunn B, Frank SJ, et al. Multiple-CT Optimization: An Adaptive Optimization Method to Account for Anatomical Changes in Intensity-Modulated Proton Therapy for Head and Neck Cancers. *Radiother Oncol* (2020) 142:124–32. doi: 10.1016/j.radonc.2019.09.010
21. Wang X, Li H, Zhu XR, Hou Q, Liao L, Jiang B, et al. Multiple-CT Optimization of Intensity-Modulated Proton Therapy–Is It Possible to Eliminate Adaptive Planning? *Radiother Oncol* (2018) 128:167–73. doi: 10.1016/j.radonc.2017.09.032

22. Thummerer A, Zaffino P, Meijers A, Marmitt GG, Seco J, Steenbakkers RJ, et al. Comparison of CBCT Based Synthetic CT Methods Suitable for Proton Dose Calculations in Adaptive Proton Therapy. *Phys Med Biol* (2020) 65:095002. doi: 10.1088/1361-6560/ab7d54
23. Kurz C, Dedes G, Resch A, Reiner M, Ganswindt U, Nijhuis R, et al. Comparing Cone-Beam CT Intensity Correction Methods for Dose Recalculation in Adaptive Intensity-Modulated Photon and Proton Therapy for Head and Neck Cancer. *Acta Oncol* (2015) 54:1651–7. doi: 10.3109/0284186X.2015.1061206
24. Arai K, Kadoya N, Kato T, Endo H, Komori S, Abe Y, et al. Feasibility of CBCT-Based Proton Dose Calculation Using a Histogram-Matching Algorithm in Proton Beam Therapy. *Physica Med* (2017) 33:68–76. doi: 10.1016/j.ejmp.2016.12.006
25. Lalonde A, Winey B, Verburg J, Paganetti H, Sharp GC. Evaluation of CBCT Scatter Correction Using Deep Convolutional Neural Networks for Head and Neck Adaptive Proton Therapy. *Phys Med Biol* (2020) 65:245022. doi: 10.1088/1361-6560/ab9fcb
26. Neppl S, Kurz C, Köpl D, Yohannes I, Schneider M, Bondesson D, et al. Measurement-Based Range Evaluation for Quality Assurance of CBCT-Based Dose Calculations in Adaptive Proton Therapy. *Med Phys* (2021). doi: 10.1002/mp.14995
27. De Ornelas M, Xu Y, Padgett K, Schmidt RM, Butkus M, Diwanji T, et al. CBCT-Based Adaptive Assessment Workflow for Intensity Modulated Proton Therapy for Head and Neck Cancer. *Int J Particle Ther* (2021) 7:29–41. doi: 10.14338/IJPT-D-20-00056.1
28. Spadea MF, Pileggi G, Zaffino P, Salome P, Catana C, Izquierdo-Garcia D, et al. Deep Convolution Neural Network (DCNN) Multiplane Approach to Synthetic CT Generation From MR Images—Application in Brain Proton Therapy. *Int J Radiat Oncol Biol Phys* (2019) 105:495–503. doi: 10.1016/j.ijrobp.2019.06.2535

Conflict of Interest: The authors declare that the research was conducted in the absence of any commercial or financial relationships that could be construed as a potential conflict of interest.

Publisher's Note: All claims expressed in this article are solely those of the authors and do not necessarily represent those of their affiliated organizations, or those of the publisher, the editors and the reviewers. Any product that may be evaluated in this article, or claim that may be made by its manufacturer, is not guaranteed or endorsed by the publisher.

frontiers | Frontiers in Oncology

MINI REVIEW
published: 14 April 2022
doi: 10.3389/fonc.2022.833364

Imaging Strategies in Proton Therapy for Thoracic Tumors: A Mini Review

Carlo Algranati[1,2] *and Lidia Strigari*[3]*

[1] Proton Therapy Department, Azienda Provinciale per i Servizi Sanitari (APSS), Trento, Italy, [2] Dipartimento di Medicina Specialistica, Diagnostica e Sperimentale (DIMES), University of Bologna, Bologna, Italy, [3] Department of Medical Physics, Istituto di Ricovero e Cura a Carattere Scientifico (IRCCS) Azienda Ospedaliero-Universitaria di Bologna, Bologna, Italy

Proton beam therapy (PBT) is often more attractive for its high gradient dose distributions than other treatment modalities with external photon beams. However, in thoracic lesions treated particularly with pencil beam scanning (PBS) proton beams, several dosimetric issues are addressed. The PBS approach may lead to large hot or cold spots in dose distributions delivered to the patients, potentially affecting the tumor control and/or increasing normal tissue side effects. This delivery method particularly benefits image-guided approaches. Our paper aims at reviewing imaging strategies and their technological trends for PBT in thoracic lesions. The focus is on the use of imaging strategies in simulation, planning, positioning, adaptation, monitoring, and delivery of treatment and how changes in the anatomy of thoracic tumors are handled with the available tools and devices in PBT. Starting from bibliographic research over the past 5 years, retrieving 174 papers, major key questions, and implemented solutions were identified and discussed; the results aggregated and presented following the methodology of analysis of expert interviews.

Keywords: proton therapy, imaging, thoracic tumors, motion management in radiotherapy, adaptive, radiotherapy

OPEN ACCESS

Edited by:
Marco Durante,
Helmholtz Association of German Research Centres (HZ), Germany

Reviewed by:
Silva Bortolussi,
University of Pavia, Italy

***Correspondence:**
Lidia Strigari
lidia.strigari@aosp.bo.it

Specialty section:
This article was submitted to Cancer Imaging and Image-directed Interventions, a section of the journal Frontiers in Oncology

Received: *11 December 2021*
Accepted: *09 February 2022*
Published: *14 April 2022*

Citation:
Algranati C and Strigari L (2022) Imaging Strategies in Proton Therapy for Thoracic Tumors: A Mini Review. Front. Oncol. 12:833364. doi: 10.3389/fonc.2022.833364

1 INTRODUCTION

Radiation therapy (RT) is an essential and effective tool in the curative treatment of different anatomical sites. Unfortunately, with photon RT, safe dose escalation, delivery of concomitant systemic therapy, or re-irradiation of the recurrent disease may not be feasible due to radiation-induced toxicities. In contrast, the finite range of proton beams in tissues offers unique dosimetric advantages that theoretically allow escalating the target dose, potentially prolonging survival while minimizing exposure of surrounding tissues and consequently radiation-induced toxicity rate.

This theoretical advantage has led to the widespread adoption of proton beam therapy (PBT) worldwide for a wide variety of thoracic malignancies, including lung cancer, esophageal cancer, mesothelioma, and thymic cancer. At the state of the art, the tremendous potential of PBT for treating thoracic cancers is only beginning to be appreciated.

PBT provided a lower total toxicity burden, particularly pulmonary, cardiac, and hematologic toxicity, within the context of previous attempts at dose escalation for lung and esophageal cancer (1). Similarly, for mesothelioma patients, the physical properties of proton therapy result in better sparing of normal tissues, particularly in treating the pleura, in both post-pneumonectomy and lung-intact settings. There are drastic dose reductions to the contralateral lung, heart, liver, kidneys, and stomach (2). Re-irradiation, advanced disease requiring extensive cardio-pulmonary irradiated

volumes, and younger patients may likely benefit from modern PBT (3). New techniques like stereotactic body radiation therapy (SBRT) and PBT are now increasingly adopted as the only radical treatment for small solitary lung tumors (4) and represent the most used non-surgical modality in treating lung cancers, permitting the improvement of treatment outcomes and favorable toxicities.

Moreover, treating thoracic cancers involves solving most technical and technological imaging, treatment plan, delivery, and adaptive problems. Several issues are relevant for improving the efficacy and safety of thoracic moving tumors or tumor shrinkage/anatomical changes during the treatment, such as the type of online imaging and the vulnerability of protons to inherent heterogeneities in the beam path. Therefore, there is an enhancing need to perform adaptive planning, representing the key to more comprehensive PBT application (1).

New approaches to combining PBT and immunotherapy (5) demand creative investigation for introducing ultrahigh dose-rate Flash, GRID/lattice, and microbeam delivery approaches in PBT (6–8). The maturity of technologies, including treatment planning and image-guided technology, is the critical issue for realizing new PBT treatment strategies.

This work focuses on imaging and motion-related devices used for PBT treatment simulation, planning, positioning, adaptation, monitoring, and delivery in thoracic tumors.

2 MATERIALS AND METHODS

2.1 Literature Search Strategy

A PubMed search was performed using the query string to identify the publication related to proton therapy in thoracic tumors, mainly represented by small-cell lung cancer (SCLC) and non-small cell lung cancer (NSCLC), mesothelioma, thymoma, and esophageal cancer. These thoracic malignancies are challenging from the treatment point of view because of relevant tissue heterogeneities, the presence of moving organs and targets, and the limited availability of onboard soft tissue imaging devices.

We included the following keywords/strings in the PubMed query search:

- "proton therapy" AND "thoracic";
- "proton therapy" AND "non-small-cell-lung-cancers";
- "proton therapy" AND "small-cell-lung-cancer";
- "proton therapy" AND "mesothelioma";
- "proton therapy" AND ("thymoma" OR "thymic malignancy");
- "proton therapy" AND "esophageal cancer".

Filters are from June 3, 2016 to June 3, 2021. The research was restricted to the last 5 years to include only the keywords in the title and/or abstract. The search was done on the June 3, 2021.

2.2 Study Selection

Two authors independently reviewed titles and abstracts to decide the study inclusion. Full articles were retrieved when the abstract was considered relevant. Only papers or abstracts published in English were considered.

Papers were selected if they contained information about the treatment of thoracic tumors with PBT and gave answers or inside view on the following medical physics questions:

1. Which is the imaging approach for simulation, planning, positioning, adaptation, monitoring, and delivery in PBT for thoracic tumors?
2. How are handled changes in the anatomy of thoracic tumors with the available tools and devices in PBT?

The data were summarized in a database with the following issues: first author, journal, year, title.

Data analysis and interpretation rely on Bogner and Menz's (9) related to Expert interviews.

3 RESULTS

3.1 Description of Included Studies and Inclusion Criteria

Based on the reported PubMed/Medline search, 190 papers and abstracts were identified. The results are represented in **Figure 1**. Substantial growth was observed looking at the included papers through the years. The number of papers related to 2021 was not complete because the inclusion criteria were limited to June 3, 2021.

Out of the 190 records, 16 were excluded as duplicates. 73 papers of 174 records screened were excluded for the following reasons: not inherent (#73) to the addressed questions. Out of the 102 full-text articles assessed for eligibility, 31 full-text articles were selected according to medical physics-related questions 1 and 2 described in paragraph study selection in *Material and Methods*.

The following groups were obtained according to the typical PBT workflow phases in a clinic (see **Figure 2**): simulation (# 24), planning (#9), treatment setup (#13), adaptation (#8), motion monitoring (#6), and treatment delivery (#6). Papers that give information about two or more groups were counted once for each group.

Additional subgroups related to subphases are identified in **Figure 2** as reported in *Results*.

3.2 Simulation

In thoracic tumors, if necessary, respiratory-gated or breath-hold radiation therapy techniques are used to accommodate tumor motion; however, most patients are treated with free-breathing, which is the more efficient technique (10). According to this, we have reported simulation imaging approaches and motion handling methods in agreement with the international guidelines in particle therapy thoracic malignancies (11).

3.2.1 Setup

Patients are mostly immobilized supine in an upper-body cradle with arms overhead (12). A small Vac-Lok cushion is used on a so-called wing board to stabilize the arms and the head. The pelvis and legs are stabilized with larger vacuum bags or directly positioned on the couch. Patients lay on the table with a gap

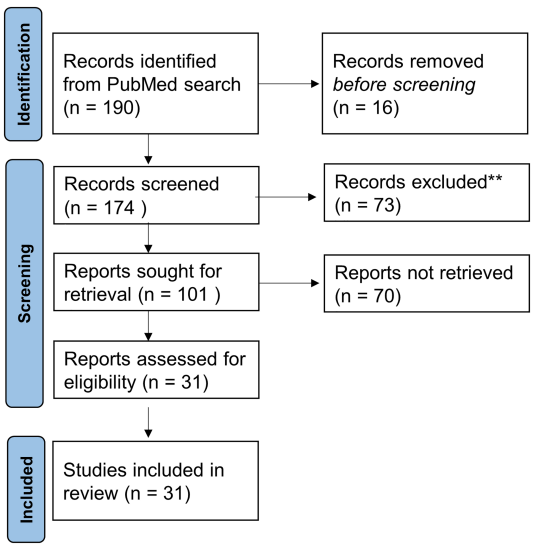

FIGURE 1 | Numbers of included and excluded papers derived from the PubMed search related to PBT in thoracic tumors.

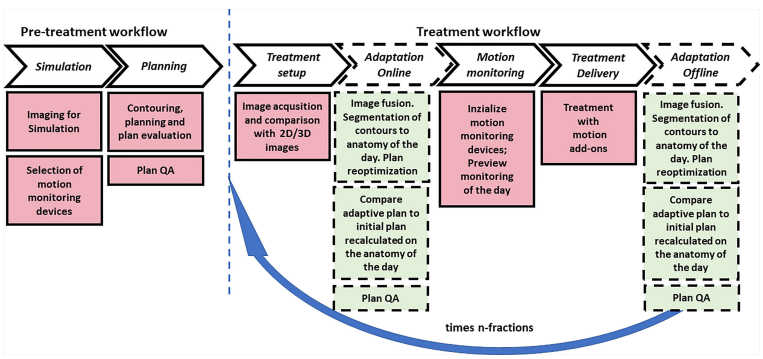

FIGURE 2 | Typical pretreatment and treatment PBT workflow with main subitems/tasks for motion management and anatomical change of organs and tumors. The dashed blocks indicate the online and off-line adaptation tasks that may be optionally applied one or more times during treatment. The blue arrow indicates the number of fractions in which the inter- and intra-fraction evaluation for motion management is applied.

between the head and pelvic vacuum bags to minimize material in the beam path (13, 14). The type of cushions is critical because they could introduce uncertainties in the alignment of different tissues along the beam path (15).

Significant internal motion is accounted for by utilizing various measures, including 4-dimensional (4D) CT imaging and abdominal compression, and/or through the placement of internal fiducials at the discretion of the treating radiation oncologist. Sometimes abdominal compression devices are reported (16).

3.2.2 Imaging for Simulation

The free-breathing patients underwent CT simulation with 4D-CT to account for respiratory motion with deformation (12, 15, 17–24). Regarding the motion assessment, a tumor motion range less than 5 mm is considered acceptable for free-breathing delivery (15). Patient respiratory waveforms were monitored throughout the procedures and recorded with a respiratory gating system (14, 17, 19, 20, 25–27). Alternatively, to mitigate intra-fractional motion in NSCLC patients, visually guided voluntary DIBH CT images are acquired (26, 28–32).

3.3 Planning

3.3.1 Contouring and Plan Evaluation

The use of ^{18}F-fluorodeoxyglucose-PET/computed tomography (CT) is well established in lung cancer and several other thoracic malignancies. Simone et al. (33) describes the expected future roles of PET/CT for thoracic tumors. In the free-breathing cases, the gross tumor volume (GTV) is often defined based on all available clinical information in the average intensity projection

reconstruction images derived from all breathing phases of the 4D-CT (19–21, 25, 34). The plan is then generated on an averaged 4D-CTs with possible density overwrites. The method reported by Fracchiolla et al. (23) is to create internal target volume (ITV) on the free-breathing CT as the union of all CTVs contoured on each phase of the 4D-CT. The plan is calculated on the free-breathing CT.

3.3.2 Range Uncertainty

In selecting imaging CT for planning, the uncertainty related to the proton-stopping-power conversion of the Hounsfield units plays an essential role. Currently, algorithms using single energy CT photon to proton stopping power calculations implement a 3%–3.5% uncertainty for each centimeter (cm) of beam path length (15). However, for planning purposes, one technical advance that undoubtedly may improve proton treatment for NSCLC is the employment of dual-energy CT (DECT) or other techniques that reduce range uncertainty for treatment delivery (35, 36).

3.3.3 Special Approaches

Incorporating 4D-CT ventilation imaging into functional proton therapy is feasible (37). In intensity-modulated proton delivery, the functional proton plans are adequate to further preserve high-functioning lung regions without degrading the PTV coverage. This approach is feasible in a subset of patients with breathing motion limited to 5–7 mm from CT0 (inhalation) to CT50 (max exhalation) (25, 37).

Sala et al. (32) propose high-frequency percussive ventilation (HFPV) to reduce motion impact drastically. This approach employs high-frequency low tidal volumes (100–400 bursts/min) to provide respiration in awake patients.

3.3.4 Motion Monitor Devices

Different motion monitoring devices are reported used in combination with X-ray imaging devices adopted for planning, setup, and delivery in PBT. They are classifiable according to the type of implemented technology in surface-guided radiotherapy (SGRT) using optical systems, spirometry, and markers.

The SGRT systems include commercial ones such as the Varian Real-time Position Management system (Varian Medical Systems, Palo Alto, CA) (19, 37), Vision RT (23), or in-house solutions (10). The spirometric systems included DIBH using the SDX system (Dyn'R-SDX, version 2.06) (30) and the Active Breathing Coordinator (ABC, Elekta Oncology Systems Ltd., Crawley, West Sussex, UK) (23). Several authors report using gold fiducial markers implanted by bronchoscopy (27, 28) or endobronchial ultrasound guidance (13). The patient's respiratory stability was evaluated by studying the marker motion as a surrogate of tumor displacement using X-ray imaging devices. Elhammali et al. (12) reported that a minimum of 3 days for a trans-thoracic approach or 2 days for a bronchoscopy approach were required to allow fiducials to stabilize before simulation. Another reported system is the Z-733 V respiratory gating system (Anzai Medical, Tokyo, Japan) (17, 20, 22, 36, 38, 39).

3.4 Treatment Setup

3.4.1 Image Acquisition and Comparison With 2D/3D Images

For standard treatments in patients with thoracic tumors, daily patient alignments are achieved by matching fiducial markers or vertebral bones with 2D/2D matching methods (10, 12, 13, 16, 17, 21, 27, 28, 34, 40). The setup is continued until the eventual fiducial markers on the digitally reconstructed radiographs are agreed within 2 mm (13, 28).

The 2D/2D fusion approach limits the visibility of soft tissues that is crucial for PBT beams and ensures adequate treatment plan delivery (21). The number of pencil beam scanned proton therapy (PBSPT) facilities equipped with cone-beam computed tomography (CBCT) imaging treating thoracic indications is constantly rising (34, 39, 40), thus allowing the implementation of dose summation and adaptive treatments. To overcome the absence of onboard 3D images, weekly CT images are acquired to generate verification and adaptive plans (18, 23).

3.5 Treatment Adaptation

Forsthoefel et al. (16) reported that treatment setup and delivery are verified with regularly scheduled quality assurance CT scans during treatment. Kharod et al. (13) reported that patients underwent verification CT scans on days 1, 2, 4, and 6 of treatment to confirm appropriate alignment. Chen et al. (41) did analyze the correlation between anatomic change and the need to adopt adaptive radiotherapy (ART).

3.5.1 Off-Line Adaptive

Iwata et al. (28) reported that CT permits evaluating tumor shrinkage at the end of PBT. Replanning was conducted if beam leakage to the distal side due to tumor volume change (shrinkage) or body mass reduction was significant. The adaptive replanning was performed when the esophagus and spinal cord dose increased and exceeded the limit dose and/or when the dose to the lung adjacent to the tumor increased by about 10%.

3.5.2 Online Adaptive

The online adaptive protocol was reported by (29) based on plan re-optimization using a fast but limited accuracy analytical algorithm that can still improve the overall treatment dose for patients with cancer in the lung and HN regions. Nevertheless, no online adaptive protocol was reported in the literature in the papers selected for this study.

3.6 Motion Monitoring and Treatment Delivery

In thoracic tumors, respiratory-gated PBT combined with image-guided techniques enables adaptive plan implementation (28). Abdominal surface motion is used as a surrogate for tumor motion, and the beam is turned on only when the monitored respiratory phase falls within the predefined gating window (17).

4 DISCUSSION AND CONCLUSIONS

To fully realize the potential of PBT for thoracic cancer, extensive improvements are needed in all the image-related aspects of the treatment process, from simulation, planning

algorithms, and volumetric image guidance to real-time tracking and treatment adaptation.

For complicated anatomy, intensity-modulated PBT should be considered with appropriate motion management (27). For centrally located lesions and re-irradiation, volumetric imaging is crucial for accurate delivery and reducing the PTV margins.

Our review of selected literature highlighted some barriers for treating moving targets with significant tissue heterogeneity and the technologic efforts underway to overcome these challenges for thoracic malignancies. One of the most important of these was the lack of 3D volumetric imaging in the PBT facilities for treatment setup and adaptation. Because visualizing tumors with non-volumetric 2-dimensional images is challenging for PBT, fiducial markers are frequently adopted, although they represent an invasive procedure and are not always feasible. When tumors are close to bony structures, these could be used as a landmark (11).

In PBT, 4D-CT, ITV generation, and free-breathing are frequently reported approaches preferred to DIBH. The free-breathing approach applies mainly when the tumor displacements are limited up to 5 mm.

SGRT PBT is a reported option based on repeated CBCT or CT analysis. In photon beam radiotherapy, the availability of 4D-CBCT and 4D-CT allows assessing the correlation between the tumor/hepatic dome and skin displacements, enabling an appropriate intra- and inter-fraction motion management (42). The spirometry represents the most extensively adopted solution in PBT.

DECT is considered of interest for a more precise and accurate estimation of range uncertainties but is not currently clinically applied.

Adopting an online adaptive strategy demands onboard setup imaging (CBCT for generating synthetic CT) or CT on-rail and dedicated software, which permits the adaptation and an *in silico* plan quality assurance.

AUTHOR CONTRIBUTIONS

LS and CA designed the study. CA performed the PubMed search. LS and CA independently reviewed the titles and abstracts to decide the study inclusion, discussed the results, and contributed to the final manuscript. All authors contributed to the article and approved the submitted version.

REFERENCES

1. Liao Z, Gandhi SJ, Lin SH, Bradley J. Does Proton Therapy Offer Demonstrable Clinical Advantages for Treating Thoracic Tumors? *Semin Radiat Oncol* (2018) 28(2):114–24. doi: 10.1016/j.semradonc.2017.11.002
2. Zeng J, Badiyan SN, Garces YI, Wong T, Zhang X, Simone CB, et al. Consensus Statement on Proton Therapy in Mesothelioma. *Pract Radiat Oncol* (2021) 11(2):119–33. doi: 10.1016/j.prro.2020.05.004
3. Patel NV, Yu NY, Koroulakis A, Diwanji T, Sawant A, Sio TT, et al. Proton Therapy for Thoracic Malignancies: A Review of Oncologic Outcomes. *Expert Rev Anticancer Ther* (2021) 21(2):177–91. doi: 10.1080/14737140.2021.1844567
4. Lee VH-F, Yang L, Jiang Y, Kong F-M. Radiation Therapy for Thoracic Malignancies. *Hematol/Oncol Clin North Am* (2020) 34(1):109–25. doi: 10.1016/j.hoc.2019.09.007
5. Liao Z, Simone IiCB. Particle Therapy in Non-Small Cell Lung Cancer. *Trans Lung Cancer Res* (2018) 7(2):141–52. doi: 10.21037/tlcr.2018.04.11
6. Esplen N, Mendonca MS, Bazalova-Carter M. Physics and Biology of Ultrahigh Dose-Rate (FLASH) Radiotherapy: A Topical Review. *Phys Med Biol* (2020) 65(23):23TR03. doi: 10.1088/1361-6560/abaa28
7. Diffenderfer ES, Verginadis II, Kim MM, Shoniyozov K, Velalopoulou A, Goia D, et al. Design, Implementation, and *In Vivo* Validation of a Novel Proton FLASH Radiation Therapy System. *Int J Radiat Oncol Biol Phys* (2020) 106(2):440–8. doi: 10.1016/j.ijrobp.2019.10.049
8. Zhang H, Wu X, Zhang X, Chang SX, Megooni A, Donnelly ED, et al. Photon GRID Radiation Therapy: A Physics and Dosimetry White Paper From the Radiosurgery Society (RSS) GRID/LATTICE, Microbeam and FLASH Radiotherapy Working Group. *Radiat Res* (2020) 194(6):665–77. doi: 10.1667/RADE-20-00047.1
9. Bogner A, Littig B, Menz W. *Interviews Mit Experten*. Wiesbaden: Springer Fachmedien Wiesbaden (2014).
10. Gelover E, Deisher AJ, Herman MG, Johnson JE, Kruse JJ, Tryggestad EJ. Clinical Implementation of Respiratory-Gated Spot-Scanning Proton Therapy: An Efficiency Analysis of Active Motion Management. *J Appl Clin Med Phys* (2019) 20(5):99–108. doi: 10.1002/acm2.12584
11. Chang JY, Zhang X, Knopf A, Li H, Mori S, Dong L, et al. Consensus Guidelines for Implementing Pencil-Beam Scanning Proton Therapy for Thoracic Malignancies on Behalf of the PTCOG Thoracic and Lymphoma Subcommittee. *Int J Radiat Oncol Biol Phys* (2017) 99(1):41–50. doi: 10.1016/j.ijrobp.2017.05.014
12. Elhammali A, Blanchard P, Yoder A, Liao Z, Zhang X, Ronald Zhu X, et al. Clinical Outcomes After Intensity-Modulated Proton Therapy With Concurrent Chemotherapy for Inoperable Non-Small Cell Lung Cancer. *Radiother Oncol* (2019) 136:136–42. doi: 10.1016/j.radonc.2019.03.029
13. Kharod SM, Nichols RC, Henderson RH, Morris CG, Pham DC, Seeram VK, et al. Image-Guided Hypofractionated Proton Therapy in Early-Stage Non–Small Cell Lung Cancer: A Phase 2 Study. *Int J Particle Ther* (2020) 7(2):1–10. doi: 10.14338/IJPT-20-00013.1
14. Jeter MD, Gomez D, Nguyen Q-N, Komaki R, Zhang X, Zhu X, et al. Simultaneous Integrated Boost for Radiation Dose Escalation to the Gross Tumor Volume With Intensity Modulated (Photon) Radiation Therapy or Intensity Modulated Proton Therapy and Concurrent Chemotherapy for Stage II to III Non-Small Cell Lung Cancer: A Phase 1 Study. *Int J Radiat Oncol Biol Phys* (2018) 100(3):730–7. doi: 10.1016/j.ijrobp.2017.10.042
15. Wong SL, Alshaikhi J, Grimes H, Amos RA, Poynter A, Rompokos V, et al. Retrospective Planning Study of Patients With Superior Sulcus Tumours Comparing Pencil Beam Scanning Protons to Volumetric-Modulated Arc Therapy. *Clin Oncol* (2021) 33(3):e118–31. doi: 10.1016/j.clon.2020.07.016
16. Forsthoefel MK, Ballew E, Unger KR, Ahn PH, Rudra S, Pang D, et al. Early Experience of the First Single-Room Gantry Mounted Active Scanning Proton Therapy System at an Integrated Cancer Center. *Front Oncol* (2020) 10:861. doi: 10.3389/fonc.2020.00861
17. Nakajima K, Iwata H, Ogino H, Hattori Y, Hashimoto S, Toshito T, et al. Clinical Outcomes of Image-Guided Proton Therapy for Histologically Confirmed Stage I Non-Small Cell Lung Cancer. *Radiat Oncol* (2018) 13(1):1–9. doi: 10.1186/s13014-018-1144-5
18. Yang P, Xu T, Gomez DR, Deng W, Wei X, Elhalawani H, et al. Patterns of Local-Regional Failure After Intensity Modulated Radiation Therapy or Passive Scattering Proton Therapy With Concurrent Chemotherapy for Non-Small Cell Lung Cancer. *Int J Radiat Oncol Biol Phys* (2019) 103(1):123–31. doi: 10.1016/j.ijrobp.2018.08.031
19. Remick JS, Schonewolf C, Gabriel P, Doucette A, Levin WP, Kucharczuk JC, et al. First Clinical Report of Proton Beam Therapy for Postoperative Radiotherapy for Non–Small-Cell Lung Cancer. *Clin Lung Cancer* (2017) 18(4):364–71. doi: 10.1016/j.cllc.2016.12.009

20. Inoue T, Widder J, van Dijk LV, Takegawa H, Koizumi M, Takashina M, et al. Limited Impact of Setup and Range Uncertainties, Breathing Motion, and Interplay Effects in Robustly Optimized Intensity Modulated Proton Therapy for Stage III Non-Small Cell Lung Cancer. *Int J Radiat Oncol Biol Phys* (2016) 96(3):661–9. doi: 10.1016/j.ijrobp.2016.06.2454
21. Boyce-Fappiano D, Nguyen Q-N, Chapman BV, Allen PK, Gjyshi O, Pezzi TA, et al. Single Institution Experience of Proton and Photon-Based Postoperative Radiation Therapy for Non–Small-Cell Lung Cancer. *Clin Lung Cancer* (2021). doi: 10.1016/j.cllc.2021.02.002
22. Meijers A, Knopf A-C, Crijns APG, Ubbels JF, Niezink AGH, Langendijk JA, et al. Evaluation of Interplay and Organ Motion Effects by Means of 4D Dose Reconstruction And Accumulation. *Radiother Oncol* (2020) 150:268–74. doi: 10.1016/j.radonc.2020.07.055
23. Fracchiolla F, Dionisi F, Giacomelli I, Hild S, Esposito PG, Lorentini S, et al. Implementation of Proton Therapy Treatments With Pencil Beam Scanning of Targets With Limited Intrafraction Motion. *Physica Med* (2019) 57:215–20. doi: 10.1016/j.ejmp.2019.01.007
24. Kang M, Huang S, Solberg TD, Mayer R, Thomas A, Teo B-KK, et al. A Study of the Beam-Specific Interplay Effect in Proton Pencil Beam Scanning Delivery in Lung Cancer. *Acta Oncol* (2017) 56(4):531–40. doi: 10.1080/0284186X.2017.1293287
25. Yu NY, DeWees TA, Liu C, Daniels TB, Ashman JB, Beamer SE, et al. Early Outcomes of Patients With Locally Advanced Non-Small Cell Lung Cancer Treated With Intensity-Modulated Proton Therapy Versus Intensity-Modulated Radiation Therapy: The Mayo Clinic Experience. *Adv Radiat Oncol* (2020) 5(3):450–8. doi: 10.1016/j.adro.2019.08.001
26. Zhu HJ, Hoppe BS, Flampouri S, Louis D, Pirris J, Nichols RC, et al. Rationale and Early Outcomes for the Management of Thymoma With Proton Therapy. *Trans Lung Cancer Res* (2018) 7(2):106–13. doi: 10.21037/tlcr.2018.04.06
27. Nantavithya C, Gomez DR, Wei X, Komaki R, Liao Z, Lin SH, et al. Phase 2 Study of Stereotactic Body Radiation Therapy and Stereotactic Body Proton Therapy for High-Risk, Medically Inoperable, Early-Stage Non-Small Cell Lung Cancer. *Int J Radiat Oncol Biol Phys* (2018) 101(3):558–63. doi: 10.1016/j.ijrobp.2018.02.022
28. Iwata H, Akita K, Yamaba Y, Kunii E, Takakuwa O, Yoshihara M, et al. Concurrent Chemo-Proton Therapy Using Adaptive Planning for Unresectable Stage 3 Non-Small Cell Lung Cancer: A Phase 2 Study. *Int J Radiat Oncol Biol Phys* (2021) 109(5):1359–67. doi: 10.1016/j.ijrobp.2020.11.035
29. Nenoff L, Ribeiro CO, Matter M, Hafner L, Josipovic M, Langendijk JA, et al. Deformable Image Registration Uncertainty for Inter-Fractional Dose Accumulation of Lung Cancer Proton Therapy. *Radiother Oncol* (2020) 147:178–85. doi: 10.1016/j.radonc.2020.04.046
30. Ntentas G, Dedeckova K, Andrlik M, Aznar MC, George B, Kubeš J, et al. Clinical Intensity Modulated Proton Therapy for Hodgkin Lymphoma: Which Patients Benefit the Most? *Pract Radiat Oncol* (2019) 9(3):179–87. doi: 10.1016/j.prro.2019.01.006
31. Gorgisyan J, Munck af Rosenschold P, Perrin R, Persson GF, Josipovic M, Belosi MF, et al. Feasibility of Pencil Beam Scanned Intensity Modulated Proton Therapy in Breath-Hold for Locally Advanced Non-Small Cell Lung Cancer. *Int J Radiat Oncol Biol Phys* (2017) 99(5):1121–8. doi: 10.1016/j.ijrobp.2017.08.023
32. Gorgisyan J, Perrin R, Lomax AJ, Persson GF, Josipovic M, Engelholm SA, et al. Impact of Beam Angle Choice on Pencil Beam Scanning Breath-Hold Proton Therapy for Lung Lesions. *Acta Oncol* (2017) 56(6):853–9. doi: 10.1080/0284186X.2017.1287950
33. Simone CB, Houshmand S, Kalbasi A, Salavati A, Alavi A. PET-Based Thoracic Radiation Oncology. *PET Clin* (2016) 11(3):319–32. doi: 10.1016/j.cpet.2016.03.001
34. Kim N, Myoung Noh J, Lee W, Park B, Park H, Young Park J, et al. Proton Beam Therapy Reduces the Risk of Severe Radiation-Induced Lymphopenia During Chemoradiotherapy for Locally Advanced Non-Small Cell Lung Cancer: A Comparative Analysis of Proton Versus Photon Therapy. *Radiother Oncol* (2021) 156:166–73. doi: 10.1016/j.radonc.2020.12.019
35. Brooks ED, Ning MS, Verma V, Zhu XR, Chang JY. Proton Therapy for Non-Small Cell Lung Cancer: The Road Ahead. *Trans Lung Cancer Res* (2019) 8 (S2):S202–12. doi: 10.21037/tlcr.2019.07.08
36. Wohlfahrt P, Troost EGC, Hofmann C, Richter C, Jakobi A. Clinical Feasibility of Single-Source Dual-Spiral 4D Dual-Energy CT for Proton Treatment Planning Within the Thoracic Region. *Int J Radiat Oncol Biol Phys* (2018) 102(4):830–40. doi: 10.1016/j.ijrobp.2018.06.044
37. Huang Q, Jabbour SK, Xiao Z, Yue N, Wang X, Cao H, et al. Dosimetric Feasibility of 4DCT-Ventilation Imaging Guided Proton Therapy for Locally Advanced Non-Small-Cell Lung Cancer. *Radiat Oncol* (2018) 13(1):1–10. doi: 10.1186/s13014-018-1018-x
38. Meijers A, Seller OC, Free J, Bondesson D, Seller Oria C, Rabe M, et al. Assessment of Range Uncertainty in Lung-Like Tissue Using a Porcine Lung Phantom and Proton Radiography. *Phys Med Biol* (2020) 65(15):155014. doi: 10.1088/1361-6560/ab91db
39. den Otter LA, Anakotta RM, Weessies M, Roos CTG, Sijtsema NM, Muijs CT, et al. Investigation of Inter-Fraction Target Motion Variations in the Context of Pencil Beam Scanned Proton Therapy in Non-Small Cell Lung Cancer Patients. *Med Phys* (2020) 47(9):3835–44. doi: 10.1002/mp.14345
40. Shin H, Noh JM, Pyo H, Ahn YC, Oh D. Salvage Proton Beam Therapy for Locoregional Recurrence of Non-Small Cell Lung Cancer. *Radiat Oncol J* (2021) 39(1):24–32. doi: 10.3857/roj.2020.01074
41. Chen M, Yang J, Liao Z, Chen J, Xu C, He X, et al. Anatomic Change Over the Course of Treatment for Non–Small Cell Lung Cancer Patients and Its Impact on Intensity-Modulated Radiation Therapy and Passive-Scattering Proton Therapy Deliveries. *Radiat Oncol* (2020) 15(1):1–11. doi: 10.1186/s13014-020-01503-9
42. Paolani G, Strolin S, Santoro M, Della Gala G, Tolento G, Guido A, et al. A Novel Tool for Assessing the Correlation of Internal/External Markers During SGRT Guided Stereotactic Ablative Radiotherapy Treatments. *Phys Med* (2021) 92:40–51. doi: 10.1016/j.ejmp.2021.10.021

Conflict of Interest: The authors declare that the research was conducted in the absence of any commercial or financial relationships that could be construed as a potential conflict of interest.

frontiers | Frontiers in Oncology

REVIEW
published: 29 July 2022
doi: 10.3389/fonc.2022.930850

Considerations for Upright Particle Therapy Patient Positioning and Associated Image Guidance

Lennart Volz[1,2], *Yinxiangzi Sheng*[1,2], *Marco Durante*[1,3] *and Christian Graeff*[1,4]*

[1] Biophysics, GSI Helmholtz Center for Heavy Ion Research GmbH, Darmstadt, Germany, [2] Department of Medical Physics, Shanghai Proton and Heavy Ion Center, Shanghai, China, [3] Institute of Condensed Matter Physics, Technical University of Darmstadt, Darmstadt, Germany, [4] Institute of Electrical Engineering and Information Technology, Technical University of Darmstadt, Darmstadt, Germany

Particle therapy is a rapidly growing field in cancer therapy. Worldwide, over 100 centers are in operation, and more are currently in construction phase. The interest in particle therapy is founded in the superior target dose conformity and healthy tissue sparing achievable through the particles' inverse depth dose profile. This physical advantage is, however, opposed by increased complexity and cost of particle therapy facilities. Particle therapy, especially with heavier ions, requires large and costly equipment to accelerate the particles to the desired treatment energy and steer the beam to the patient. A significant portion of the cost for a treatment facility is attributed to the gantry, used to enable different beam angles around the patient for optimal healthy tissue sparing. Instead of a gantry, a rotating chair positioning system paired with a fixed horizontal beam line presents a suitable cost-efficient alternative. Chair systems have been used already at the advent of particle therapy, but were soon dismissed due to increased setup uncertainty associated with the upright position stemming from the lack of dedicated image guidance systems. Recently, treatment chairs gained renewed interest due to the improvement in beam delivery, commercial availability of vertical patient CT imaging and improved image guidance systems to mitigate the problem of anatomical motion in seated treatments. In this review, economical and clinical reasons for an upright patient positioning system are discussed. Existing designs targeted for particle therapy are reviewed, and conclusions are drawn on the design and construction of chair systems and associated image guidance. Finally, the different aspects from literature are channeled into recommendations for potential upright treatment layouts, both for retrofitting and new facilities.

Keywords: upright CT, upright treatment, particle therapy, image guidance, seated treatment, treatment chair

OPEN ACCESS

Edited by:
Joao Seco,
German Cancer Research Center (DKFZ), Germany

Reviewed by:
Uwe Titt,
University of Texas MD Anderson Cancer Center, United States
Nicolas Depauw,
Massachusetts General Hospital and Harvard Medical School, United States

***Correspondence:**
Christian Graeff
c.graeff@gsi.de

Specialty section:
This article was submitted to Cancer Imaging and Image-directed Interventions, a section of the journal Frontiers in Oncology

Received: *28 April 2022*
Accepted: *17 June 2022*
Published: *29 July 2022*

Citation:
Volz L, Sheng Y, Durante M and Graeff C (2022) Considerations for Upright Particle Therapy Patient Positioning and Associated Image Guidance. Front. Oncol. 12:930850. doi: 10.3389/fonc.2022.930850

INTRODUCTION

Particle therapy, available in the form of proton or heavier ion therapy, has received an ever-increasing interest over recent decades, with currently over 100 facilities in operation (1), and several more planned or under construction. Primarily, this interest results from the superior depth

dose profile of charged particles over that of photons used in conventional radiotherapy: particles have a finite range in the patient and deposit the maximum dose at their stopping point - the Bragg peak. The Bragg peak enables delivery of a high dose to the target with minimum dose to surrounding healthy tissue. Sufficient target coverage can already be achieved with few treatment fields, therefore the low-dose bath typically delivered to a large volume for photon therapy. In case of heavier ions, the Bragg peak is also the point of highest relative biological effectiveness (RBE), further increasing tumor dose relative to that in healthy tissue (2).

This physical advantage of particle therapy over photon therapy, however, is opposed by the increased capital investment required for a particle therapy facility. This is attributed to the larger and more complex accelerator equipment needed to produce medical ion beams. Especially for heavy ions, a large part of the overall investment is needed for the gantry, used to enable treatment from different angles around the patient (3). It is therefore not surprising that several groups have been, or are currently, investigating options for gantry-less particle therapy, including treatment delivery with the patient in an upright or seated position. In fact, for the pioneering studies on ion beam therapy, conducted at the Lawrence Berkeley National Laboratory (LBNL), patients were fixed in an upright position using a rotating chair setup and a vertical CT was installed (4). Gantry-less carbon ion therapy with a custom chair and even associated vertical CT imaging was reported by Kamada et al. (5). A chair system for head and neck patients was also designed at GSI Helmholtz Center for Heavy Ion Research GmbH during its carbon ion therapy pilot project (6). Yet, despite the increased cost and size, gantries are regarded as the best option for enabling flexible beam angles, due to their universal applicability for different treatment sites. The declined interest in chair systems can be attributed to the limited availability of vertical CT systems, and the resulting limited knowledge on anatomical deformations in an upright position.

Indeed, dedicated image guidance is a central aspect when it comes to installing a system to treat patients in the upright position. With the advent of modern image guidance systems (7), like in-room Cone-Beam CT (CBCT), optical surface guidance, as well as dual-energy CT and particle imaging, particle therapy has recently enjoyed a boost in achievable treatment accuracy. Now, with commercial options for vertical CT systems (8, 9), and the drive for reducing the upfront investment for opening new particle therapy centers (3, 10), upright treatment positioning systems have gained renewed interest (11, 12). Moreover, advanced techniques for intra-treatment verification and adaptation (13–15) are currently reaching clinical maturity. These techniques could, not only overcome the previous issues associated with anatomical motion for upright treatment positions, but together with upright treatment postures, further open possibilities for advanced beam delivery schemes, e.g., particle arc therapy (16) with continuous patient rotation.

In this review, we aim to outline key requirements for a flexible upright particle therapy patient positioning system with associated imaging. To this end, we will summarize the clinical rationale for upright treatments and go over existing chair systems that have been constructed in the past or are currently available, focusing on those targeted for particle therapy. An overview over the requirements for an upright positioning system for photon therapy can be found in the recent review by Hegarty et al. (17). We will discuss engineering considerations for upright positioning systems and options for image guidance for an upright treatment position. Finally, we will channel the available literature into recommendations for future upright particle therapy patient positioning systems and associated image guidance.

POSSIBLE BENEFIT OF AN UPRIGHT POSITIONING SYSTEM

Economical Arguments

The key rationale for upright treatment positioning is, that it is cheaper to move the patient and not the beam. Gantries for proton, and especially for heavier ion therapy, are large, costly pieces of machinery. While it can cost less than half a million Euro to build a head&neck targeted chair positioning system, building a gantry is an investment of several million Euro for protons and even more for heavier ions. There is also operational cost: precise rotation of the up to several hundred ton gantry is by no means a simple task, and requires sophisticated installation and maintenance. For example, a shift of the isocenter position of up to ~1.2 mm during rotation of a proton gantry was reported by Moyers et al. (18). This shift can be effectively compensated by modern scanning delivery systems, but the shift results in additional workload for beam commissioning under different gantry angles. In addition, the large size of a proton, let alone a heavy ion gantry necessitates building a large shielded bunker (up to 25 m in length and three stories height in case of the carbon ion gantry at the Heidelberg Ion-Beam Therapy Center (19)), further adding to the facility cost.

While new designs for compact gantry systems are being explored, e.g., the static toroidal gantry proposed by Bottura et al. (20), moving the patient instead of the gantry presents a possibly simpler and thus attractive option. Especially for existing centers, retrofitting an upright positioning system is conceivably less challenging compared to retrofitting a gantry. Further arguments on cost-reduction could be the potential of faster setup time with an upright positioning system due to easier patient access (21). An upright positioning system may also enable easier inclusion of advanced image guidance techniques, like prompt gamma or particle imaging (13) to the setup, due to more free space around the isocenter.

At the same time, a gantry-less treatment room equipped with a flexible patient positioning system could provide similar versatility compared to a gantry, as demonstrated in the study by Yan et al. (22). An upright positioning system would also naturally provide an efficient way for advanced beam delivery options, like particle arc therapy (16, 23), by rotating the patient during treatment.

Overall, a chair system could be the solution for more widespread access to particle therapy, reducing cost and size of particle therapy centers. An upright proton therapy system has

been speculated to possibly fit into a single shielded bunker (3, 24) and could foster greater availability also in low income countries. For heavy ion therapy, where currently only two gantry systems are in operation worldwide, upright patient positioning could be the key to promote this technology from few centers with fixed horizontal beam lines to similar availability levels as current proton therapy.

Clinical Arguments

Aside from the economical arguments, there have been a small, but growing number of studies indicating a possible therapeutic benefit of upright treatment as well. Upright positioning could provide greater comfort for head&neck patients suffering from increased saliva production (25), and patients suffering orthopnea, dyspnea or dysphagia in supine position (26).

Dellamonica et al. (27) report increased lung volume and oxygenation for upright compared to supine position. Using an upright MRI scanner, Yang et al. (28) also demonstrated increased lung volume in upright positioning compared to supine, as well as showing a reduced motion amplitude from respiration. The greater lung volume implies greater distance between target and organs at risk, as well as lower mean lung dose, which has been used to argue for better healthy tissue sparing possibility (25). For particle therapy, the important quantity is the water equivalent thickness, which would not change relevantly with greater air volume in the lungs. In contrary, the reduced lung density could reduce the dose conformity at the distal target edge. This could be offset by both a reduced breathing amplitude resulting in smaller lateral margins, as well as the aforementioned distances to organs at risk. The net effect is probably patient-specific and needs to be investigated in treatment planning studies.

Considering that patients spend most of their days in upright or seated posture prior to treatment, upright treatment may also provide certain benefits regarding organ drift. For example, slow liver drift motion occurring over tens of minutes after supine positioning of patients was reported by von Siebenthal et al. (29), and attributed to the change in the direction of gravity compared to the patients 'normal' upright posture. Similar reasoning could be made also for other organs in the abdomen.

In a recent study based on upright MRI, Mackie et al. (21) have reported benefits for prostate therapy in upright position, with further details available in (30). Gravitational push of organs like the bladder into the pelvic bone reduced uncertainties in prostate position compared to supine. Since gas moves upwards the bowel for upright posture, the risk of unexpected bowel gas movement during prostate therapy possibly might be reduced.

Most recently, Sun et al. (31) presented results from clinical implementation of a chair positioning system targeted for head&neck cancers at the Shanghai Proton and Heavy Ion Center (SPHIC). Of 320 patients treated for head&neck, 15 showed a clear dosimetric benefit compared to a treatment with couch and fixed horizontal or 45° inclined beam line. Chair systems also were shown in the past to be well accepted by the patients. For example, McCarroll et al. (26) reported overall good patient comfort for their prototype chair design, but noted that upright positioning might not be possible for all patients, e.g., due to certain medical conditions.

Yan et al. (24) in a treatment planning study have demonstrated the robustness and high quality of upright plans for head&neck cancer patients for pencil-beam scanning proton therapy at a fixed beam line. While they used only a subset of the beam angles available for gantry treatments for upright planning, the authors note that the use of more beam angles could further benefit organ-at risk sparing.

Chair positioning systems are already well established standard for particle therapy treatments of cancers in the eye (32). If the beam line is capable of handling also the special requirements for eye cancer treatment (33), a head&neck upright positioning system may also be useful for eye treatments. Experience on head fixation devices for eye treatments, like chin bars with mouth pieces for the patient to bite into for immobilization, may be transferable also to treatments of brain tumors, although to a limited extent.

BRIEF OVERVIEW OVER EXISTING SOLUTIONS

In this section, existing solutions for upright positioning devices targeted specifically for particle therapy will be briefly reviewed. **Figure 1** shows examples of upright positioning prototypes constructed for or used at particle therapy centers. A historical overview of upright patient positioning systems for radiotherapy in general can be found in the recent review by Rahim et al. (34).

For the pioneering studies at LBNL investigating particle therapy using various ion species, patients could be positioned in both recumbent and in upright, standing or sitting, treatment position (36, 37). Patient positioning was achieved using dedicated upright accessories added to the 'ISAH' (38) 5-degree-of-freedom patient positioning system (36). A vertical CT was used for position verification in the upright position (4) Kamada et al. (5) have presented a chair positioning system for head&neck cancer patients used at the Heavy Ion Medical Accelerator Center (HIMAC) in Chiba, Japan. The device was mounted on a rail system to move it from treatment to parking position and a vertical CT scanner was specifically installed for imaging in the seated position. The CT scanner, mounted to the ceiling of the treatment bunker, was lowered over the patient to acquire images.

Heeg et al. (6) report on the design of a patient chair to be used at the GSI Helmholtz Center for Heavy Ion Research GmbH, with further refinements detailed in (39). The chair enabled a tilt of up to 19°, a 360° rotation around the vertical axis and featured a height adjustable patient mask holder mounted to a steel frame with counterweights for safe handling. Similar to the chair system by Kamada et al. (5), the chair by Heeg et al. (6) was mounted on a rail system to make way for the couch when not in use. The chair system is still operational and located in the now dedicated research room (40) at GSI, but it was never used clinically.

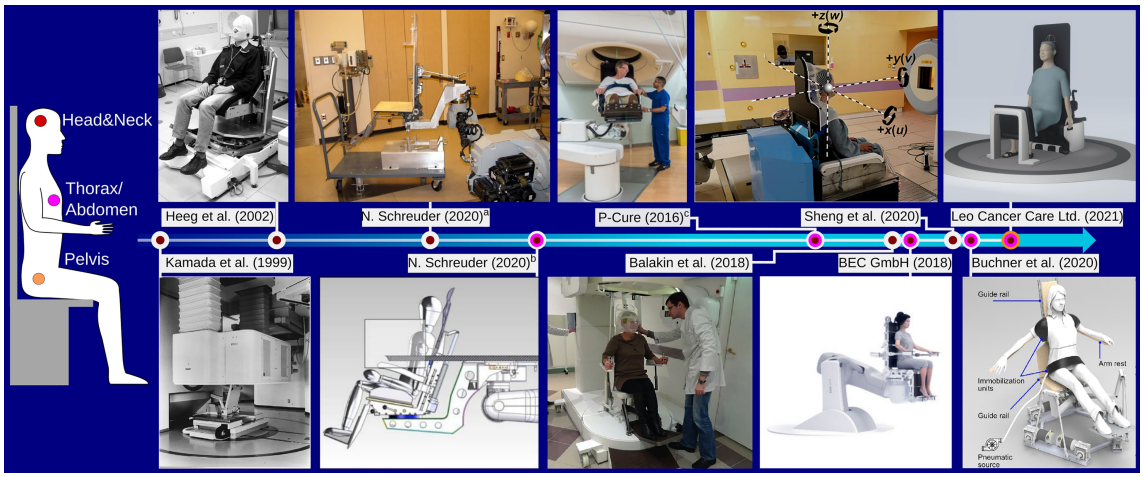

FIGURE 1 | Overview over different chair designs targeted for particle therapy found in literature, focusing on those that were constructed as prototype. The color of the time line connectors indicates the chair's intended use with respect to different treatment sites, as shown on the left. [a]The chair was installed at the Indiana University Health Proton Therapy Center prior to 2006, as described by Schreuder (30). [b]The device was installed at the Oklahoma Proton Center as described in (30). The figure shows the couch overlayed on the chair. [c]The chair system is installed at Northwestern Medicine Chicago Proton Center and was designed by P-Cure[1]. Image reprinted with kind permission by Dr. M. Pankuch (Northwestern Medicine Chicago Proton Center). Images [a,b], and the Leo Cancer Care Ltd (2021). were reprinted with kind permission by Dr. N. Schreuder (Leo Cancer Care Ltd.). Kamada et al. (1999): Reprinted from Kamada et al. (5) with permission from Elsevier. Buchner et al. (2020): ©2020 IEEE. Reprinted, with permission, from Buchner et al. (35).

Schreuder (30) discusses the design and construction of a chair system at the Indiana University Health Proton Therapy Center (Bloomington, Indiana, USA), reportedly used for patient treatment prior to the installation of a proton gantry. The device was attached to the couch robot, and could be mounted on a transport cart. Of note is the use of a wooden back plate which was individually manufactured for each patient for accurate positioning. In some cases, patient specific cutouts were made in the back plate to reduce material in the beam path.

Schreuder (30) also reports on the further development of the treatment chair continued at the Oklahoma Proton Center (Oklahoma City, Oklahoma, USA). The follow up device considered a 20° tilted backrest made from carbon fibre. Again, it was equipped with the same coupling structure as also used by the treatment couch, enabling efficient switching between couch and chair. Further design improvement of the chair described in (30) were adopted by P-Cure (P-Cure Ltd., Shilat Industrial Zone, Israel) for a commercial chair and vertical imaging system. The system was installed 2016 at Nothwestern Medicine Chicago Proton Center (NWMCPC, Chicago, Illinois, USA), where it is currently in clinical use. The P-Cure system features a carbon fibre chair with up to 20° tiltable back plate mounted to a robotic arm, capable of moving the chair between isocenter and an in-room vertical x-ray CT scanner (41), also installed at NWMCPC. The chair is targeted for not only head&neck, but also thoracic cancer patients, enabling imaging and treatment down to the diaphragm.

Balakin et al. (42) presented an upright patient positioning system for the Prometheus proton therapy complex at P.N. Lebedev Physical Institute of the Russian Academy of Sciences, Physical Technical Center (Protvino,Russia) the idea of which was proposed in (43). Their design considers an armchair targeted for head&neck cancer patients, that is height adjustable by 500 mm to accommodate patients of different size and enables a full 360° rotation around the vertical axis. Balakin *et al.* report initial experience on patient immobilization.

Recently, Zhang et al. (44) presented design considerations for a patient chair for particle therapy based on a Steward hexapod platform to provide the six-degree-of-freedom (6DOF) motion required for positioning and position correction following image guidance. For improved stability of the device, they propose an additional push rod attached to the center of the treatment chair guiding the motion of the hexapod. In addition, they describe a prototype design for a head&neck immobilization device in upright position with chin support for the patient to rest their head on.

Zhang et al. (45) present extensive design considerations for a patient chair. In an effort to retrofit a patient chair to an existing fixed horizontal beam line with limited available space, they based their design also on a hexapod platform. In their work, detailed stress simulations and experimental validations were performed to ensure highest safety of the components and accuracy of the treatment chair motion under patient load. Clinical implementation of the device with dedicated quality assurance protocol is reported in (46) and first experience with patient treatments is presented in (31).

Buchner et al. (35) report on the design of a novel treatment chair and soft robot immobilization device. Their design is based on a commercially available hexapod platform intended for being used as flight simulator. They developed soft robot immobilization devices to achieve highest positioning accuracy individually adaptable to every patient.

The company BEC GmbH (Pfullingen, Germany), which is offering high-precision robotics solutions for particle therapy, also has a design for a commercial patient chair in their 'exacure' radiotherapy portfolio (47), first presented in (48). The chair takes a similar route as the first chair design by Schreuder (30): for allowing high flexibility to accommodate patients and minimize uncertainties in the beam path, the chair is entirely based on small rectangular carbon fiber plates which can be individually removed/arranged.

Finally, another commercial option for an upright positioning system is offered by Leo Cancer Care (Smallfield, Horley, Surrey, UK). Their ambitious design, named EVE™, aims towards enabling upright treatments for head&neck, thoracic/abdominal as well as pelvic treatment sites. The systems' flexible design will enable different patient postures from sitting to half-standing or standing position. Initial positioning experience with the device was reported in (21).

MECHANICAL DESIGN: REQUIREMENTS AND PITFALLS

General Requirements

The ideal upright patient positioning and image guidance system should enable at least the same treatment flexibility as achievable with a gantry, without compromising on efficiency and accuracy compared to the current standard. An upright positioning system should therefore be:

1. Modular, in order to enable treatments of most patient sites
2. Flexible, in order to provide the optimal positioning and immobilization for all patients
3. Providing sub-millimeter/sub-degree positioning accuracy that remains stable over the treatment duration
4. Capable of quickly correcting the patient position according to image guidance
5. Simple and efficient to use

The first point is perhaps the most challenging, as there will likely always be a percentage of patients for whom the upright treatment position may not be a suitable option. In order to facilitate efficient patient throughput, the patient positioning device should be able to cope with different treatment sites without requiring considerable extra setup changing time.

The need for the positioning and image guidance system to allow flexibility for treating different patient sites, combined with the fixed beam line height poses the key design constraint for an upright positioning system with associated imaging (6, 45). The vertical and lateral translational motion required to adapt the patient positioning system and immobilization devices to the varying height and size of all patients needs to considered. Anthropometric data of European adults for machinery and workplace designs can be found for example in (49). The implications on chair design are indicated in **Figure 2** and summarized in **Table 1**. A straight upright posture of the patient's back was assumed for calculating required vertical ranges, i.e., rectangular bending angles between tibia/femur and femur/torso. Note that a half standing posture, shown in **Figure 2** as proposed by Leo Cancer Care Ltd (8, 50), would not change the required vertical range of motion of the positioning system to accommodate different treatment sites. It, however, would reduce the weight stress on the chair seat. Lateral ranges assume the rotational center of the patient positioning system to coincide with the lateral geometrical center of the patient. The need to compensate additional eccentricity otherwise adds to the required lateral range of motion.

For treatment sites below the thorax, the patient needs to be lifted considerably. For treatment of the prostate, the patient's head may reach up to 985 mm above the isocenter. Enough space above the isocenter is thus mandatory, especially if a vertical CT is to be mounted to the ceiling, which for existing centers may not necessarily be available.

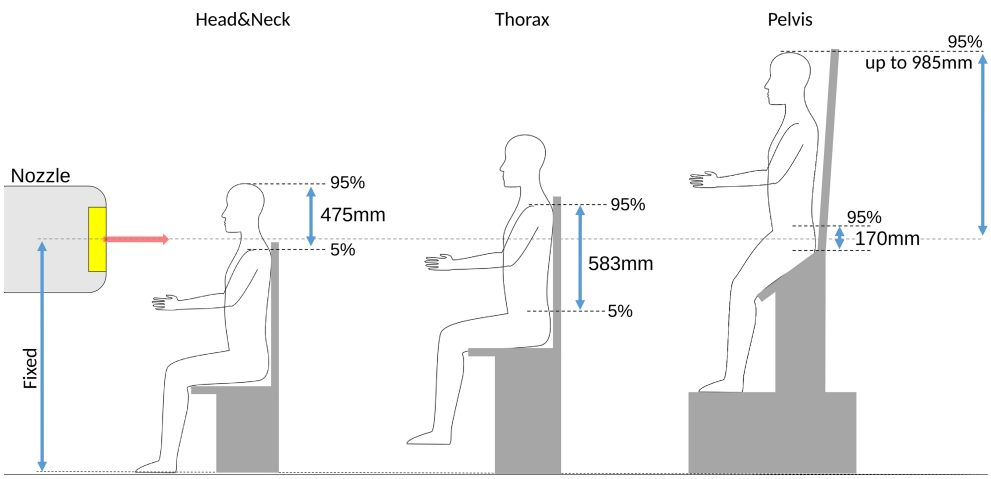

FIGURE 2 | Overview over the required vertical ranges (not to scale) of adjustment for different treatment sites for European adults, computed as the difference between 5 and 95 percentiles from anthropomorphic data in (49). An important constraint for an upright positioning device targeted for a fixed beam line is the fixed height of the isocenter. For pelvis treatments, the patient head can reach up to ~1m above the isocenter.

TABLE 1 | Requirements placed on a chair system for different treatment sites.

Treatment site	Head&Neck	Thorax/ Abdomen	Pelvis	Total
Height from chair seat (Hi/Lo) [mm]	985/510	695/112	170/0	–
Popliteal height (Hi/Lo) [mm]	–	–	–	495/ 380
Vertical range [mm]	~475	~583	~170	~985
Lateral range [mm]	±103	±270	±220	±270

Ranges are calculated based on anthropometric data for European adults in (49), reporting the largest value in the range of European adults (i.e., between 5 and/or 95 percentiles). A straight upright sitting posture with rectangular tibia/femur and femur/torso angles was assumed. The range required for pelvis treatments was approximated from the thigh clearance.

For greatest flexibility, the positioning system should also provide a 360° motion around the vertical axis to enable all treatment directions. Existing prototypes, in addition, consider up to ± 20° tilt around the lateral axis (6, 8, 9, 44, 45). Sufficient experience for the optimal tilt around the lateral axis for different treatment sites is not yet reported in literature, such that the current generation of chair designs may provide more/less flexibility than needed.

In terms of mechanical stability, according to the IEC 60601-1 norm (51), any patient positioning system must be able to safely move a mass of 135 kg plus the weight of accessories. Assuming the weight of the chair and patient immobilization devices (mask, head rest, and connections with chair) to be around 50 kg (45), this necessitates the support structure to comfortably lift 185 kg. In addition, any equipment intended for the patient to step on needs to support at least 270 kg for a minute. These regulations put strong constraints on the engineering choices for the positioning system.

Considerations on Posture

Patient posture is important when considering upright treatments, as it can have a significant effect on the patient comfort as well as intra-fraction movement, and has direct implications for the image guidance setup. Different published postures are shown in **Figure 3**.

Sun et al. (31) report patient discomfort for a head&neck chair system, where the patients are positioned in a straight upright position (i.e., a 90° angle between seat and backrest). Patients reportedly tended to sag their heads within the thermoplastic immobilization masks. For long treatments, this may result in increased intra-treatment displacement and patient discomfort. Moreover, especially for long treatments, the comfort for the patients back and bottom becomes important, where e.g. vacuum cushions or simple office chair supply cushions may provide sufficient support. More ideal, however, would potentially be a posture where the back rest is tilted 15-20° backwards pushing the patients into the backrest (21, 31). In fact, most chair solutions for particle therapy consider such a posture (5, 6, 35, 41, 50). Similar findings have been reported by McCarroll et al. (26) who considered a 'reverse' chair setup, where the patients are forward leaning against a chest support plate. Additional support for chin and forehead was included in their prototype following initial patient experience, to provide more patient comfort. The forward leaning posture may also be interesting for prone irradiation, for example, in case of treatment of the whole central nervous system.

To provide stability in a leaned-back position, a posture comparable to that in a race car seat (i.e., femur slightly inclined upwards, and bent knees), may be chosen, as done, e.g., by P-Cure Ltd (9, 41). This has the additional benefit that it provides more room for a robot arm underneath the chair, which otherwise could collide with the patient legs (45). Alternatively, a vertical rest for the patients knees to push against, as envisioned by Leo Cancer Care Ltd (8)., may be used to prevent sagging.

For any body site below the thorax, a half standing posture, as proposed by Leo Cancer Care Ltd (8)., is the only viable option. They envision a bending angle between 135° and 165° between femur and torso (50). For seated positions, the patient legs would prohibit a vertical CT scan in the lower body regions.

6-Degree-of-Freedom Positioning System

The need to adapt to different patients, treatment sites and beam angles, alongside the need to adapt residual alignment following the image guidance system, necessitates the use of a highly accurate 6DOF support structure. To provide the necessary motion, sequential or linear robotic systems are suitable candidates.

As sequential support structure, a robotic arm as used for patient couches (52) could be used, as for example chosen by P-Cure Ltd (9). The robot arm offers a great flexibility, also in regards of moving the patient from the isocenter to an in-room vertical CT or moving the chair out of the way of other equipment. However, depending on the patient's posture and the robot position, the patients legs may interfere with the robot (45), limiting the achievable range of motion. Due to its bulky size, retrofitting an additional robot system for an upright positioning system into an existing treatment room may be infeasible alongside the other equipment. Utilizing an available couch robot to also mount the upright positioning system, with a shared coupling mechanism (30), would be the more practical solution.

In contrast, hexapod platforms present a compact solution (35, 44, 45). Hexapods are well suited to support the patient and can achieve high positioning accuracy (45). However, hexapods have a limited range of motion, allowing only restricted position correction when in extreme positions, e.g., when fully vertically

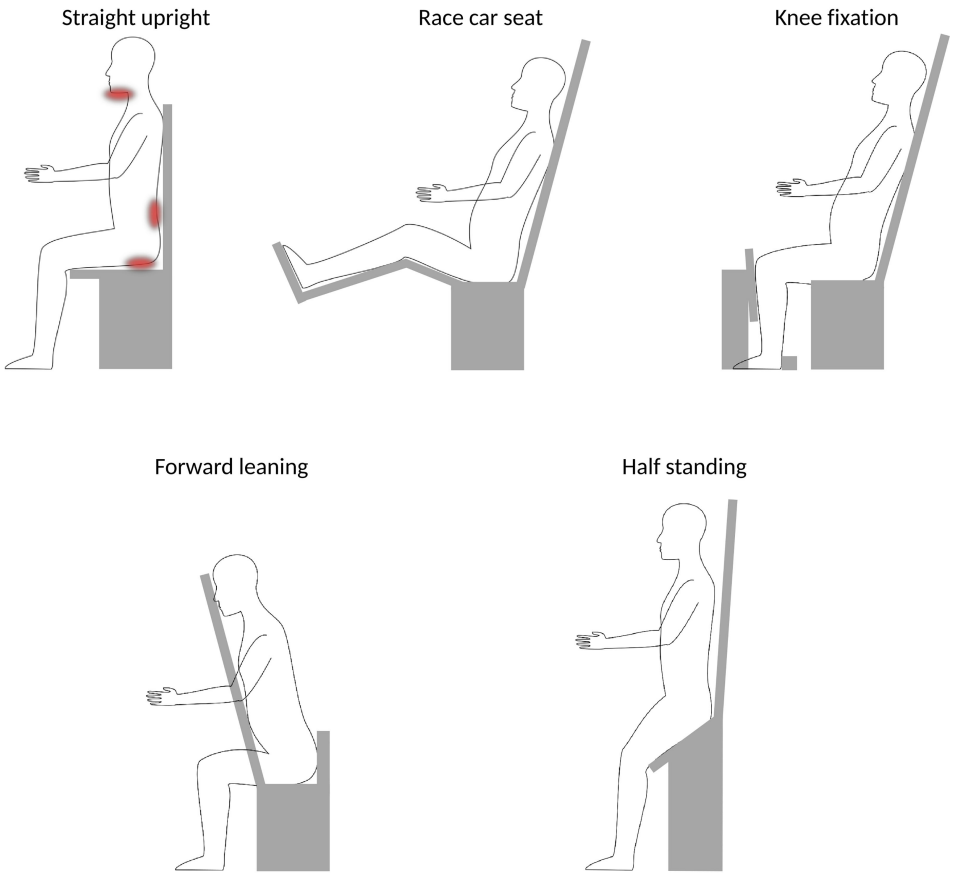

FIGURE 3 | Schematic overview over different postures. A straight upright posture [e.g (42)., and (31)] has been noted to induce stress on chin (for head&neck patients) and may be uncomfortable for long treatment duration, as indicated by the red areas. More ideal would be ~20° reclined position, where the forward push on the pelvis could be stabilized by a race-car seat posture [e.g (9)], or by adding a knee fixation [e.g (8)] or a belt strap [e.g (35)]. Alternative postures could be forward leaning for head&neck or possibly spine irradiations [e.g (26)] or half-standing, enabling to image and treat sites below the thorax [e.g (8)].

extended, and provide a limited range of rotation (44). Zhang et al. (45) circumvented these problems, by adding a translational platform on top of the hexapod and a 360° platform underneath it, effectively increasing the work space to that desired for patient positioning in head&neck cases. In order to provide flexibility for moving the chair to/from the isocenter, a rail system underneath the hexapod may be added as reported in (46).

Alternative designs to robot positioning systems have also been reported in literature. For example, the chair by Heeg et al. (6) features separate mechanisms for rotation, tilt and vertical adjustment in a steel frame. This design was chosen for stability, but is also relatively bulky. The EVE™ design by Leo Cancer Care Ltd (8) considers a height adjustable seat and tiltable back plate to adjust the patient's back angle. Immobilization devices, like masks and arm rests, will be attached to the back plate. Pitch and lateral position adjustment are achieved by tilting or moving the platform the chair is mounted on. The upright positioning system is placed on a large circular floor platform which provides full 360° rotation and can be lifted to accommodate treatments in lower body regions (abdomen and pelvis).

Immobilization Devices and Setup Accuracy

Immobilization is crucial especially for particle therapy to conserve beam ranges estimated from planning imaging. For an upright position, in contrast to supine, immobilization devices may need to support part of the patient's weight. Heeg et al. (39) for their head&neck targeted chair design reported that "the realisation of a secure and precise fixation unit required some rather unconventional details in the construction". They achieved better than 0.5 mm accuracy by using a steel frame with vertically adjustable mask holder. Steel frames can however, also cause artefacts in x-ray CT.

Zhang et al. (44) report on the development of a head fixation unit with adjustable screws and chin support, but indicated only limited accuracy. Sheng et al. (46) used thermoplastic masks mounted to a carbon fiber back plate for their head&neck targeted chair, which in a later study achieved high patient position accuracy (31). Balakin et al. (42) studied patient movement within thermoplastic masks for head&neck patients in seated position and report larger position variations

of up to several millimeters in some cases. In order to restrain patient mobility within the masks, additional immobilization devices may hence be needed. It has to be noted that the design by Balakin et al. considered a straight upright posture, which was found sub-optimal regarding patient motion in (31).

Buchner et al. (35) present the development of soft robots as immobilization devices to counter patient slouching in the seated position. The soft robots based on fluid-driven origami inspired artificial muscles have the advantage of being highly adaptive, providing individually optimized support for the patient. Hence, the soft robot technology may present several advantages over conventional immobilization devices for upright positioning. For example, they can provide the best position for the day, without the need to make and store several immobilization devices. Buchner et al. report promising results for immobilization and positioning with their device.

To fixate the pelvis and thereby stabilise the upper body, Leo Cancer Care Ltd. (8) have proposed a knee rest and heel fixation, using the patient's femur to push the pelvis into the chair seat. Such a device might provide stability for avoiding patient sagging, removing load from upper body or head fixation masks. It can be speculated that the knee support may also benefit the reproducibility of the femur-hip angle, which is a known issue for particle prostate therapy (53).

Mackie *et al.* (21) used a prototype of the Leo Cancer Care upright positioning system to investigate positioning accuracy for different treatment sites with an optical system. Deviations in setup accuracy for thorax patients were comparable to those found in literature for supine treatments. It should be noted that they measured external motion shifts only, but not potential motion of the tumor inside the body, which might differ from supine positions.

Most recently, Sun et al. (31) published a clinical study on the first experience for patient intra- and inter-treatment position changes with the SPHIC chair system, reporting an accuracy comparable to that of traditional supine positioning. Similar, McCarroll et al. (26) for their forward leaning design report head&neck positioning accuracy comparable to that in traditional supine position, except for one patient, where large displacement in the order of centimeters was observed.

Similar to a conventional couch system, any upright positioning device requires regular quality assurance to verify its required clinical accuracy better than 0.5°/1 mm (54). Especially for 6DOF support devices consisting of multiple individual components, agreement of their intrinsic coordinate systems with each other must be ensured, and potential variations be accurately corrected for, in order to avoid error propagation (55). reported a framework for coordinate system alignment and correction of systematic errors in the movement of the SPHIC treatment chair. Quality assurance reported for chair systems, so far, considered rigid phantoms (e.g., in (46)). However, to ensure quality of immobilization devices for upright positioning, one may also need to consider the support against deformations in upright posture. New, targeted quality assurance strategies may therefore be advisory.

IMAGE GUIDANCE FOR UPRIGHT POSITIONS

Significant anatomical variation can be expected for nearly all treatment sites, with the possible exception of the brain as it is enclosed in the rigid skull. The relative change of the gravity vector and the accompanying change in muscle tension will cause non-rigid changes to most organs. Yan et al. (56) investigated patient alignment between supine and upright (slightly reclined) position using an upright MRI scanner. They report good alignment for the head, but already note deformations in the neck region. Organs in abdomen or thorax are associated with larger differences between supine and upright (28, 56, 57). The success of upright treatment therefore crucially depends on the availability of an upright CT scanner for treatment simulation.

A dedicated x-ray CT system for upright treatments was implemented by Kamada et al. (5). The system was attached to the ceiling of the treatment room, and lowered down over the positioned patient. A contact sensor on the lower surface of the scanner was used to avoid collisions with the chair or patient. Shah et al. (58) report the use of a vertical CT scanner at Fermi Lab for a special patient case that could not tolerate supine positioning due to their medical condition. Schreuder (30) designed a system for vertical CT imaging from any angle between vertical and horizontal. P-Cure Ltd (9) offers a commercial system for upright CT imaging, which was installed at the Northwestern Medicine Chicago Proton Center in 2016, and has been used in clinical routine since then. However, to the best of the authors knowledge, no study on the system performance, nor patient data is yet presented in literature. Notably, for sitting patient postures, i.e., those with legs in ~90° angle to the torso, imaging below the diaphragm is not possible due to the limited CT bore diameter. Most recently Leo Cancer Care Ltd (8) have proposed a design for a rotatable Dual-Energy CT scanner. The system, which is a follow up of the design presented by Schreuder (30), is intended to be mounted between two supporting columns with a central rotation axis, enabling imaging at any angle between supine to upright position. As for previous vertical CT designs, the system would then slide over the patient for image acquisition. It is intended to enable full CT imaging of treatment sites down to the pelvis in combination with a half standing or standing patient posture as provided by their upright positioning device.

While a vertical x-ray CT scanner positioned directly at isocenter may provide the greatest accuracy, it may not be feasible due to space limitations, especially above the isocenter. In addition, if a switch to a treatment couch is desired, installation of a vertical x-ray CT on columns lateral to the isocenter may be challenging due to the lateral clearance (±2m) needed for full couch motion. If setup uncertainties between an out-of-room planning vertical CT are deemed too large, or no space for a second upright positioning system with vertical CT is available, in-room x-ray CT not at isocenter may be more practical. In a recent study, Nesteruk et al. (59) have found no significant difference between in-isocenter cone-beam CT

(CBCT) based treatment planning, and treatment planning based on a CT-on-rails for supine position. The same may be the case for upright, such that an in-room CT instead of one at isonceter may provide sufficient accuracy. This then requires a suitable option to move the chair between CT and isocenter is available (robot arm, rail).

CBCT at isocenter also presents a viable option for verification, as done in (31), and plan simulation. The flexibility to rotate the patient instead of the imaging device for CBCT acquisition has already been explored in (60) and was recently taken into account for the design of the MARIE™ proton therapy solution by Leo Cancer Care Ltd (8). If options for upright and supine positioning are foreseen, robotic CBCT systems should be able to provide the necessary flexibility, especially since they allow for non-co-planar image acquisition (61). CBCT may be a more practical solution for imaging at isocenter compared to vertical CT, not least with the recent boost in achievable CBCT image accuracy *via* iterative and machine learning based algorithms (7). Even accurate 4D-CBCT based proton therapy dose calculations were made possible (62), making CBCT particularly attractive for upright particle therapy.

Treatment planning typically involves modalities beyond X-ray CT, especially for contouring of target volumes and organs at risk, such as MRI or PET. A vertical PET for the patient in seated position was already considered by Heeg et al. (6). Upright MRI systems have been used in various studies for investigating anatomical differences between upright and supine positions (28, 29, 56, 57, 63). To provide best possible accuracy, having both the MRI and x-ray CT in upright posture would be preferential, as increased uncertainties in the deformable registration between the two postures are to be expected. Still, vertical MRI and PET scanners with the same image quality as current clinical systems for recumbent patients might be difficult to achieve, due to the size and geometry of the involved detector and acquisition systems. The viability of upright treatments considering the whole treatment planning chain therefore needs to be carefully investigated (23).

Particle radiography (pRad) and particle CT (pCT) present interesting options for at-isocenter imaging in particle therapy, and are particularly suited for upright patient positions. For particle imaging, the particle beam energy is increased beyond the therapeutic level such that the particles fully cross the patient, which enables to reconstruct images of the patient's integral water equivalent thickness (64, 65). pRad has shown good capability for position (66, 67) and anatomy (68) verification from beams eye view, and for optimization of the x-ray CT relative stopping power calibration (69–71). By rotating the patient, full pCT scans may be acquired. pCT scans may be used directly for treatment planning, where the direct nature of assessing the relative stopping power provides high stopping power and range prediction accuracy (72–75). pCT and upright treatment posture are inherently a well suited match, since pCT acquisition would be easier with a fixed beam and detector setup and rotating patient compared to acquisition with a rotating gantry. In fact, all currently existing pCT prototypes use rotating platforms to rotate the object for pCT acquisition. Moreover, the absence of beam hardening or metal artifacts for pCT (76) could prove useful for upright treatments, as it permits more flexible choice of materials for the immobilization devices and still obtain artifact free images.

Optical guidance systems are suitable to quickly verify the patient position. Commercial optical guidance systems have already been the system of choice to verify the accuracy of upright positioning solutions for different studies found in literature (21, 35, 45, 46) As such, an optical tracking system may be considered as a standard with upright treatment postures.

In terms of treatment plan simulation and optimization, the same infrastructure can be used for both upright and supine/prone positions, through the introduction of a simple coordinate transformation, as introduced by Krämer et al. (77) to the experimental treatment planning platform TRiP98 (78). This is advantageous regarding the introduction of an upright positioning system into daily clinical routine. Recently, an option for a seated patient position was implemented in the commercially available treatment planning system RayStation (RaySearch Laboratories, Stockholm, Sweden) for proton therapy and was validated with a commercial radiotherapy chair solution offered by Q-fix (Avondale, Pennsylvania, USA) (79). Hegarty et al. (17) note additional constraints concerning the patient tolerance of rotational speed and acceleration of the chair during treatment planning for photon IMRT or VMAT treatments. This is of less relevance for particle therapy, which is typically applied through few fields between which the chair rotation can be comfortably adapted. Nevertheless, this would need to be considered in the context of particle arc therapy, where varying rotational speed during delivery is present (16).

DISCUSSION

In the following, we briefly summarize the key points to take from previous literature. Then we present some recommendations for future systems, where we distinguish between retrofitting an upright positioning system into an existing facility and designing a new facility upfront with upright positioning.

Key Take-Aways From Literature

It is evident from literature, that a chair system aimed for different treatment sites needs to be highly modular and flexible. Different postures, ranges of motion and fixation devices are required for different treatment sites, with the optimal solution for each site still being subject of further research. While a one-fits-all upright patient positioning system would certainly be most efficient in terms of clinical workflow, it might not necessarily be the best solution for each site. For example, a mounting mechanism for the patient mask made of steel provides excellent accuracy for head&neck treatment (39, 46). But steel in the backrest would likely prohibit thoracic treatments, due to the CT artifacts and risk of activation that this entails. Moreover, an upright treatment will not be suited for all patients, who would then be excluded by a chair-only solution (26).

The most important question to ask prior to designing a chair system is therefore which patient cohorts are to be treated. A clinic aiming to be the main particle therapy provider for a large geographical region will have different aspirations compared to a specialized treatment facility in a region with existing alternative centers. A similar argument can also be made regarding the number of available treatment rooms in the facility.

A key challenge for upright treatments that has been pointed out in several publications is the different requirements placed on immobilization devices. While an inaccurate position, for example from mechanical sagging of the chair, may be corrected through adequate quality assurance (45), individual sagging of the patients in the immobilization devices would necessitate online image guidance to be detected, as well as a framework for real-time adaptive radiotherapy to be corrected for. Immobilization devices therefore should be a center point in the design of new upright positioning systems.

In the same line of thought, vertical imaging is paramount to the success of upright treatment. While conventional x-ray radiography image guidance systems have been used successfully in (31) for patient alignment, CBCT would be better and more flexible. In-room CT or in-isocenter CT may not be necessary for patient positioning, however, vertical, planning-quality CT imaging needs to be available somewhere in the facility, if patient sites other than the head are to be treated. Optical surface guidance, in addition, has shown to be a useful tool for verifying and monitoring upright patient position.

Particle CT could be a well suited candidate for in-isocenter CT with limited available space. However, long scan acquisition times and the need for higher-than-treatment beam energies are still limiting factors (80). With advances in technology, particle CT could be the preferred option of choice compared to in-isocenter x-ray CT.

In terms of posture, there is currently too little evidence to conclude on an ideal posture for the different indications beside head&neck, for which a slightly reclined posture seems to be ideal. For treatments at or above the thorax, any position that enables secure fixation of the pelvis in a reproducible position may work to restrain patient sagging. For treatment below diaphragm, however, a half-standing or standing posture is the only feasible option.

At least initially, the limited experience on anatomical changes for upright treatments will likely necessitate the use of increased safety margins. These, however, will be reduced with increasing experience with the upright position. Frequent, and ideally, isocentric planning-quality image guidance should be performed during the pioneering phase of upright treatments.

Retrofitting an Upright Positioning System to an Existing Facility

When retrofitting an upright positioning system to an existing (fixed beam line) facility, the major limiting factor is the available space. Equipment, like a couch robot, already in the treatment room needs to be considered and the fixed floor-isocenter-ceiling heights pose a major constraint.

For a multi-room facility, a dedicated specialized treatment room with an upright positioning system, where existing equipment for recumbent positioning may be discarded, could be a viable option. For single- or two-room facilities, the capability to switch to a supine/prone treatment position is a key to ensure efficacy. The most preferential/cost-efficient solution would hence be one that can be coupled to the existing robot positioning devices used already for the treatment couch. The robot arm could be used to also mount or park the individual modules for easier handling (30).

Having both a couch and upright treatment positioning system in isocenter makes the additional installation of an in-isocenter vertical CT, capable of imaging in both postures, challenging, due to the clearance required for couch motion. If not enough room for an in-isocenter, or in-room rotatable CT is available, at least x-ray radiography image guidance or CBCT suitable for upright position verification appears mandatory. Due to the flexible acquisition trajectories, a C-arm CBCT system suitable for both couch and upright positioning system would be the preferred option.

For accurate simulation, a vertical CT will be necessary for most treatment sites. Even if an in-room vertical CT exists, a more efficient workflow might be achievable if space for an upright CT scanner and upright positioning system was available somewhere in the facility for simulation. Otherwise, the treatment room would be blocked for planning CT acquisition. These issues should be thoroughly considered with the clinical staff before installation of an upright patient positioning system. Due to the missing constraint placed by the fixed beam height, a not-in-isocenter vertical CT requires lower ceiling height compared to one positioned at isocenter, which renders installation easier.

Designing a New Facility With an Upright Positioning System

Modeling of patient numbers, treatments sites and division of patients to the different rooms should be carried out carefully. The chair design greatly depends on the intended treatment sites, which also dictates different options for imaging and necessary range of motion. A restriction to certain treatments can greatly reduce cost, not only in the chair itself, but especially in terms of room size. However, a too narrow specification might hinder an efficient workflow later on, and prove even more costly long term.

Again, a central point is the number of rooms to be available at the facility. If multiple rooms are planned, a dedicated room for upright treatments could be designed. Here, the choice of 6DOF support structure would not need to consider space limitations nor a switch to couch. This room also should feature enough space to accommodate in-isocenter image guidance systems. The facility design should also consider optimizing the height of the isocenter with respect to the upright positioning system. This should maximize the number of patients that can be treated for the intended body sites, while minimizing the displacement required of the chair positioning system, especially for hexapods with limited workspace.

All current single room designs feature a gantry. A fixed beam single room with a chair would likely be possible on a previously not achievable low budget, so that also a highly specialized solution may become plausible in the future. This could focus only on a select subset of patients, such as only thoracic and H&N patients, and could offer a dedicated solution for this subgroup. As such, it could potentially offer treatment quality for its patients comparable to a gantry-based system, but at lower cost. However, careful modeling would be necessary to judge clinical and commercial viability.

Additional space for a vertical CT should be planned, or patients would have to be positioned without planning quality imaging. This might be challenging especially to early adopters, when clinical experience is still limited. A separate vertical CT scanner that can enable imaging both in upright and supine position would ensure highest efficacy. Installation of an open bore/upright MRI at the facility could be considered, but further studies on errors in deformable registration between recumbent and upright positions are needed to support any decision.

CONCLUSION

Upright patient positioning has distinct economical and clinical benefits that may make it a key technology for the next generation particle therapy facilities. Still, an upright positioning system brings many clinical and also engineering challenges, to achieve highly accurate and stable patient positioning. In addition, limited experience in the difference between patient anatomy in supine or upright position is available. However, we are currently seeing a boost in knowledge with several developments towards upright patient positioning systems driven by the need to reduce particle therapy cost and increase efficiency. In this review, we aimed at highlighting key points from these developments to make recommendations for an ideal upright system. It seems that a one-fits-all solution is hard or even impossible to achieve. The clinical benefit of an upright positioning device therefore needs to be thoroughly evaluated for different patient sites to identify, where the upright position would provide the greatest benefit, and to tailor the patient positioning system design. Such studies are currently underway, and we are expecting exciting developments of upright positioning systems that will bring a paradigm shift for the future of particle therapy.

AUTHOR CONTRIBUTIONS

LV — conceptualization, literature review, writing (original draft), writing (revision). YS — conceptualization, writing (revision). MD — conceptualization, supervision, funding acquisition, writing (revision). CG — conceptualization, supervision, funding acquisition, writing (original draft), writing (revision). All authors contributed to the article and approved the submitted version.

FUNDING

This project has received funding from the European Union's Horizon 2020 research and innovation programme under grant agreement No 101008548.

ACKNOWLEDGMENTS

The authors would like to thank Ryan Fullarton (currently with University College London) for his help with proofreading the manuscript.

REFERENCES

1. Particle Therapy Co-Operative Group. *Particle Therapy Facilities in Clinical Operation (Last Update: (November 2021)* (2021). Available at: https://www.ptcog.ch/index.php/patient-statistics.
2. Durante M, Paganetti H. Nuclear Physics in Particle Therapy: A Review. *Rep Prog Phys* (2016) 79:96702. doi: 10.1088/0034-4885/79/9/096702
3. Paganetti H, Beltran C, Both S, Dong L, Flanz J, Furutani K, et al. Roadmap: Proton Therapy Physics and Biology. *Phys Med Biol* (2021) 66(5):05RM01. doi: 10.1088/1361-6560/abcd16.
4. Jäkel O, Kraft G, Karger CP. The History of Ion Beam Therapy in Germany. *Z für Med Physik* (2022) 32:6–22. doi: 10.1016/j.zemedi.2021.11.003
5. Kamada T, Tsujii H, Mizoe JE, Matsuoka Y, Tsuji H, Osaka Y, et al. A Horizontal Ct System Dedicated to Heavy-Ion Beam Treatment. *Radiother Oncol* (1999) 50:235–7. doi: 10.1016/S0167-8140(99)00005-5
6. Heeg P, Kuhn S, Schardt D, Schultz-Ertner D. A Treatment Chair for the Therapy Facility. In: *GSI Report*, vol. vol. 2000-1. . Darmstadt: GSI (2000). p. 167. Wissenschaftlicher Ergebnisbericht der GSI, GSI Annual Report.
7. Landry G, Hua Ch.. Current State and Future Applications of Radiological Image Guidance for Particle Therapy. *Med Phys* (2018) 45:e1086–95. doi: 10.1002/mp.12744
8. Leo Cancer Care Ltd. *Leo Cancer Care Ltd. Website* (2021). Available at: www.leocancercare.com (Accessed Dec. 9, 2021).
9. P-cure. *Patient Centric Proton Therapy Website* (2021). Available at: www.p-cure.com (Accessed Dec. 9, 2021).
10. Bortfeld TR, MFd V, Yan S. The Societal Impact of Ion Beam Therapy. *Z fur med Physik* (2021), 31(2):102-104. doi: 10.1016/j.zemedi.2020.06.007
11. Mazal A, Vera Sanchez JA, Sanchez-Parcerisa D, Udias JM, España S, Sanchez-Tembleque V, et al. Biological and Mechanical Synergies to Deal With Proton Therapy Pitfalls: Minibeams, Flash, Arcs, and Gantryless Rooms. *Front Oncol* (2021) 10:613669. doi: 10.3389/fonc.2020.613669
12. Durante M, Debus J, Loeffler JS. Physics and Biomedical Challenges of Cancer Therapy With Accelerated Heavy Ions. *Nat Rev Phys* (2021) 3:777–90. doi: 10.1038/s42254-021-00368-5
13. Parodi K, Polf JC. *In Vivo* Range Verification in Particle Therapy. *Med Phys* (2018) 45:e1036–50. doi: 10.1002/mp.12960
14. Lis M, Newhauser W, Donetti M, Wolf M, Steinsberger T, Paz A, et al. Dosimetric Validation of a System to Treat Moving Tumors Using Scanned Ion Beams That are Synchronized With Anatomical Motion. *Front Oncol* (2021) 11:712126. doi: 10.3389/fonc.2021.712126
15. Paganetti H, Botas P, Sharp GC, Winey B. Adaptive Proton Therapy. *Phys Med Biol* (2021) 66:22TR01. doi: 10.1088/1361-6560/ac344f
16. Li X, Liu G, Janssens G, De Wilde O, Bossier V, Lerot X, et al. The First Prototype of Spot-Scanning Proton Arc Treatment Delivery. *Radiother Oncol* (2019) 137:130–6. doi: 10.1016/j.radonc.2019.04.032
17. Hegarty S, Hardcastle N, Korte J, Kron T, Everitt S, Rahim S, et al. Please Place Your Seat in the Full Upright Position: A Technical Framework for Landing

Upright Radiation Therapy in the 21st Century. *Front Oncol* (2022) 12:821887. doi: 10.3389/fonc.2022.821887
18. Moyers MF, Lesyna W. Isocenter Characteristics of an External Ring Proton Gantry. *Int J Radiat Oncol Biol Phys* (2004) 60:1622–30. doi: 10.1016/j.ijrobp.2004.08.052
19. Haberer T, Debus J, Eickhoff H, Jäkel O, Schulz-Ertner D, Weber U. The Heidelberg Ion Therapy Center. *Radiother Oncol* (2004) 73:S186–90. doi: 10.1016/S0167-8140(04)80046-X
20. Bottura L, Felcini E, De Rijk G, Dutoit B. Gatoroid: A Novel Toroidal Gantry for Hadron Therapy. *Nucl Instrum Methods Phys Res Section A: Accelerators Spectrometers Detectors Associated Equip* (2020) 983:164588. doi: 10.1016/j.nima.2020.164588
21. Mackie TR, Towe S, Schreuder N. Is Upright Radiotherapy Medically and Financially Better? *AIP Conf Proc* (2021) 2348:020002. doi: 10.1063/5.0051770
22. Yan S, Lu HM, Flanz J, Adams J, Trofimov A, Bortfeld T. Reassessment of the Necessity of the Proton Gantry: Analysis of Beam Orientations From 4332 Treatments at the Massachusetts General Hospital Proton Center Over the Past 10 Years. *Int J Radiat Oncol Biol Phys* (2016) 95:224–33. doi: 10.1016/j.ijrobp.2015.09.033
23. Schreuder N, Ding X, Li Z. Fixed Beamlines can Replace Gantries for Particle Therapy. *Med Phys* (2022) 49(4):2097–2100. doi: 10.1002/mp.15531
24. Yan S, Depauw N, Adams J, Gorissen BL, Shih HA, Flanz J, et al. Technical Note: Does the Greater Power of Pencil Beam Scanning Reduce the Need for a Proton Gantry? *study head-and-neck Brain tumors Med Phys* (2022) 49:813–24. doi: 10.1002/mp.15409
25. Court L, Yang J, Fullen D, Han N, Ko J, Mason S, et al. Su-E-T-359: Patients Could (and Should) be Treated in an Upright Position. *Med Phys* (2013) 40:287–7. doi: 10.1118/1.4814793
26. McCarroll RE, Beadle BM, Fullen D, Balter PA, Followill DS, Stingo FC, et al. Reproducibility of Patient Setup in the Seated Treatment Position: A Novel Treatment Chair Design. *J Appl Clin Med Phys* (2017) 18:223–9. doi: 10.1002/acm2.12024
27. Dellamonica J, Lerolle N, Sargentini C, Hubert S, Beduneau G, Marco FD, et al. Effect of Different Seated Positions on Lung Volume and Oxygenation in Acute Respiratory Distress Syndrome. *Intensive Care Med* (2013) 39:1121–7. doi: 10.1007/s00134-013-2827-x
28. Yang J, Chu D, Dong L, Court LE. Advantages of Simulating Thoracic Cancer Patients in an Upright Position. *Pract Radiat Oncol* (2014) 4:e53–8. doi: 10.1016/j.prro.2013.04.005
29. von Siebenthal M, Székely G, Lomax AJ, Cattin PC. Systematic Errors in Respiratory Gating Due to Intrafraction Deformations of the Liver. *Med Phys* (2007) 34:3620–9. doi: 10.1118/1.2767053
30. Schreuder AN. *Technological Developments Allowing For The Widespread Clinical Adoption Of Proton Radiotherapy*. London, United Kingdom: University College London (2020).
31. Sun J, Kong L, Chen Z, You D, Mao J, Guan X, et al. Clinical Implementation of a 6d Treatment Chair for Fixed Ion Beam Lines. *Front Oncol* (2021) 11:694749. doi: 10.3389/fonc.2021.694749
32. Hrbacek J, Mishra KK, Kacperek A, Dendale R, Nauraye C, Auger M, et al. Practice Patterns Analysis of Ocular Proton Therapy Centers: The International Optic Survey. *Int J Radiat Oncol Biol Phys* (2016) 95:336–43. doi: 10.1016/j.ijrobp.2016.01.040
33. Ciocca M, Magro G, Mastella E, Mairani A, Mirandola A, Molinelli S, et al. Design and Commissioning of the non-Dedicated Scanning Proton Beamline for Ocular Treatment at the Synchrotron-Based Cnao Facility. *Med Phys* (2019) 46:1852–62. doi: 10.1002/mp.13389
34. Rahim S, Korte J, Hardcastle N, Hegarty S, Kron T, Everitt S. Upright Radiation Therapy—a Historical Reflection and Opportunities for Future Applications. *Front Oncol* (2020) 10:213. doi: 10.3389/fonc.2020.00213
35. Buchner T, Yan S, Li S, Flanz J, Hueso-González F, Kielty E, et al. (2020). A Soft Robotic Device for Patient Immobilization in Sitting and Reclined Positions for a Compact Proton Therapy System, in: *8th IEEE RAS/EMBS International Conference for Biomedical Robotics and Biomechatronics (BioRob)*, pp. 981–8. doi: 10.1109/BioRob49111.2020.9224389
36. Castro JR, Quivey JM, Lyman JT, Chen GTY, Tobias CA, Kanstein LL, et al. *Heavy Ion Therapy (Division of Biological and Environmental Research U.S* Vol. vol. LBL-5610. Energy Research and Development Administration (1977) p. 198–218.
37. Castro JR, Quivey JM, Lyman JT, Chen GTY, Phillips TL, Tobias CA, et al. Current Status of Clinical Particle Radiotherapy at Lawrence Berkeley Laboratory. *Cancer* (1980) 46:633–41. doi: 10.1002/1097-0142(19800815)46:4<633::AID-CNCR2820460402>3.0.CO;2-O
38. Gunn JT, Lyman JT. A Versatile Patient Positioner for Radiation Therapy. *IEEE Trans Nucl Sci* (1973) 20:1022–4. doi: 10.1109/TNS.1973.4327314
39. Heeg P, Schardt D, Störmer J. The Patient Fixation Unit for the Treatment Chair in Cave M. In: *GSI Report*, vol. vol. 2002-1. . Darmstadt: GSI (2002). p. 279 p.
40. Lis M, Newhauser W, Donetti M, Durante M, Weber U, Zipfel B, et al. A Facility for the Research, Development, and Translation of Advanced Technologies for Ion-Beam Therapies. *J Instrum* (2021) 16:T03004. doi: 10.1088/1748-0221/16/03/t03004
41. Marash M, Shpunt M. . Apparatus and method for providing patient imaging (2013). U.S. patent application US20150208992A1; Assignee: P-Cure Ltd.
42. Balakin VE, Belikhin MA, Pryanichnikov AA, Shemyakov AE, Strelnikova NS. Clinical Application of New Immobilization System in Seated Position for Proton Therapy. *KnE Energy* (2018) 3:45–51. doi: 10.18502/ken.v3i2.1790
43. Balakin V. *Charged Particle Treatment, Rapid Patient Positioning Apparatus and Method of Use Thereof (2012).* , US patent US9056199B2; Assignee: V. A. Balakin, V. P. Balakin.
44. Zhang Y, Yang Z, Jiang J, Dai X, Qin P, Guo S, et al. Design Analysis and Experimental Study of Robotic Chair for Proton Heavy Ion Radiotherapy. *Appl Bionics Biomech* (2019) 2019:6410941. doi: 10.1155/2019/6410941
45. Zhang X, Hsi WC, Yang F, Wang Z, Sheng Y, Sun J, et al. Development of an Isocentric Rotating Chair Positioner to Treat Patients of Head and Neck Cancer at Upright Seated Position With Multiple Nonplanar Fields in a Fixed Carbon-Ion Beamline. *Med Phys* (2020) 47:2450–60. doi: 10.1002/mp.14115
46. Sheng Y, Sun J, Wang W, Stuart B, Kong L, Gao J, et al. Performance of a 6d Treatment Chair for Patient Positioning in an Upright Posture for Fixed Ion Beam Lines. *Front Oncol* (2020) 10:122. doi: 10.3389/fonc.2020.00122
47. BEC GmbH. *Exacure Website* (2021). Available at: www.exacure.com (Accessed Dec. 21, 2021).
48. Bouraoui MW, Buck M. *Sitzvorrichtung Für Eine Patientenpositioniereinrichtung Und Patientenpositioniereinrichtung Mit Einer Sitzvorrichtung*. BEC GmbH (2018). Available at: https://depatisnet.dpma.de/DepatisNet/depatisnet?action=bibdat&docid=DE102016015530A1
49. Jürgens H, Matzdorff I, Windberg J. *International Anthropometric Data for Work-Place and Machinery Design. Arbeitswissenschaftliche Erkenntnisse*, Dortmund, Germany: Bundesanstalt für Arbeitsschutz und Arbeitsmedizin Vol. 108. (1998). p. 11. Available at: https://www.baua.de/DE/Angebote/Publikationen/AWE/AWE108e.html
50. Feain I, Towe S, Strangeman M. *Patient Positioning Apparatus*. Leo Cancer Care Ltd (2017).
51. Comission IE.. *Medical Electrical Equipment – ALL PARTS*. Geneva, CH: International standard, International Electronical Commission (2021).
52. Nairz O, Winter M, Heeg P, Jäkel O. Accuracy of Robotic Patient Positioners Used in Ion Beam Therapy. *Radiat Oncol* (2013) 8:124. doi: 10.1186/1748-717X-8-124
53. Trofimov A, Nguyen PL, Efstathiou JA, Wang Y, Lu HM, Engelsman M, et al. Interfractional Variations in the Setup of Pelvic Bony Anatomy and Soft Tissue, and Their Implications on the Delivery of Proton Therapy for Localized Prostate Cancer. *Int J Radiat oncol biol Phys* (2011) 80:928–37. doi: 10.1016/j.ijrobp.2010.08.006
54. Klein EE, Hanley J, Bayouth J, Yin FF, Simon W, Dresser S, et al. Task Group 142 Report: Quality Assurance of Medical Acceleratorsa). *Med Phys* (2009) 36:4197–212. doi: 10.1118/1.3190392
55. Zhang X, Hsi W, Yang F, Zhou R. Verification and Validation (VnV) of Control Software for an Isocentric Rotation Chair Positioner Used to Treat Patients With Head/Neck Cancers in a Fixed Carbon-Ion Beamline. *J Instrum* (2022) 17:P01021. doi: 10.1088/1748-0221/17/01/p01021
56. Yan S, Greenhalgh J, Li S, Bortfeld T, Flanz J. (2020). An Mri Study of Organ Shape Variations Between Upright, Reclined and Recumbent Positions: Implications for Compact Gantry-Less Particle Therapy, in: *Proceedings to the 58th Annual Conference of the Particle Therapy Cooperative Group (PTCOG58), International Journal of Particle Therapy* Vol. 6. pp. 45–491. doi: 10.14338/IJPT.19-PTCOG-6.4

57. Hayes AR, Gayzik FS, Moreno DP, Martin RS, Stitzel JD. Comparison of Organ Location, Morphology, and Rib Coverage of a Midsized Male in the Supine and Seated Positions. *Comput Math Methods Med* (2013) 2013:419821. doi: 10.1155/2013/419821
58. Shah AP, Strauss JB, Kirk MC, Chen SS, Kroc TK, Zusag TW. Upright 3d Treatment Planning Using a Vertical Ct. *Med Dosimetry* (2009) 34:82–6. doi: 10.1016/j.meddos.2008.05.004
59. Nesteruk KP, Bobić M, Lalonde A, Winey BA, Lomax AJ, Paganetti H. Ct-On-Rails Versus in-Room Cbct for Online Daily Adaptive Proton Therapy of Head-and-Neck Cancers. *Cancers* (2021) 13(23). doi: 10.3390/cancers13235991
60. Fave X, Yang J, Carvalho L, Martin R, Pan T, Balter P, et al. Upright Cone Beam Ct Imaging Using the Onboard Imager. *Med Phys* (2014) 41:061906. doi: 10.1118/1.4875682
61. Hatamikia S, Biguri A, Kronreif G, Kettenbach J, Russ T, Furtado H, et al. Optimization for Customized Trajectories in Cone Beam Computed Tomography. *Med Phys* (2020) 47:4786–99. doi: 10.1002/mp.14403
62. Schmitz H, Rabe M, Janssens G, Bondesson D, Rit S, Parodi K, et al. Validation of Proton Dose Calculation on Scatter Corrected 4d Cone Beam Computed Tomography Using a Porcine Lung Phantom. *Phys Med Biol* (2021) 66:175022. doi: 10.1088/1361-6560/ac16e9
63. Abdulaziz M, Kavanagh A, Stothers L, Macnab AJ. (2018). Relevance of Open Magnetic Resonance Imaging Position (Sitting and Standing) to Quantify Pelvic Organ Prolapse in Women, in: *Canadian Urological Association journal = Journal de l'Association des urologues du Canada*, , Vol. 12. pp. E453–60. doi: 10.5489/cuaj.5186
64. Collins-Fekete CA, Brousmiche S, Portillo SKN, Beaulieu L, Seco J. A Maximum Likelihood Method for High Resolution Proton Radiography/Proton CT. *Phys Med Biol* (2016) 61:8232. doi: 10.1088/0031-9155/61/23/8232
65. Deffet S, Farace P, Macq B. Sparse Deconvolution of Proton Radiography Data to Estimate Water Equivalent Thickness Maps. *Med Phys* (2020) 47:509–17. doi: 10.1002/mp.13917
66. Palaniappan P, Meyer S, Kamp F, Belka C, Riboldi M, Parodi K, et al. Deformable image registration of the treatment planning CT with proton radiographies in perspective of adaptive proton therapy. *Physics in Medicine & mathsemicolon Biology* (2021) IOP Publishing 66:045008. doi: 10.1088/1361-6560/ab8fc3
67. Deffet S, Macq B, Righetto R, Vander Stappen F, Farace P. Registration of Pencil Beam Proton Radiography Data With X-Ray Ct. *Med Phys* (2017) 44:5393–401. doi: 10.1002/mp.12497
68. Sarosiek C, DeJongh EA, Coutrakon G, DeJongh DF, Duffin KL, Karonis NT, et al. Analysis of Characteristics of Images Acquired With a Prototype Clinical Proton Radiography System. *Med Phys* (2021) 48:2271–8. doi: 10.1002/mp.14801
69. Collins-Fekete CA, Brousmiche S, Hansen DC, Beaulieu L, Seco J. Pre-Treatment Patient-Specific Stopping Power by Combining List-Mode Proton Radiography and X-Ray Ct. *Phys Med Biol* (2017) 62:6836. doi: 10.1088/1361-6560/aa7c42
70. Gianoli C, Göppel M, Meyer S, Palaniappan P, Rädler M, Kamp F, et al. Patient-Specific Ct Calibration Based on Ion Radiography for Different Detector Configurations in 1h, 4he and 12c Ion Pencil Beam Scanning. *Phys Med Biol* (2020) 65(24):245014. doi: 10.1088/1361-6560/aba319
71. Meijers A, Free J, Wagenaar D, Deffet S, Knopf AC, Langendijk JA, et al. Validation of the Proton Range Accuracy and Optimization of CT Calibration Curves Utilizing Range Probing. *Phys Med Biol* (2020) 65:03NT02. doi: 10.1088/1361-6560/ab66e1
72. Meyer S, Kamp F, Tessonnier T, Mairani A, Belka C, Carlson DJ, et al. Dosimetric Accuracy and Radiobiological Implications of Ion Computed Tomography for Proton Therapy Treatment Planning. *Phys Med Biol* (2019) 64:125008. doi: 10.1088/1361-6560/ab0fdf
73. Dedes G, Dickmann J, Niepel K, Wesp P, Johnson RP, Pankuch M, et al. Experimental Comparison of Proton CT and Dual Energy X-Ray CT for Relative Stopping Power Estimation in Proton Therapy. *Phys Med Biol* (2019) 64:165002. doi: 10.1088/1361-6560/ab2b72
74. Bär E, Volz L, Collins-Fekete CA, Brons S, Runz A, Schulte RW, et al. Experimental Comparison of Photon Versus Particle Computed Tomography to Predict Tissue Relative Stopping Powers. *Med Phys* (2022) 49:474–87. doi: 10.1002/mp.15283
75. Volz L, Collins-Fekete CA, Bär E, Brons S, Graeff C, Johnson RP, et al. The Accuracy of Helium Ion CT Based Particle Therapy Range Prediction: An Experimental Study Comparing Different Particle and X-Ray CT Modalities. *Phys Med Biol* (2021) 66:235010. doi: 10.1088/1361-6560/ac33ec
76. Civinini C, Scaringella M, Brianzi M, Intravaia M, Randazzo N, Sipala V, et al. Relative Stopping Power Measurements and Prosthesis Artifacts Reduction in Proton {CT}. *Phys Med Biol* (2020) 65:225012. doi: 10.1088/1361-6560/abb0c8
77. Krämer M, Grözinger SO, Hasch B, Jäkel O, Heeg P. Treatment Planning for the GSI Radiotherapy. In: *GSI Report*, vol. vol. 2005-1. . Darmstadt: GSI (2005). p. 496 p.
78. Krämer M, Jkel O, Haberer T, Kraft G, Schardt D, Weber U. Treatment Planning for Heavy-Ion Radiotherapy: Physical Beam Model and Dose Optimization. *Phys Med Biol* (2000) 45:3299–317. doi: 10.1088/0031-9155/45/11/313
79. Maes D, Janson M, Regmi R, Egan A, Rosenfeld A, Bloch C, et al. Validation and Practical Implementation of Seated Position Radiotherapy in a Commercial Tps for Proton Therapy. *Phys Med: Eur J Med Phys* (2020) 80:175–85. doi: 10.1016/j.ejmp.2020.10.027
80. Volz L, Collins-Fekete CA, Piersimoni P, Seco J. *Recent Developments in Proton Imaging*. CRC Press, Boca Raton (2021) p. 64–82. chap. 5. doi: 10.1201/9781003212485

Conflict of Interest: Authors LV, YS, MD and CG were employed by GSI Helmholtz Center for Heavy Ion Research GmbH.

frontiers | Frontiers in Oncology

TYPE Original Research
PUBLISHED 31 August 2022
DOI 10.3389/fonc.2022.982417

OPEN ACCESS

EDITED BY
Ilja Ciernik,
Städtische Klinikum Dessau, Germany

REVIEWED BY
James Chow,
University of Toronto, Canada
Karl T Butterworth,
Queen's University Belfast,
United Kingdom

*CORRESPONDENCE
Elke Beyreuther
e.beyreuther@hzdr.de

†These authors have contributed equally to this work and share first authorship

‡These authors have contributed equally to this work and share last authorship

SPECIALTY SECTION
This article was submitted to Cancer Imaging and Image-directed Interventions, a section of the journal Frontiers in Oncology

RECEIVED 30 June 2022
ACCEPTED 02 August 2022
PUBLISHED 31 August 2022

CITATION
Schneider M, Bodenstein E, Bock J, Dietrich A, Gantz S, Heuchel L, Krause M, Lühr A, von Neubeck C, Nexhipi S, Schürer M, Tillner F, Beyreuther E, Suckert T and Müller JR (2022) Combined proton radiography and irradiation for high-precision preclinical studies in small animals. *Front. Oncol.* 12:982417. doi: 10.3389/fonc.2022.982417

Combined proton radiography and irradiation for high-precision preclinical studies in small animals

Moritz Schneider[1,2†], Elisabeth Bodenstein[1,3†], Johanna Bock[1], Antje Dietrich[1,4], Sebastian Gantz[1,3], Lena Heuchel[5], Mechthild Krause[1,3,4,6,7], Armin Lühr[1,3,5], Cläre von Neubeck[1,4,8], Sindi Nexhipi[1,3], Michael Schürer[1,6], Falk Tillner[1,3,7], Elke Beyreuther[1,2*], Theresa Suckert[1,4‡] and Johannes Richard Müller[1,9‡]

[1]OncoRay, National Center for Radiation Research in Oncology- Faculty of Medicine and University Hospital Carl Gustav Carus- Technische Universitat Dresden-Helmholtz-Zentrum Dresden-Rossendorf, Dresden, Germany, [2]Helmholtz-Zentrum Dresden-Rossendorf, Institute of Radiation Physics, Dresden, Germany, [3]Helmholtz-Zentrum Dresden-Rossendorf, Institute of Radiooncology - OncoRay, Dresden, Germany, [4]German Cancer Consortium Deutsches Konsortium für Translationale Krebsforschung (DKTK), partner site Dresden- German Cancer Research Center DKFZ, Heidelberg, Germany, [5]Technical University (TU) Dortmund- Faculty of Physics, Medical Physics and Radiotherapy, Dortmund, Germany, [6]National Center for Tumor Diseases (NCT), Partner Site Dresden, Dresden, Germany, [7]Department of Radiotherapy and Radiation Oncology, Faculty of Medicine and University Hospital Carl Gustav Carus, Technische Universitat Dresden, Dresden, Germany, [8]Department of Particle Therapy, University Hospital Essen, University of Duisburg-Essen, Essen, Germany, [9]Deutsche Forschungsgemeinschaft Cluster of Excellence 'Physics of Life', Technische Universität Dresden, Dresden, Germany

Background and purpose: Proton therapy has become a popular treatment modality in the field of radiooncology due to higher spatial dose conformity compared to conventional radiotherapy, which holds the potential to spare normal tissue. Nevertheless, unresolved research questions, such as the much debated relative biological effectiveness (RBE) of protons, call for preclinical research, especially regarding *in vivo* studies. To mimic clinical workflows, high-precision small animal irradiation setups with image-guidance are needed.

Material and Methods: A preclinical experimental setup for small animal brain irradiation using proton radiographies was established to perform planning, repositioning, and irradiation of mice. The image quality of proton radiographies was optimized regarding the resolution, contrast-to-noise ratio (CNR), and minimal dose deposition in the animal. Subsequently, proof-of-concept histological analysis was conducted by staining for DNA double-strand breaks that were then correlated to the delivered dose.

Results: The developed setup and workflow allow precise brain irradiation with a lateral target positioning accuracy of<0.26mm for *in vivo* experiments at minimal imaging dose of<23mGy per mouse. The custom-made software for

image registration enables the fast and precise animal positioning at the beam with low observer-variability. DNA damage staining validated the successful positioning and irradiation of the mouse hippocampus.

Conclusion: Proton radiography enables fast and effective high-precision lateral alignment of proton beam and target volume in mouse irradiation experiments with limited dose exposure. In the future, this will enable irradiation of larger animal cohorts as well as fractionated proton irradiation.

KEYWORDS

proton therapy, mouse brain irradiation, proton radiography, preclinical (*in vivo*) studies, DNA damage, relative biological effectiveness (RBE)

1 Introduction

Proton therapy is an increasingly used treatment modality for cancer patients (1). However, open research questions, such as the variable relative biological effectiveness (RBE) along the proton beam or novel therapeutics, call for preclinical experiments in a clinical like setting (2–4). The irradiation of organ subvolumes and orthotopic tumors in small animals offers high translational value (2, 5) and is in many aspects similar to clinical treatment, providing the right experimental conditions. Amongst others, researchers need to consider down-scaling of the target volumes, accurate small-field dosimetry, beam energies, and how to integrate appropriate imaging modalities into their workflow (6). Suitable equipment for irradiating small animals with protons that provides high positioning accuracy and clinical relevance is not available off-the-shelf and often needs to be custom-made. In recent years, several setups have been developed for small animal proton irradiation. The implemented solutions include visual positioning with digital cameras for image guidance (7), side illumination with a thin-foil mirror (8), and alignment lasers (9, 10). More advanced, but also cost-intensive, X-ray based commercial setups can be used to acquire CT images of small animals prior to the irradiation in order to precisely position the animal in the beam (11, 12). Technologically sophisticated ion-based tomographic imaging has been proposed for both animal studies and patient treatment (13–15). This imaging technique offers the advantage of using the same coordinate reference for imaging and irradiation as well as a precise stopping power estimation. 2D proton radiography is a basic form of ion radiography that uses a flat panel detector. This approach provides on-beam imaging, while being easy and cost-effective to implement. So far, it has been shown to be an effective means for setup verification (16); however, image quality has been deemed insufficient for small animal positioning (17).

In this manuscript, we describe a workflow for the image-guided proton irradiation of small animals using proton radiography to image live mice during treatment positioning. The irradiation process incorporates the basic procedures of clinical therapy, i.e., planning, positioning, and irradiation of defined target volumes. High image resolution at low imaging dose is achieved by optimizing setup and imaging parameters. As proof-of-concept we overlaid a Monte Carlo simulation of the applied dose and the immunohistochemically quantified occurrence of DNA double-strand breaks. We use this method to demonstrate the induction of biological damage at the designated target region in the brain.

2 Material and methods

2.1 Irradiation setup

Mouse irradiation was performed at the horizontal fixed beamline in the experimental hall of the Universitats Protonen Therapie Dresden (UPTD). The irradiation setup, its basic components, inline treatment planning, and positioning verification workflow have been described previously (16–18). The partly remodelled setup used for this manuscript consists of beam-shaping elements, an animal positioning stage, and a flat panel detector (see Figure 1). The scatterers are mounted on motorized stages for quick position adjustment. The detector is fixed on an optical table, can be moved manually and shielded from radiation when necessary. The setup allows for two principal modes of operation, i.e. “Imaging” and “Irradiation”.

The elemental compositions and dimensions of the beam-shaping elements, i.e., the scatterers and the collimators, have been previously described by Helmbrecht et al. (18). For mouse brain irradiation, an aluminium collimator (12mm thickness) with a circular aperture of either 3*mm* or 4*mm* diameter was

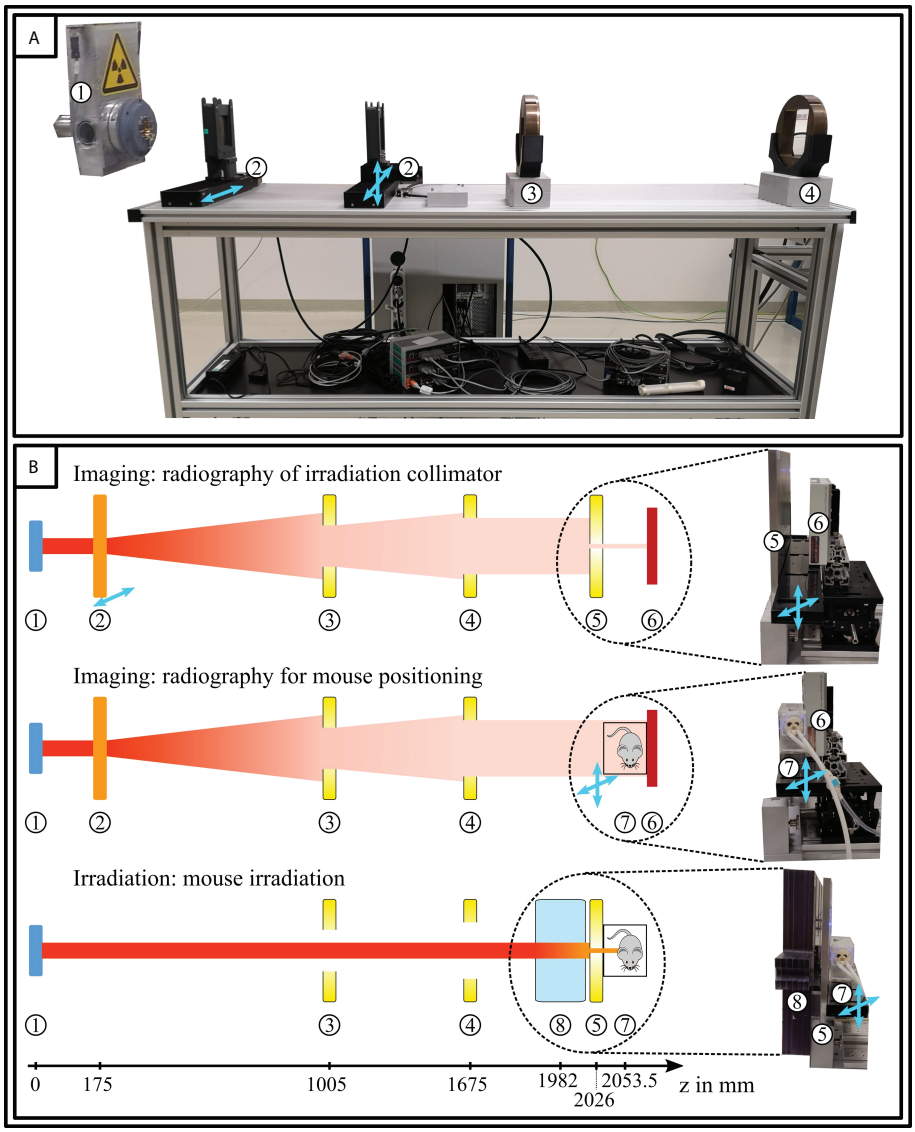

FIGURE 1
Irradiation setup for mouse irradiation. **(A)** Beamline of the irradiation setup with **(B)** schematic overview of possible modes of operation. The components are (1) the proton beam nozzle, (2) scatterers, (3) first (7.75×7.70 cm^2) and (4) second collimator (11.50×11.55 cm^2), (5) irradiation collimator (Ø × 3.0 or 4.0 mm), (6) flatpanel detector, 7) animal stage with mouse in transport box, and (8) PC range shifter. The animal bedding unit and the beam scatterers are mounted on motorized stages for quick position adjustment and switching between modes of operation ("Imaging" and "Irradiation"), respectively. Only the first scatterer is needed for radiography.

added adjacent to the mouse bedding unit. To ensure the correct location of the Bragg peak within the mouse brain, polycarbonate (PC) pc plates (thickness: 46.51mm, water equivalent thickness: 53.16mm for 90MeV) acting as a range shifter were placed in front of the irradiation collimator. The appropriate thicknesses for the shifter have been determined as previously described (16) by characterizing the beam with a Giraffe multilayer ionization chamber (IBA Dosimetry, Schwarzenbruck, Germany) and EBT3 dosimetry films (Ashland Inc., Wilmington, Delaware, USA). For C57BL/6 mice, an additional 1.38mm pc slab was added in the beam path onto the transport box due to their smaller body size.

The two scatterers and the animal bedding unit are mounted on precision (<25µm) linear stages (LTM80F-300-HSM, LTM80F-100-HSM, LTM80P-75-HSM, OWIS GmbH, Staufen im Breisgau, Germany) for quick lateral displacement. The position of all axes can be changed remotely by the in-house developed interfaces *ScattERR* (https://github.com/

schneidorlein/ScattERR) and *RadiAiDD* (https://github.com/jo-mueller/RadiAiDD, Version 0.1.0). The mouse was placed within a multi-modality bedding platform; the components and features as previously described by Müller et al. (19).

2.2 Proton radiography image acquisition

For on-beam radiographic imaging of mice, we deployed a C9320DK-02 CMOS flat panel detector (Hamamatsu Photonics K.K., Hamamatsu City, Japan) that features 10321012 pixels with a pitch of 0.05 mm to acquire images with a size of 52.8x52.8 mm^2 and a frame rate of 8.4 Hz. The software for detector read-out was custom written in-house using the National Instruments Software Interface NI-IMAQ (version 3.7, National Instruments Corporation, Austin, USA).

To assess the image quality as a function of the beam parameters (i.e., beam energy and fluence), a MicroCT hole grid phantom (QRM GmbH, Mohrendorf, Germany, see Figure 3C) and a rectangular polymethylmethacrylat (PMMA) phantom (see Figure S1) were placed at irradiation position. Radiographic images were then acquired at proton energies of 150 MeV and 200 MeV to calculate the signal-to-noise ratio (SNR) and contrast-to-noise ratio (CNR) as follows:

$$snr = \frac{S}{\sigma}, \qquad cnr = \frac{S_a - S_b}{\sigma}, \tag{1}$$

where S and σ refer to the mean signal value and the respective standard deviation. a and b denote the respective values from adjacent regions of high and low contrast.

The lead grid phantom L659036 (PTW Freiburg, Freiburg, Germany) features line pairs with a resolution of 0.6 mm^{-1} to 6.0 mm^{-1}. Radiographic images were acquired to resolve the optimal distances between first scatterer, radiography object, and detector. The grid phantom was imaged at increasing distances (23 mm-100 mm) from the detector using a 200 MeV proton beam at 0.1 nA resulting in a dose of 19.8 mGy for an irradiation time of 10 s.

Moreover, the CT phantom was used to measure the visual resolution as a function of the applied dose. Here, the CT phantom was placed at a detector-object distance of 20mm, which corresponds to the animal's position during irradiation. Dose deposition by radiographic imaging was determined with a PinPoint 3D ionization chamber (Type 31014, PTW Freiburg, Freiburg, Germany) at mouse position according to beam quality correction factor given in TRS-398 (20).

2.3 Animals

All animal experiments were approved by the local authorities (Landesdirektion Sachsen, DD24.1-5131/394/50 and DD24.1-5131/449/32) and conducted according to national (TierSchG) and European (EU Directive 2010/63/EU) animal welfare guidelines. Female C57BL/6JRj and C3H/NeNRj mice were supplied by Janvier Labs (Saint Berthevin Cedex, France) at least one week prior to the start of the experiments. The age at brain irradiation was 8-14 weeks. Animals were kept at a 12/12 h light/dark cycle in Euro Standard Type III cages with food and water *ad libitum*. Nesting material and igloos were provided as cage enrichment.

2.4 Irradiation workflow

The workflow for small animal irradiation consists of the consecutive steps of planning, positioning, and irradiation.

2.4.1 Planning

A cone beam computed tomography (CBCT) scan of each animal within the bedding unit was acquired one week before irradiation for determination of target position and later dose simulation using the small animal image-guided radiation therapy system (21). Imaging took place under isofluorane anesthesia (1.5-2% vol in O_2) with the mouse in the multi-modality bedding unit (19). Subsequently, 15-25 sagittal slices from the reconstructed CBCT image data showing the central planes of the mouse skull, were averaged using a maximum intensity projection. Similarly, we created a multilabel image from the DSURQE anatomical brain atlas (22–26) (https://wiki.mouseimaging.ca/119 display/MICePub/Mouse+Brain+Atlases) and generated a sagittal maximum projection. The resulting two-dimensional label image features three labels, namely hippocampal region, rest of the brain, and background. The Big Warp (27) plug-in of Fiji (ImageJ Version 1.53d or higher, 64-bit Windows) (28) was used to register the two projected images, with the CBCT- derived image serving as fixed image. The resulting transformed image was then used as treatment plan image A. Figure 2 gives an overview of the treatment planning pipeline and shows exemplary registered image data.

Inter- and intra-observer variation within this procedure were analyzed by a planning study on a subset of 10 animals. The animals were chosen so that both strains, different beam times, and different "difficulty levels" (i.e. how well the mouse was (re) positioned inside the bedding unit) were included. Three observers (MoS, TS, JM) of varying experience performed the planning procedure for each of the animals. In addition, each animal was planned three times by one observer on three separate days. Inter- and intra-observer agreement were quantified by calculating the Jaccard coefficients J_i for each observer for the target region of interest, i.e., the projected hippocampal region. The majority-voted plan **F** for a particular animal served as the reference planning image:

$$J_i = \frac{|A_i \cap F|}{|A_i \cup F|}, \qquad F = majority(A_1, A_2, A_3), \tag{2}$$

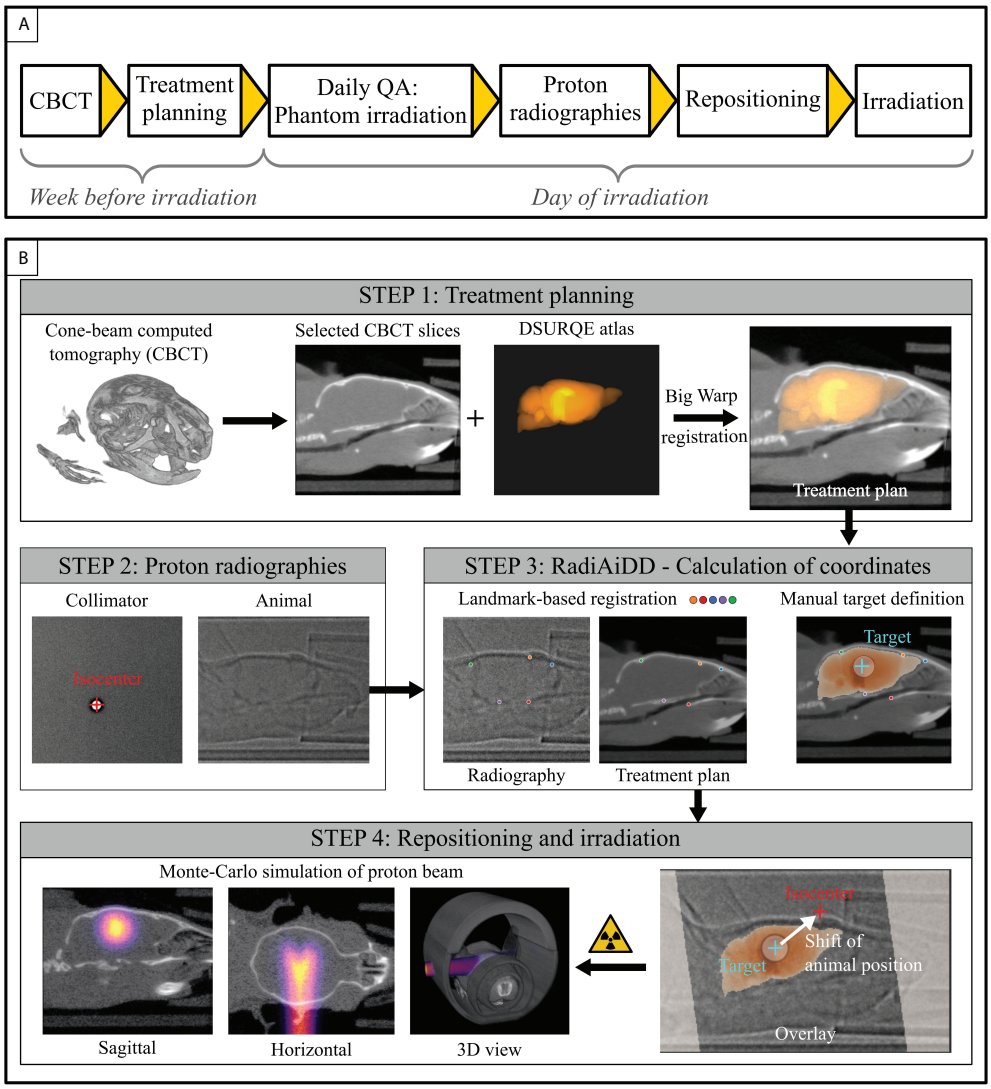

FIGURE 2
Workflow for proton brain irradiation. **(A)** Schematic diagram of the consecutive steps. **(B)** Individual steps for planning and repositioning. A CBCT serves as basis for treatment planning to the DSURQE brain atlas in the week prior to irradiation. Directly before irradiation, proton radiographies of collimator and animal are acquired to derive the beam isocenter and the animal repositioning parameters, respectively. Registration of the on-beam image with the treatment plan is performed based on five manually placed landmarks. The target coordinates are defined by positioning the collimator location onto the target area (i.e., the hippocampus). Then, the table coordinates for correct proton irradiation of the target area are calculated and the animal is shifted to this position. Post irradiation, Monte Carlo simulations compute the dose distribution within the brain based on the CBCT.

2.4.2 Positioning

Before positioning the animal at the beam site, a proton radiograph of the irradiation collimator (see Figure 1) was acquired to determine the treatment beam position. Then, the irradiation collimator was removed and the animal (within the bedding unit and transport box) was placed on the positioning stage for radiographic imaging. Subsequently, the *RadiAiDD* software was used to calculate the correct stage position for brain irradiation. For this purpose, the treatment plan image A was aligned with the acquired proton radiography of the mouse using a landmark-based similarity transformation (isocentric scaling, rotation and translation). The correct stage position for irradiation can then be calculated from the isocenter position obtained from the radiographic image of the irradiation collimator and the obtained transformation parameters.

Similar to the planning process, positioning involves manual steps that introduce inter- and intra-observer variations. To elucidate these variations, a registration study on the same subset of animals was conducted as described above. We then evaluated the variations in each of the manually set parameters, the calculated transformation parameters and the resulting motor stage coordinates.

2.4.3 Irradiation

After moving the animal to the determined treatment position, irradiation was performed according to (16) with 90MeV protons. For this, the animals were anesthetized with Ketamine/Xylazine (i.p.; 100ml/10ml per kg body weight) and positioned into the multi-modality bedding unit and the transport box (19). Eyes were protected from drying out with Bepanthen eye ointment (Bayer Vital GmbH, Leverkusen, Germany). Anesthetized animals were ventilated with surgical air and heated during the entire transportation and irradiation procedure. The C3H/HeN mice used for histology in this paper were irradiated using a collimator of 3mm diameter at a dose rate of 3.3Gy with a single fraction of 8Gy. Animals were sacrificed by cervical dislocation 30min post irradiation.

2.4.4 Daily QA

The positioning workflow was tested daily by irradiating a high-Z target (steel ball in the rectangular phantom, see Figure S1). We furthermore inserted EBT3 dosimetry films (Ashland Inc., Wilmington, Delaware, USA) into the phantom behind the steel ball. Correct planning and irradiation resulted in a black collimator-sized spot with the shadow of the steel ball visible as unirradiated area in the spot's center (see Figure S1).

2.5 Monte Carlo simulation

Dose and (LET) simulations were performed using the (TOPAS) (29) software (version 3.6.p1) with default physics settings optimized for proton therapy (30). A previously validated dedicated beam model of the setup (16) was used to calculate dose and let distributions in the mouse CBCT image. Following the technique developed by Schneider et al. (31), the converter integrated in TOPAS was used to convert the CBCT data to stopping power ratio data. The positioning of the CBCT in TOPAS was based on the target coordinates determined by *RadiAiDD*.

2.6 Immunohistochemistry

Excised brains were fixed in 4% formalin for approximately 24h at room temperature and processed for paraffin-embedding in a semi-enclosed Benchtop Tissue Processor (Leica Biosystems, Wetzlar, Germany). Tissue sections of 3µm thickness were cut throughout the whole brain in either the sagittal or the horizontal direction with a distance of 100 µm (equates to approximately 150µm in fresh tissue) and mounted onto Starfrost Advanced Adhesive microscope slides (Engelbrecht GmbH, Edermünde, Germany, 11270). For immunohistochemistry, sections were dewaxed in xylene and rehydrated in a decreasing ethanol series and pbs. Heat-induced antigen retrieval was performed by boiling in citrate buffer (pH 6) for 20min. Sections within the buffer were allowed to cool on ice for at least 15min and then washed in pbs. Subsequently, 1x Rotiblock (Carl Roth, Karlsruhe, Germany, A151) supplemented with 0.1% Triton X-100 (SERVA Electrophoresis GmbH, Heidelberg, Germany, 37240) was applied for1h. Antibody incubation was conducted in 1x Rotiblock at room temperature for 1h each; using rabbit anti-γH2AX antibody (Bethyl Laboratories, Montgomery, USA, IHC-00059, dilution 1:500) as primary and anti-rabbit AlexaFluor488 (Thermo Fisher Scientific, A11034, dilution 1:500) as secondary antibody. Sections were rinsed with pbs in between all staining steps. Counter-staining in 4',6-diamidino-2-phenylindole (DAPI) was applied for 10 min before coverslipping with fluorescence mounting medium (Agilent Technologies, Santa Clara, USA, S302380).

2.7 Microscopy image acquisition and analysis

Image acquisition was performed with a 20x objective (Plan-Apochromat 20x/0.8 M27, Carl Zeiss AG, Oberkochen, Germany) at the Axio Scan.Z1 digital slide scanner (Carl Zeiss AG, Oberkochen, Germany) by the Light Microscopy Facility of the Center for Molecular and Cellular Bioengineering (CMCB). The used software was Zeiss ZEN 3.1 (blue). Excitation/emission wavelengths were 353nm/465nm and 493nm/517nm for DAPI and AlexaFluor488, respectively. Images were stored with 16-bit depth and a pixel size of 0.325µm x 0.325µm using an ORCA-Flash 4.0 V3 Digital CMOS camera (Hamamatsu Photonics K.K., Hamamatsu City, Japan). For microscopy image representation, the data was post-processed (i.e., brightness-contrast adjustment and background removal) using Zeiss ZEN 2.3 lite and Fiji ImageJ (version v1.52n). Images were analyzed with the pipeline described in (16). In brief, the spatial relative DNA damage distribution was calculated (https://github.com/Theresa-S/Cell-ratio-detection) using optimized prominence values for the Maxima Finder (DAPI: 600; γH2AX: 1400; see Figure S2) and a tile size of 256 x 256 pixels. The relative DNA damage maps were subsequently registered to the CBCT of the respective animal using the Slice2Volume workflow (https://github.com/jo-mueller/Slice2Volume). This enables the overlay of the induced relative DNA damage to the applied dose for a pixel-wise correlation.

3 Results

3.1 Optimized setup and imaging workflow

3.1.1 Setup adaptation

Figure 3A shows the border between the CT phantom and air at 150MeV and 200MeV. The scattering in the phantom causes an

inhomogeneous proton fluence at the phantom's edge with a loss of fluence in regions of dense materials (PMMA) and an increase of fluence in the surrounding regions. The comparison of both energies reveals that the peak-to-valley edge width increases at lower energy (peak difference ΔFWHM = 0.08mm between the two energies), which is detrimental to the resolution and visibility of more detailed structures.

The resolution increases for smaller distances between object and detector (see Figure 3B). The smallest possible distance between object and detector that satisfied the spatial constraints given by the experimental setup (mainly the transport box) was 23mm. To minimize scattering, the thickness of the transport box wall adjacent to the radiography detector was reduced to 1mm.

The investigation of SNR and CNR shows that both depend on dose and proton energy for acquisition times up to 19s. SNR and CNR at 200MeV are larger than at 150MeV (see Figure S3). The detectability of details in the hole grid phantom (see Figure 3C) increases with increasing number of frames (and, hence, acquisition time) and dose (see Figure 3D), due to the decreasing noise and thereby increasing SNR and CNR. The smallest apertures of 0.3mm diameter are clearly recognisable and distinguishable from the noise after approximately 30 frames, 3.6s, and 10.2mGy. Since image quality correlates with the applied dose (see Figure 3D), a proton energy of 200MeV, beam current of 0.1nA, and acquisition time of 8s were chosen for animal radiography to limit the radiation exposure to approximately 23mGy while accomplishing a high quality radiography.

3.1.2 Imaging workflow

After adjusting the physical parameters for animal proton radiography, the imaging process was optimized. Obtaining a homogeneous background intensity in the acquired images required to subtract both the off- and on-beam image background. To correct for the detector-induced background signal (I_{dark}), 300 frames were recorded and averaged prior to proton imaging. Next, the beam fluence-induced image background I_{beam} was determined by averaging another set of 300 frames at (200MeV, 0.1nA, 30s). Both background images I_{dark} and I_{beam} are automatically subtracted from all subsequently acquired frames. The obtained background-corrected frames can then be combined by calculating the median pixel values acrossall frames for robustness against salt-and-pepper noise.

3.1.3 Planning study and beam target variability

The Jaccard coefficient for the inter- and intra-observer variability in the planning process was 0.84±0.10 and 0.92±0.05, respectively. To visualize the extent of the occurring deviations, the projected plan datasets resulting in the lowest and highest Jaccard coefficients are shown in Figure 4A, B. The animal-wise Jaccard coefficients for inter- and intra-observer variations are shown in the Supplementary Materials (Figure S4).

We furthermore determined the inter- and intra-observer variations of the target coordinates, which were calculated during the repositioning process. The inter- and intra-observer variabilities were 0.26±0.10mm and 0.22±0.10mm, respectively. The resulting irradiation target coordinates obtained by all observers overlaid with the respective radiographic images are shown in Figure 4C, D) for the same selected mice. The animal-wise inter- and intra-observer variations for the calculated target coordinates as well as all derived transformation parameters are depicted in the supplementary materials (Figure S5-S11).

3.2 Biological verification

The correct beam application was verified biologically in two irradiated brains. Sagittal (see Figure 5A) and horizontal (see Figure 5B) slices of mouse brains visualize the position of the proton beam in x, y (anterior-posterior, dorsal-ventral) and x, z (anterior-posterior, depth) directions, respectively. The distribution of radiation-induced DNA damage (see Figure 5) proves that the animals were hit in the hippocampal target location and that the beam stops within the brain.

We then evaluated the relation between applied dose and biological effect. Figure 6 shows the resulting overlays of relative biological damage and simulated dose for two representative sections in the sagittal and coronal plane, where the cell distribution enabled direct analysis. Image analysis of DNA damage using the described analysis workflow clearly visualizes the beam path in the tissue. The underlying cellular composition of the brain tissue introduces variation in the biological read-out, which impacts the results to varying degrees depending on the analyzed brain section (data not shown). The profile lines, however, indicate a good correlation between deposited physical dose and induced biological damage.

4 Discussion

Research questions in proton radiooncology aim to address important aspects of clinical outcome and require preclinical *in vivo* data. These questions include the RBE of protons (32), proton-specific normal tissue damage, and novel combination treatments (33). One challenge for such experiments is the precise irradiation of small animal models, which is required for meaningful translation into clinical trials due to the necessary down-scaling of spatial dimensions. The goal of the presented study was to develop an improved positioning workflow by including on-beam proton radiography of living mice into the existing pipeline (16, 17). The achieved increase in reproducibility and precision, as well as the streamlined

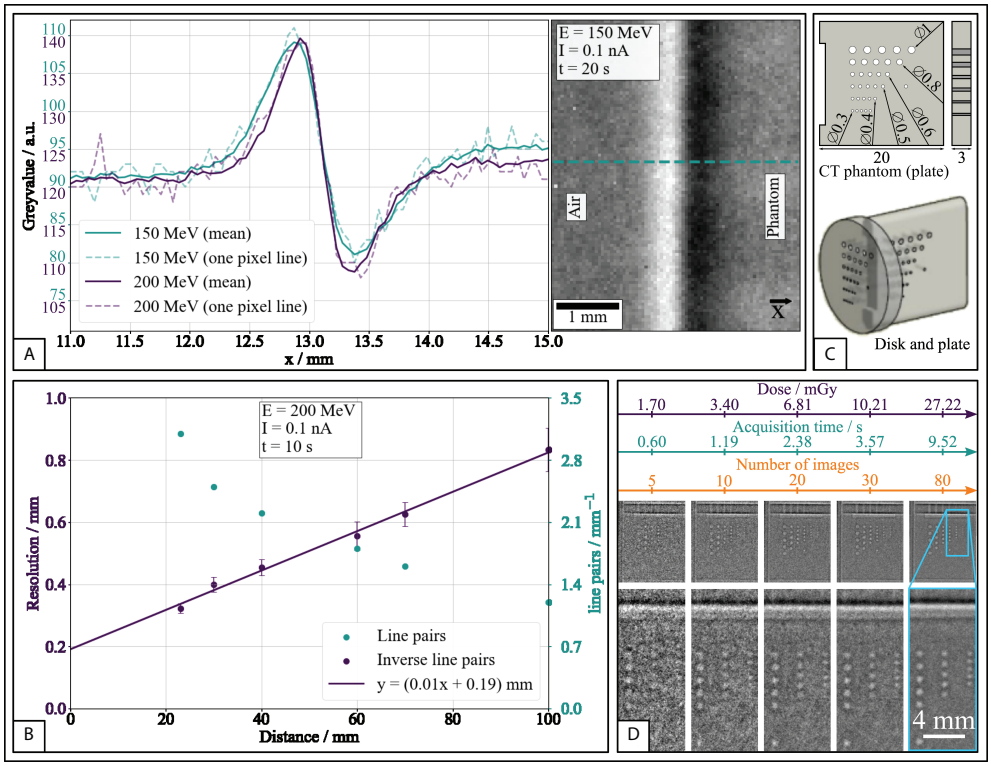

FIGURE 3
Results of proton radiography resolution experiments. **(A)** Proton fluence at the edge between air and phantom (PMMA) for two beam energies either along one pixel line (dashed) or as mean over 100 pixel lines (solid). **(B)** Image resolution and line pairs determined from the lead grid phantom as a function of distance between phantom and flat panel detector. **(C)** Schematics of the used MicroCT hole grid phantom. The hole pattern in the disk is analogous to the plate. All units are given in mm. **(D)** Image resolution determined from the hole phantom as a function of applied dose, acquisition time, and number of acquired frames.

irradiation workflow will enable further preclinical studies requiring high precision proton irradiation of small animals.

The presented irradiation setup puts high value on cost-effectiveness, relative technical simplicity, and open code distribution to facilitate reproduction and adaptation. The used components are readily-available to allow implementation with little technical preconditions at other experimental centers with quasi mono-energetic proton beams. In addition, the redesigned radiation setup provides novel opportunities to external users of our facility, e.g. through European transnational access of the INSPIRE network (34). The applied software for planning (Big Warp, Fiji (27, 28)), registration (*RadiAiDD*), and component interaction (*ScattERR*) are open source. The operation modes of the setup ("Imaging" and "Irradiation") allow for image acquisition of setup and animals, repositioning, and irradiation. The usage of motorized elements enables remote control of the used components and thereby ensures radiation protection of the personnel. Quality assurance of the workflow, similar to the clinics (35, 36), is performed daily with phantom irradiation.

Benchmark experiments were performed to determine the optimal radiography acquisition parameters for beam energy, dose, and object-detector distance. As a result of these experiments, we provide setup parameters that allow for sufficiently high-resolution radiographic imaging with a commercial flat panel detector, while exposing the targets to reasonable (low-LET) proton radiation doses of approximately 23mGy. If necessary, this dose can be further reduced by shielding of the animal body outside the field-of-interest. The chosen beam energy of 200MeV can be delivered by common clinical and experimental cyclotrons. The achieved spatial resolution of 0.3mm allows to resolve relevant anatomical landmarks. In comparison to other reported ion-based radio- or tomographic techniques (14, 37–39), our method yields competitive resolution. The implemented method benefits considerably from placing the detector close to the object and

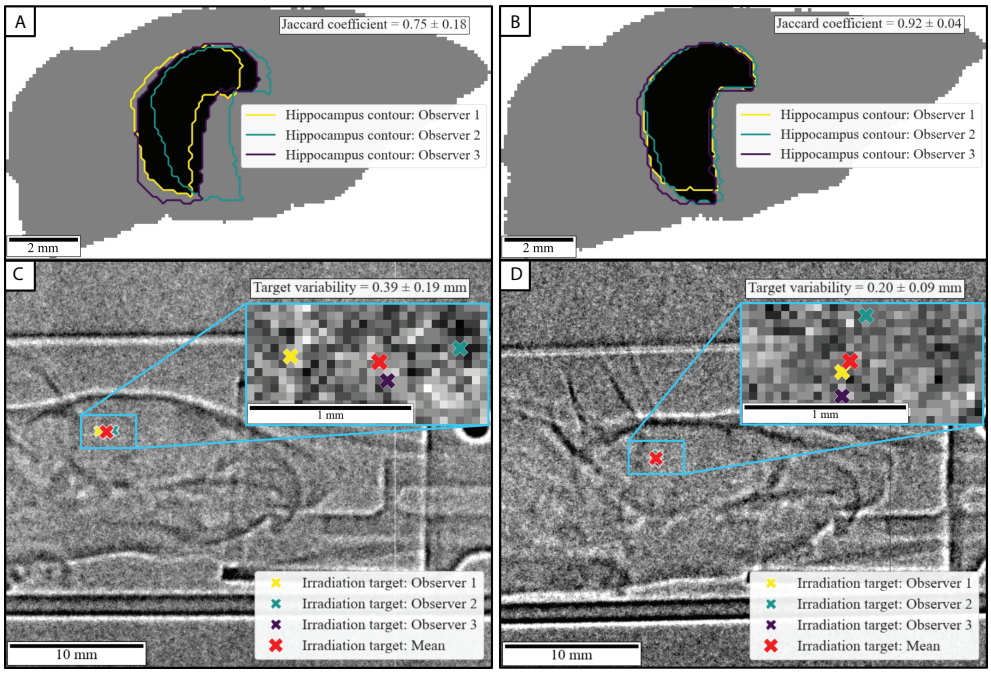

FIGURE 4
Representative variability in planning and registration. The upper row shows inter-observer variations and Jaccard coefficients of the projected target region for the animals with **(A)** the lowest and **(B)** the highest inter-observer agreement. In the lower row, **(C)** and **(D)** show the resulting variation of the registration-derived target coordinate for the animals in **(A)** and **(B)**, respectively.

exploiting changes in proton fluence rather than particle stopping, which is consistent with the theoretical description (40) as well as previously reported experiments regarding object-detector distance (17). Due to the requirements regarding object-detector distance and object thickness, the used radiographic method may not be viable for clinical use. Preclinical experiments, however, provide suitable physical and spatial conditions to exploit the used mode of proton radiographic images for high-precision positioning and irradiation. The choice of beam energy and acquisition time had to be weighted against the applied dose. Using the plateau-region of the beam in a shoot-through fashion allows to achieve the above-reported resolution at a dose of approximately 23mGy. This represents an improvement over other reported implementations (e.g., Darne et al. (38): 47.2 mGy, Harms et al. (41): 50mGy). Technically highly sophisticated techniques yield low per-image doses at high beam energies (Durante et al. (13), 10mGy, 800MeV), but do not provide the cost-effectiveness or availability, which are key features of the presented method.

The planning study shows inter- and intra-observer variations in the registration of brain atlas and CBCT, which impact the resulting overall targeting accuracy. In general, the inter-observer variability was lower than the intra-observer variability (mean Jaccard indices: 0.84±0.10 vs. 0.92±0.05), which highlights the highly subjective perception of sufficiently good agreement when performing registration tasks. Since the true registration is not known in such scenarios, this is an inherent problem of both manual and automated registration (42) and subsequently applies to the performed planning experiment. The inter- and intra-observer Jaccard coefficients obtained in this study are comparable to similar clinical investigations. Wohlfahrt et al. (43) found a Jaccard coefficient of 0.80±0.05 for an experienced radiooncologist contouring the tumor gross volume of lung cancer on two different days. For 3D-CT contouring of pancreatic ductal adenocarcinoma, Choi et al. (44) noted inter-observer Jaccard coefficients of 0.521-0.783 for three medical specialists. Alasti et al. (45) reported Jaccard coefficients of 0.665-0.811 between different observers and 0.851-0.917 for repeated delineations by the same observer for CT contouring of prostate tumors. To address the variations in the present planning study, it is notable that the disagreement between observers occurs predominantly in the basal part of the hippocampus. In our case, the defined target region was located in the upper part of the hippocampus. Thus, the practically achieved planning precision may be higher as suggested by the calculated Jaccard coefficients. The registration and, consequently, the positioning procedure yielded good agreement between observers. The determined variations in the calculated beam target coordinates are consistently in the sub-millimeter domain (<0.41±0.19mm; mean inter- and intra-

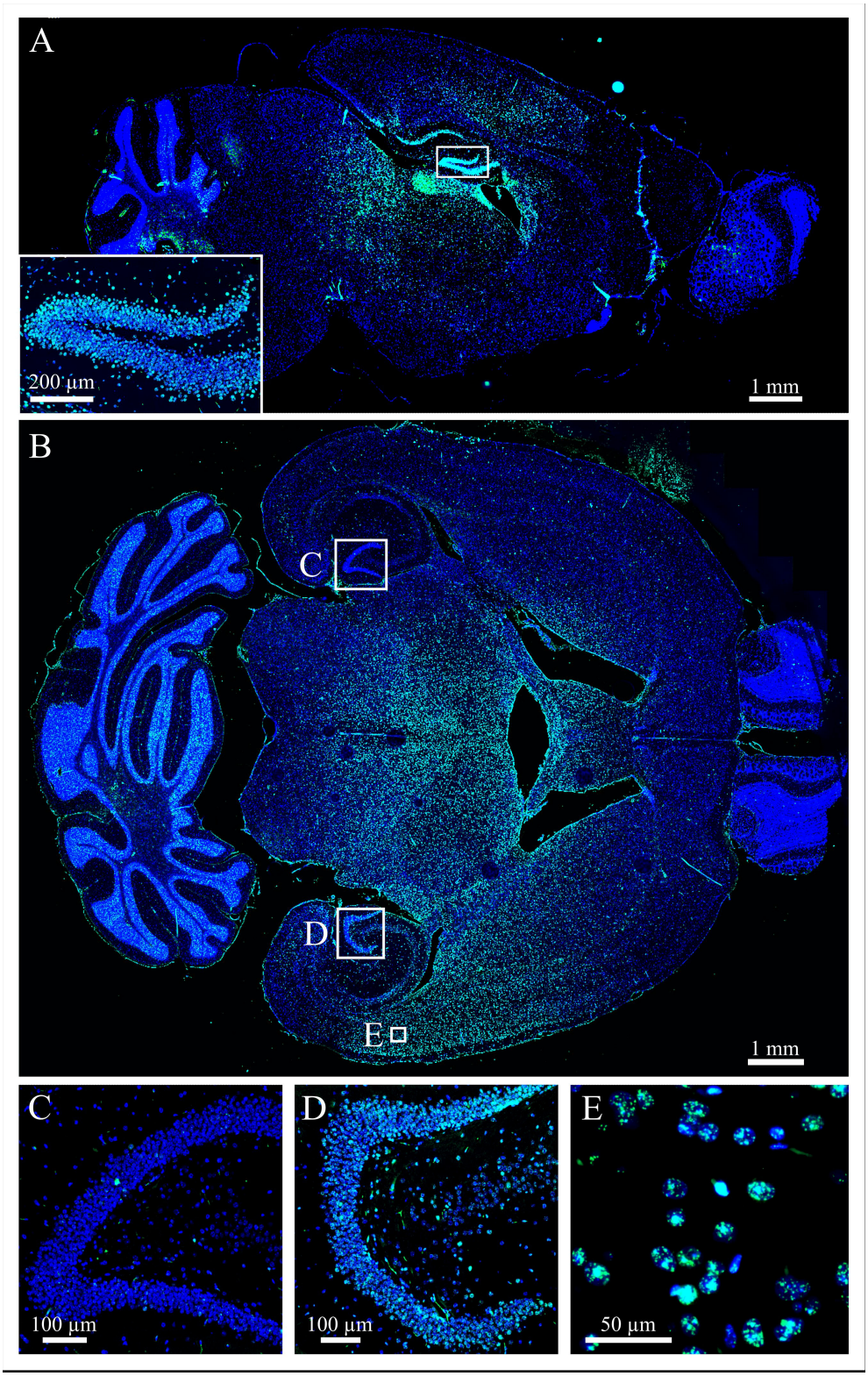

FIGURE 5
Biological verification of the irradiation workflow. DNA damage in the brain cells (DAPI, blue) was stained *via* γH2AX (green) 30 min after 8 Gy irradiation. **(A)** The sagittal section shows that the beam was correctly applied to the target location, the hippocampal area. **(B)** The horizontal section additionally reveals that the proton beam stops in the middle of the brain. The **(C)** non-irradiated hippocampus has no elevated damage, whereas the **(D)** irradiated one shows increased γH2AX expression. **(E)** Higher magnification of cells in the beam path visualize radiation-induced foci.

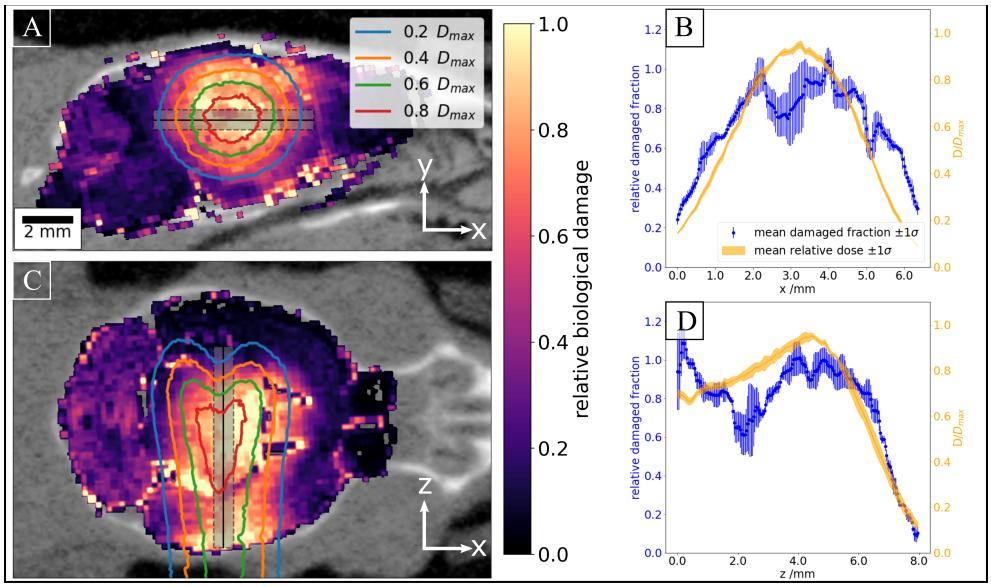

FIGURE 6
Correlation of biological damage with applied dose. **(A)** Overlay of aligned relative DNA damage and simulated dose in a representative sagittal plane. The grey box indicates the profile line along which average dose and relative biological damage have been calculated as shown in **(B)**. **(C)** and **(D)** show the respective plots for a coronal plane.

observer variations of 0.26±0.10mm and 0.22±0.10mm). While setups with on-site X-ray imaging provide slightly higher positioning accuracy [0.08mm (46) or 0.24mm (11)], such performances often come at the price of significant technical expense. It should be noted that the registration and positioning procedure encompasses the manual, interactive placement of the desired beam target location (with respect to the desired projected target region, i.e., the hippocampal region). Thus, the ensuing variability of the calculated target position is composed of variation of the derived transformation parameters as well as the chosen beam target. The implemented workflow allows for further simplifications that address this shortcoming to a certain degree. For instance, the target could be set automatically based on objective criteria such as the center of gravity of the hippocampal area. To further minimize intra- and inter-observer variability, observer training sessions prior to experimental campaigns are advisable (47).

It is worth mentioning, that – while allowing for high lateral precision in irradiation – the implemented radiographic method does not yield additional information for choosing the beam range. This is of particular importance for not well-localized targets such as orthotopic tumors in the brain, which can show considerable variation in their location and thus require an individualized irradiation field. While the measurement of water-equivalent thickness by means of proton radiography has been described previously (17), it is desirable to include tomographic information for the determination of the appropriate beam range. The irradiation of specific normal tissue regions in the brain as demonstrated in this manuscript, however, provides the necessary conditions for using a generalized beam range, which is highlighted by the overlay of simulated dose and DNA damage.

The DNA damage analysis was performed to verify our workflow using a pre-defined beam-range. Histology proved that the DNA damage induction was located in the delineated target region. After subsequent image analysis, a clear accordance was shown between the proton beam and radiation-induced DNA damage. Thus, we could replicate the data from our previous study on small animal irradiation (16) while streamlining the radiation workflow considerably. It has to be noted that despite parameter optimization, the algorithm used for calculating the relative DNA damage distributions has some weaknesses. The maxima finder, which is the core method for cell counting, does not perform equally well in regions of high or low cell density, or when inhomogeneous fluorescence intensity is present. Specifically, a slight overestimation of DNA damage was noted in unirradiated or low-dose irradiated brain areas. Nevertheless, the algorithm provides fast and objective analysis of spatial tissue characteristics, which we considered sufficiently accurate for the research question at hand, i.e., visualizing the proton beam *via* the induced DNA damage in the tissue. Relating the damage to the applied dose further revealed the translational value of our model: the congruence of physical effect and biological outcome is a valuable tool in elucidating underlying radiobiological mechanisms. Future studies could, for example, include the let or beam quality (48) to investigate the relation between the

different physical parameters and the ensuing biological effects in a preclinical *in vivo* setting. One drawback of RBE studies in brain is the inherent heterogeneity of the organ. Differing cell compositions and densities, as well as the four brain ventricles complicate a clean correlation of dose and damage. Hence, irradiation of larger organs with high cellular homogeneity such as the liver could provide additional benefits for *in vivo* RBE investigations. On the other hand, moving organs are more difficult to irradiate and cannot be distinguished as clearly as the skull bones in proton radiography. Additionally, cranial tumors are often considered an indication for proton therapy; therefore, normal tissue studies on brain are highly needed. The optimal solution to handle organ heterogeneity is cell-wise dose mapping, where each cell is analyzed individually. This approach requires not only precise dosimetric measurements and dose simulations, but also high precision irradiation, which can be provided by our workflow.

In conclusion, we could show that high-precision subvolume irradiation of small animals can be achieved with image-guidance from proton radiography using a flat panel detector. The imaging dose was limited to an acceptable amount and biological validation proved successful treatment of the hippocampal target area. The robustness and cost-effectiveness of the setup and the streamlined and clinic-orientated workflow enable a wide range of preclinical proton experiments. Possible future applications include irradiation of larger animal cohorts, fractionated proton irradiation, additional normal tissue studies on other organs and sub-volumes, and the treatment of orthotopic tumors. This will facilitate animal studies in proton radiooncology and help to provide much needed *in vivo* data for a range of clinically relevant research topics.

Data availability statement

The datasets presented in this study can be found in the online repository Zenodo under the access link doi: 10.5281/zenodo.6778020.

Ethics statement

The animal study was reviewed and approved by Landesdirektion Sachsen.

Author contributions

EBo, TS, EBe, AD, AL, and JM contributed to the conception and design of the study. TS, EBe, AD, and CN were responsible for animal ethics. EBo, EBe, MK, AL, and JM offered supervision during the project. Methodology was done by MoS, EBo, TS, JB, MiS, AL, and JM. Software was provided by MoS, JB, FT, and JM. MoS, EBo, TS, EBe, JB, AD, SG, LH, SN, and JM acquired data and MoS, TS, and JM were involved in data curation. Data analysis and interpretation were performed by MoS, TS, JB, and JM. MoS, EBo, TS, JB, and JM visualized the data and MoS, TS, LH, and JM wrote the original draft of the manuscript, EBe and AL contributed major revisions. All authors read and approved the final version of the manuscript.

Funding

The experimental part of the University Proton Therapy Dresden (UPTD) facility has received funding from the European Union's Horizon 2020 research and innovation program under grant agreement No. 730983 (INSPIRE).

Acknowledgments

The authors would like to thank Dorothee Pfitzmann, Liane Stolz-Kieslich, Katja Schumann, and Daniela Pollack for their excellent technical assistance on animal experiments and histology. We would like to acknowledge the help of Anne Dreyer, Gerd Rothe and Michael Reiche from the mechanical workshop. This work was supported by the Light Microscopy Facility, a Core Facility of the cmcb Technology Platform at TU Dresden, especially by Ellen Geibelt. We further want to thank the Teams of University Proton Therapy Dresden (UPTD) and IBA for their support during the proton irradiation experiments.

Conflict of interest

In the past 5 years, MK received funding for her research projects by Merck KGaA (2014-2018 for preclinical study; 2018-2020 for clinical study) and Medipan GmbH (2014-2018). She is involved in an ongoing publicly funded (German Federal Ministry of Education and Research) project with the companies Medipan, Attomol GmbH, GA Generic Assays GmbH, Gesellschaft fur medizinische und wissenschaftliche genetische Analysen, Lipotype GmbH, and PolyAn GmbH. For the present study, MK confirms that none of the above mentioned funding sources were involved.

The remaining authors declare that the research was conducted in the absence of any commercial or financial relationships that could be construed as a potential conflict of interest.

Publisher's note

All claims expressed in this article are solely those of the authors and do not necessarily represent those of their

affiliated organizations, or those of the publisher, the editors and the reviewers. Any product that may be evaluated in this article, or claim that may be made by its manufacturer, is not guaranteed or endorsed by the publisher.

Supplementary material

The Supplementary Material for this article can be found online at: https://www.frontiersin.org/articles/10.3389/fonc.2022.982417/full#supplementary-material

References

1. Particle Therapy Co-Operative Group. (2022). Available at: https://www.ptcog.ch/ (Accessed May 02, 2022).

2. Suckert T, Nexhipi S, Dietrich A, Koch R, Kunz-Schughart L, Bahn E, et al. Models for translational proton radiobiology–from bench to bedside and back. *Cancers* (2021) 13(16):4216. doi: 10.3390/cancers13164216

3. Lühr A, von Neubeck C, Krause M, Troost E. Relative biological effectiveness in proton beam therapy – current knowledge and future challenges. *Clin Trans Radiat Oncol* (2018) 9:35–41. doi: 10.1016/j.ctro.2018.01.006

4. Coleman CN, Higgins GS, Brown JM, Baumann M, Kirsch DG, Willers H, et al. Improving the predictive value of preclinical studies in support of radiotherapy clinical trials. *Clin Cancer Res* (2016) 22(13):3138—3147. doi: 10.1158/1078-0432.ccr-16-0069

5. Voshart DC, Wiedemann J, van Luijk P, Barazzuol L. Regional responses in radiation-induced normal tissue damage. *Cancers* (2021) 13(3):367. doi: 10.3390/cancers13030367

6. Verhaegen F, Dubois L, Gianolini S, Hill MA, Karger CP, Lauber K, et al. Estro acrop: Technology for precision small animal radiotherapy research: Optimal use and challenges. *Radiother Oncol* (2018) 126(3):471–8. doi: 10.1016/j.radonc.2017.11.016

7. Patriarca A, Fouillade C, Auger M, Martin F, Pouzoulet F, Nauraye C, et al. Experimental set-up for FLASH proton irradiation of small animals using a clinical system. *Int J Radiat Oncol Biol Physics* (2018) 102(3):619–26. doi: 10.1016/j.ijrobp.2018.06.403

8. Kourkafas G, Bundesmann J, Fanselow T, Denker A, Ehrhardt VH, Gollrad J, et al. FLASH proton irradiation setup with a modulator wheel for a single mouse eye. *Med Phys* (2021) 48(4):1839–45. doi: 10.1002/mp.14730

9. Bijl H, van Luijk P, Coppes R, Schippers J, Konings A, van der Kogel A. Unexpected changes of rat cervical spinal cord tolerance caused by inhomogeneous dose distributions. *Int J Radiat Oncol Biol Phys* (2003) 57(1):274–81. doi: 10.1016/S0360-3016(03)00529-7

10. Athanasiadi I, Perez WD, Plantenga JM, Jones-Hall Y, Perez-Torres CJ. Feasibility of a mini-pig model of radiation-induced brain injury to one cerebral hemisphere. *Radiat Oncol* (2021) 16(30):1–8. doi: 10.1186/s13014-021-01753-1

11. Ford E, Emery R, Huff D, Narayanan M, Schwartz J, Cao N, et al. An image-guided precision proton radiation platform for preclinical *in vivo* research. *Phys Med Biol* (2016) 62(1):43. doi: 10.1088/1361-6560/62/1/43

12. Kim M, Irmen P, Shoniyozov K, Verginadis I, Cengel K, Koumenis C, et al. Design and commissioning of an image-guided small animal radiation platform and quality assurance protocol for integrated proton and x-ray radiobiology research. *Phys Med Biol* (2019) 64:135013. doi: 10.1088/1361-6560/ab20d9

13. Prall M, Durante M, Berger T, Przybyla B, Graeff C, Lang P, et al. High-energy proton imaging for biomedical applications. *Sci Rep* (2016) 6:27651. doi: 10.1038/srep27651

14. Volz L, Collins-Fekete CA, Piersimoni P, Johnson RP, Bashkirov V, Schulte R, et al. Stopping power accuracy and achievable spatial resolution of helium ion imaging using a prototype particle CT detector system. *Curr Dir Biomed Eng* (2017) 3(2):401–4. doi: 10.1515/cdbme-2017-0084

15. Parodi K, Assmann W, Belka C, Bortfeldt J, Clevert DA, Dedes G, et al. Towards a novel small animal proton irradiation platform: the SIRMIO project. *Acta Oncol* (2019) 58(10):1470—1475. doi: 10.1080/0284186x.2019.1630752

16. Suckert T, Müller J, Beyreuther E, Azadegan B, Brüggemann A, Bütof R, et al. High-precision image-guided proton irradiation of mouse brain sub-volumes. *Radiother Oncol* (2020) 146:205–12. doi: 10.1016/j.radonc.2020.02.023

17. Müller J, Neubert C, von Neubeck C, Baumann M, Krause M, Bütof R, et al. Proton radiography for inline treatment planning and positioning verification of small animals. *Acta Oncol* (2017) 56(11):1–7. doi: 10.1080/0284186X.2017.1352102

18. Helmbrecht S, Baumann M, Fiedler F, Krause M, Lühr A. Design and implementation of a robust and cost-effective double-scattering system at a horizontal proton beamline. *J Instrumentation* (2016) 11:T11001–1. doi: 10.1088/1748-0221/11/11/T11001

19. Müller J, Schürer M, Neubert C, Tillner F, Beyreuther E, Suckert T, et al. Multi-modality bedding platform for combined imaging and irradiation of mice. *Biomed Phys Eng Express* (2020) 6:037003. doi: 10.1088/2057-1976/ab79f1

20. Andreo P, Burns DT, Hohlfeld K, Huq MS, Kanai T, Laitano F. et al. *Absorbed dose determination in external beam radiotherapy*. Vienna: International Atomic Energy Agency (2001).

21. Tillner F, Thute P, Löck S, Dietrich A, Fursov A, Haase R, et al. Precise image-guided irradiation of small animals: A flexible non-profit platform. *Phys Med Biol* (2016) 61(8):3084. doi: 10.1088/0031-9155/61/8/3084

22. Dorr AE, Lerch JP, Spring S, Kabani N, Henkelman RM. High resolution three-dimensional brain atlas using an average magnetic resonance image of 40 adult C57Bl/6J mice. *NeuroImage* (2008) 42(1):60–9. doi: 10.1016/j.neuroimage.2008.03.037

23. Steadman PE, Ellegood J, Szulc KU, Turnbull DH, Joyner AL, Henkelman RM, et al. Genetic effects on cerebellar structure across mouse models of autism using a magnetic resonance imaging atlas. *Autism Res* (2014) 7(1):124–37. doi: 10.1002/aur.1344

24. Ullmann JF, Watson C, Janke AL, Kurniawan ND, Reutens DC. A segmentation protocol and MRI atlas of the C57BL/6J mouse neocortex. *NeuroImage* (2013) 78:196–203. doi: 10.1016/j.neuroimage.2013.04.008

25. Richards K, Watson C, Buckley RF, Kurniawan ND, Yang Z, Keller MD, et al. Segmentation of the mouse hippocampal formation in magnetic resonance images. *NeuroImage* (2011) 58(3):732–40. doi: 10.1016/j.neuroimage.2011.06.025

26. Qiu LR, Fernandes DJ, Szulc-Lerch KU, Dazai J, Nieman BJ, Turnbull DH, et al. Mouse MRI shows brain areas relatively larger in males emerge before those larger in females. *Nat Commun* (2018) 9:1–15. doi: 10.1038/s41467-018-04921-2

27. Bogovic JA, Hanslovsky P, Wong A, Saalfeld S. Robust registration of calcium images by learned contrast synthesis. *IEEE 13th International Symposium on Biomedical Imaging* (2016) 1123–6. doi: 10.1109/ISBI.2016.7493463

28. Schindelin J, Arganda-Carreras I, Frise E, Kaynig V, Longair M, Pietzsch T, et al. Fiji: an open-source platform for biological-image analysis. *Nat Methods* (2012) 9:676–82. doi: 10.1038/nmeth.2019

29. Perl J, Shin J, Schuemann J, Faddegon B, Paganetti H. TOPAS: An innovative proton Monte Carlo platform for research and clinical applications. *Med Phys* (2012) 39(11):6818–37. doi: 10.1118/1.4758060

30. Zacharatou Jarlskog C, Paganetti H. Physics settings for using the Geant4 toolkit in proton therapy. *IEEE Trans Nucl Sci* (2008) 55(3):1018–25. doi: 10.1109/TNS.2008.922816

31. Schneider U, Pedroni E, Lomax A. The calibration of CT hounsfield units for radiotherapy treatment planning. *Phys Med Biol* (1996) 41(1):111–24. doi: 10.1088/0031-9155/41/1/009

32. Sørensen BS. Commentary: RBE in proton therapy–where is the experimental *in vivo* data? *Acta Oncol* (2019) 58(10):1337–9. doi: 10.1080/0284186X.2019.1669819

33. Lühr A, von Neubeck C, Pawelke J, Seidlitz A, Peitzsch C, Bentzen SM, et al. "Radiobiology of proton therapy": Results of an international expert workshop. *Radiother Oncol* (2018) 128(1):56–67. doi: 10.1016/j.radonc.2018.05.018

34. Henthorn NT, Sokol O, Durante M, De Marzi L, Pouzoulet F, Miszczyk J, et al. Mapping the future of particle radiobiology in europe: The inspire project. *Front Phys* (2020) 8. doi: 10.3389/fphy.2020.565055

35. Branco D, Taylor P, Zhang X, Li H, Guindani M, Followill D. An anthropomorphic head and neck quality assurance phantom for credentialing of intensity-modulated proton therapy. *Int J Particle Ther* (2018) 4(3):40–7. doi: 10.14338/ijpt-17-00005.1

36. Arjomandy B, Sahoo N, Zhu XR, Zullo JR, Wu RY, Zhu M, et al. An overview of the comprehensive proton therapy machine quality assurance procedures implemented at the university of Texas m. d. Anderson cancer center proton therapy center-Houston. *Med Phys* (2009) 36(6):2269–82. doi: 10.1118/1.3120288

37. Collins-Fekete CA, Brousmiche S, Portillo SK, Beaulieu L, Seco J. A maximum likelihood method for high resolution proton radiography/proton CT. *Phys Med Biol* (2016) 61:8232. doi: 10.1088/0031-9155/61/23/8232

38. Darne CD, Alsanea F, Robertson DG, Guan F, Pan T, Grosshans D, et al. A proton imaging system using a volumetric liquid scintillator: a preliminary study. *Phys Med Biol* (2019) 5(4):045032. doi: 10.1088/2057-1976/ab2e4a

39. Tanaka S, Nishio T, Matsushita K, Tsuneda M, Kabuki S, Uesaka M. Development of proton CT imaging system using plastic scintillator and CCD camera. *Phys Med Biol* (2016) 61:4156–67. doi: 10.1088/0031-9155/61/11/4156

40. Highland VL. Some practical remarks on multiple scattering. *Nucl Instruments Methods* (1975) 129(2):497–9. doi: 10.1016/0029-554X(75)90743-0

41. Harms J, Maloney L, Sohn JJ, Erickson A, Lin Y, Zhang R. Flat-panel imager energy-dependent proton radiography for a proton pencil-beam scanning system. *Phys Med Biol* (2020) 65:145001. doi: 10.1088/1361-6560/ab9981

42. Klein S, Staring M, Murphy K, Viergever MA, Pluim JP. Elastix: a toolbox for intensity-based medical image registration. *IEEE Trans Med Imaging* (2009) 29 (1):196–205. doi: 10.1109/TMI.2009.2035616

43. Wohlfahrt P, Troost EG, Hofmann C, Richter C, Jakobi A. Clinical feasibility of single-source dual-spiral 4D dual-energy CT for proton treatment planning within the thoracic region. *Int J Radiat Oncol Biol Phys* (2018) 102 (4):830–40. doi: 10.1016/j.ijrobp.2018.06.044

44. Choi W, Xue M, Lane BF, Kang MK, Patel K, Regine WF, et al. Individually optimized contrast-enhanced 4D-CT for radiotherapy simulation in pancreatic ductal adenocarcinoma. *Med Phys* (2016) 43(10):5659–66. doi: 10.1118/1.4963213

45. Alasti H, Cho YB, Catton C, Berlin A, Chung P, Bayley A, et al. Evaluation of high dose volumetric CT to reduce inter-observer delineation variability and PTV margins for prostate cancer radiotherapy. *Radiother Oncol* (2017) 125(1):118–23. doi: 10.1016/j.radonc.2017.08.012

46. van Luijk P, Bijl HP, Coppes RP, van der Kogel AJ, Konings AW, Pikkemaat J, et al. Techniques for precision irradiation of the lateral half of the rat cervical spinal cord using 150 MeV protons. *Phys Med Biol* (2001) 46:2857. doi: 10.1088/0031-9155/46/11/307

47. Konert T, Vogel WV, Everitt S, MacManus MP, Thorwarth D, Fidarova E, et al. Multiple training interventions significantly improve reproducibility of PET/CT-based lung cancer radiotherapy target volume delineation using an IAEA study protocol. *Radiother Oncol* (2016) 121(1):39–45. doi: 10.1016/j.radonc.2016.09.002

48. Lühr A, von Neubeck C, Helmbrecht S, Baumann M, Enghardt W, Krause M. Modeling *in vivo* relative biological effectiveness in particle therapy for clinically relevant endpoints. *Acta Oncol* (2017) 56(11):1392–8. doi: 10.1080/0284186X.2017.1356468

frontiers | Frontiers in Oncology

TYPE Original Research
PUBLISHED 20 September 2022
DOI 10.3389/fonc.2022.901390

OPEN ACCESS

EDITED BY
Ryogo Minamimoto,
National Center For Global Health and Medicine, Japan

REVIEWED BY
Bogdan Malkowski,
Nicolaus Copernicus University in Toruń, Poland
Miguel Pampaloni,
University of California, San Francisco, United States

*CORRESPONDENCE
Maximilian Knoll
m.knoll@dkfz.de

SPECIALTY SECTION
This article was submitted to Cancer Imaging and Image-directed Interventions, a section of the journal Frontiers in Oncology

RECEIVED 21 March 2022
ACCEPTED 17 August 2022
PUBLISHED 20 September 2022

CITATION
Waltenberger M, Furkel J, Röhrich M, Salome P, Debus C, Tawk B, Gahlawat AW, Kudak A, Dostal M, Wirkner U, Schwager C, Herold-Mende C, Combs SE, König L, Debus J, Haberkorn U, Abdollahi A and Knoll M (2022) The impact of tumor metabolic activity assessed by ^{18}F-FET amino acid PET imaging in particle radiotherapy of high-grade glioma patients.
Front. Oncol. 12:901390.
doi: 10.3389/fonc.2022.901390

The impact of tumor metabolic activity assessed by ^{18}F-FET amino acid PET imaging in particle radiotherapy of high-grade glioma patients

Maria Waltenberger[1,2,3,4,5], Jennifer Furkel[1,2,3,4], Manuel Röhrich[6], Patrick Salome[1,2,3,4], Charlotte Debus[1,2,3,4,7], Bouchra Tawk[1,2,3,4], Aoife Ward Gahlawat[1,2,3,4], Andreas Kudak[1,3], Matthias Dostal[1,3], Ute Wirkner[1,2,3,4], Christian Schwager[1,2,3,4], Christel Herold-Mende[8], Stephanie E. Combs[5,9,10], Laila König[3,4], Jürgen Debus[1,3,4], Uwe Haberkorn[6], Amir Abdollahi[1,2,3,4] and Maximilian Knoll[1,2,3,4]*

[1]Department of Radiation Oncology, University Hospital of Heidelberg, Heidelberg, Germany, [2]Clinical Cooperation Unit Radiation Oncology, German Cancer Research Center (DKFZ), Heidelberg, Germany, [3]Heidelberg Institute for Radiation Oncology (HIRO), University Hospital of Heidelberg, Heidelberg, Germany, [4]Translational Radiation Oncology, German Cancer Consortium (DKTK), National Center for Tumor Diseases (NCT), German Cancer Research Center (DKFZ), Heidelberg, Germany, [5]Department of Radiation Oncology, Klinikum rechts der Isar, Technical University of Munich (TUM), Munich, Germany, [6]Department of Nuclear Medicine, University Hospital Heidelberg, Heidelberg, Germany, [7]Steinbuch Centre for Computing (SCC), Karlsruhe Institute of Technology (KIT), Eggenstein-Leopoldshafen, Germany, [8]Department of Experimental Neurosurgery, University Hospital Heidelberg, Heidelberg, Germany, [9]German Cancer Consortium (DKTK), Partner Site Munich, Munich, Germany, [10]Institute of Radiation Medicine (IRM), Helmholtz Zentrum Munich, Munich, Germany

Background: Selective uptake of (18)F-fluoro-ethyl-tyrosine (^{18}F-FET) is used in high-grade glioma (HGG) to assess tumor metabolic activity *via* positron emission tomography (PET). We aim to investigate its value for target volume definition, as a prognosticator, and associations with whole-blood transcriptome liquid biopsy (WBT lbx) for which we recently reported feasibility to mirror tumor characteristics and response to particle irradiation in recurrent HGG (rHGG).

Methods: ^{18}F-FET-PET data from n = 43 patients with primary glioblastoma (pGBM) and n = 33 patients with rHGG were assessed. pGBM patients were irradiated with photons and sequential proton/carbon boost, and rHGG patients were treated with carbon re-irradiation (CIR). WBT (Illumina HumanHT-12 Expression BeadChips) lbx was available for n = 9 patients from the rHGG cohort. PET isocontours (40%–70% SUVmax, 10% steps) and MRI-based treatment volumes (MRIvol) were compared using the conformity index (CI) (pGBM, n = 16; rHGG, n = 27). Associations with WBT lbx data were tested on

gene expression level and inferred pathways activity scores (PROGENy) and from transcriptome estimated cell fractions (CIBERSORT, xCell).

Results: In pGBM, median SUVmax was higher in PET acquired pre-radiotherapy (4.1, range (R) 1.5–7.8; n = 20) *vs.* during radiotherapy (3.3, R 1.5–5.7, n = 23; p = 0.03) and in non-resected (4.7, R 2.9–7.9; n = 11) *vs.* resected tumors (3.3, R 1.5–7.8, n = 32; p = 0.01). In rHGG, a trend toward higher SUVmax values in grade IV tumors was observed (p = 0.13). Median MRIvol was 32.34 (R 8.75–108.77) cm^3 in pGBM (n = 16) and 20.77 (R 0.63–128.44) cm^3 in rHGG patients (n = 27). The highest median CI was observed for 40% (pGBM, 0.31) and 50% (rHGG, 0.43, all tumors) isodose, with 70% (40%) isodose in grade III (IV) rHGG tumors (median CI, 0.38 and 0.49). High SUVmax was linked to shorter survival in pGBM (>3.3, p = 0.001, OR 6.0 [2.1–17.4]) and rHGG (>2.8, p = 0.02, OR 4.1 [1.2–13.9]). SUVmax showed associations with inferred monocyte fractions, hypoxia, and TGFbeta pathway activity and links to immune checkpoint gene expression from WBT lbx.

Conclusion: The benefits of ^{18}F-FET-PET imaging on gross tumor volume (GTV) definition for particle radiotherapy warrant further evaluation. SUVmax might assist in prognostic stratification of HGG patients for particle radiotherapy, highlights heterogeneity in rHGG, and is positively associated with unfavorable signatures in peripheral whole-blood transcriptomes.

KEYWORDS

particle therapy, 18F-FET-PET, liquid biopsy, whole blood transcriptome, conformity index (CI), high grade glioma (HGG)

Introduction

Despite intensive research and a multimodal treatment approach, the prognosis for glioblastoma (GBM) and recurrent high-grade glioma (rHGG) remains poor (1, 2). Therapy of treatment-naïve GBM consists of maximal safe resection followed by radiotherapy with concomitant and adjuvant temozolomide chemotherapy (3), which may be accompanied by Tumor-Treating Fields (4). For recurrent disease, no standard therapy has been defined; however, resection, radiotherapy (5), and chemotherapy (6) are frequently delivered.

Particle therapy might be a promising treatment strategy for glioma patients. It allows for better normal tissue sparing due to higher physical dose conformity (7) and delivers a higher relative biological effectiveness (RBE) as compared to photon radiotherapy (RBE of 1.87–3.44) (8). Preclinical data suggest benefits from carbon ion radiotherapy (CIR) through improved cell killing of glioma tumor cells in a hypoxic milieu, reduction of angiogenesis, and overcoming a local immunosuppressive milieu (9). In line with these findings, the first clinical data show promising results (10–13).

Metabolic imaging with (18)F-fluoro-ethyl-tyrosine positron emission tomography (18F-FET-PET) has been proposed to help delineate target volumes in glioma (14), which is currently mainly based on contrast-enhanced T1-weighted MRI. It has been hypothesized that 18F-FET-PET is able to detect aggressive tumor subregions and lesions beyond contrast enhancement in MRI (15–17). However, evaluation of 18F-FET-PET-positive isocontour-defined volumes and gross tumor volumes (GTVs) in 26 rHGG patients revealed only low conformity between both volumes with maximum conformities of 0.42–0.51 observed at isocontour 40% (18). A precise algorithm for the integration of 18F-FET-PET into treatment planning is lacking and the subject of ongoing research (19). In addition to target volume definition, 18F-FET-PET imaging has been evaluated for its prognostic value in grade II–IV gliomas (20) and rHGG (18): a poorer outcome for higher tracer uptake has been described in both studies.

Whole-blood transcriptome (WBT) liquid biopsy (lbx) data have been used as a surrogate to monitor disease states (21, 22). Different blood components have the potential to yield information about the tumor with minimal intervention, i.e., circulating tumor cells, or other fractions of blood cells, which might be exposed to a number of transcriptome-altering factors (e.g., irradiation, drug treatments, and transversion through

tumor tissue and modulation by cytokines). We recently reported the feasibility of WBT lbx to monitor response to treatment (particle irradiation in rHGG) and to mirror tumor characteristics (23). We therefore aim to evaluate if tracer uptake is linked to a specific whole-blood transcriptome fingerprint.

With this study, we aimed to investigate the value of 18F-FET-PET for tumor delineation in treatment planning and outcome prediction in primary glioblastoma (pGBM) and rHGG treated with particle radiotherapy and to assess a link between WBT lbx readouts and 18F-FET-PET-based tumor metabolic activity quantification.

Methods

Ethics approval and consent to participate

All patients consented to participate in this study, and ethical approval was obtained by the IRB-Ethics Committee of the Medical Faculty of Heidelberg University (approval numbers S-421/2015 and S-540/2010).

Study cohort and radiotherapy

n = 76 patients with pGBM (n = 43) or rHGG (n = 33) were included in this study. All patients underwent high-precision charged particle beam radiotherapy (RT) at the Heidelberg Ion Beam Therapy Center (HIT) between 2010 and 2017. Clinical data were retrospectively recorded in the institute's own database.

Patients with pGBM were treated in or analogous to the CLEOPATRA trial (24) for incompletely resected primary glioblastoma (residual macroscopic tumor visible at least on MRI). In a two-stage target volume concept, they received a standard postoperative fractionated photon RT up to a cumulative dose of approx. 50 Gy to the contrast-enhanced areas in T1-weighted magnetic resonance tomography (MRT), the T2-hyperintense areas, and the resection cavity, followed by a proton (5 × 2 Gy) or carbon ion (6 × 3 Gray equivalents (GyE)) boost to the macroscopic tumor remnant.

Patients with rHGG (n = 33) were treated in or according to the CINDERELLA trial (10) and received CIR at a dose of 10 to 16 × 3 GyE to the macroscopic tumor. The macroscopic tumor was defined based on contrast enhancement in T1-weighted MRI both for primary and recurrent tumors. As per the study protocol, information from 18F-FET-PET imaging could be optionally considered for the target volume definition of particle RT.

For pGBM, 18F-FET-PET information was not considered for photon RT treatment planning but could be used for particle boost delineation. In the rHGG cohort, 18F-FET-PET information was not considered for GTV delineation but was included in clinical target volume (CTV) delineation; i.e., areas with high tracer uptake were effectively irradiated with CIR. No patient received particle RT in both the primary and recurrent settings.

A static amino acid 18F-FET positron emission tomography (PET) CT scan was available before the start of particle RT for every patient. Tracer uptake and survival analyses were performed on the entire cohort (n = 76). For analyses on the impact of 18F-FET-PET on tumor delineation (see section "Imaging processing and analysis") in pGBM patients, 18F-FET-PET-derived isocontours were compared to MRI-based GTV for photon RT. Analyses were carried out for n = 16 (37%) pGBM patients. N = 27 patients could not be included due to one or more of the following reasons: photon RT was delivered at another institution, and RT plans were not available for further analyses (n = 14); photon RT planning MRI was not extractable from the institution's picture archiving and communication system (PACS), i.e., imaging performed at another institution (n = 8); PET showed unspecific tracer uptake without significant evidence of residual tumor (n = 6); PET was carried out >50 days prior to photon RT start (n = 2).

N = 27 (82%) patients with rHGG were included in analyses on the impact of 18F-FET-PET on tumor delineation. 18F-FET-PET-derived isocontours were compared to MRI-based GTV. N = 6 patients could not be included because CIR planning MRI was not extractable from the institution's PACS (n = 3), because PET was carried out >50 days prior to CIR start (n = 1), which showed uncharacteristic low tracer uptake (n = 1), or imaging was performed at another institution and without a corresponding CT dataset needed for further data procession (n = 1).

Since a relevant proportion of patients could not be included in the analyses of PET vs. MRI-based treatment volumes, it was evaluated whether the characteristics of the enrolled patients were different from those excluded (Supplementary Tables 3, 4).

MRI showing tumor progression after particle (re)RT was available for n = 34 (79%) pGBM patients and n = 25 (76%) rHGG patients. Recurrence patterns were analyzed in a semiquantitative approach classifying tumors into one or more of the following categories: 1) recurrence in the area of initial contrast uptake in T1-MRI/MRI-based treatment volume, 2) recurrence in the area of increased PET signal, and 3) distant recurrence.

Whole-blood transcriptome data (Illumina HumanHT-12 Expression BeadChips) were available for n = 9 patients of the rHGG cohort participating in a liquid biopsy study for the effect of CIR in rHGG (for details, see [1]). Blood samples were collected before the start of CIR and at different time points after CIR (see Supplementary Figure 1).

Imaging data

Image data consist of treatment planning MRI and static 18F-FET-PET/CT scans. In pGBM patients, 18F-FET-PET imaging

was performed at different time points: before surgery (n = 3), between two surgeries (n = 1, whereby both procedures consisted of a biopsy), between surgery and start of photon RT (n = 16), and during photon RT (n = 23). In rHGG patients, PET images were acquired before CIR in all cases (n = 33), with one patient having had a partial tumor resection between PET acquisition and RT start. Most PET/CT scans were performed with Biograph 6 (n = 61). Other PET/CT devices used were Biograph 64 (n = 5), Biograph mCT Flow (n = 4), Biograph HiRes Model 1080 (n = 2), Biograph TruePoint Model 1094 (n = 2), and Biograph 40 (n = 1; all Siemens Healthineers, Erlangen, Germany) and Gemini TF 16 (n = 1; Philips Medical Systems, Hamburg, Germany).

Imaging processing and analysis

For analyses of PET imaging data, the standardized uptake value (SUV) was determined. The required parameters (injected activity, injection time, acquisition time, and body weight) were extracted from the static PET DICOM files with Loni Inspector (V 2.11, University of Southern California Mark and Mary Stevens Neuroimaging and Informatics Institute, Los Angeles, USA) software. Median injected activity was 180 (R 124–314) MBq and 2.2 (R 1.39–4.24) MBq/kg body weight for pGBM patients and 198 (R 130–270) MBq and 2.49 (R 1.69–4.15) MBq/kg body weight for rHGG patients. The median time from injection to image acquisition was 12 min (R 5–42) in pGBM patients and 11 min (R 2–41) in rHGG patients.

SUV was determined voxel-wise for all patients using the software MITK (The Medical Imaging Interaction Toolkit, www.mitk.org) (18, 25). In the next step, a large region of interest (ROI) enclosing the primary or recurrent tumor was defined. If required, structures with increased tracer uptake such as vessels and basal ganglia were omitted in ROI delineation. The SUVmax of the ROI was extracted. Next, a maximum standardized uptake ratio (SURmax) was determined for each tumor. SURmax was calculated as the quotient of SUVmax of the ROI and mean SUV of a reference region. The reference region represents the background signal and was drawn in the contralateral hemisphere or, in case of a tumor near the midline, in the unaffected anterior or posterior part of the brain, encompassing both gray and white matter (26).

18F-FET-PET-based tumor volumes were generated as isocontours from SUVmax in increments of 10 from 40% to 70% within the ROI encompassing the tumor. PET images were registered to the treatment planning MRI (rigid registration). To assess differences in PET-derived isocontours (PETvol) and MRI-derived RT treatment volumes (MRIvol), different 3D structures were created and analyzed (see Supplementary Table 2). Concordance between volumes was quantified using the conformity index (CI = intersection of PETvol and MRIvol divided by their union). The isocontour with the largest CI was identified as the "best matching isocontour".

Whole-blood transcriptome profiling

RNA was extracted from whole blood (PAX gene blood RNA tubes), using the PAXgene Blood RNA Kit (Qiagen, Valencia, CA, USA). Expression was quantified from 200 ng of quality-controlled RNA (Bioanalyzer, Agilent) on Illumina HumanHT-12 Expression BeadChip array in the genomics Core Facility DKFZ (Heidelberg, Germany). xCell (27) and PROGENy (28) were used to estimate cell type fractions and pathway activities from transcriptome data. Kyoto Encyclopedia of Genes and Genomes (KEGG) pathway analysis was conducted with enrichR (29).

Statistical analysis

Statistical analyses were conducted with IBM SPSS Statistics Version 27 (IBM, Armonk, New York, NY, USA) and R v 4.0.5 (R 30). Time-to-event analyses were conducted with Cox-PH models and parametric survival models assuming log-logistic distribution with the survival (31) and dataAnalysisMisc packages (32). Survival was calculated from the onset of photon RT to progression or death in pGBM and from the onset of CIR to progression or death in rHGG patients. Patients lost to follow-up (FU) were censored at the time point of the last contact. Differences were tested using non-parametric methods (Wilcoxon test, rankFD (33), t-tests, and linear models. Robust p-values were computed using the robustbase package (34). Random forest analyses were conducted with the randomForest package (35). The significance level is set to $\alpha = 0.05$ (two-sided) if not stated otherwise. The Benjamini–Hochberg procedure was used for multiplicity adjustment (false discovery rate (FDR)) if not stated otherwise.

Results

Patient characteristics

An overview of the cohort, treatment, and patients' characteristics is shown in Table 1 and Figure 1A.

The median age at diagnosis of pGBM was 58 years (R 21–75), with a median Karnofsky Performance Score (KPS) of 90% (R 60–100). Prior to RT, 33 (77%) patients underwent resection (partial resection, 13 (30%); subtotal resection, 20 (47%)), and 10 patients (23%) underwent biopsy only. The sequential particle boost was delivered with protons (5 × 2 Gy) in 26 cases (60%) and CIR (6 × 3 GyE) in 17 cases (40%). Tumor tissue was available from all pGBM patients, and the diagnosis of glioblastoma was based on the 2007 WHO Classification of Tumors of the Central Nervous System (36) in most cases (n = 41, 95%). Two patients were classified according to the 2016 WHO classification (37). IDH1 status was available in 28 cases (65%), all of which showed IDH1-

TABLE 1 Combined table of treatment and patient characteristics for the pGBM (n = 43) and rHGG (n = 33) cohorts.

Feature	Specification	pGBM n (%)	rHGG n (%)
Sex	Male	30 (70)	21 (64)
	Female	13 (30)	12 (36)
Age at initial diagnosis [years]	pGBM: 21–64/rHGG: 16–41	33 (77)	16 (48)
	pGBM: 65–75/rHGG: 42–67	10 (23)	17 (52)
	Median (range)	58 (21–75)	42 (16–67)
Age at CIR [years]	22–64	—–	29 (88)
	65–71	—–	4 (12)
	Median (range)	—–	54 (22–71)
Karnofsky Performance Score* [%]	60–80	10 (23)	7 (21)
	90–100	28 (56)	25 (76)
	N/A	5 (12)	1 (3)
	Median (range)	90 (60–100)	90 (60–100)
Tumor localization	pGBM: unifocal/rHGG: local^{+}	38 (88)	30 (91)
	pGBM: multifocal/rHGG: distant^{+}	5 (12)	3 (9)
Time from first course of RT to CIR [months]	7–19	—–	16 (48)
	23–208	—–	17 (52)
	Median (range)	—–	23 (7–208)
WHO grade primary tumor	II	0 (0)	10 (30)
	III	0 (0)	8 (24)
	IV	43 (100)	15 (76)
IDH status	Mutation (R132H)	0 (0)	—–
	Wild type	28 (65)	—–
	N/A	15 (35)	—–
MGMT promoter methylation status	Methylated	5 (12)	—–
	Hypomethylated	11 (25)	—–
	N/A	27 (63)	—–
WHO grade recurrence	III	—–	16 (48)
	IV	—–	17 (52)
Maximum extent of surgery	Biopsy	10 (23)	4 (12)
	Resection	33 (77)	29 (88)
	Partial resection	13 (30)	N/A
	Subtotal resection	20 (47)	N/A
Time from last surgery to ^{18}F-FET-PET	<5 years	—–	27 (82)
	>5 years	—–	6 (18)
	Median (range) [months]	—–	12 (0–289)
Time from initial RT to ^{18}F-FET-PET	<5 years	—–	23 (70)
	>5 years	—–	10 (30)
	Median (range) [months]	—–	22 (6–208)
Tumor progression before RT	Yes	5 (12)	—–
	No	38 (88)	—–
Re-resection performed	Yes	—–	20 (47)
	No	—–	18 (55)
Particle (re)RT	pGBM: protons, 5 × 2 Gy/rHGG: 30–33	26 (60)	14 (42)
	pGBM: carbon ions, 6 × 3 GyE/rHGG: 36–45	17 (40)	19 (58)
	rHGG: median (range)	—–	36 (30–45)
PTV CIR [ml]	5.74–80.82	—–	16 (48)
	83.88–242.44	—–	16 (48)
	N/A	—–	1 (3)

(Continued)

TABLE 1 Continued

Feature	Specification	pGBM n (%)	rHGG n (%)
	Median (range)	—–	82.35 (5.74–242.44)
Concurrent chemotherapy	Yes	43 (100)	3 (9)
	No	0 (0)	30 (91)
Follow-up (FU)	FU data available for	37 (86)	31 (94)
	Median FU (range)	7 (1–36)	9 (1–79)

Parameters are presented in absolute numbers and percentages related to the respective cohort.
pGBM, primary glioblastoma; rHGG, recurrent high-grade glioma; CIR, carbon re-irradiation; RT, radiotherapy; PTV, planning target volume; N/A, not available.
*rHGG: CIR.
†rHGG: in relation to primary tumor.

wild-type glioblastoma. Median overall survival (OS) was 16.2 months (95% CI 13.3–19.7). Median progression-free survival (PFS) was 6.4 months (95% CI 5.2–7.8).

In the rHGG cohort, the median age at the time of CIR was 54 (R 22–71) years, and the median KPS was 90% (R 60–100). For rHGG patients, tumor tissue was available for n = 15 (45%) patients at the time point of recurrence. Tumor classification was mostly based on the 2007 WHO Classification (n = 14, 93%) with one case being classified according to the 2016 WHO Classification. In n = 18 (55%) patients, where no biopsy or resection was performed at recurrence, the diagnosis was based on imaging criteria suggestive of rHGG (contrast medium enhancement) and an interdisciplinary consensus (tumor board). At disease recurrence, 16 (48%) patients had a WHO grade III, and 17 (52%) patients had a WHO grade IV tumor. The initial diagnosis was determined histologically in all rHGG patients. The underlying primary tumor was low-grade glioma (LGG) in n = 10 (30%) and HGG in n = 23 (70%) cases, with n = 8 (24%) grade III vs. n = 15 (45%) grade IV gliomas. In the primary setting, classification was according to the 2007 WHO classification in n = 23 (70%) and according to previous versions in the remaining n = 10 (30%) cases. The median time from the first course of photon RT to CIR was 22 months (R 6–208). Initially, n = 29 (88%) patients underwent tumor resection vs. n = 4 (12%) biopsy only. Re-resection had been performed in 15 cases (45%). The median time between the last resection and 18F-FET-PET was 14 months (R 1–289). CIR was delivered at a median dose of 39 GyE (R 30–45) in 3-GyE fractions. Median OS in rHGG was 17.5 months (95% CI 11.3–27.2) with the date of death known for 23 (70%) patients. PFS was 5.0 months (95% CI 3.4–7.6).

Tracer uptake in primary glioblastoma and recurrent high-grade glioma

Tracer uptake, as quantified by SUVmax and SURmax, is shown for both cohorts in Figure 1. Both parameters show high concordance (Figure 1A), and no clear improvement using SURmax in performed analyses was observed (data not shown). Thus, SUVmax-based analyses were retained going forward. Median SUVmax was 3.5 (R 1.48–7.82) in pGBM. 18F-FET-PET tracer uptake was significantly lower in patients with resected tumors and in images acquired after the start of photon RT (Figure 1B). There was no interaction between resection status and time point of 18F-FET-PET imaging (p = 0.82, Figure 1B). For resected tumors under RT, there was a non-significant association for decreasing 18F-FET-PET uptake if imaging was performed at later stages of RT (Figure 1C, p = 0.12, one-sided).

In rHGG, PET images yielded a median SUVmax of 3.09 (R 1.1–8.39). A trend toward higher SUVmax values in grade IV tumors was observed (Figure 1D). This trend was preserved after pooling pGBM and rHGG cohorts, with higher SUVmax values in grade IV vs. grade II tumors (p = 0.08) (Figure 1E).

Prognostic value of tracer uptake

To test the prognostic value of SUVmax for OS, patients from both cohorts were split into “higher than median” vs. “lower than median” SUVmax uptake using the median SUVmax value of each cohort as a cutoff (pGBM cutoff, 3.5; rHGG cutoff, 3.09; Figure 2, top row). For patients with pGBM, SUVmax ≥ 3.5 was prognostic for OS (p = 0.01), whereas in rHGG, an uptake > 3.09 was associated with a non-significant trend for worsened survival outcomes. A combination of grade IV tumors from pGBM and rHGG confirmed a prognostic value of SUVmax for median cutoff (3.37, Figure 2, right). In the pooled grade IV tumors from pGBM and rHGG, median SUVmax (>3.37) was prognostic for worsened OS (p = 0.01). Additionally, we attempted to identify the best prognostic SUVmax threshold by evaluating the impact of varying cutoffs on OS. SUVmax optimal was defined as the cutoff associated with the smallest p-value for OS (Figure 2, bottom row). In rHGG, an optimal cutoff of 2.8 was prognostic of outcome (p < 0.05). For pGBM, SUVmax optimal was 3.3. For ranges of cutoffs leading to the separation of groups with p < 0.05 or p < 0.1, see Supplementary Table 2.

SUVmax as a continuous covariate was significant for worsened OS in pGBM (OR = 1.36, p = 0.051). SUVmax median cutoff and SUVmax optimal cutoff were also prognostic factors for OS (OR = 3.21, p = 0.31 and OR = 5.99,

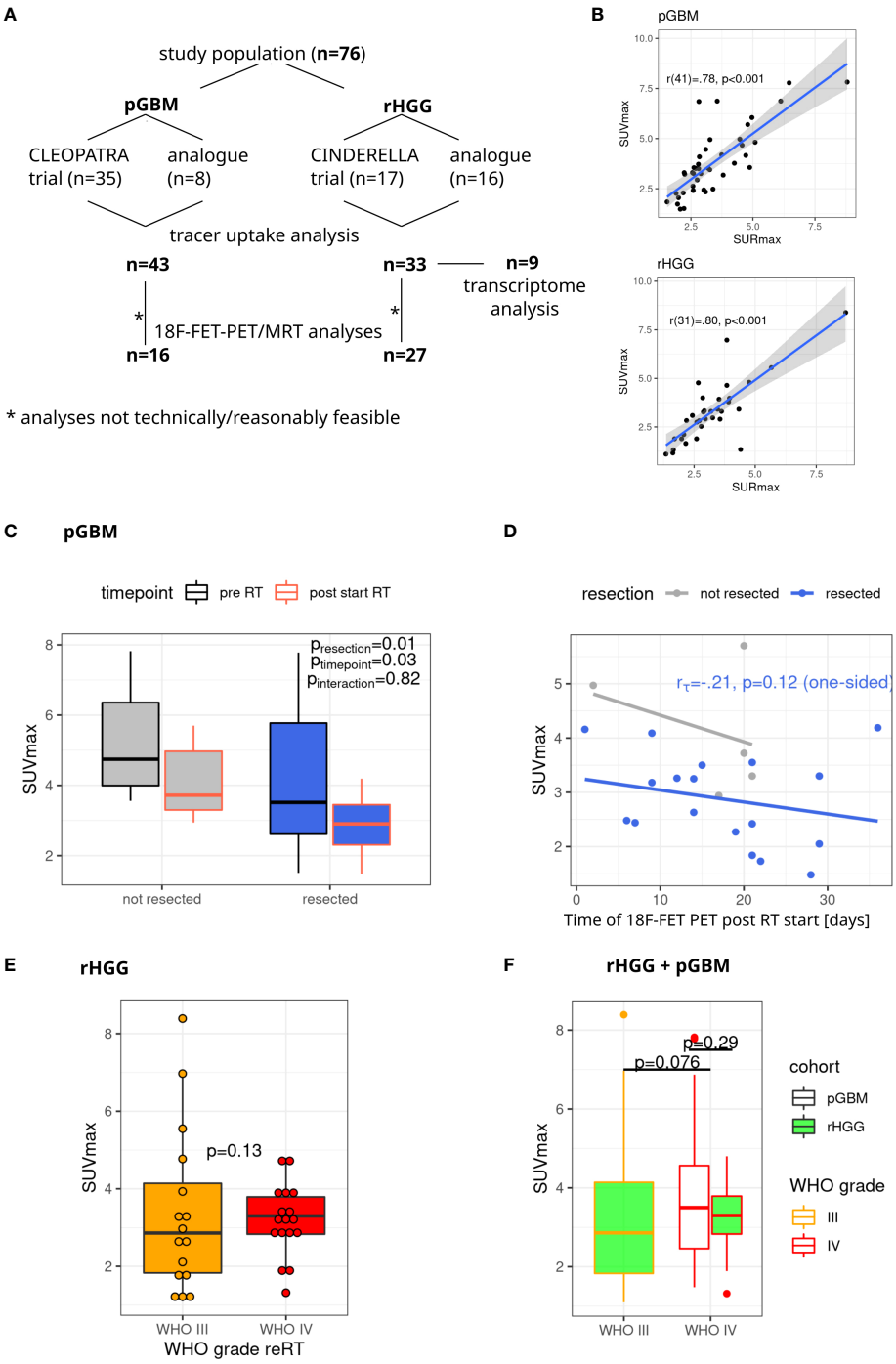

FIGURE 1
Study cohort and tracer uptake in pGBM and rHGG. **(A)** Overview of the study cohort. **(B)** A strong correlation (r = 0.80) is observed between SUVmax and SURmax values (Pearson's correlation). **(C)** SUVmax in pGBM depending on resection status and time point after RT start. Non-parametric model analysis (rankFD). **(D)** SUVmax values after irradiation start. Linear model fit, Kendall's tau for resected samples (one-sided p-value). **(E)** SUVmax in rHGG, one-sided p-value, robust p-value (robustbase). **(F)** SUVmax in grade III and IV tumors. One-sided robust p-value (robustbase). pGBM, primary glioblastoma; rHGG, recurrent high-grade glioma; RT, radiotherapy.

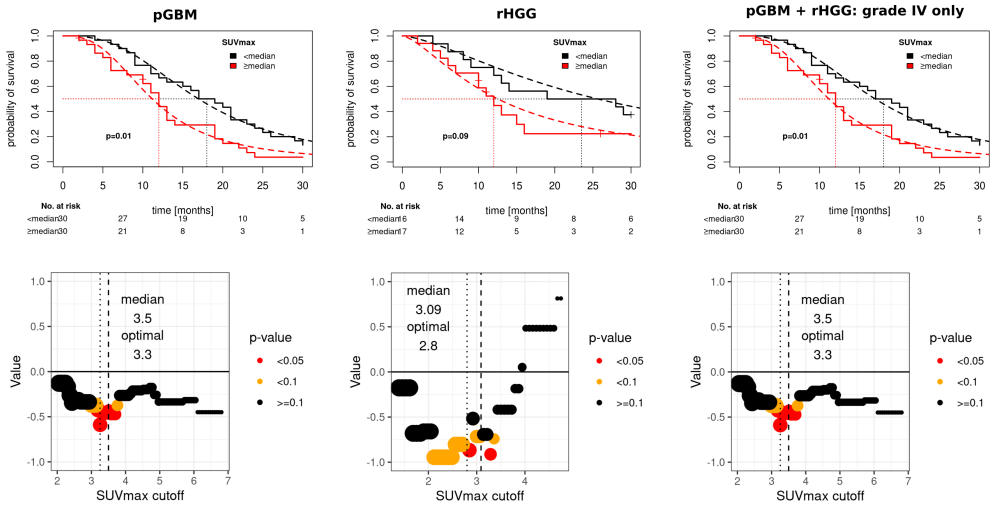

FIGURE 2
Prognostic value of SUVmax in pGBM and rHGG. Top row: Kaplan–Meier survival curves, log-logistic parametric survival regression fits (dashed line). Wald type p-value. Bottom row: model coefficients for varying cutoffs (bottom row), median (dashed line), and optimal cutoffs (minimal p-value, dotted line). pGBM, primary glioblastoma; rHGG, recurrent high-grade glioma.

p = 0.001 respectively). Other prognostic variables on the univariate analysis included age (≥ 65 vs. <65 years, OR = 3.7, p = 0.047) and degree of resection, whereby partial resection (OR = 0.14, p = 0.03) and subtotal resection (OR = 0.2, p = 0.053) were associated with improved OS. Multivariate analysis confirmed SUVmax optimal (OR = 2.73, p = 0.007) and age ≥ 65 years (OR = 2.97, p = 0.048) as independent adverse prognostic markers for OS in pGBM (Figure 3).

In rHGG, SUVmax as a continuous variable was not prognostic of OS on univariate analysis (Figure 3). SUVmax median showed a trend for worsened OS (OR = 2.91, p = 0.086), and SUVmax optimal was prognostic for OS (OR = 4.12, p = 0.023). Additionally, age at initial diagnosis (OR = 1.05, p = 0.015), initial WHO grade IV (HR = 7.8, p = 0.008), and WHO grade IV at CIR (HR = 21.7, p = 0.001) were inversely associated with OS. Multivariate analysis confirmed SUVmax optimal (OR = 2.73, p = 0.042) and WHO grade IV at CIR (OR = 12.24, p = 0.013) as independent prognostic markers for OS in rHGG (Figure 3).

SUVmax optimal cutoff was also prognostic for PFS in pGBM (cutoff 2.3, OR 11.9 [95% CI 1.95–71.9], p = 0.007) and rHGG (cutoff, 4.4, OR 4.36 [95% CI 1.15–16.52], p = 0.03). The data are shown in Supplementary Figure 2.

Isocontour concordance with irradiated volume

Comparison of 18F-FET-PET-defined isocontours with MRI-based treatment volumes was carried out for a subset of patients due to the limited availability of data (see Figure 1A and "Methods"). Treatment and patients' characteristics of the subcohorts are shown in Supplementary Table 3 and SUVmax metrics in Supplementary Table 4.

GTV was utilized as MRIvol for pGBM in all 16 cases. In rHGG, GTV was used in n = 24 (89%) and CTV in 3 (11%) cases, where GTV was not defined but where areas of high tracer uptake morphologically corresponded to contrast enhancement in T1-MRI. Concordance between 18F-FET-PET isocontours and MRIvol was assessed with CI (Figures 4, 5) and Dice coefficient (Supplementary Figure 3). Figure 4A illustrates the calculation of CI for a given GTV volume and a range of isocontours (Ix). Figure 4B shows images of a patient from the pGBM cohort and Figure 4C of a patient from the rHGG cohort with resection of the initial and no resection of the recurrent tumor.

The highest conformity was observed for isocontour 40% in pGBM and isocontour 50% in rHGG (Figures 5A, C). Stratification by resection status in pGBM showed for biopsy and subtotal resection high conformity for 50% isocontour and only for partial resection isocontour 40% showed the highest median CI. In rHGG, conformity decreased for higher isocontours in grade IV tumors. The opposite was observed in grade III rHGG whereby higher conformity was seen for I70 (Figures 5A, C). Finally, the relationship between CI and SUVmax was investigated in each group. In pGBM (Figure 5B), the CI was negatively associated with SUVmax at higher isodoses (I70: red line). In contrast, CI was positively correlated with increasing SUVmax for isodoses 50 (blue line) and 40 (black line). Similar correlations were seen in rHGG (Figure 5D).

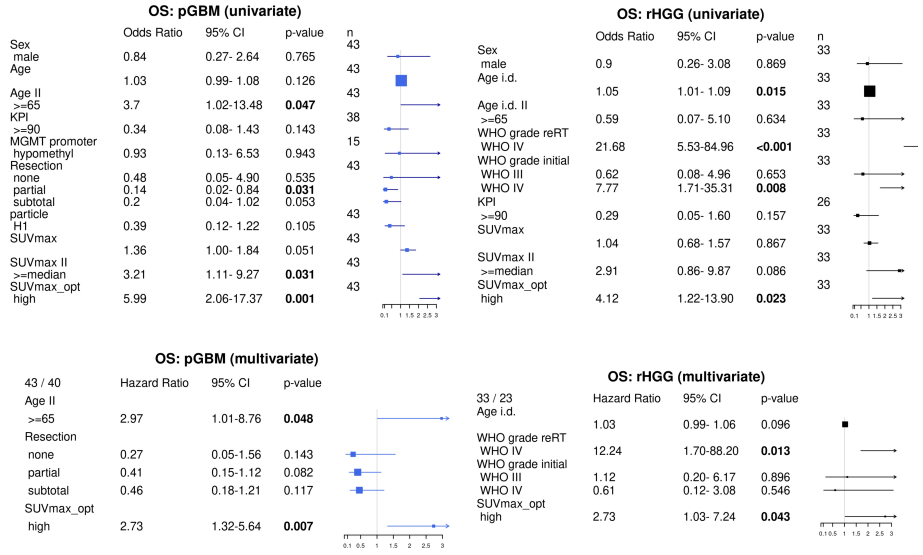

FIGURE 3
Uni- and multivariate survival analyses in pGBM and rHGG. Univariate analysis: parametric survival model (log-logistic distribution). pGBM: reference level for resection: biopsy. Age i.d.: age at initial diagnosis. Multivariate analysis includes variables significant in univariate analysis, Cox PH survival model. SUVmax_opt: optimal separation (minimal p-value). pGBM, primary glioblastoma; rHGG, recurrent high-grade glioma.

In pGBM/rHGG, the median volume of "best matching isocontour" was 22.59 (R 5.72–192.68)/24.35 (R 2.42–1,407.04) cm3. Its union with GTV resulted in a median 26% (R 3–328)/37% (R 0.2–4836) increase in volume, with the median absolute volume added by "best matching isocontour" being 8.35 (1.37–159.04)/6.3 (R 0.13–73.03) cm3. Absolute volumes for each patient are visualized in Supplementary Figure 4

Radiographic features are associated with recurrent high-grade glioma grade

Next, volumetric parameters in rHGG were evaluated (intersections of isocontour volumes and MRI-based target volumes) as well as tracer uptake metrics (SUVmax, SURmax; see the full list in Supplementary Table 2). Radiographic features separated patients with rHGG into two separate populations on the two-dimensional umap representation (Figure 5E). This separation corresponded to rHGG tumor grade (Figure 5E, top part), with umap-1 showing significantly different values between grades ($p = 0.04$, Figure 5E, bottom part). Next, random forest analyses with resampling were used to identify which features dominate separation by grade (Figure 5F, bottom part). Random forest selected features in increasing order of importance. Interestingly, the top-ranked features were those features associated with isocontour 40/50. In contrast, SURmax and SUVmax were only ranked in positions 11 and 12. Iso 40 ADD was the top-ranked feature and was enough to separate patients according to grade (Figure 5F, right).

Patterns of recurrence

Assessment of recurrence patterns for the pGBM cohort (subcohort of n = 34 patients with follow-up imaging showing progress), where 18F-FET-PET was only utilized for boost delineation, showed n = 21 (62%) local recurrences, n = 5 (15%) distant recurrences, and simultaneous local and distant recurrences for n = 8 (24%) patients at first progression. In four cases, recurrences occurred in areas with increased tracer uptake (SUVmax: 3.25, 3.51, 5.7, and 7.82), one of which did not show contrast enhancement on MRI and the remaining three being partially included in photon-RT MRIvol.

In rHGG (subcohort of n = 25 patients with follow-up imaging showing progress), where 18F-FET-PET was used for CTV delineation, no local recurrence was observed in 18F-FET-PET-positive/MRI T1ce-negative areas. N = 3 (12%) patients showed distant recurrences, n = 17 (68%) local recurrences, and n = 5 (20%) simultaneous local and distant recurrences at first progression.

SUVmax correlates with whole-blood transcriptomes

We assessed if SUVmax correlates with whole-blood transcriptomes. Analysis of the most variable 10% of genes adjusted for initial tumor grade identified 38 genes as being associated with SUVmax (Bonferroni-adjusted p-value <0.05) and 936 genes with an FDR < 0.05 (Figure 6A). As an example,

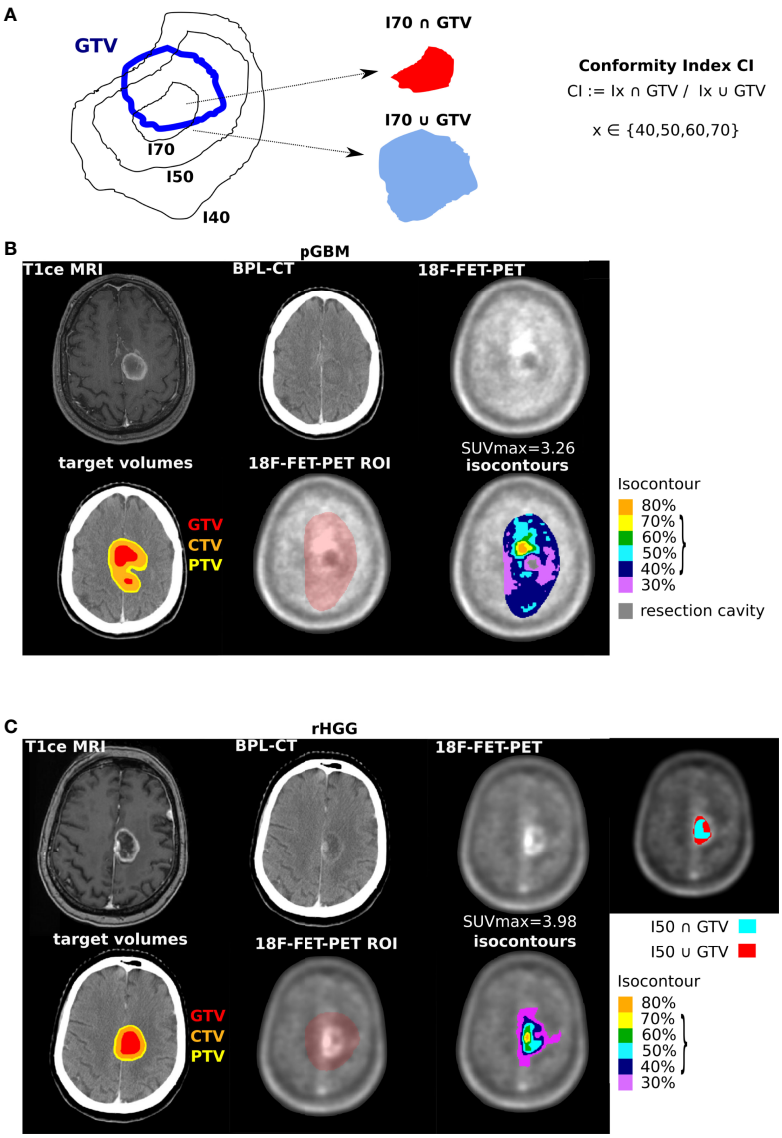

FIGURE 4
Concordance between ^{18}F-FET-PET defined volumes and target volumes. **(A)** Schematics of evaluated volumes with isocontour I (I40%, 50%, and 70% shown as an example) and conformity index (CI) definition. **(B)** Representative images with radiotherapy volumes and isocontours for a patient with primary glioblastoma, from left to right in the first row: MRI at initial diagnosis, planning CT, ^{18}F-FET-PET imaging before radiotherapy; in the second row: planning CT with MRI-based tumor volumes (GTV in red, CTV in orange, and PTV in yellow), defined region of interest (ROI) in ^{18}F-FET-PET imaging, and ^{18}F-FET-PET-based isocontours (30% in purple, 40% in blue, 50% in turquoise, 60% in green, 70% in yellow, and 80% in orange). **(C)** Representative images with radiotherapy volumes and isocontours for a patient with recurrent high-grade glioma, imaging, and color coding similar to panel **(B)** Additional illustration of a representative image for I50 and GTV with intersection of volumes shown in turquoise and union of volumes shown in red. Parentheses, values further evaluated; see Figure 5. GTV, gross tumor volume; CTV, clinical target volume; PTV, planning target volume.

representative expression values for POLD4 are shown in Figure 6A (top middle), demonstrating an association between gene expression and SUVmax as a function of the initial WHO grade. KEGG pathway enrichment identified Glioma, PI3K pathway components, and specific HLA genes associated with SUVmax (Supplementary Figure 5).

Higher SUVmax showed positive associations with hypoxia, TGFbeta, and EGFR transcriptome signatures as inferred by PROGENy (Figure 6B). Fractions of cell types, inferred with CIBERSORT and xCell, showed higher fractions of macrophages/monocytes in higher SUVmax tumors and depletion of CD4+ naïve T cells (Figure 6C). Finally, the

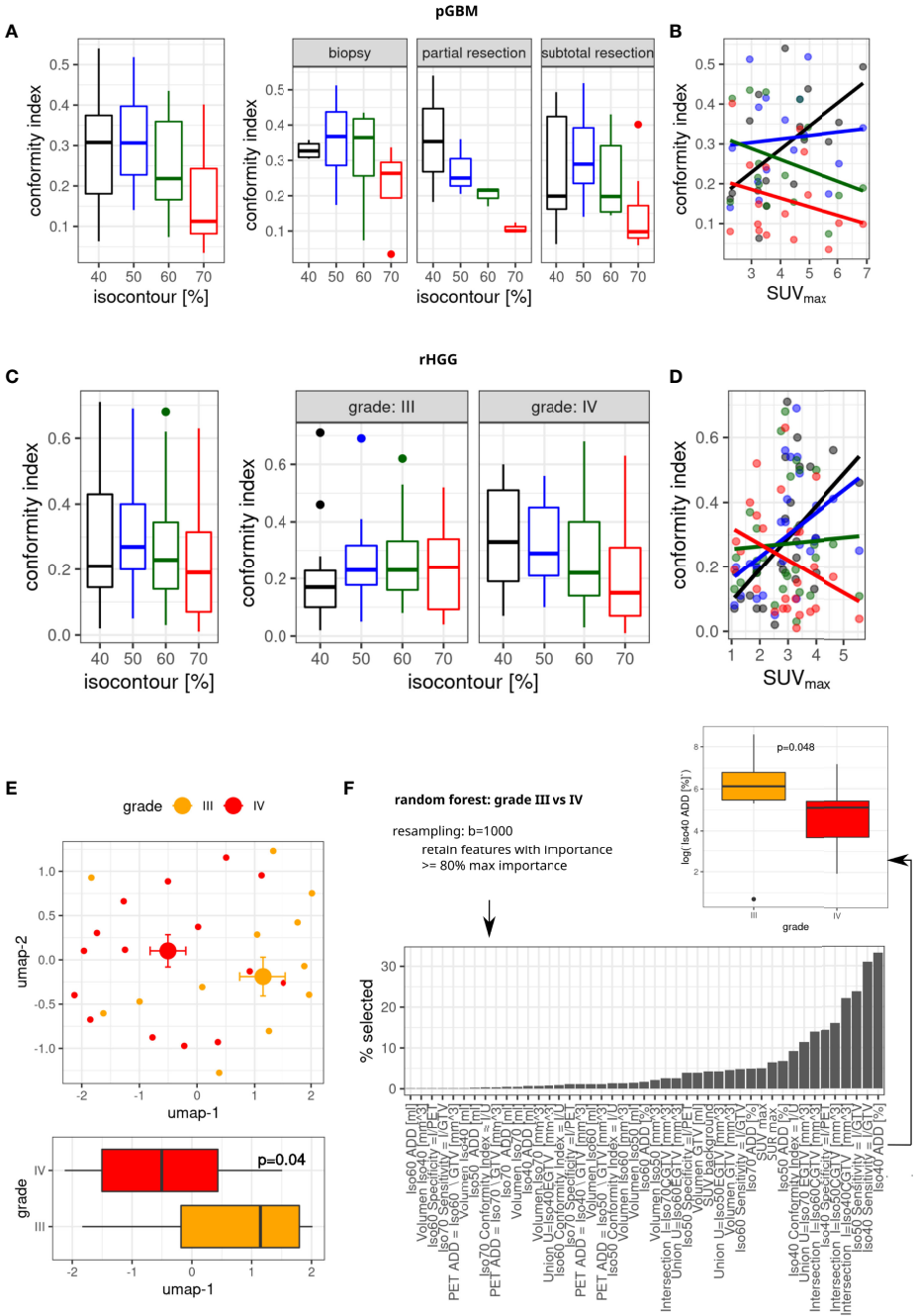

FIGURE 5
Concordance between GTV and ^{18}F-FET-PET isocontours. Conformity index (CI) for different isocontours **(A, C)**, split by degree of resection (pGBM, A, right) and radiographic reRT tumor grade (C, right). **(B, D)** Association between SUVmax and conformity index (linear model fits). **(E)** Umap representation of all n = 45 volumetric features, median, and SE (top part). Bottom part: differences in umap-1 values between tumor grades (linear model Wald type p-value). **(F)** Identification of features separating grade using random forests analysis (top part); distribution of feature frequencies in bottom part, and differences in top-ranked feature is shown on the right (linear model p-value). n = 27 patients. GTV, gross tumor volume; pGBM, primary glioblastoma.

evaluation of immune-checkpoint gene expression showed a trend toward a positive association of SUVmax and PD-L1 and negative associations for LAG3 (p = 0.11) and CTLA4 (p = 0.005) (Figure 6D).

Discussion

In this study, we report on the value of 18F-FET-PET imaging for target volume definition in pGBM treated with

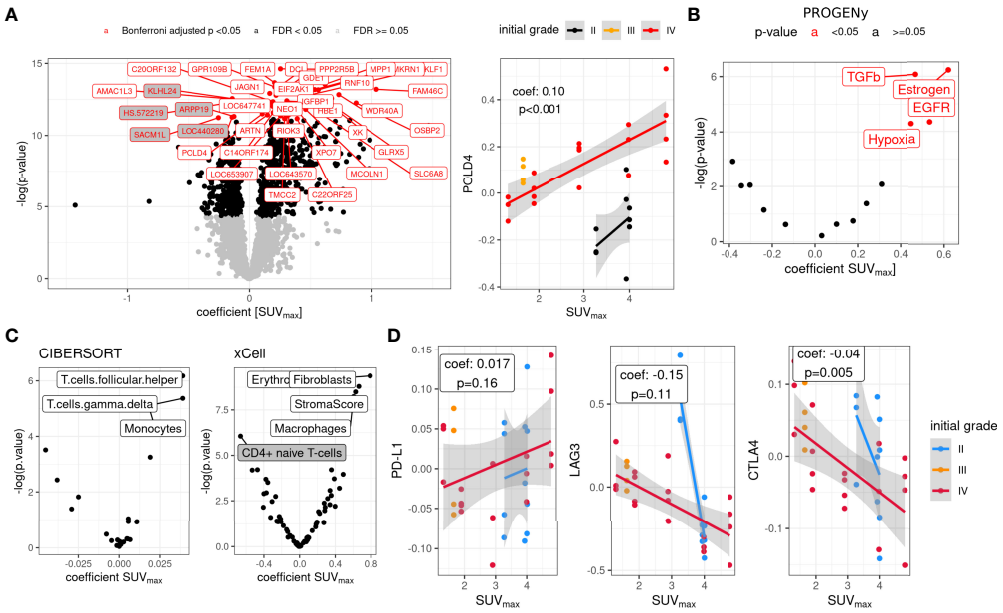

FIGURE 6
Whole-blood transcriptome associations with SUVmax in the rHGG cohort. **(A)** Genes associated with SUVmax, adjusted for initial WHO grade (most variable 10% of genes: median absolute deviation, gray background, coefficient < 0) and representative data for POLD4 (right) with linear fits. **(B)** PROGENy estimated pathway activity from transcriptome data (non-adjusted p-value). **(C)** CIBERSORT and xCell estimated cell fractions associated with SUVmax (adjusted for initial tumor grade, z-scaled data, non-adjusted p-value). **(D)** Association of SUVmax with immune checkpoint gene expression (linear mixed models). n = 9 patients. rHGG, recurrent high-grade glioma.

photon irradiation with particle boost and rHGG treated with carbon particle therapy, as well as its use for prognosis estimation and a link to minimally invasive whole-blood transcriptome liquid biopsy readouts.

Particle therapy provides an attractive therapeutic option for pGBM (11, 38) and rHGG (11, 38). However, tumors inevitably recur, preferentially in-field in patients treated with conventional photon radiotherapy (39) and at field margins in rHGG patients treated with carbon ions (18). Thus, identification of tumor (sub-)regions that might require intensified treatment as they are more prone to recurrence is crucial. In this study, however, we did not observe a clear preference for local vs. distant recurrences, which might be caused by a much less fine-granular qualitative classification in local vs. distant recurrence.

18F-FET-PET has been proposed to help delineate aggressive tumor regions and lesions not detected on T1 contrast-enhanced (ce) MRI (15–17, 40, 41). In our analyses, we see only a low degree of concordance between 18F-FET-PET and MRI-based target volumes, with the highest observed CIs for isocontours of 40% to 50%. This supports the hypothesis that T1ce MRI and 18F-FET-PET imaging show different aspects of the tumor and that additional information can be obtained by 18F-FET-PET imaging. “Best matching isocontours” were not necessarily larger than MRI-derived treatment volumes; however, we showed that their addition to GTV could likely result in a substantial increase in the treatment volume. A low threshold of I50 also implies a relatively large volume based on 18F-FET-PET, which might lead to intolerable toxicities. In pGBM, this relatively low overlap can be to some extent explained by the inclusion of the resection cavity into the MRI-based target volume; however, in rHGG, the resection cavity was generally not included in the target volumes. In line with these findings, Debus et al. also reported a low CI of 0.42–0.51 at I40% (18). More detailed analyses revealed a positive association of CI with SUVmax up to isocontour 50%; however, resection status and tumor grade had an influence on the optimal isocontour (maximal CI) in our cohorts and should be considered as covariates in future studies.

To further examine the hypothesis that 18F-FET-PET delineates highly aggressive tumor regions, we simultaneously assessed a number of tracer uptake metrics and volumetric features derived from isocontour/target volume intersections in rHGG tumors. We observed a separation of tumors by grade, and random forest analysis identified I40 features as being able to discriminate between tumor grades. The added volume based on I40 is higher in grade III tumors vs. grade IV tumors, and accordingly, the median CI for I40 is lower for grade III vs. IV. Thus, the overlap of 18F-FET-PET and target volumes

is higher in grade IV rHGG, thus supporting the hypothesis that 18F-FET-PET may be better suited for more aggressive tumors.

In this line, we found significantly increased tracer uptake for non-irradiated (18F-FET-PET acquisition before RT) as well as non-resected GBM and a trend toward higher SUVmax in GBM. It seems plausible that higher metabolic activity resulting in a higher tracer uptake is observed in untreated and more aggressive tumors.

Tracer uptake as a prognostic factor has been described previously. Gempt et al. reported that a tumor-to-normal ratio (SUVmean tumor/SUVmean background) of 1.88 was best in discriminating OS in patients with primary WHO grade II to IV glioma (40), whereas Sweeney et al. identified SUVmax of 2.6 as the cutoff for survival prognosis in their cohort of primary WHO grade II to IV patients (20). For recurrent WHO grade IV gliomas, Debus et al. reported a poorer prognosis with SUVmax > 2.92 (18).

We confirmed that tracer uptake is associated with prognosis both in the primary (pGBM) and in the recurrent setting (rHGG). Our identified thresholds/threshold ranges leading to prognostic separation are in line with the reported data. Thus, tracer uptake may allow for prognostic stratification independent of the therapeutic situation (primary vs. recurrent tumor). However, determination of a fixed tracer uptake cutoff for prognostication is difficult, as tracer uptake not only is dependent on the tumor itself but also reflects the imaging protocol used. It is also biased by previous therapies, as shown in our analyses, and the prognosis is obviously dependent on antitumor treatment and patient-related factors as well.

In our study, analyses of tracer uptake were based on SUVmax. We also calculated SURmax values, which are the SUVmax values corrected for the appropriate SUV background signal (26), and we observed a high concordance between both metrics. Thus, more complex background-adjusted metrics are not necessarily required.

Finally, using WBT profiling of a subset of the rHGG cohort, we found gene expression differences associated with SUVmax, adjusted for initial tumor grade (stable initial grade WBT signature as recently reported (23)). Among them were genes involved in DNA repair (ATM and POLD4). Pathway activity analysis showed an association of unfavorable pathways with higher SUVmax values (TGFbeta and hypoxia) (9, 42), and inferred monocyte/macrophage fractions were enriched in high SUVmax tumors. In addition, immune checkpoint gene expression showed differential regulation, especially CTLA4 (low expression in high SUVmax tumors). This supports the hypothesis of glioma as a systemic disease, with a pronounced exchange between the tumor and its environment (39).

The main limitation of the present study is the limited number of patients, especially for the whole-blood transcriptome analyses. Here, further independent studies including larger cohorts should be performed to validate our findings. Technical differences (different scanners), missing data, and (molecular) heterogeneity within the group of recurrent high-grade glioma might affect the present results. In addition, dynamic 18F-FET PET might reveal additional insights into tumor metabolism.

Conclusion

18F-FET PET has a prognostic value in both treatment-naïve glioblastoma and recurrent high-grade glioma. Its value on target volume definition remains less clear, with overall low concordance between 18F-FET-PET and target volumes. High metabolic activity, as quantified by SUVmax, is linked to worse prognosis and unfavorable whole-blood transcriptome liquid biopsy readouts. Our results warrant confirmation in larger, prospective studies.

Data availability statement

The raw data supporting the conclusions of this article will be made available by the authors, without undue reservation.

Ethics statement

This study was reviewed and approved by IRB-Ethics Committee of the Medical Faculty of Heidelberg University (approval number S-421/2015 and S-540/2010). The patients/participants provided their written informed consent to participate in this study.

Author contributions

Conceptualization and methodology: MW, MR, JF, PS, JD, UH, MK, LK, CD, AG, AK, MD, UW, CH-M, SC, AA. Formal analysis: MW, MK. Investigation: MW, MK, CS, UW. Writing - original draft: MW, BT, AG, MK, AA. All authors contributed to the article and approved the submitted version.

Funding

This research was funded by the German Research Foundation Collaborative Research Center (DFG, SFB 1389, Unite, Project-ID 404521405), EU Predict, and intramural funds of the National Center for Tumor Diseases (NCT).

Conflict of interest

The authors declare that the research was conducted in the absence of any commercial or financial relationships that could be construed as a potential conflict of interest.

Publisher's note

All claims expressed in this article are solely those of the authors and do not necessarily represent those of their affiliated organizations, or those of the publisher, the editors and the reviewers. Any product that may be evaluated in this article, or claim that may be made by its manufacturer, is not guaranteed or endorsed by the publisher.

Supplementary Material

The Supplementary Material for this article can be found online at: https://www.frontiersin.org/articles/10.3389/fonc.2022.901390/full#supplementary-material

References

1. Gorlia T, van den Bent MJ, Hegi ME, Mirimanoff RO, Weller M, Cairncross JG, et al. Nomograms for predicting survival of patients with newly diagnosed glioblastoma: prognostic factor analysis of EORTC and NCIC trial 26981-22981/CE.3. *Lancet Oncol* (2008) 9(1):29–38. doi: 10.1016/s1470-2045(07)70384-4

2. Niyazi M, Adeberg S, Kaul D, Boulesteix AL, Bougatf N, Fleischmann DF, et al. Independent validation of a new reirradiation risk score (RRRS) for glioma patients predicting post-recurrence survival: A multicenter DKTK/ROG analysis. *Radiother Oncol* (2018) 127(1):121–7. doi: 10.1016/j.radonc.2018.01.011

3. Stupp R, Mason WP, van den Bent MJ, Weller M, Fisher B, Taphoorn MJ, et al. Radiotherapy plus concomitant and adjuvant temozolomide for glioblastoma. *N Engl J Med* (2005) 352(10):987–96. doi: 10.1056/NEJMoa043330

4. Stupp R, Taillibert S, Kanner A, Read W, Steinberg D, Lhermitte B, et al. Effect of tumor-treating fields plus maintenance temozolomide vs maintenance temozolomide alone on survival in patients with glioblastoma: A randomized clinical trial. *JAMA* (2017) 318(23):2306–16. doi: 10.1001/jama.2017.18718

5. Kazmi F, Soon YY, Leong YH, Koh WY, Vellayappan B. Re-irradiation for recurrent glioblastoma (GBM): a systematic review and meta-analysis. *J Neurooncol* (2019) 142(1):79–90. doi: 10.1007/s11060-018-03064-0

6. Wick W, Gorlia T, Bendszus M, Taphoorn M, Sahm F, Harting I, et al. Lomustine and bevacizumab in progressive glioblastoma. *N Engl J Med* (2017) 377 (20):1954–63. doi: 10.1056/NEJMoa1707358

7. Durante M, Debus J. Heavy charged particles: Does improved precision and higher biological effectiveness translate to better outcome in patients? *Semin Radiat Oncol* (2018) 28(2):160–7. doi: 10.1016/j.semradonc.2017.11.004

8. Chiblak S, Tang Z, Campos B, Gal Z, Unterberg A, Debus J, et al. Radiosensitivity of patient-derived glioma stem cell 3-dimensional cultures to photon, proton, and carbon irradiation. *Int J Radiat Oncol Biol Phys* (2016) 95 (1):112–9. doi: 10.1016/j.ijrobp.2015.06.015

9. Chiblak S, Tang Z, Lemke D, Knoll M, Dokic I, Warta R, et al. Carbon irradiation overcomes glioma radioresistance by eradicating stem cells and forming an antiangiogenic and immunopermissive niche. *JCI Insight* (2019) 4(2). doi: 10.1172/jci.insight.123837

10. Combs SE, Burkholder I, Edler L, Rieken S, Habermehl D, Jakel O, et al. Randomised phase I/II study to evaluate carbon ion radiotherapy versus fractionated stereotactic radiotherapy in patients with recurrent or progressive gliomas: the CINDERELLA trial. *BMC Cancer* (2010) 10:533. doi: 10.1186/1471-2407-10-533

11. Adeberg S, Bernhardt D, Harrabi SB, Uhl M, Paul A, Bougatf N, et al. Sequential proton boost after standard chemoradiation for high-grade glioma. *Radiother Oncol* (2017) 125(2):266–72. doi: 10.1016/j.radonc.2017.09.040

12. Knoll M, Waltenberger M, Bougatf N, Bernhard D, Adeberg S, Budach V, et al. Efficacy of re-irradiation with carbon ions (RiCi) in patients with recurrent high-grade glioma (rHGG) compared to the standard re-irradiation with photons (RiP): The reference multicenter cohort of the German cancer consortium radiation oncology group (DKTK-ROG). *J Clin Oncol* (2019) 37:2057. doi: 10.1200/JCO.2019.37.15_suppl.2057

13. Malouff TD, Peterson JL, Mahajan A, Trifiletti DM. Carbon ion radiotherapy in the treatment of gliomas: a review. *J Neurooncol* (2019) 145 (2):191–9. doi: 10.1007/s11060-019-03303-y

14. Grosu AL, Astner ST, Riedel E, Nieder C, Wiedenmann N, Heinemann F, et al. An interindividual comparison of O-(2-[18F]fluoroethyl)-L-tyrosine (FET)- and l-[methyl-11C]methionine (MET)-PET in patients with brain gliomas and metastases. *Int J Radiat Oncol Biol Phys* (2011) 81(4):1049–58. doi: 10.1016/j.ijrobp.2010.07.002

15. Grosu AL, Weber WA, Riedel E, Jeremic B, Nieder C, Franz M, et al. L-(methyl-11C) methionine positron emission tomography for target delineation in resected high-grade gliomas before radiotherapy. *Int J Radiat Oncol Biol Phys* (2005) 63(1):64–74. doi: 10.1016/j.ijrobp.2005.01.045

16. Arbizu J, Tejada S, Marti-Climent JM, Diez-Valle R, Prieto E, Quincoces G, et al. Quantitative volumetric analysis of gliomas with sequential MRI and ^{11}C-methionine PET assessment: patterns of integration in therapy planning. *Eur J Nucl Med Mol Imaging* (2012) 39(5):771–81. doi: 10.1007/s00259-011-2049-9

17. Albert NL, Weller M, Suchorska B, Galldiks N, Soffietti R, Kim MM, et al. Response assessment in neuro-oncology working group and European association for neuro-oncology recommendations for the clinical use of PET imaging in gliomas. *Neuro Oncol* (2016) 18(9):1199–208. doi: 10.1093/neuonc/now058

18. Debus C, Waltenberger M, Floca R, Afshar-Oromieh A, Bougatf N, Adeberg S, et al. Impact of (18)F-FET PET on target volume definition and tumor progression of recurrent high grade glioma treated with carbon-ion radiotherapy. *Sci Rep* (2018) 8(1):7201. doi: 10.1038/s41598-018-25350-7

19. Oehlke O, Mix M, Graf E, Schimek-Jasch T, Nestle U, Götz I, et al. Amino-acid PET versus MRI guided re-irradiation in patients with recurrent glioblastoma multiforme (GLIAA) - protocol of a randomized phase II trial (NOA 10/ARO 2013-1). *BMC Cancer* (2016) 16(1):769. doi: 10.1186/s12885-016-2806-z

20. Sweeney R, Polat B, Samnick S, Reiners C, Flentje M, Verburg FA. O-(2-[(18)F]fluoroethyl)-L-tyrosine uptake is an independent prognostic determinant in patients with glioma referred for radiation therapy. *Ann Nucl Med* (2014) 28 (2):154–62. doi: 10.1007/s12149-013-0792-7

21. Liangos O, Domhan S, Schwager C, Zeier M, Huber PE, Addabbo F, et al. Whole blood transcriptomics in cardiac surgery identifies a gene regulatory network connecting ischemia reperfusion with systemic inflammation. *PloS One* (2010) 5(10):e13658. doi: 10.1371/journal.pone.0013658

22. Zabel-du Bois A, Wagner-Ecker M, Milker-Zabel S, Schwager C, Wirkner U, Debus J, et al. Gene expression signatures in the peripheral blood after radiosurgery of human cerebral arteriovenous malformations. *Strahlenther Onkol* (2010) 186 (2):91–8. doi: 10.1007/s00066-010-2034-4

23. Knoll M, Waltenberger M, Furkel J, Wirkner U, Gahlawat AW, Dokic I, et al. Whole blood transcriptional fingerprints of high-grade glioma and longitudinal tumor evolution under carbon ion radiotherapy. *Cancers (Basel)* (2022) 14(3):684. doi: 10.3390/cancers14030684

24. Combs SE, Kieser M, Rieken S, Habermehl D, Jäkel O, Haberer T, et al. Randomized phase II study evaluating a carbon ion boost applied after combined radiochemotherapy with temozolomide versus a proton boost after radiochemotherapy with temozolomide in patients with primary glioblastoma: the CLEOPATRA trial. *BMC Cancer* (2010) 10:478. doi: 10.1186/1471-2407-10-478

25. Nolden M, Zelzer S, Seitel A, Wald D, Müller M, Franz AM, et al. The medical imaging interaction toolkit: challenges and advances: 10 years of open-source development. *Int J Comput Assist Radiol Surg* (2013) 8(4):607–20. doi: 10.1007/s11548-013-0840-8

26. Schober O, Heindel W. *PET-CT hybrid imaging*. Stuttgart, New York: Georg Thieme (2010).

27. Aran H. xCell: digitally portraying the tissue cellular heterogeneity landscape. *Genome Biol* (2017) 18(220). doi: 10.1186/s13059-017-1349-1

28. Schubert M, Klinger B, Klunemann M, Sieber A, Uhlitz F, Sauer S, et al. Perturbation-response genes reveal signaling footprints in cancer gene expression. *Nat Commun* (2018) 9(1):20. doi: 10.1038/s41467-017-02391-6

29. Kuleshov MV, Jones MR, Rouillard AD, Fernandez NF, Duan Q, Wang Z, et al. 'Enrichr: A comprehensive gene set enrichment analysis web server 2016 update.' *Nucleic Acids Res*. (2016) 44(Web Server issue):W90–W97. doi: 10.1093/nar/gkw377 (see https://cran.r-project.org/web/packages/enrichR/vignettes/enrichR.html)

30. Core Team R. *R: A language and environment for statistical computing* (2018). Vienna, Austria: R Foundataion for Statistical Computing. Available at: https://www.R-project.org/ (Accessed 2021-09-13).

31. Therneau T, Grambsch P. *Modeling survival data: Extending the cox model*. Springer, New York (2000).

32. Knoll M. dataAnalysisMisc: Collection of functions for daily tasks. In: *R package version 0.99.11* (2020). Available at: http://github.com/mknoll/dataAnalysisMisc.

33. Konietschke F, Friedrich S, Brunner E, Pauly M. *rankFD: Rank-based tests for general factorial designs* (2020). Available at: https://CRAN.R-project.org/package=rankFD (Accessed 2021-09-13).

34. Maechler M, Rousseeuw P, Croux C, Todorov V, Ruckstuhl A, Salibian-Barrera M, et al. *Robustbase: Basic robust statistics r package version 0.93-* (2021). Available at: http://CRAN.R-project.org/package=robustbase (Accessed 2021-12-06).

35. Liaw A, Wiener M. Classification and regression by randomForest. *R News* (2002) 2(3):18–22.

36. Louis DN, Ohgaki H, Wiestler OD, Cavenee WK, Burger PC, Jouvet A, et al. The 2007 WHO classification of tumours of the central nervous system. *Acta Neuropathol* (2007) 114(2):97–109. doi: 10.1007/s00401-007-0243-4

37. Louis DN, Perry A, Reifenberger G, von Deimling A, Figarella-Branger D, Cavenee WK, et al. The 2016 world health organization classification of tumors of the central nervous system: a summary. *Acta Neuropathol* (2016) 131(6):803–20. doi: 10.1007/s00401-016-1545-1

38. Rieken S, Habermehl D, Haberer T, Jaekel O, Debus J, Combs SE. Proton and carbon ion radiotherapy for primary brain tumors delivered with active raster scanning at the Heidelberg ion therapy center (HIT): early treatment results and study concepts. *Radiat Oncol* (2012) 7:41. doi: 10.1186/1748-717x-7-41

39. Debus J, Abdollahi A. For the next trick: new discoveries in radiobiology applied to glioblastoma. *Am Soc Clin Oncol Educ Book* (2014):e95-99. doi: 10.14694/EdBook_AM.2014.34.e95

40. Gempt J, Bette S, Ryang YM, Buchmann N, Peschke P, Pyka T, et al. 18F-fluoro-ethyl-tyrosine positron emission tomography for grading and estimation of prognosis in patients with intracranial gliomas. *Eur J Radiol* (2015) 84(5):955–62. doi: 10.1016/j.ejrad.2015.01.022

41. Katsanos AH, Alexiou GA, Fotopoulos AD, Jabbour P, Kyritsis AP, Sioka C. Performance of 18F-FDG, 11C-methionine, and 18F-FET PET for glioma grading: A meta-analysis. *Clin Nucl Med* (2019) 44(11):864–9. doi: 10.1097/rlu.0000000000002654

42. Lan Y, Moustafa M, Knoll M, Xu C, Furkel J, Lazorchak A, et al. Simultaneous targeting of TGF-β/PD-L1 synergizes with radiotherapy by reprogramming the tumor microenvironment to overcome immune evasion. *Cancer Cell* (2021) 39(10):1388–1403.e1310. doi: 10.1016/j.ccell.2021.08.008

frontiers | Frontiers in Oncology

TYPE Original Research
PUBLISHED 26 September 2022
DOI 10.3389/fonc.2022.929949

OPEN ACCESS

EDITED BY
Lanchun Lu,
The Ohio State University,
United States

REVIEWED BY
Peter Dendooven,
University of Groningen, Netherlands
Fernando Hueso-González,
University of Valencia, Spain

*CORRESPONDENCE
Aafke Christine Kraan
aafke@pi.infn.it

SPECIALTY SECTION
This article was submitted to Cancer Imaging and Image-directed Interventions, a section of the journal Frontiers in Oncology

RECEIVED 27 April 2022
ACCEPTED 20 June 2022
PUBLISHED 26 September 2022

CITATION
Moglioni M, Kraan AC, Baroni G, Battistoni G, Belcari N, Berti A, Carra P, Cerello P, Ciocca M, De Gregorio A, De Simoni M, Del Sarto D, Donetti M, Dong Y, Embriaco A, Fantacci ME, Ferrero V, Fiorina E, Fischetti M, Franciosini G, Giraudo G, Laruina F, Maestri D, Magi M, Magro G, Malekzadeh E, Marafini M, Mattei I, Mazzoni E, Mereu P, Mirandola A, Morrocchi M, Muraro S, Orlandi E, Patera V, Pennazio F, Pullia M, Retico A, Rivetti A, Da Rocha Rolo MD, Rosso V, Sarti A, Schiavi A, Sciubba A, Sportelli G, Tampellini S, Toppi M, Traini G, Trigilio A, Valle SM, Valvo F, Vischioni B, Vitolo V, Wheadon R and Bisogni MG (2022) *In-vivo* range verification analysis with in-beam PET data for patients treated with proton therapy at CNAO.
Front. Oncol. 12:929949.
doi: 10.3389/fonc.2022.929949

In-vivo range verification analysis with in-beam PET data for patients treated with proton therapy at CNAO

Martina Moglioni[1,2], Aafke Christine Kraan[1*], Guido Baroni[3,4], Giuseppe Battistoni[5], Nicola Belcari[1,2], Andrea Berti[1,2,6], Pietro Carra[1,2], Piergiorgio Cerello[7], Mario Ciocca[3], Angelica De Gregorio[8,9], Micol De Simoni[8,9], Damiano Del Sarto[1,2], Marco Donetti[3], Yunsheng Dong[5,10], Alessia Embriaco[11], Maria Evelina Fantacci[1,2], Veronica Ferrero[7], Elisa Fiorina[3,7], Marta Fischetti[9,12], Gaia Franciosini[8,9], Giuseppe Giraudo[7], Francesco Laruina[1,2], Davide Maestri[3], Marco Magi[12], Giuseppe Magro[3], Etesam Malekzadeh[3,13], Michela Marafini[9,14], Ilaria Mattei[5], Enrico Mazzoni[1], Paolo Mereu[7], Alfredo Mirandola[3], Matteo Morrocchi[1,2], Silvia Muraro[5], Ester Orlandi[3], Vincenzo Patera[9,12], Francesco Pennazio[7], Marco Pullia[3], Alessandra Retico[1], Angelo Rivetti[7], Manuel Dionisio Da Rocha Rolo[7], Valeria Rosso[1,2], Alessio Sarti[9,12], Angelo Schiavi[9,12], Adalberto Sciubba[12,15], Giancarlo Sportelli[1,2], Sara Tampellini[3], Marco Toppi[12,15], Giacomo Traini[9,14], Antonio Trigilio[8,9], Serena Marta Valle[5], Francesca Valvo[3], Barbara Vischioni[3], Viviana Vitolo[3], Richard Wheadon[7] and Maria Giuseppina Bisogni[1,2]

[1]Istituto Nazionale di Fisica Nucleare, Sezione di Pisa, Pisa, Italy, [2]Dipartimento di Fisica, Università di Pisa, Pisa, Italy, [3]Centro Nazionale di Adroterapia Oncologica, Pavia, Italy, [4]Politecnico di Milano, Milano, Italy, [5]Istituto Nazionale di Fisica Nucleare, Sezione di Milano, Milano, Italy, [6]Istituto di Scienza e Tecnologie dell'Informazione, Consiglio Nazionale delle Ricerche, Pisa, Italy, [7]Istituto Nazionale di Fisica Nucleare, Sezione di Torino, Torino, Italy, [8]Dipartimento di Fisica, Sapienza Università di Roma, Roma, Italy, [9]Istituto Nazionale di Fisica Nucleare, Sezione di Roma, Roma, Italy, [10]Dipartimento di Fisica, Università di Milano, Milano, Italy, [11]Istituto Nazionale di Fisica Nucleare, Sezione di Pavia, Pavia, Italy, [12]Dipartimento di Scienze di Base e Applicate per l'Ingegneria, Sapienza Universit `a di Roma, Roma, Italy, [13]Department of Medical Physics, Tarbiat Modares University, Teheran, Iran, [14]Museo Storico della Fisica e Centro Studi e Ricerche "E. Fermi", Roma, Italy, [15]Istituto Nazionale di Fisica Nucleare, Sezione dei Laboratori di Frascati, Frascati, Italy

Morphological changes that may arise through a treatment course are probably one of the most significant sources of range uncertainty in proton therapy. Non-invasive *in-vivo* treatment monitoring is useful to increase treatment quality. The INSIDE in-beam Positron Emission Tomography (PET) scanner performs *in-vivo* range monitoring in proton and carbon therapy treatments at the National Center of Oncological Hadrontherapy (CNAO). It is currently in a clinical trial (ID:

NCT03662373) and has acquired in-beam PET data during the treatment of various patients. In this work we analyze the in-beam PET (IB-PET) data of eight patients treated with proton therapy at CNAO. The goal of the analysis is twofold. First, we assess the level of experimental fluctuations in inter-fractional range differences (sensitivity) of the INSIDE PET system by studying patients without morphological changes. Second, we use the obtained results to see whether we can observe anomalously large range variations in patients where morphological changes have occurred. The sensitivity of the INSIDE IB-PET scanner was quantified as the standard deviation of the range difference distributions observed for six patients that did not show morphological changes. Inter-fractional range variations with respect to a reference distribution were estimated using the Most-Likely-Shift (MLS) method. To establish the efficacy of this method, we made a comparison with the Beam's Eye View (BEV) method. For patients showing no morphological changes in the control CT the average range variation standard deviation was found to be 2.5 mm with the MLS method and 2.3 mm with the BEV method. On the other hand, for patients where some small anatomical changes occurred, we found larger standard deviation values. In these patients we evaluated where anomalous range differences were found and compared them with the CT. We found that the identified regions were mostly in agreement with the morphological changes seen in the CT scan.

KEYWORDS

proton therapy, in-beam PET imaging, *in-vivo* treatment verification, morphological changes, inter-fractional range differences, clinical trial

1 Introduction

Proton therapy is a type of radiation therapy that uses protons to treat cancer. The advantage of proton therapy with respect to conventional radiotherapy (X-rays and electrons) is related to the characteristic depth dose profile of charged particles (Bragg peak) (1). The accuracy of proton therapy strongly depends on the determination of the Bragg peak position. Uncertainties in the knowledge of the proton range can affect the dose distribution. These uncertainties include anatomical changes (physiological or morphological, organ motion, tumour regression, weight loss arising during the course of treatment), patient setup uncertainties, and range errors from uncertainties in CT Hounsfield units (HU), conversion of HU into particle stopping power, and reconstruction artifacts (2–6). In patients where anatomical changes are expected to occur, generally a control CT is acquired at some point during the treatment course (4–9). The scheduling of the control CT is variable and based on the clinical experience of the radiation oncologist. Based on the CT outcome, the radiation oncologist may decide for treatment replanning.

In-vivo range monitoring is desirable in order to support the radiation oncologist in the decision on when to perform a control CT (7, 10). One of the most consolidated monitoring techniques is Positron Emission Tomography (PET) (10–13). Nuclear interactions of the therapeutical beam with the tissue result in the production of β^+ -isotopes, which decay emitting a positron, that annihilates into a 511 keV photon pair. The detection of these photon pairs by means of a PET system yields an activity image, that is indirectly correlated with the dose. Of all PET data acquisition modalities, in-beam (IB) data acquisition is generally considered the most attractive, providing real-time information about the treatment (10, 14, 15).

INSIDE (16) (*INnovative Solution for In-beam Dosimetry in hadronthErapy*) is a bimodal imaging system installed at the National Center of Oncological Hadrontherapy (CNAO), in Pavia, Italy (17). It consists of a particle tracker called *Dose Profiler* (18) and an IB-PET scanner (16). This bimodal architecture allows for the detection of annihilation photons with a PET detector, as well as for the detection of charged particles, also produced as a result of nuclear interactions. Since 2019 INSIDE is under clinical trial. During this trial (ClinicalTrials.gov ID: NCT03662373), we acquired IB-PET data for eight patients that received proton therapy treatments, fractionated in 6 weeks (about 30 sessions) along the entire course of their treatment. The first phase of the trial was completed in March 2020.

The goal of this study is twofold. First, we wish to investigate the level of experimental fluctuations in inter-fractional range differences observed in the INSIDE system, which drives the

sensitivity to detect range differences. Such fluctuations can be due to the limited statistics of the acquired PET images, differences in irradiation and data acquisition conditions, PET cart setup errors, fluctuations due to random patient setup errors, and so on. This will be done by studying inter-fractional range shifts for patients that had no morphological changes, using the Most-Likely-Shift (MLS) from Frey et al. (19), where it was applied to offline PET data. To establish the efficacy of the MLS method for IB-PET images, we made a comparison with the Beam's Eye View method (20). Second, we will compare the results with patients that did show morphological changes, and we will investigate whether it is possible to identify the regions affected by the changes with the MLS method. It must be noted that this is the first study that includes all the available data of the patients treated with proton therapy and monitored with INSIDE. It is also the first time that the MLS method will be applied to IB-PET data.

2 Materials and methods

2.1 The INSIDE in-beam PET scanner

The design, construction and initial clinical tests of the INSIDE IB-PET system are described in detail in previous works (16, 21–24), and only the most relevant information is given here. The system consists of two planar heads placed at 30 cm from the isocenter, for a total distance between them of 60 cm. Each head has an active area of 10 × 25 cm^2 and consists of 2 × 5 modules produced by Hamamatsu Photonics (25). Each module is a square matrix of 16 × 16 scintillating crystals of lutetium fine silicate (LFS) (26), each with dimension 3 × 3 × 20 mm^3. Thus the total number of channels in one PET head is 2560. LFS is a commercial name of the set of Ce-doped silicate scintillation crystals (26, 27). The density (7.35 g/cm^3) and light yield (80% with respect to NaI:Tl) are comparable to lutetium oxyorthosilicate and LYSO but with improved time performance: it has a ~36-ns decay constant. These crystals are optically coupled one-to-one to silicon photomultipliers (SiPMs). Their temperature was maintained at 18°C with the help of an integrated cooling system.

The 2 × 2560 PET detector channels are read by front-end electronics (FE), based on 64 TOFPET ASICs channels (28), which gives the time stamp of the event encoded through a time-to-digital converter with a resolution of 50 ps. The energy information was obtained with the time over threshold (TOT) method. The signals from the FE ASICs are processed locally by Field Programmable Gate Array (FPGA) boards. The channel dead time is imposed by the FE and is below 300 ns for a 511 keV event (28). The energy resolution for 511 keV photons was ~13%, as measured with a β^+ source of ^{22}Na. The measured coincidence time resolution (sigma) was 450 ps. The acquisition is performed all along the treatment during both irradiation (spill) and beam pauses (inter-spill). However, in this analysis we have only used the data acquired during the inter-spill beam pauses, as well as data acquired a short time after the delivery of the field (see Section *Pre-processing*).

The 3D image reconstruction is performed on-the-fly with an iterative multicore Maximum Likelihood Expectation Maximization (MLEM) (29) algorithm, and its results are provided online during the treatment. Advanced analysis of the PET images is done offline (see Section *Analysis*). The reconstructed image FOV is 224 × 112 × 264 mm^3, with a voxel size of 1.6 × 1.6 × 1.6 mm^3. The IB-PET reference system is reported in Figure 1A, where the z axis is parallel to the beam direction. Figure 1B shows a PET image in the three main projections. Due to the partial angular coverage of the PET system, the images suffer from artefacts in the direction perpendicular to the planes (30), as well as from limited statistics [see also (31)].

2.2 Dose delivery at CNAO

At CNAO protons are delivered with a modulated pencil beam scanning technique in a fixed beam-line, while the patient couch can rotate. The Dose Delivery System (DDS) (32) guides and monitors the proton beams accelerated by the synchrotron, and distributes the dose with a full 3D scanning technique. The dose results from the superposition of a large number of beams conveyed to the tumour volume. The irradiated volume is divided into several energy layers (slices), each of which is irradiated by various overlapping iso-energetic beams (spots) arranged in a grid of 3 mm pitch. A typical proton therapy treatment has 20 to 30 fractions. Each treatment fraction is delivered through two or more fields, each consisting of many thousands of spots to cover the target. For more details about the beam specifications, scanning technique and the CNAO particle accelerator we refer to previously published works (17, 32).

The DDS provides a log-file in which the information about the actually delivered particles is stored, including the number of delivered primaries, energy and the lateral position of the spot. The information from this log-file was converted into a binary mask in the same reference frame and with the same voxel size as the PET images (see Figures 1A, B), in which the non-zero values define a volume-of-interest, where PET activity can be present. This volume-of-interest will be referred to as the expected activity mask. The dose delivery time for the patients was typically a few minutes. The temporal structure of the beam extraction was 1 s of spill, during which the protons are delivered, and 2 s of pause between spills (inter-spill periods). The INSIDE PET system is mounted on a cart that is positioned before data acquisition. The position accuracy is about 1 mm, thanks to a dedicated cart positioning system. The presence of

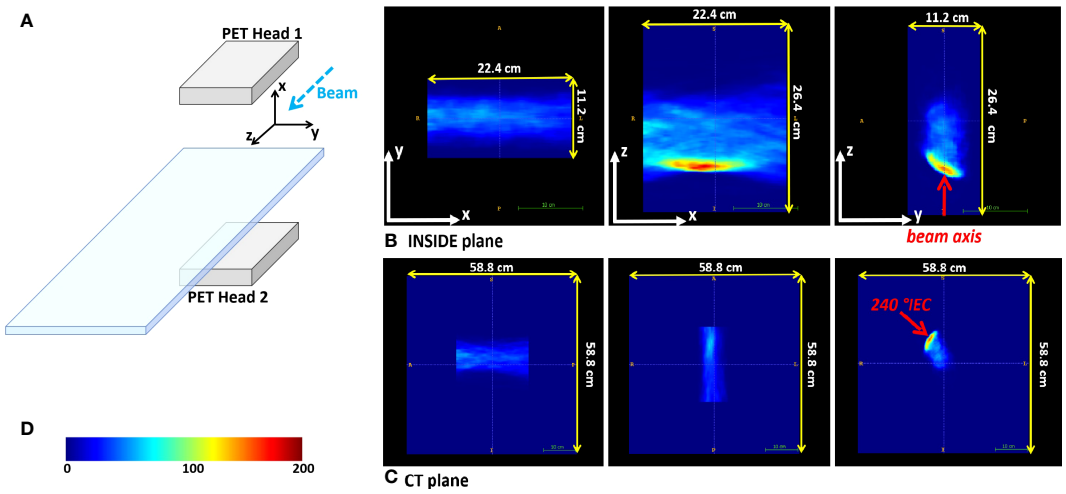

FIGURE 1
Reference frames. **(A)** Sketch of the INSIDE setup and reference frame. **(B)** Example of the three orthogonal projections of a reconstructed PET image for patient 002P (see 2.3). **(C)** The same reconstructed PET image in the CT reference frame. In **(B, C)** the beam axis is indicated with the red arrow. **(D)** The color-scale of the PET images

the cart has limited the number of patients that could be enrolled in the trial: it was only possible to monitor patients with beam angles without mechanical incompatibilities of the INSIDE setup with the patient couch movements.

2.3 Patient dataset

We analyzed the IB-PET data of the patients treated with protons. A patient treated with protons at the CNAO typically receives a total dose of 60 Gy divided into fractions of 2 Gy each.

Table 1 reports the patients analyzed, with the patient ID, the pathology, the number of fields N_{fields}, the number of treatment fractions delivered N_{frac}, the number of treatment fractions with PET data that could be included in the analysis, N_{PET}, the control CT outcome, as evaluated by the radiation oncologist, and the monitored treatment angle. The control CT is acquired approximately during the third week from the start of treatment. Two of the monitored patients (006P and 007P) showed morphological changes, nevertheless, they were not replanned because the treatment plan quality was still deemed acceptable. In this work we used the PET data for each patient in Table 1, that were acquired during the first field delivered. In this way contamination of the activity from the other fields was avoided. The choice of the field was made by clinical personnel.

Figure 2 reports the planning CT scan (upper row) and the control CT (lower row) of patient 006P. Figure 3 reports the same for patient 007P. In this case there are two anatomical modifications: a mild emptying in the GTV for a possible tumor response and also some inflammation reaction (mucositis) in the CTV within the nasal cavity.

TABLE 1 Patients treated with protons analyzed in this work, with patient ID, pathology, number of fields, number of fractions delivered, number of fractions monitored, the control CT outcome, as evaluated by the radiation oncologist, and the monitored treatment angle.

Patient ID	Pathology	N_{fields}	N_{frac}	N_{PET}	Control CT outcome	Monitored angle [°IEC]
002P	Meningioma	2	30	12	unchanged	240
003P	Meningioma	2	27	9	unchanged	235
004P	Meningioma	2	31	8	unchanged	245
005P	Chordoma	2	27	10	unchanged	5
006P	Adenoid Cystic Carcinoma	2	35	10	changed	175
007P	Adenoid Cystic Carcinoma	3	33	5	changed	270
008P	Adenoid Cystic Carcinoma	3	33	11	unchanged	0
009P	Chondrosarcoma	3	27	10	unchanged	0

2.4 Pre-processing

In this work we used the IB-PET data acquired over the time-interval from the start of irradiation until 10 seconds after the end of the irradiation, whereby during irradiation only the inter-spill data were used. Although at the CNAO synchrotron the exact number of spills used for a given treatment is quite stable, small variations are possible from day-to-day, depending on the accelerator conditions. Therefore the reconstructed activity can depend on the beam conditions. For the same total dose delivered, the induced activity can change somewhat if the dose delivery time is different. An example of this is shown in Figure 4, where two reconstructed PET images acquired in two different days are displayed. Here the total delivered dose was the same, but the dose delivery and acquisition times were different. These differences cannot be simply corrected by normalizing, because the PET signal is time dependent. Therefore we used only those fractions with similar temporal profiles in the analysis. The number of such fractions is given in the fifth column of Table 1.

To reduce salt-and-pepper noise in the images we applied a 5 mm radius median filter. According to the couch angle, the PET images could be rotated into the CT imaging coordinate system expressed in International Electrotechnical Commission (IEC) standard. Figure 1C gives an example of a rotated image.

2.5 Analysis

The analysis was divided into two parts. First, we wished to investigate the level of experimental fluctuations in inter-fractional range differences observed by the INSIDE system, referred to as sensitivity. This was done by studying inter-fractional range shifts for patients that had no morphological changes (see Table 1). Second, we compared these results with patients that did show morphological changes. For the latter patients, we also verified whether the region of the observed range differences is correlated to the presence of real morphological changes in the CT scan.

The strategy that we followed for the analysis is based on an interfractional comparison between a reference PET image and

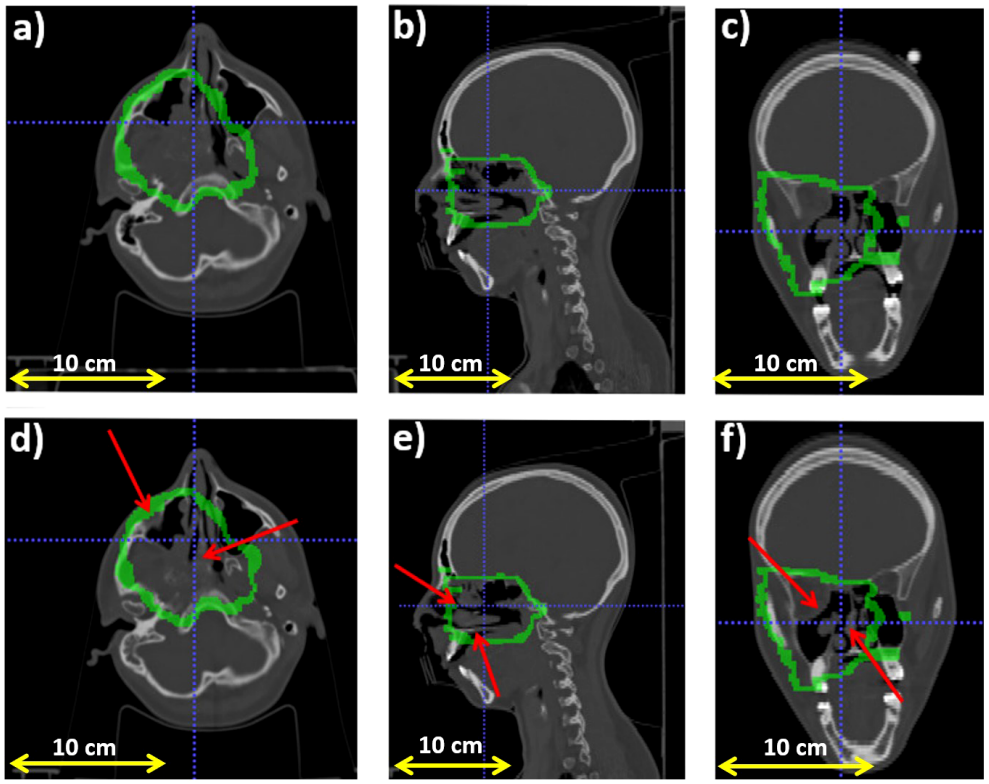

FIGURE 2
Planning CT (upper row) and control CT (lower row) for patient 006P. **(A)** Axial, **(B)** sagittal and **(C)** coronal views for the planning CT, and **(D)** Axial, **(E)** sagittal and **(F)** coronal views for the control CT. The morphological change is highlighted with a red arrow. Also, the CTV (Clinical Target Volume) area is highlighted with a green line.

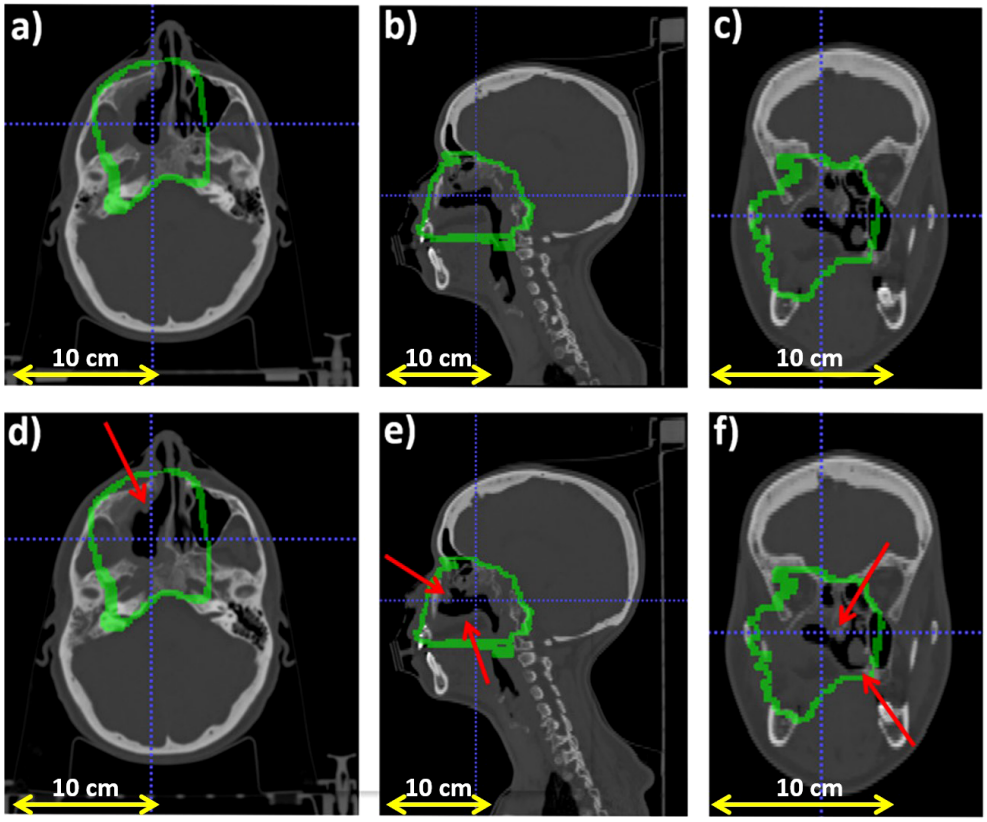

FIGURE 3
Planning CT (upper row) and control CT (lower row) for patient 007P. **(A)** Axial, **(B)** sagittal and **(C)** coronal views for the planning CT, and **(D)** Axial, **(E)** sagittal and **(F)** coronal views for the control CT. The morphological change is highlighted with a red arrows and the CTV (Clinical Target Volume) area is highlighted with a green line.

an image acquired during a subsequent fraction *j*. In order to mitigate statistical fluctuations, the reference image was calculated as the average of the first two monitored fractions.

2.5.1 Most-Likely-Shift method

To compare the PET images of the subsequently monitored fractions with the reference image, we used the Most-Likely-Shift method, originally proposed by Frey et al. for off-line PET monitoring images (19) and recently applied also in (33). This is the first time that the MLS method was applied to IB-PET images. Given that such images suffer from artifacts due to the partial angular coverage and limited (see Figure 1), it is not a-priori obvious whether the MLS method works.

In summary, given a PET image of a monitored fraction *j*, for each pair of coordinates (*x,y*) in the transverse plane (in the INSIDE reference system), we compared the 1-D activity profile along the beam direction *z* in their distal fall-off with the corresponding reference profile.The MLS method considers profiles belonging to two different treatment fractions for the same pair of coordinates in the transverse plane (*x,y*) and calculates the most probable shift necessary to align these two profiles, normalised at their maximum, along the beam direction. We included only those (*x,y*) pairs into the analysis that were part of the expected activity mask. Moreover, to exclude profiles with low activity from the analysis, we included here only those profiles with an integrated activity of at least 30% of the profile with highest integrated activity. The reader is referred to the original paper by Frey et al. (19) for a detailed description of the MLS method.

We applied the method exactly as described in Frey et al., with three exceptions. First, the value for $z_{min}(x,y)$ (the *z*-value of that activity profile where to start the analysis) was set at 15% of the maximum of the normalized reference profile at coordinates *x,y*. Second, $z_{max}(x,y)$, i.e., the *z*-value where to end the analysis, was set at 2% of the maximum of the normalized reference profile. These modifications were done in order to focus more on the distal fall-off part of the profiles. Third, the shift value δ was limited between -16 and 16 mm, with steps of 1 mm. An algorithm was implemented that provided for each *x,y* pair the optimal shift distance δ_{MLS}. The calculation of the range difference δR_{MLS} is done by minimizing the absolute profile differences in the distal part ($z_{MLS} \leq z \leq z_{max}$) of two activity depth profiles, shifted against each other, as follows (19, 34):

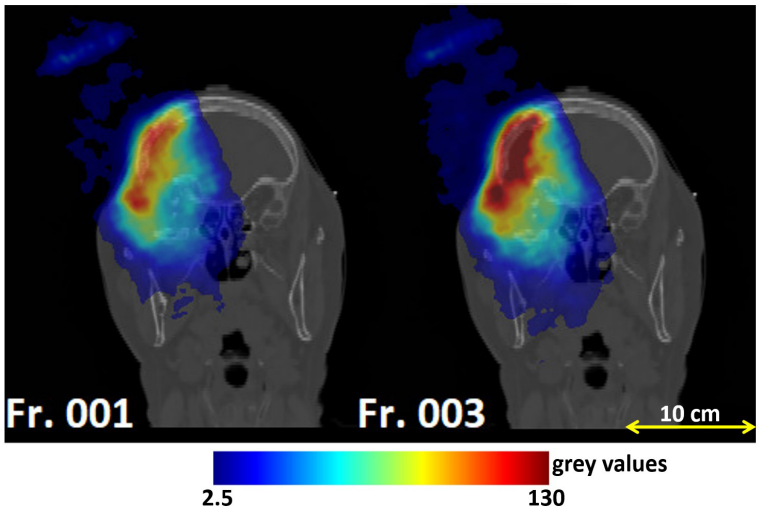

FIGURE 4
Coronal views of the planning CT of patient 004P: reconstructed PET images corresponding to the monitored fractions 1 and 3. The left and right image had different dose delivery and acquisition times, resulting in different activities. Fraction 3 had to be excluded because of the larger activity compared to the other fractions.

$$\delta R_{MLS} = \arg \min_{\delta_{MLS}} \left(\sum_{z_{MLS}}^{z_{max}} \left| A_{ref}(z) - A_j(z - \delta_{MLS}) \right| \right) \quad (1)$$

with A_{ref} and A_j corresponding to the reference activity profile and that of the fraction to be compared, respectively.

Then, a distribution of all the $\delta R_{MLS}(x,y)$values was created for each fraction j. These distributions were fitted with an asymmetric skew-normal distribution and its mean, μ_{MLS} , and standard deviation, σ_{MLS} , were evaluated for all monitored fractions j of a given patient. For each patient, we then evaluated:

- the average of μ_{MLS} over all the fractions. This average is denoted by Δ_{MLS}, giving an indication of the size of typical inter-fractional range shifts between the reference image and the subsequent fractions for this patient;
- the average of σ_{MLS} over all the fractions, indicated by Σ_{MLS}, giving an indication of the fluctuations in such shifts for a given patient.

Then, to investigate the level of fluctuations in our PET data in absence of any morphological changes, we extracted for the six patients without any morphological changes the average of Σ_{MLS} over these six patients, yielding $\langle \sigma_{MLS} \rangle$. Such inter-fractional range fluctuations are accidental and can be due to the low statistics of the images, patient setup-errors, INSIDE cart setup errors, small differences in irradiation conditions, and so on.

Then, for each patient and each analyzed fraction, a three-dimensional outliers map $O_{MLS}(x,y,z)$ of anomalously large shifts was created in order to visualise the largest range difference obtained. The map $O_{MLS}(x,y,z)$ was filled for each voxel with coordinate x,y,z, which had $z \leq z_{min}$ as:

$$\begin{cases} O_{\mathrm{MLS}}(x,y,z) = \delta R_{\mathrm{MLS}}(x,y), \text{if } \delta R_{\mathrm{MLS}}(x,y) \leq -2 \cdot \langle \sigma_{MLS} \rangle \\ \text{or} \quad \text{if} \quad \delta R_{\mathrm{MLS}}(x,y) \geq +2 \cdot \langle \sigma_{MLS} \rangle \\ O_{\mathrm{MLS}}(x,y,z) = 0 \quad \text{otherwise} \end{cases} \quad (2)$$

For $z > z_{min}$ (close to the end of range), $O_{\mathrm{MLS}}(x,y,z) = 0$. Thus, the outliers maps are represented as 3-dimensional distributions, but each point along the z-axis was filled by copying $\delta R_{MLS}(x,y)$ from z=0 up to $z = z_{min}$. These maps graphically identify the position of the distal fall-off part of the activity distribution, and they highlight the entire region along a pencil beam path that is possibly affected by a range shift with respect to the reference. These maps were re-oriented on the patient's CT refersence frame, in order to verify if the real morphological change seen in the CT was identified.

The implementation was validated as in (19), i.e., by creating artificially shifted PET distributions and verifying that the MLS analysis correctly identified the introduced shift.

2.5.2 Comparison with Beam's Eye View method

To confirm the validity of the Most-Likely-Shift method for our PET images, we compared the result with another existing range verification method that performs interfractional comparisons based on 1-D activity profiles: the Beam Eye View method. Details can be found elsewhere (20, 22, 35). This method is based on a multi-threshold approach to extract

iso-activity surfaces. Thresholds from 2% up to 8% on the maximum of the entire PET image at 0.5% steps were considered. Briefly summarizing, similar to the MLS method, for each pair of coordinates x,y in the transverse plane (in the INSIDE reference system), the profile belonging to treatment fraction j was compared with the profile of the reference image A_{ref}. For a given threshold t, the shift between these two profiles, $\delta R_{\mathrm{BEV,t}}(x,y)$, was defined to be the difference between the maximum depth value reached at threshold for the reference profile, $R_t^{ref}(x,y)$ and that for a monitored fraction, $R_t^j(x,y)$. To obtain the final value of the range difference between the profiles at a given x,y point, $\delta R_{\mathrm{BEV}}(x,y)$, the average was taken over the thresholds. In other words:

$$\delta R_{\mathrm{BEV}}(x,y) = \frac{1}{N}\sum_{t=1}^{N}\delta R_{\mathrm{BEV,t}}(x,y) = \frac{1}{N}\sum_{t=1}^{N}\left(R_t^{ref}(x,y) - R_t^j(x,y)\right) \tag{3}$$

where N is the total number of thresholds considered, which was 13 in our case.

The remaining procedure is exactly as done for the MLS method. For each patient a distribution, containing all the $\delta R_{\mathrm{BEV}}(x,y)$ value, was created for each fraction j. These were fitted with an asymmetric skew-normal distribution, yielding the mean μ_{BEV} and standard deviation σ_{BEV} , for each monitored fraction j. For each patient we then extracted:

- the average of μ_{BEV} over all the fractions, denoted by Δ_{BEV}.
- the average of σ_{BEV} over all the fractions, indicated by Σ_{BEV}.

We extracted for the six patients without any morphological changes the average of Σ_{BEV}, yielding $<\sigma_{BEV}>$.

For each patient and each analyzed fraction, a three-dimensional outliers map O_{BEV} (x, y, z) was created, whose interpretation is the same as for the MLS maps. For each voxel (x,y,z), the map was filled when $z \le R_t^j(x,y)$, with t=8%, as:

$$\begin{cases} O_{\mathrm{BEV}}(x,y,z) = \delta R_{\mathrm{BEV}}(x,y) & \text{if } \delta R_{\mathrm{BEV}}(x,y) \le -2\cdot<\sigma_{BEV}> \text{ or if} \\ \delta R_{\mathrm{BEV}}(x,y) \ge +2\cdot<\sigma_{BEV}> & \\ O_{\mathrm{BEV}}(x,y,z) = 0 & \text{otherwise} \end{cases} \tag{4}$$

For $z > R_t^j(x,y)$, with t=8%, we put $O_{BEV}(x,y,z) = 0$. Then the $O_{BEV}(x,y,z)$ maps were superimposed to the CT images, so that they could be compared with the $O_{MLS}(x,y,z)$ maps as well as with the CT.

The BEV implementation was validated by creating artificially shifted distributions, and verifying that the analysis correctly identified the shift.

3 Results

In Figure 5A we show an example of a distribution of range differences δR_{MLS} with , respect to the reference for a few of the available fractions in a patient that does not change (005P). Each histogram entry represents a value of $\delta R(x,y)$. The same is given for the BEV method in Figure 5B.

Figure 6A gives the interfractional standard deviation σ_{MLS} for each patient with MLS method as a function of the fraction compared with the reference. Squares and triangles stand for the standard deviation obtained for the set of unchanged and changed patients, respectively. For the patients that do not change (squares), we observe that the values for σ_{MLS} are somewhat lower than 3 mm, the spatial resolution of the INSIDE PET scanner (16). Moreover, we see for these patients that the standard deviation is roughly

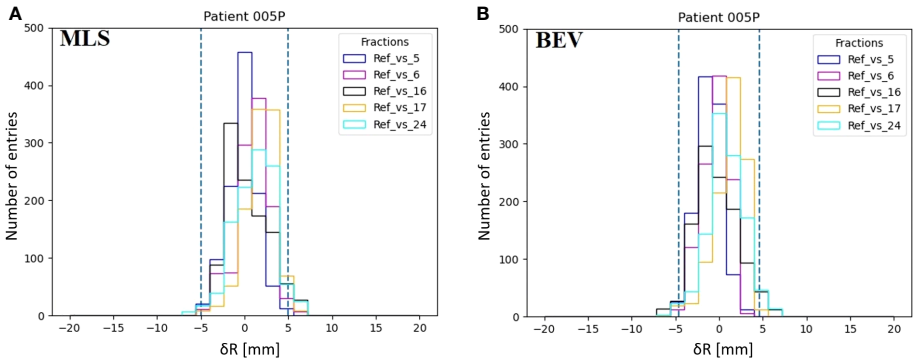

FIGURE 5
Examples of the distributions of inter-fractional range differences $\delta R(x,y)$ of various fractions with respect to the reference (M) in patient 005P for the MLS method **(A)** and the BEV method **(B)**. The dashed lines represent the 95% confidence interval tailored for, the MLS (5.0 mm) and the BEV method (4.6 mm) as 2<σ>.

constant during the course of the treatment. For patients subject to morphological changes (triangles), the standard deviation values mostly exceed 3 mm. In particular for patient 007P, we see that after the 14th fractions σ_{MLS} is larger than 5 mm.

Figure 6B is the same as Figure 6A, but now for the BEV method. We see that the results are in agreement with Figure 6A: the unchanged patients (squares) had generally a lower standard deviation than the changed patients (triangles), the values are mostly below 3 mm, and the values for the patients that changed are larger.

Table 2 summarizes the results for each patient obtained by the MLS method in terms of average range activity difference observed over all the fractions with respect to the reference. In the first, second and third column, we report the patient ID, Δ_{MLS} and Σ_{MLS}, respectively. The reported error for Δ_{MLS} and Σ_{MLS} is the standard deviation calculated over the various fractions, considering all fractions as independent measurements. The average over the fractions for all the patients that did not present anatomy changes, $<\sigma_{MLS}>$ (see Section *Most-Likely-Shift method*), was calculated to be 2.5 mm. For the two patients that changed, the values for Σ_{MLS} were found to be larger.

The corresponding values for the BEV method, Δ_{BEV} and Σ_{BEV}, are given in the fourth and fifth column of Table 2, respectively. The average over the fractions for all the patients that did not present anatomychanges, $<\sigma_{BEV}>$ (see Section *Comparison with Beam's Eye View method*), was calculated to be 2.3 mm. Again, for the two patients that changed, the values for Σ_{BEV} were found to be larger than those for patients that did not change.

To establish whether the group of changed patients was statistically different from the group of unchanged patients, we

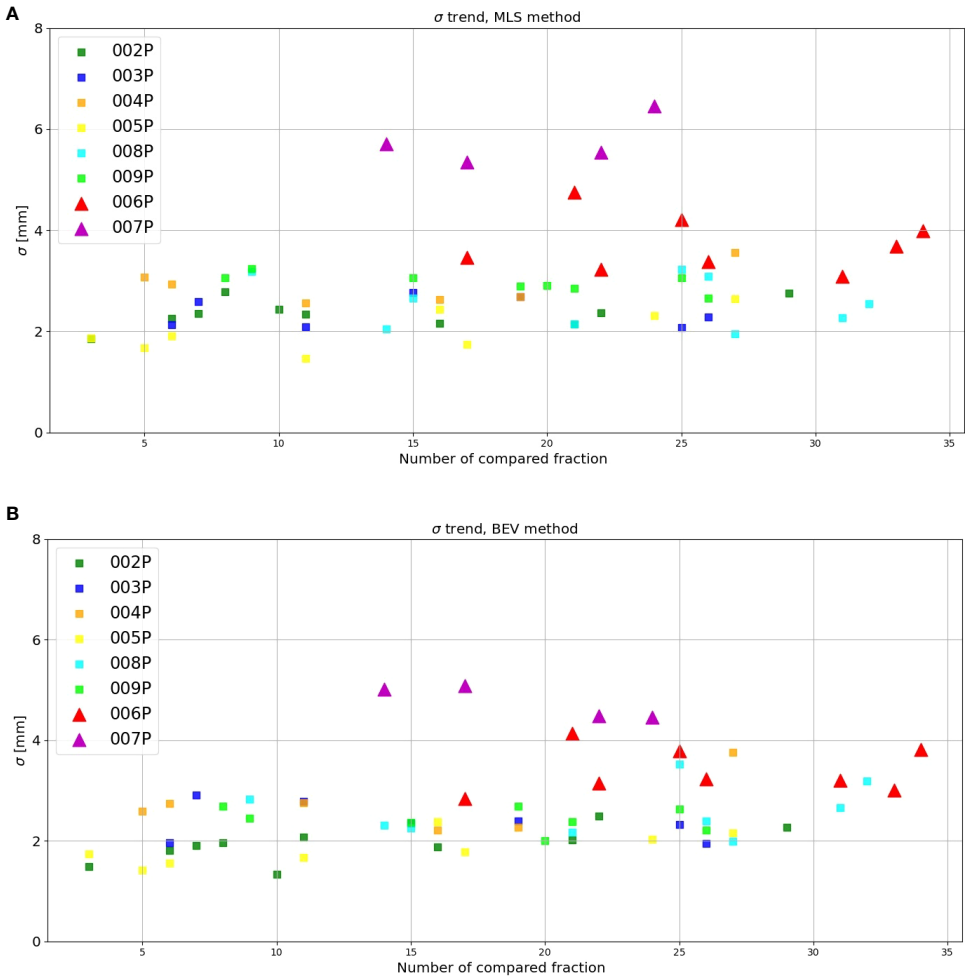

FIGURE 6
Inter-fractional standard deviation of the range difference distribution as obtained with the **(A)** MLS and **(B)** BEV method for each patient (y-axis) as a function of the number of the fraction compared with the reference (x-axis). The triangles stand for those patients where morphological changes where identified in the control CT, while the squares represent the patients that did not show changes.

TABLE 2 For each patient, the average inter-fractional range difference Δ_{MLS} and average standard deviation $\sum_{MLS}$ obtained with the MLS method, together with the corresponding values Δ_{BEV} and $\sum_{MLS}$ for the BEV method.

Patient	Δ_{MLS} [mm]	Σ_{MLS} [mm]	Δ_{BEV} [mm]	Σ_{BEV} [mm]
002P	0.2±1.0	2.3±0.3	0.3±0.9	1.9±0.3
003P	1.2±0.7	2.4±0.3	0.1±1.0	2.4±0.3
004P	-1.0±0.7	2.9±0.3	-0.6±0.9	2.7±0.5
005P	1.0±1.1	2.0±0.4	0.3±1.4	1.8±0.4
008P	2.0±0.8	2.6±0.5	1.5±0.6	2.6±0.5
009P	-0.6±0.9	3.0±0.2	-0.1±0.8	2.4±0.2
006P	1.2±0.6	3.7±0.5	1.6±1.1	3.4±0.4
007P	-0.8±1.1	5.8±0.4	-2.6±1.8	4.8±0.3

performed the Student's t-test over the values of Δ and ∑. While the Δ values were not statistically different (for the MLS method t = 0.27, p = 0.79, and for the BEV method t = 0.67, p = 0.53), for the ∑ values we found a significant difference (for the MLS method t = -3.90, p = 0.008, and for the BEV method t = -4.19, p = 0.006).

Figure 7A displays the outliers $O_{MLS}(x,y,z)$ maps obtained for patient 006P by the MLS method. This is a patient which was subject to small morphological changes, as observed by the radiation oncologist and demonstrated in Figure 2. The colored area represents the pencil beam paths that had anomalous range differences with respect to the reference, see Eq. 2. The red color indicates a positive range difference with respect to the initial situation (overshoot). We see that the red color becomes darker as the number of the treatment fractions increases, strongly indicating a range overshoot that increases along the treatment course. In the penultimate fraction (fraction 33) of the treatment course, we observe range differences as large as 16 mm, i.e., a substantial range overshoot. The cause of the range overshoot becomes clear when looking at Figure 2. Comparing Figures 2A–C (planning CT) with Figures 2D–F (control CT), a cavity is seen that is emptied in the control CT. The fact that the regions highlighted in Figure 7A cover those of the anatomical change in the control CT is a strong indication that our PET images are sensitive to such changes. We therefore believe that the MLS method can be successfully applied to IB-PET images to detect morphological changes like cavity emptying.

Figure 7B shows the outliers maps $O_{BEV}(x,y,z)$ obtained for patient 006P by the BEV method. The colored areas are seen to be similar to those of Figure 7A. Thus, the MLS and BEV method are roughly in agreement.

In Figure 8A we display the outliers maps $O_{MLS}(x,y,z)$ for patient 007P by the MLS method. In this case, the map shows both range overshoots with respect to the reference (identified by the red color) and undershoots (identified by the blue color). By comparing Figure 3 with Figure 8A, we see that the region where the cavity has emptied is only weakly highlighted (orange). The blue zones that are identified may correspond to inflammation effects (see discussion).

Finally, in Figure 8B we demonstrate the outliers maps $O_{BEV}(x,y,z)$, obtained for patient 007P by the BEV method. Also in this case the zones that are highlighted are those affected by beam overshoots (identified by the red color) and undershoots (identified by the blue color) with respect to the reference. They are similar to the regions that were identified with the MLS method, but the colored regions are somewhat larger (see discussion).

4 Discussion

In this work we analyzed for the first time all of the available IB-PET patient data for proton therapy treatments monitored during the INSIDE clinical trial. To evaluate the experimental level of inter-fractional fluctuations in IB-PET images in absence of anatomical changes (sensitivity), we studied six patients that did not show morphological changes. Using the MLS method we found for these patients an overall standard deviation $<\sigma_{MLS}>$ in activity range difference of 2.5 mm. This is smaller than 3 mm, which is the spatial resolution of the INSIDE PET scanner (16).

Regarding the observed differences between changed and unchanged patients, we saw that the average standard deviations Σ_{MLS} were larger for changed patients than those for unchanged patients. Moreover, the outliers maps in Figures 7A, 8A include approximately the regions that were also seen to change in the control CT. In patient 007P, the situation is complicated because the beam goes through highly heterogeneous tissue. Still, the results are encouraging, given the small size of the anatomical changes (order of a few ml).

We evaluated to what extend the values in Table 2 for the MLS analysis were affected by the choice of the parameters chosen (see Section *Most-Likely-Shift method*). Varying the threshold value for inclusion of the profiles from 30% (default) to 20% and 35%, the results did not change significantly. Also, varying the z_{min} (default 15%) between 10% and 20%, no significant range differences were observed. Regarding z_{max} (default 2%), this value should be as small as possible in order to include as much activity in the fall-off region

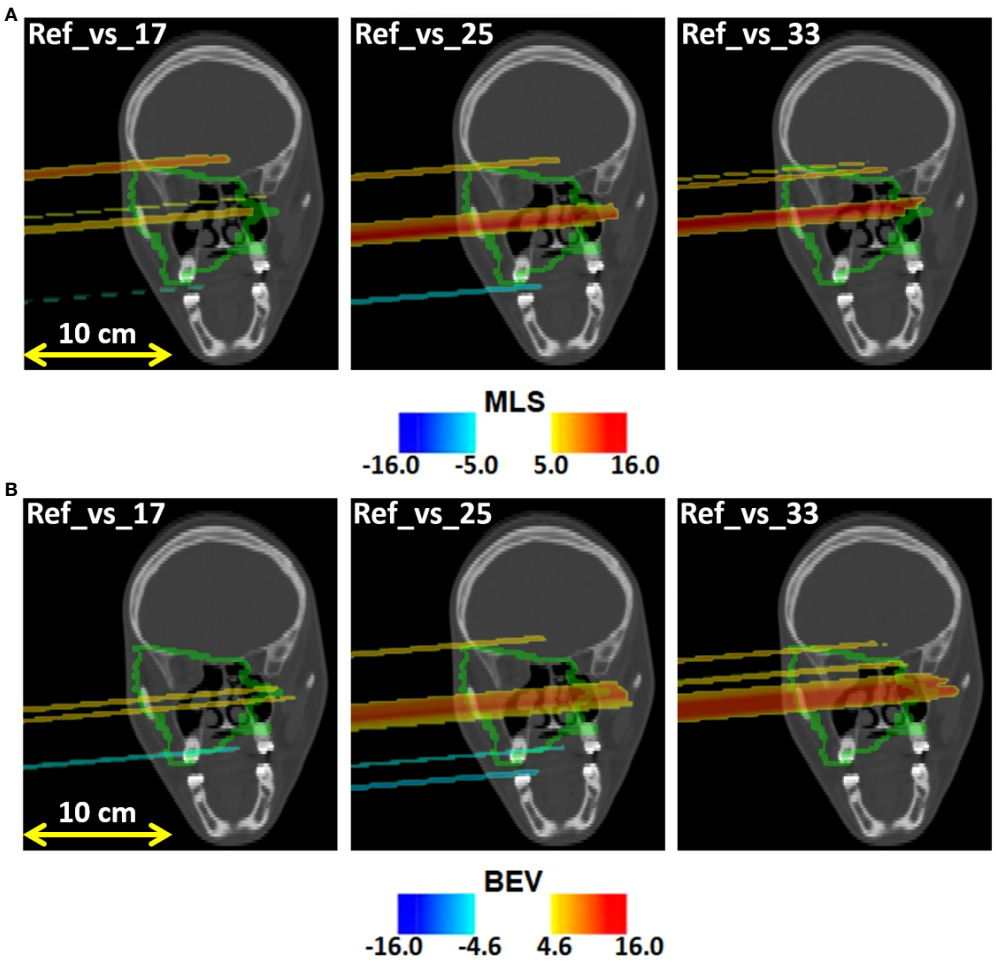

FIGURE 7
Coronal views of the control CT of patient 006P, with the **(A)** MLS outliers map $O_{MLS}(x,y,z)$ and the **(B)** BEV outliers map $O_{BEV}(x,y,z)$ superimposed, obtained by comparing fraction 17, fraction 25, and fraction 33 with the reference. The colored areas are the pencil beam paths that lead to anomalous range differences with respect to the reference, with red indicating a range overshoot with respect to the initial situation. The overshoot is especially pronounced in fraction 25 and 33. The colormaps were obtained as described in 2.5.1 and 2.5.2 for the MLS and the BEV method, respectively.

as possible. However the noise level was found to be 2% so using lower values resulted in inconsistent results. Thus, the results were sufficiently robust.

Comparing the MLS and BEV methods, we saw that the MLS method gave results that were similar to those obtained with the BEV method for all patients. Thus, the methods are mostly in agreement with each other. An example where the methods gave slightly different results was in patient 007P (see Figures 8A, B), where the identified zones were partly different. The advantage of the MLS method with respect to the BEV method is that it evaluates point by point the most suitable shift to align two profiles, and does not only look at the most distal values like the BEV method.

We also verified that our results for the BEV method were in agreement with those published previously for three of the eight patients (20). Small differences could be attributed to differences in the fit procedure and in the choice of the reference PET image, which was in the case of (20) defined to be the first acquired PET fraction, while we took the mean of the first two acquired images as reference.

Several aspects in the analysis deserve more discussion. First, the number of analyzed patients and the number of fractions that could be included in the analysis was small (Table 1). The differences between changed and unchanged patients could in principle have been caused by other factors, including the small statistics of the PET images, differences in patient setup, tumor type, tumor size, depth of the irradiated region, irradiation, etc. The influence of these sources of uncertainty should be investigated in more detail by monitoring more patients. At

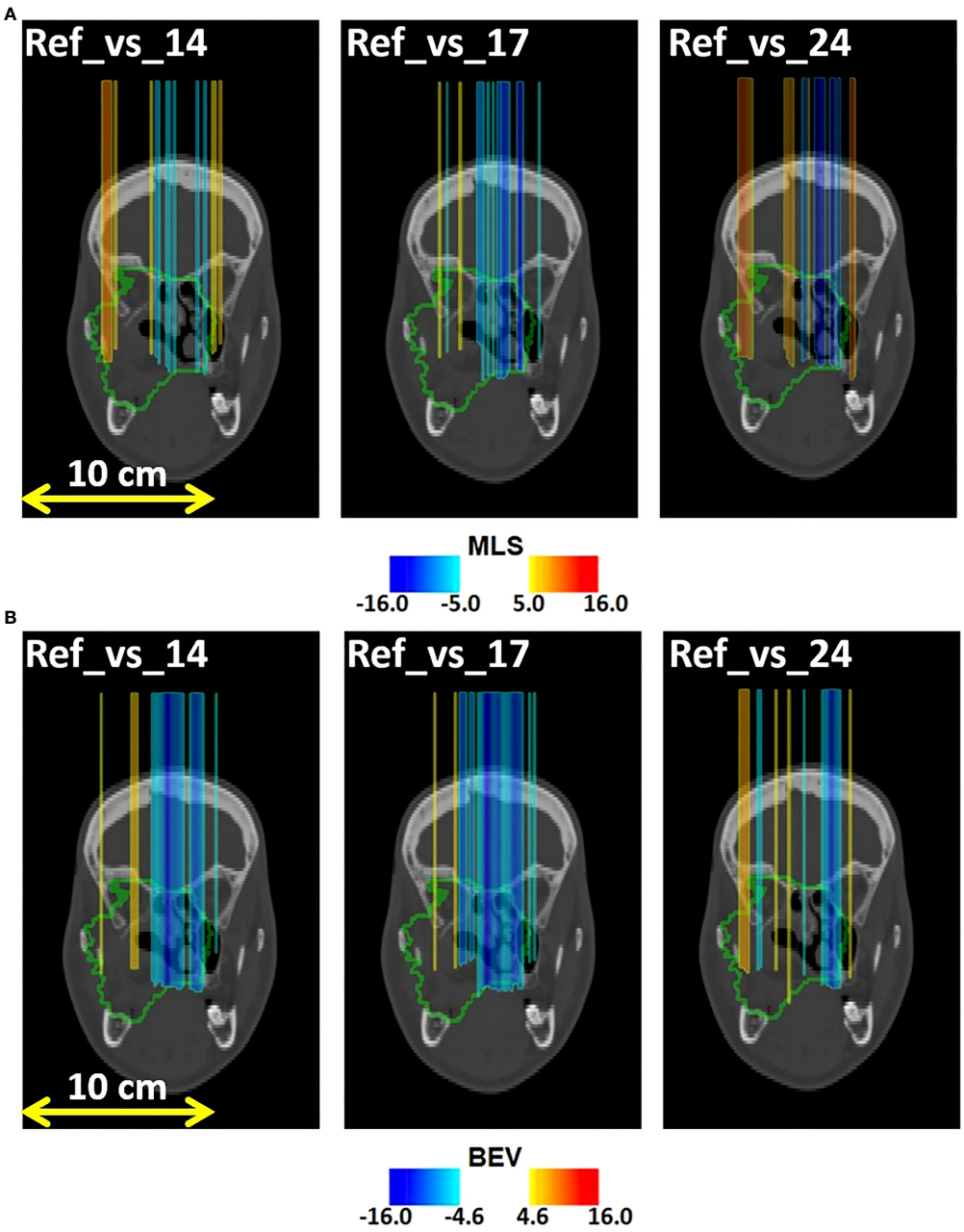

FIGURE 8
Coronal views of the control CT of patient 007P, with superimposed the **(A)** MLS outliers map $O_{MLS}(x,y,z)$ and **(B)** BEV outliers map $O_{BEV}(x,y,z)$, obtained by comparing fraction 14, fraction 17, and fraction 24 with the reference. The colored areas are the pencil beam paths that lead to anomalous range differences with respect to the reference, with red and blue indicating a range overshoot and undershoot with respect to the initial situation, respectively. Most clear are the beam undershoots (the blue areas). The colormaps were obtained as described in 2.5.1 and 2.5.2 for the MLS and the BEV method, respectively.

the same time, the outliers maps agreed approximately with the zones that were seen to change in the control CT. Thus, we believe that the INSIDE IB-PET images can give indications about inter-fractional range differences. The MLS and BEV methods can both be applied for this purpose. This was especially visible in Figures 7, 8, where the colors indicating beam overshoots and undershoots become more intense as the number of treatment fractions increased. However, the effect is small and more patient data are needed to confirm whether such trends through the course of treatment are observable.

Second, it must be noted that we monitored only one of the fields, i.e., the first field delivered. In some cases we had $N_{fields} = 3$ (see Table 1), resulting in a very limited overall statistics of the PET signal. This can possibly be improved by assuring that the field delivered first is the one with largest activity, or by combining fields (36).

Finally, the size of the morphological changes of patient 6 and 7 was small (order of a few ml). In fact, these changes were considered small enough to not require replanning, since the recalculation of the treatment plan on such modified anatomy did not show any clinically significant modification of the DVHs both for target and OARs. Increasing the number of patients with larger expected changes is foreseen for the second phase of the INSIDE clinical trial. This can better confirm the validity of the INSIDE in-beam PET system in detecting morphological changes.

Despite the small number of patients and fractions that could be included in this study, the above results are encouraging. For future in-beam PET data acquisitions, we suggest to only compare PET images which are acquired under approximately the same irradiation conditions, to monitor the first field delivered to avoid contamination from other fields, and to monitor as many fractions as possible.

5 Conclusion

In this work we performed an inter-fractional range difference analysis including all the available patient data for proton treatments acquired during the INSIDE clinical trial: six patients not subject to morphological change, and two patients subject to morphological change. We applied the Most-Likely-Shift (MLS) method for detecting inter-fractional range differences, which, to the best of our knowledge, was the first time it was applied for IB-PET images. It was compared with the Beam Eye View (BEV), that was previously applied to a subset of the patients included in the clinical trial.

When putting together all fractions and all patients that did not have morphological changes, the standard deviation of the range variations in activity profiles, $<\sigma_{MLS}>$, was found to be 2.5 mm with the MLS method. The corresponding value for the BEV method was $<\sigma_{BEV}>$ =2.3 mm. On the other hand, for patients where anatomical changes occurred, we found larger standard deviation values.

For the patients with anatomical changes we created outliers maps to indicate anomalous range variations. These were superimposed on the control CT, and the regions affected by an anomalous range difference approximately covered those with real anatomical variations observed in the control CT. The results are encouraging and suggest that the MLS method can possibly be used as a support tool by clinical personnel to detect anomalous situations during the treatment course and to guarantee the effectiveness of the treatment plan.

Data availability statement

The data that support the findings of this study are partly available on request from the corresponding author. The data are not publicly available due to privacy or ethical restrictions.

Ethics statement

The studies involving human participants were reviewed and approved by Comitato etico del Policlinico San Matteo di Pavia. The patients/participants provided their written informed consent to participate in this study.

Author contributions

The analysis and manuscript was prepared by MMog, ACK and MGB. All authors have contributed to the publication, being variously involved in the design and the construction of the detectors, in writing software, calibrating subsystems, operating the detectors, acquiring data and finally analysing the processed data. The INSIDE Collaboration members discussed and approved the scientific results reported in the submitted document. The work was subject to an internal collaboration-wide review process. All authors contributed to the article and approved the submitted version.

Funding

The INSIDE project was funded by the Italian Ministry of Education (PRIN MIUR 2010P98A75, 2013–2016), the Italian Institute of Nuclear Physics (RDH and INFN-RT2 PETRA 172800 projects, since 2016), the Historical Museum of Physics and the Enrico Fermi Study and Research Center, the Tuscany Government (POR FSE 2014–2020, INFN-RT2 PETRA 172800 Project, 2018-2019), and the CNAO Foundation (INSIDE2, since 2017).

Conflict of interest

The authors declare that the research was conducted in the absence of any commercial or financial relationships that could be construed as a potential conflict of interest.

Publisher's note

References

1. Loeffler J, Durante M. Charged particle therapy–optimization, challenges and future directions. *Nat Rev Clin Oncol* (2013) 10:411–24. doi: 10.1038/nrclinonc.2013.79

2. Paganetti H. *Proton therapy physics*. Boca Raton, Florida:CRC Press (2012).

3. Paganetti H, Botas P, Sharp G, Winey B. Adaptive proton therapy. *Physics in Medicine & Biology 66* (2021). doi: 10.1088/1361-6560/ac344f

4. Albertini F, Matter M, Nenoff L, Zhang Y, Lomax A. Online daily adaptive proton therapy. *Br J Radiol* (2020) 93:20190594. doi: 10.1259/bjr.20190594

5. Placidi L, Bolsi A, Lomax AJ, Schneider RA, Malyapa R, Weber DC, et al. Effect of anatomic changes on pencil beam scanned proton dose distributions for cranial and extracranial tumors. *Int J Radiat Oncol Biol Phys* (2017) 97:616–23. doi: 10.1016/j.ijrobp.2016.11.013

6. Cubillos-Mesías M, Troost EG, Lohaus F, Agolli L, Rehm M, Richter C, et al. Including anatomical variations in robust optimization for head and neck proton therapy can reduce the need of adaptation. *Radiother Oncol* (2019) 131:127–34. doi: 10.1016/j.radonc.2018.12.008

7. Mackay R. Image guidance for proton therapy. *Clin Oncol* (2018) 30:293–298. doi: 10.1016/j.clon.2018.02.004

8. Morgan H, Sher D. Adaptive radiotherapy for head and neck cancer. *Cancers Head Neck* (2020) 5. doi: 10.1186/s41199-019-0046-z

9. Kraan AC, van de Water S, Teguh DN, Al-Mamgani A, Madden T, Kooy HM, et al. Dose uncertainties in impt for oropharyngeal cancer in the presence of anatomical, range, and setup errors. *Int J Radiat Oncol Biol Phys* (2013) 87(5):888–96. doi: 10.1016/j.ijrobp.2013.09.014

10. Parodi K, Polf J. *In vivo* range verification in particle therapy. *Med Phys* (2018) 45:e1036–50. doi: 10.1002/mp.12960

11. Enghardt W, Crespo P, Fiedler F, Hinz R, Parodi K, Pawelke J, et al. Charged hadron tumour therapy monitoring by means of pet. *Nucl Instruments Methods Phys Res Section A: Accelerators Spectrometers Detectors Associated Equip* (2004) 525:284–88. doi: 10.1016/j.nima.2004.03.128

12. Nishio T, Miyatake A, Ogino T, Nakagawa K, Saijo N, Esumi H. The development and clinical use of a beam on-line pet system mounted on a rotating gantry port in proton therapy. *Int J Radiat Oncol Biol Phys* (2010) 76:277–86. doi: 10.1016/j.ijrobp.2009.05.065

13. Knopf A, Lomax A. *In vivo* proton range verification: a review. *Phys Med Biol* (2013) 58:R131–160. doi: 10.1088/0031-9155/58/15/R131

14. Kraan AC. Range verification methods in particle therapy: Underlying physics and monte carlo modeling. *Front Oncol* (2015) 5:150. doi: 10.3389/fonc.2015.00150

15. Dendooven P, Buitenhuis T, Diblen F, Heeres P, Biegun A, Fiedler F, et al. Short-lived positron emitters in beam-on pet imaging during proton therapy. *Phys Med Biol* (2015) 60:8923–47. doi: 10.1088/0031-9155/60/23/8923

16. Bisogni G, Attili A, Battistoni G, Belcari N, Camarlinghi N, Cerello P, et al. Inside in-beam positron emission tomography system for particle range monitoring in hadrontherapy. *J Med Imaging* (2016) 4(1)011005–12. doi: 10.1117/1.JMI.4.1.011005

17. Rossi S. The status of cnao. *Eur Phys J Plus* (2011) 126:78–116. doi: 10.1140/epjp/i2011-11078-8

18. Traini G, Mattei I, Battistoni G, Giuseppina M, De Simoni M, Dong Y, et al. Review and performance of the dose profiler, a particle therapy treatments online monitor. *Physica Med* (2019) 65:84–93. doi: 10.1016/j.ejmp.2019.07.010

19. Frey K, Unholtz D, Bauer J, Debus J, Min CH, Bortfeld T, et al. Automation and uncertainty analysis of a method for *in-vivo* range verification in particle therapy. *Phys Med Biol* (2014) 59:5903–19. doi: 10.1088/0031-9155/59/19/5903

20. Fiorina E, Ferrero V, Baroni G, Battistoni G, Belcari N, Camarlinghi N, et al. Detection of interfractional morphological changes in proton therapy: A simulation and *in vivo* study with the inside in-beam pet. *Front Phys* (2021) 8:578388. doi: 10.3389/fphy.2020.578388

21. Piliero M, Belcari N, Bisogni M, Camarlinghi N, Cerello P, Coli S, et al. First results of the INSIDE in-beam PET scanner for the on-line monitoring of particle therapy treatments. *J Instrumentation* (2016) 11. doi: 10.1088/1748-0221/11/12/c12011

22. Ferrero V, Fiorina E, Morrocchi M, Pennazio F, Baroni G, Battistoni G, et al. Online proton therapy monitoring: Clinical test of a silicon-photodetector-based in-beam pet. *Sci Rep* (2018) 8. doi: 10.1038/s41598-018-22325-6

23. Kostara E, Sportelli G, Belcari N, Camarlinghi N, Cerello P, Guerra AD, et al. Particle beam microstructure reconstruction and coincidence discrimination in PET monitoring for hadron therapy. *Phys Med Biol* (2019) 64:035001. doi: 10.1088/1361-6560/aafa28

24. Piliero MA, Pennazio F, Bisogni MG, Camarlinghi N, Cerello PG, Guerra AD, et al. Full-beam performances of a PET detector with synchrotron therapeutic proton beams. *Phys Med Biol* (2016) 61:N650–66. doi: 10.1088/0031-9155/61/23/n650

25. Hamamatsu, Photonics. *Photon is our business*. Japan:Vendor's site (2016).

26. Zagumennyi A, Zavartsev Y, Kutovoi S. *Scintillation substances (variants). patent US 7132060*. (2004).

27. Doroud K, Williams M, Zichichi A, Zuyeuski R. Comparative timing measurements of lyso and lfs-3 to achieve the best time resolution for tof-pet. *Nucl Instruments Methods Phys Res Section A: Accelerators Spectrometers Detectors Associated Equip* (2015) 793:57–61. doi: 10.1016/j.nima.2015.04.056

28. Rolo MD, Bugalho R, Gonçalves F, Mazza G, Rivetti A, Silva JC, et al. TOFPET ASIC for PET applications. *J Instrumentation* (2013) 8:C02050–0. doi: 10.1088/1748-0221/8/02/c02050

29. Camarlinghi N, Sportelli G, Battistoni G, Belcari N, Cecchetti M, Cirrone GAP, et al. An in-beam PET system for monitoring ion-beam therapy: test on phantoms using clinical 62 MeV protons. *J Instrumentation* (2014) 9:C04005–5. doi: 10.1088/1748-0221/9/04/c04005

30. Crespo P, Shakirin G, Enghardt W. On the detector arrangement for in-beam pet for hadron therapy monitoring. *Phys Med Biol* (2006) 51. doi: 10.1088/0031-9155/51/9/002

31. Kraan A, Berti AC, Retico A, Baroni G, Battistoni G, Belcari N, et al. Localization of anatomical changes in patients during proton therapy with in-beam pet monitoring: A voxel-based morphometry approach exploiting monte carlo simulations. *Med Phys* (2022) 49:23–40. doi: 10.1002/mp.15336

32. Giordanengo S, Garella M, Marchetto F, Bourhaleb F, Ciocca M, Mirandola A, et al. The cnao dose delivery system for modulated scanning ion beam radiotherapy. *Med Phys* (2015) 42:263–275. doi: 10.1118/1.4903276

33. Zhang J, Lu Y, Sheng Y, Wang W, Hong Z, Sun Y, et al. A comparative study of two *in vivo* pet verification methods in clinical cases. *Front Oncol* (2021) 11:617787. doi: 10.3389/fonc.2021.617787

34. Knopf A, Parodi K, Paganetti H, Cascio E, Bonab A, Bortfeld T. Quantitative assessment of the physical potential of proton beam range verification with PET/CT. *Phys Med Biol* (2008) 53:4137–51. doi: 10.1088/0031-9155/53/15/009

35. Pennazio F, Battistoni G, Bisogni MG, Camarlinghi N, Ferrari A, Ferrero V, et al. Carbon ions beam therapy monitoring with the INSIDE in-beam PET. *Phys Med Biol* (2018) 63:145018–145029. doi: 10.1088/1361-6560/aacab8

36. Ferrero V, Bisogni MG, Camarlinghi N, Fiorina E, Giraudo G, Morrocchi M, et al. Double-field hadrontherapy treatment monitoring with the inside in-beam pet scanner: Proof of concept. *IEEE Trans Radiat Plasma Med Sci* (2018) 2:588–93. doi: 10.1109/TRPMS.2018.2870478

Frontiers in Oncology

Advances knowledge of carcinogenesis and tumor progression for better treatment and management

The third most-cited oncology journal, which highlights research in carcinogenesis and tumor progression, bridging the gap between basic research and applications to imrpove diagnosis, therapeutics and management strategies.

Discover the latest Research Topics

See more →

Frontiers

Avenue du Tribunal-Fédéral 34
1005 Lausanne, Switzerland
frontiersin.org

Contact us

+41 (0)21 510 17 00
frontiersin.org/about/contact